

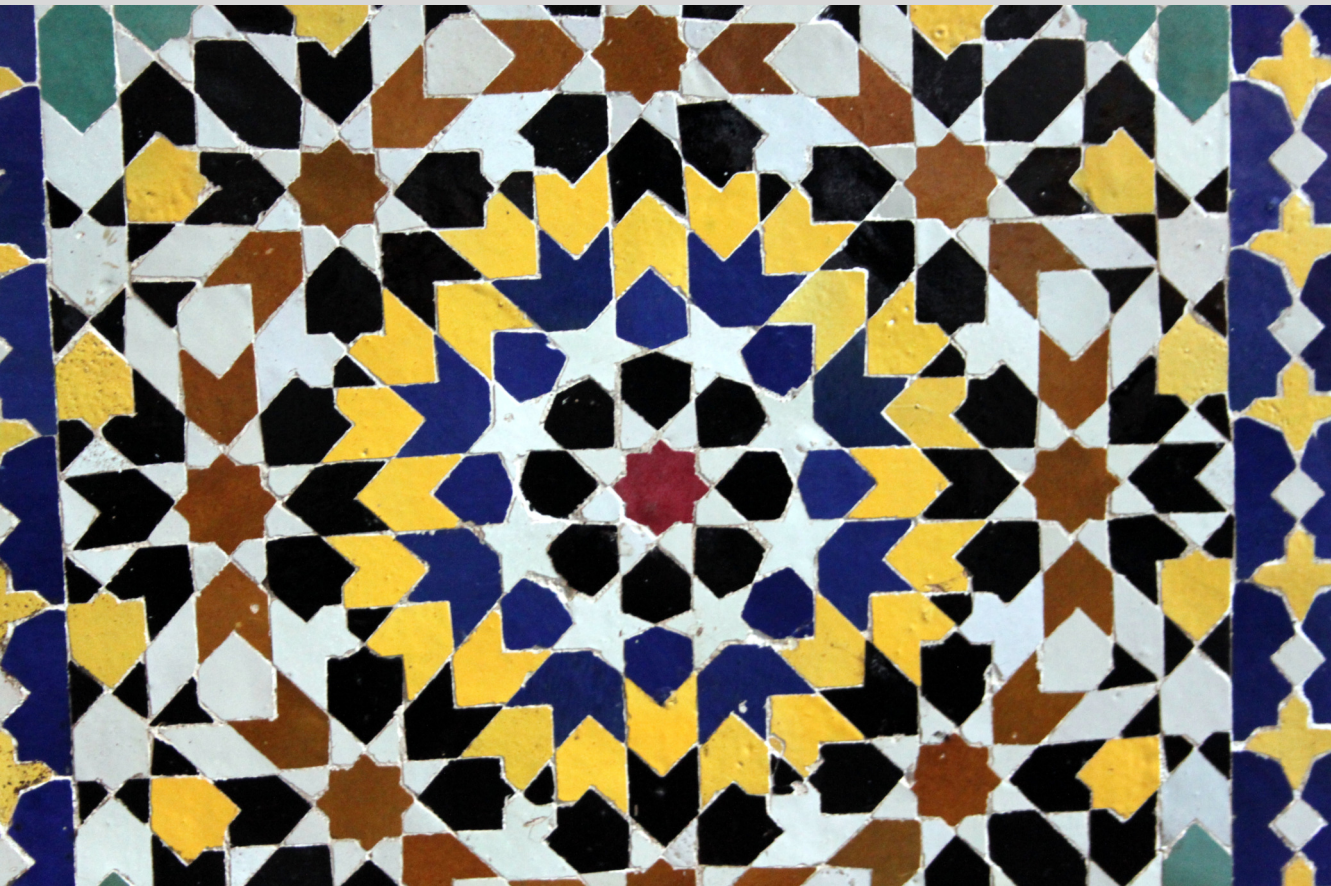


UNIVERSITAT  
ROVIRA i VIRGILI

## Advanced Characterisation and Modelling of Charge Transfer in Perovskite Solar Cells

---

ILARIO GELMETTI



DOCTORAL THESIS  
2019







Ilario Gelmetti

# ADVANCED CHARACTERIZATION AND MODELLING OF CHARGE TRANSFER IN PEROVSKITE SOLAR CELLS

DOCTORAL THESIS IN ELECTRONIC ENGINEERING

Supervised by: Prof. Dr. Emilio Jose Palomares Gil

Departament d'Enginyeria Electrònica, Elèctrica i Automàtica  
Palomares Research Group



UNIVERSITAT ROVIRA I VIRGILI  
INSTITUTE OF CHEMICAL RESEARCH OF CATALONIA

---

Tarragona, July 2019





UNIVERSITAT  
ROVIRA i VIRGILI

FAIG CONSTAR que aquest treball, titulat "Advanced Characterization and Modelling of Charge Transfer in Perovskite Solar Cells", que presenta Ilario Gelmetti per a l'obtenció del títol de Doctor amb Menció Internacional, ha estat realitzat sota la meva direcció al ICIQ i al Departament d'Enginyeria Electrònica, Elèctrica i Automàtica d'aquesta universitat.

---

HAGO CONSTAR que el presente trabajo, titulado "Advanced Characterization and Modelling of Charge Transfer in Perovskite Solar Cells", que presenta Ilario Gelmetti para la obtención del título de Doctor con Mención Internacional, ha sido realizado bajo mi dirección en el ICIQ y en el Departamento de Ingeniería Electrónica, Eléctrica y Automática de esta universidad.

---

I STATE that the present study, entitled "Advanced Characterization and Modelling of Charge Transfer in Perovskite Solar Cells", presented by Ilario Gelmetti for the award of the degree of Doctor with International Mention, has been carried out under my supervision at the ICIQ and the Department of Electrical Electronic Engineering and Automation of this university.

---

Tarragona, 2019-05-15

El director de la tesi doctoral  
El director de la tesis doctoral  
Doctoral Thesis Supervisor

Prof. Dr. Emilio Jose Palomares Gil



# Acknowledgements

“ubuntu”

“*I am what I am because of who we all are.*” (L. Gbowee definition)

Aaaaaand here I am, in the very last hour of thesis writing. Here I'll thank all of you who made these four (and a half!) years a truly enriching experience.

In latitude order, Andrea and Daniel thanks for all the amazing moments in both the hemispheres!

The mosaicist who created the amazing artwork I used for the front cover, thanks!

Thanks to all my flatmates in Tarragona, each of you was amazing in a different way!

Thanks to all the Iberian hacktivists, activists, libertarians, political okupas, cooperativists, and social movement members: you are amazing. Just some names in random order: Diana, G10h4ck, Marc, Eva, Anna, Nuria, Gemma, Josep, Gianni, David, Viktor, Radikal, Bryan, Lluis, Dj Matusalem, Laia, Robi, Miguel, Marc, Aurora thanks! And some more: thanks to the whole LibreMesh community. Also thanks to all the people developing all the free-as-in-free-speech software I used for writing this thesis!

Thanks to all the people I had the chance to work with, I learnt a lot from you, both on the human and on the scientific point of view :D Thanks to Tsung Yu, Ece, Santi, Cristina, Jonas, Dora, Eyyup, Gowri, Lydia, Lijun, Sarika, Georgiana, Daniel, Iker for all the good time! Thanks to Jesús, Nuria, Werther (ciao Wertheer!!!), Maria for helping me with all the great scientific discussions!

Thanks to all the people that made hanging out in Tarragona and Barcelona a surprise every time: Michael, Micol, Stefano, Franz, Giuliano,

Irene, Barbara, Marcos, Laura, Luca, Raffaela, Antonella, Elena, Marc, Ivan, Iacopo I constantly missss you.

Thanks to Pilar and Vicenç for accepting me like one more in their family!

Thanks to my source of love, entropy, happiness, energy, and optimism for the future together: it looks shiny! You have no idea of how special your are, thanks Sofia!

Thanks to my supervisor Emilio Palomares, for supporting and trusting me so much, I hope you won't regret it!

Thanks to Sofia, Phil, Nuria, Maria, and Jesús for helping me with the correction of this thesis, it was most useful!

Thanks to Lannari Mannari all over the world and in Verona, just mentioning the kernel of it: Bruz and Cò < 3 < 3, Warrins, Skizzo, Dani, Lukez, Ghidappo, Tama, Stekkas, Sara looking forward to see you here or there!

Thanks to all the other amazing humans in Verona: Naar, Erica, Giulia, Pugliezza, Anteo, Ale, Kandels, and all the folk dancing people!

Thanks to my mother for always reminding me that job is far from being the most important thing in life and for taking care of all the mess I left behind in Verona (and for being amazing, you are).

Thanks to my Rosetta, Valentino, Teresa, Gianni, Maria Rosa, Giuseppe, Lucia for all the support over all this time!

Thanks to all the people who helped me to survive in London: Marche, Annalisa, Gianmaria, William, Francesco every excursion and every lunch or dinner I felt like at home, thanks, seriously.

Thanks to Phil, Mohammed, and Jun for being so amazing, each of you, I loved working, travelling, and hanging out with you! I hope to meet you as frequently as possible in the future!

Thanks to Piers RadioFrequency [4] Barnes and to Jenny Nelson: all your curiosity, enthusiasm, honesty and ability to motivate students with a positive attitude is the best science can hope for!

Copyright 2019 Ilario Gelmetti

Some rights are reserved as specified by Creative Commons Attribution-NonCommercial-NoDerivs version 3.0 licence, which can be accessed on <https://creativecommons.org/licenses/by-nc-nd/3.0/>.



# Contents

<b>Acknowledgements</b>	<b>i</b>
<b>Abstract</b>	<b>xx</b>
<b>Summary of the Thesis</b>	<b>xxii</b>
<b>Contributions to Scientific Literature</b>	<b>xxiv</b>
<b>Oral and Poster Presentations at Conferences</b>	<b>xxv</b>
<b>1 Introduction</b>	<b>1</b>
1.1 Why Photovoltaics? . . . . .	3
1.2 Relevant Physics for Stacked Semiconductor Thin Films	5
1.3 Perovskite Solar Cells . . . . .	23
1.4 Motivation and Aims . . . . .	29
<b>2 Experimental Methods</b>	<b>31</b>
2.1 Materials . . . . .	33
2.2 Equipment . . . . .	34
2.3 Synthesis, Handling and Purification . . . . .	39
2.4 Perovskite Solar Cell Fabrication . . . . .	42
<b>3 Characterisation Techniques: Description and Interpretation</b>	<b>51</b>
3.1 Conventions and General Remarks . . . . .	54
3.2 Current-Voltage Sweeps . . . . .	60
3.3 $V_{OC}$ and $J_{SC}$ Dependence on Light Intensity . . . . .	63
3.4 Charge Extraction (CE) . . . . .	66
3.5 Transient PhotoVoltage (TPV) . . . . .	78
3.6 Transient PhotoVoltage Referenced to Charge Density (TPV-CE) . . . . .	92

3.7	Transient PhotoCurrent (TPC) . . . . .	95
3.8	Differential Capacitance (DC) . . . . .	98
3.9	Voltage and Current Reconstruction . . . . .	104
3.10	Impedance Spectroscopy . . . . .	105
<b>4</b>	<b>Comparison of HTMs in Bottom Cathode CsFAMAP-bIBr Solar Cells</b>	<b>107</b>
4.1	Introduction . . . . .	109
4.2	Molecular Characterisation . . . . .	112
4.3	Thin Films Morphological Characterisation . . . . .	114
4.4	Current-Voltage Sweeps . . . . .	117
4.5	Chemical Capacitance . . . . .	118
4.6	Transient Lifetime . . . . .	119
4.7	Work function of Stacked Materials . . . . .	122
4.8	Conclusions . . . . .	123
<b>5</b>	<b>Insights into Charge Storage via Thickness Variation of Layers in Top Cathode MAPI Solar Cells</b>	<b>125</b>
5.1	Introduction . . . . .	128
5.2	Varying $\text{MAPbI}_3$ Thickness (Absorber) . . . . .	129
5.3	Varying $\text{PC}_{70}\text{BM}$ Thickness (ETM) . . . . .	134
5.4	Varying PEDOT:PSS Thickness (HTM) . . . . .	137
5.5	Conclusions . . . . .	138
<b>6</b>	<b>Modelling the Influence of Ionic Migration on Impedance Spectroscopy</b>	<b>139</b>
6.1	Introduction . . . . .	142
6.2	Driftfusion software . . . . .	144
6.3	Simulating impedance spectroscopy . . . . .	145
6.4	Simulated apparent capacitance spectra characteristics .	150
6.5	Comparison of simulated and experimental impedance spectra	162
6.6	Further development . . . . .	164
6.7	Implementation of impedance spectroscopy . . . . .	167
6.8	Conclusions . . . . .	175
<b>7</b>	<b>Software Development for Drift-Diffusion Modelling, Data Acquisition, and Data Analysis</b>	<b>177</b>
7.1	Contributions to Driftfusion . . . . .	181
7.2	PyPV: An easy Current-Voltage curves acquisition interface	194
7.3	Robust and quick data analysis via R scripts . . . . .	205
7.4	Contributions to mppTracker . . . . .	210

<b>Overall Conclusions</b>	<b>211</b>
<b>Bibliography</b>	<b>215</b>

# List of Figures

1.1	Geographical distribution of development, sunlight and consumption. . . . .	4
1.2	Representation of HOMO and LUMO levels. . . . .	5
1.3	Schematic representation of the density of states, Fermi-Dirac distribution, and electronic population for a crystalline intrinsic semiconductor. . . . .	7
1.4	Representation of the relation between quasi-Fermi level distance from respective band and carriers concentration. . . . .	8
1.5	Representation of drift and diffusion of charged particles. . . . .	10
1.6	Schematics of a <i>p-i-p</i> homojunction, with emphasis on depletion layers and representation of Poisson equation. . . . .	11
1.7	Representation of current and displacement current. . . . .	13
1.8	Electric field by two planes of opposite charges. . . . .	14
1.9	Representation of absorption and generation of an exciton. . . . .	19
1.10	Simulation of a <i>p-i-n</i> homojunction device illuminated at open circuit. . . . .	21
1.11	Crystal structure of $\text{MAPbI}_3$ perovskite. . . . .	22
1.12	NREL chart of “Best Research-Cell Efficiencies” . . . . .	23
2.1	Solar cells layers layout. . . . .	43
2.2	Top cathode solar cell. . . . .	44
2.3	Bottom cathode solar cell. . . . .	46
2.4	Degradation due to oxygen and illumination combination. . . . .	49
3.1	Solar cells parameters from current-voltage sweeps. . . . .	55
3.2	Illuminated area after a shadowing mask. . . . .	57
3.3	Kinks in J-V sweep due to autoscale. . . . .	60
3.4	Hysteretic current-voltage scan. . . . .	61
3.5	Simulated effect on the ionic profile of the application of a voltage equal to the built-in voltage. . . . .	65
3.6	Scheme of CE experiment. . . . .	66

3.7	Strategies for reducing the instrumental noise in a single CE integration. . . . .	68
3.8	Evolution of energy levels during CE. . . . .	70
3.9	Simulation of a single CE current profiles without or with mobile ions. . . . .	71
3.10	Charge extraction time is related to a RC time. . . . .	72
3.11	Comparison between CE and TPV exponential decay times. . . . .	73
3.12	Simulated electron density profile during a CE experiment. . . . .	75
3.13	Simulated energy levels in a homojunction device with mobile ions at open circuit conditions at different light intensities. . . . .	77
3.14	Simulation of a complete CE experiment: charge <i>versus</i> light bias with or without mobile ions. . . . .	78
3.15	Scheme of TPV experiment. . . . .	79
3.16	Robust and normal fitting comparison. . . . .	81
3.17	Example of lifetimes <i>versus</i> light bias plot obtained from a TPV experiment. . . . .	84
3.18	Simulation of TPV at low background intensities with mobile ions. . . . .	86
3.19	Simulated TPV without and with mobile ions. . . . .	88
3.20	TPV time has an upper bound due to discharge through oscilloscope. . . . .	90
3.21	Example of TPV-CE processed in different ways. . . . .	93
3.22	Scheme of TPC experiment. . . . .	95
3.23	Example of TPC experiment at dark and 1 sun background illumination. . . . .	96
3.24	Capacitance dependence on applied voltage. . . . .	100
3.25	Comparison of methods for obtaining DC experiments. .	102
4.1	Chemical structures of HTM utilised for bottom cathode solar cells. . . . .	110
4.2	Representation of HOMO and LUMO energies for the materials composing the studied cells. . . . .	113
4.3	Topography of HTM layered on top of perovskite, measured <i>via</i> AFM. . . . .	115
4.4	X-Ray diffraction pattern for complete devices with different HTM. . . . .	116
4.5	Current-voltage sweeps for champion devices with different HTM. . . . .	118

4.6	CE and DC of devices with different HTM, highlighting the varying chemical capacitance. . . . .	119
4.7	Total carrier lifetime for devices with different HTM. . . . .	121
5.1	Top view ESEM images of annealed perovskite layers with various thicknesses. . . . .	131
5.2	Current-voltage sweeps for champion devices with different MAPI thicknesses. . . . .	132
5.3	CE and DC of devices with different MAPI thicknesses, highlighting the varying geometric capacitance. . . . .	134
5.4	Current-voltage sweeps for champion devices with different PC <sub>70</sub> BM thicknesses. . . . .	135
5.5	CE and DC of devices with different PC <sub>70</sub> BM thicknesses, highlighting the varying geometric capacitance. . . . .	136
5.6	Current-voltage sweeps for champion devices with different PEDOT:PSS thicknesses. . . . .	137
5.7	CE and DC of devices with different PEDOT:PSS thicknesses, highlighting the varying geometric capacitance. . . . .	138
6.1	Example of demodulation on a large perturbation simulation.	147
6.2	Simulated apparent capacitance spectra of an illuminated perovskite solar cell at open circuit and dark applied voltage.	151
6.3	Net charge profile variation in a period of oscillating voltage at high and mid frequencies. . . . .	152
6.4	Simulated accumulation capacitance spectra compared with capacitance due to charge accumulation. . . . .	154
6.5	Capacitance representation with or without mobile ions.	154
6.6	Simulated apparent capacitance and phase spectra compared with capacitance due to ionic migration. . . . .	156
6.7	Band diagram, energy barriers, and circuit representation of a diode or a transistor. . . . .	158
6.8	Simulated apparent capacitance spectra and Nyquist plot compared with capacitance due to recombination current.	160
6.9	Simulated Nyquist plot for large perturbations simulation.	162
6.10	Experimental data from impedance spectroscopy. . . . .	163
6.11	Preliminary simulations of impedance on heterojunction model. . . . .	165
6.12	Example of Fourier transformation of bi-exponential current decays to impedance spectra. . . . .	167
6.13	Flowchart of impedance simulation modules. . . . .	168

7.1	Legacy software for current-voltage sweep measurement.	194
7.2	PyPV graphical user interface. . . . .	197
7.3	Current-voltage plot window of PyPV. . . . .	200
7.4	Additional output of PyPV. . . . .	202
7.5	Example of maximum power tracking measurement. . . .	210

# List of Tables

2.1	PEDOT:PSS deposition conditions and resulting thickness	44
2.2	MAPbI <sub>3</sub> two step deposition: conditions for the PbI <sub>2</sub> and MAI spin coating and resulting perovskite film thickness.	45
2.3	PC <sub>70</sub> BM deposition conditions and resulting thickness, with a concentration of 30 mg ml <sup>-1</sup>	46
4.1	Molecular properties of tested HTM.	111
4.2	HTM and related average performances of bottom cathode cells.	117
4.3	Parameters fitted from TPV, TPV-CE, and TPV-DC data, from devices with different HTM.	120
4.4	Work function of different HTM when deposited on perovskite.	122
5.1	Layers thicknesses and related average performances of top cathode cells.	129
5.2	Parameters fitted from CE and DC data, from devices with different layers' thicknesses.	133
6.1	Drift-diffusion simulation parameters.	146

# Glossary, Acronyms, and Symbols

**A** area.

**AC-AFM** alternating current atomic force microscopy.

**AFM** atomic force microscopy.

**$\alpha$**  power law exponent in current *versus* illumination intensity relationship.

**C** capacitance.

**$C_{DC}$**  Voltage dependent capacitance obtained from DC measurements.

**$C_g$**  geometric capacitance.

**$C_{ion}$**  ionic capacitance.

**CE** charge extraction.

**CPD** contact potential difference.

**CsFAMAPbIBr** cesium formamidinium methylammonium lead iodide bromide.

**d** distance, thickness.

**DC** differential capacitance.

**DCM** dichloromethane.

**DFT** density functional theory.

**DMF** N,N-dimethylformamide.

**DMSO** dimethyl sulfoxide.

**DOS** density of states.

**DSSC** dye sensitized solar cells.

**$E_{\text{CB}}$**  conduction band energy.

**$E_g$**  band gap.

**$E_{\text{VB}}$**  valence band energy.

**EDX** energy-dispersive X-ray analysis.

**$\epsilon_r$**  relative permittivity.

**$\epsilon_0$**  electric constant.

**EQE** external quantum efficiency.

**ESEM** environmental scanning electron microscopy.

**ETM** electron transporting material.

**$f$**  mathematical function.

**FAI** formamidinium iodide.

**FAMAPbIBr** formamidinium methylammonium lead iodide bromide.

**FF** fill factor.

**$\nu$**  frequency.

**FTO** fluorine tin oxide.

**$g$**  charges photo-generation rate.

**GUI** graphical user interface.

**HOMO** highest-energy occupied molecular orbital.

**HTM** hole transporting material.

**ITO** indium tin oxide.

**$J$**  current or current density.

**$J_0$**  dark diode saturation current.

**$J_{\text{ph}}$**  photogenerated current.

**$J_{\text{rec}}$**  recombination current.

**$J_{\text{SC}}$**  short circuit current.

**$k$**  recombination rate constant.

**$k_B$**  Boltzmann constant.

**KPFM** Kelvin probe force microscopy.

**LED** light emitting diode.

**LiTFSI** bis(trifluoromethane)sulfonimide lithium salt.

**LOESS** locally estimated scatterplot smoothing.

**LUMO** lowest-energy unoccupied molecular orbital.

**$m$**  ideality of charge density versus light bias.

**MABr** methylammonium bromide.

**MAI** methylammonium iodide.

**MAPbI<sub>3</sub>** methylammonium lead iodide.

**MAPbI<sub>3-x</sub>Cl<sub>x</sub>** methylammonium lead iodide chloride.

**MPPT** maximum power point tracking.

**$\mu$**  internal chemical potential.

**$\bar{\mu}$**  electrons electrochemical potential, the Fermi or quasi-Fermi level energy of electrons including the local electrostatic potential.

**$\mu_{(n|p|a)}$**  mobility of electrons or holes or ions.

**$n$**  ionic density.

**$n_{\text{CE}}$**  excess charge observable via charge extraction.

**$n_{\text{DOS}}$**  density of states.

**$n_{\text{eq}}$**  equilibrium carrier density (electrons and holes participating in conduction) for an intrinsic (non-doped) semiconductor.

**$n_{\text{id}}$**  ideality factor.

**NMR** nuclear magnetic resonance.

**$\omega$**  angular frequency.

**OSC** organic solar cells.

**$P$**  electrical power.

**$p$**  electron holes density.

**PC<sub>60</sub>BM** [6,6]-phenyl C<sub>61</sub> butyric acid methyl ester.

**PC<sub>70</sub>BM** [6,6]-phenyl C<sub>71</sub> butyric acid methyl ester.

**PCE** power conversion efficiency.

**PEDOT:PSS** poly(3,4-ethylenedioxythiophene) poly(styrenesulfonate).

**PES** polyethersulfone.

**$\Phi$**  reaction order.

**$\phi$**  illumination intensity.

**PL** photoluminescence.

**PTAA** poly[bis(4-phenyl)(2,4,6-trimethylphenyl)amine].

**PTFE** polytetrafluoroethylene.

**$Q$**  generic charge per area.

**$q$**  elementary charge.

**$R_s$**  series resistance.

**$R_{\text{sh}}$**  shunt resistance.

**RC time** characteristic time of a circuit composed of a resistance in parallel to a capacitance.

**$\rho$**  net charge density.

**RT** room temperature.

**SCLC** space charge limited current.

**SEM** scanning electron microscope.

**SOMO** singly occupied molecular orbital.

**spiro-OMeTAD** N<sup>2</sup>,N<sup>2</sup>,N<sup>2'</sup>,N<sup>2'</sup>,N<sup>7</sup>,N<sup>7</sup>,N<sup>7'</sup>,N<sup>7'</sup>-octakis(4-methoxyphenyl)-9,9'-spirobi[9H-fluorene]-2,2',7,7'-tetramine.

**SRH** Shockley-Read-Hall recombination.

**T** temperature.

**t** time.

**TAE-1** tetra{4-[N,N-(4,4'-dimethoxydiphenylamino)]phenyl}ethene.

**TAE-3** 3,3',6,6'-tetrakis[N,N-bis(4-methoxyphenyl)amino]-9,9'-bifluorenylidene.

**TAE-4** 3,3',6,6'-tetrakis(3,6-dimethoxy-9H-carbazol-9-yl)-9,9'-bifluorenylidene.

**$\tau$**  small perturbation recombination life-time.

**$\tau_0$**  carriers' lifetime extrapolated at zero applied voltage.

**$\tau_{(n|p)}$**  traps mediated recombination constants for electrons or holes.

**$\tau_{pfo}$**  pseudo first order recombination life-time.

**TCSPC** time-correlated single photon counting.

**$\theta$**  phase.

**THF** tetrahydrofuran.

**TPC** transient photocurrent.

**TPV** transient photovoltaic.

**TPV-CE** transient photovoltaic referred to charge from charge extraction.

**TPV-DC** transient photovoltaic referred to charge from differential capacitance.

**TRPL** time-resolved photoluminescence.

**U** charges recombination rate.

**u<sub>x</sub>** placeholder for useless constants.

**UPS** ultraviolet photoelectron spectroscopy.

**UV-vis** ultraviolet-visible.

**V** voltage.

**v** ideality of pseudo first order life-time *versus* light bias.

**V<sub>BI</sub>** built-in voltage.

**V<sub>E</sub>** electrostatic potential, energy for adding a positive elementary charge.

**V<sub>OC</sub>** open circuit voltage.

**XRD** X-ray diffraction.

**Z'** real component of complex impedance.

**Z''** imaginary component of complex impedance.

*Dedicata a Sofia.*

# Abstract - Sinopsis - Sinopsi

**English.** This thesis includes the work done in ICIQ about fabrication, characterisation, and modelling of hybrid perovskite solar cells. Coming from other kind of solar cells, the analysis tools, the methods, and, most importantly, their interpretation have been analysed and adapted to this new kind of device. Then, these techniques have been employed for analysing and understanding the influence of four different and novel hole transport materials on perovskite solar cells open circuit voltage. Another study focussed on the electrons' accumulation in devices employing small variations in each stacked layer thickness and analysing the samples using the same techniques. From my international stay in Dr. Piers Barnes and Prof. Jenny Nelson groups in Imperial College London, another study was originated: we interpreted complex impedance spectroscopy results when applied on perovskite solar cells with mobile ions. Finally, all the free software that has been developed for data acquisition, processing, and for drift-diffusion modelling of perovskite solar cells has been exposed.

---

**Spanish.** En esta tesis se presenta todo el trabajo realizado en el ICIQ sobre la fabricación, caracterización y modelización de celdas solares de tipo perovskita híbrida, incluyendo las herramientas de análisis, los métodos y, sobretodo, la interpretación de datos obtenidos de diferentes celdas investigadas previamente. Estas técnicas se han utilizado para el análisis e interpretación de la influencia que tienen cuatro diferentes y nuevas moléculas utilizadas como transportadores de huecos electrónicos sobre el voltaje de las celdas solares de perovskita.

El segundo proyecto descrito en esta tesis es el estudio sobre la acumulación electrónica en dispositivos al modificar mínimamente el grosor de las distintas capas que lo conforman. Durante la estancia internacional en los grupos del Dr. Piers Barnes y la Prof. Jenny Nelson en el Imperial College London, se desarrolló un estudio para dar respuesta a la difícil interpretación de los datos obtenidos con la espectroscopía de impedancia en celdas solares de perovskita, y a la influencia que tienen los iones móviles sobre ellos. Finalmente, se describe todo el software libre desarrollado durante la tesis para la adquisición de datos, su procesamiento, y la modelización con *drift-diffusion* en celdas solares de tipo perovskita.

---

**Catalan.** Aquesta tesis descriu el treball realitzat a l'ICIQ sobre la fabricació, caracterització, i modelització de cel·les solars de perovskita híbrida. Originades des de la recerca en altres tipus de cel·les solars; les eines d'anàlisi, les metodologies i, el més important, la seva interpretació han sigut analitzades i adaptades a aquest nou tipus de dispositiu. Així, aquestes tècniques han estat utilitzades per analitzar i entendre la influència de quatre transportadors de forats electrònics diferents sobre el voltatge de cel·les de perovskita. El segon projecte descrit en aquesta tesis es basa en l'estudi sobre l'acumulació dels electrons en les cel·les mitjançant petits canvis en el gruix de cada capa i analitzant les mostres amb les mateixes tècniques. A partir de la meva estada internacional als grups del Dr. Piers Barnes i la Prof. Jenny Nelson a l'Imperial College London, s'ha dut a terme un altre estudi sobre la complexa interpretació dels resultats d'espectroscòpia d'impedància en presència de ions mòbils en les cel·les de perovskita. També està exposat tot el programari lliure que ha estat desenvolupat per a l'adquisició i processament de dades, i per a la modelització del tipus deriva-difusió de cel·les solars de perovskita.

# Summary of the Thesis

*tl; dr*

In chapter 1, an overview on the solar cells main concepts and working mechanisms are presented. Perovskite solar cells are inserted in the provided framework and the aims of thesis are listed.

In chapter 2, materials, equipment, and fabrication of the studied perovskite solar cells are described in detail.

In chapter 3, followed conventions, routine, and advanced characterisation techniques are described. For each characterisation technique, the involved concepts, formalism, and equations required for the data analysis are explained. Additionally, I presented here my own observations and thoughts about the interpretation of characterisation output, presenting also unpublished results from drift-diffusion modelling.

In chapter 4, the performances of bottom cathode perovskite solar cells fabricated using four different hole transporting materials are compared. Then, the origin of the observed differences are studied by means of small perturbation transient techniques. Part of this chapter has been published in [3].

In chapter 5, top cathode solar cells have been fabricated varying the thickness of each layer. For each device, the advanced characterisation output have been compared, obtaining insight on the charge storage location. Part of this chapter has been published in [1].

In chapter 6, drift-diffusion modelling of perovskite solar cells is employed for understanding the features observed in impedance spectroscopy. Specifically, the implemented simulation is described and the origin of apparent capacitance at different illumination, bias, and frequency is explained. Part of this chapter has been published in [2].

In chapter 7, various software I implemented during my thesis is described. First, the implementation of more functions and simulations for

drift-diffusion modelling is shown. Second, the development of a graphical user interface for current-voltage sweeps acquisition is presented. Third, the scripts used for automated and reliable data analysis are reported; they have been used for plotting most of the graphics included in this thesis.

# Contributions to Scientific Literature

- [1] I. Gelmetti, L. Cabau, N. F. Montcada, and E. Palomares. “Selective Organic Contacts for Methyl Ammonium Lead Iodide (MAPI) Perovskite Solar Cells: Influence of Layer Thickness on Carriers Extraction and Carriers Lifetime”. In: *ACS Applied Materials & Interfaces* 9.26 (July 2017), pp. 21599–21605. DOI: [10.1021/acsami.7b06638](https://doi.org/10.1021/acsami.7b06638) (cit. on pp. xxii, 74, 125, 129, 212).
- [2] D. Moia, I. Gelmetti, P. Calado, W. Fisher, M. Stringer, O. Game, Y. Hu, P. Docampo, D. Lidzey, E. Palomares, J. Nelson, and P. R. F. Barnes. “Ionic-to-electronic current amplification in hybrid perovskite solar cells: ionically gated transistor-interface circuit model explains hysteresis and impedance of mixed conducting devices”. In: *Energy & Environmental Science* 12.4 (May 2019), pp. 1296–1308. DOI: [10.1039/C8EE02362J](https://doi.org/10.1039/C8EE02362J). arXiv: [1805.06446](https://arxiv.org/abs/1805.06446) (cit. on pp. xxii, 15, 27, 58, 61, 76, 106, 139, 142, 143, 148, 161, 163, 164, 166, 212).
- [3] I. Gelmetti, N. F. Montcada, A. Pérez-Rodríguez, E. Barrena, C. Ocal, I. García-Benito, A. Molina-Ontoria, N. Martín, A. Vidal-Ferran, and E. Palomares. “Energy alignment and recombination in perovskite solar cells: weighted influence on the open circuit voltage”. In: *Energy & Environmental Science* 12.4 (2019), pp. 1309–1316. DOI: [10.1039/C9EE00528E](https://doi.org/10.1039/C9EE00528E) (cit. on pp. xxii, 24, 25, 27, 33, 43, 68, 81, 84, 92, 93, 96, 100, 101, 107, 111, 113–115, 117, 211).

# Oral and Poster Presentations at Conferences

- 45 min plenary oral presentation, at *International Krutyn Summer School on Advanced Perovskite, Hybrid and Thin-film Photovoltaics* in Krutyn, Poland on June the 14th, 2016 titled “*How to make efficient perovskite solar cells and charge transfer reactions in perovskite solar cell*”
- 20 min plenary oral presentation at *Workshop on Flexible Electronics* in DEEEA-URV, Tarragona, Spain on June the 29th, 2016 titled “*Photophysical characterization of charge transfer and recombination in hybrid lead halide perovskite solar cells*”
- 15 min plenary oral presentation at *Stability of Emerging Photovoltaics Conference (SEPV18)* in Barcelona, Spain on February the 20th, 2018 titled “*The Relevance of the Energy Alignment Shift in Organic Semiconductor/Perovskite Interface: Influence in the Open Circuit Voltage*”
- Poster at *International Conference on Hybrid and Organic Photovoltaics* (HOPV17) in Lausanne, Switzerland on May the 22nd, 2017 titled “*Quasi-Fermi Energy Shift for Hole Transport Material in Perovskite Solar Cells*”
- 30 min invited seminar oral presentation in INAM-UJI, Castelló, Spain on June the 26th, 2018 titled “*Simulating Impedance Spectroscopy of Perovskite-based Devices via Time-Dependent 1D Drift-Diffusion Model*”
- 15 min plenary oral presentation in *Graduate Students Meeting on Electronics Engineering* in DEEEA-URV, Tarragona, Spain on June the 28th, 2018 titled “*Simulating the impedance spectroscopy of an*

*hybrid perovskite solar cells via time-dependent 1D driftdiffusion model”*

- 15 min oral presentation in *NanoBio Conference 2018* in Heraklion, Crete, Greece on September the 27th, 2018 titled “*Perovskite solar cells impedance spectroscopy explained via 1D time dependent drift-diffusion modelling*”

# Chapter 1

## Introduction

*“It’s good, unless you have vertigo.”*  
*“...are you talking about PhD?”*

---

**Table of Contents**

---

**Why Photovoltaics?**

Abundance, 3 • Availability, 3 • Resilience, 3 • More energy is not enough, 3 • And more research is needed, 5

**Relevant Physics for Stacked Semiconductor Thin Films****ENERGY LEVELS AND OCCUPANCY**

HOMO and LUMO, 5 • Valence and conduction bands in crystalline solids, 6 • Valence and conduction bands in amorphous solids, 6 • Boltzmann and Fermi-Dirac statistics, 6 • Fermi level, 7 • Doping, 8 • Quasi-Fermi level, 8 • Quasi-Fermi level and occupancy, 9 • Quasi-Fermi levels and current, 9

**ELECTROSTATICS**

Charged particles drift, 9 • Particles diffusion, 9 • Poisson equation, 10 • Space charge layers and electric field screening, 11 • Debye length, 12

**ELECTRODYNAMICS**

Displacement current – definition, 13 • Displacement current – interpretation, 13 • Continuity equation, 15

**CHARGE RECOMBINATION**

Primary geminate recombination, 15 • Radiative recombination, 15 • SRH trap mediated recombination, 16 • Surface recombination, 17 • Auger recombination, 18

**CHARGE GENERATION**

Light absorption, 18 • Exciton and exciton binding energy, 19

**PHOTOVOLTAIC EFFECT**

Charges reaching the interfaces via diffusion, 20 • Charge collection due to drift, 20 • Current, 21 • Voltage, 22

**Perovskite Solar Cells**

Perovskite Absorber Synthesis, 24 • Recombination mechanisms, 24 • Open circuit voltage, 24 • Ionic defects, 25 • Ionic migration, 26 • Field free absorber, 26 • Diffusion as the main transport mechanism, 26 • Hysteresis, 27 • Characterisation, 27 • Stability, 27

**Motivation and Aims**

---

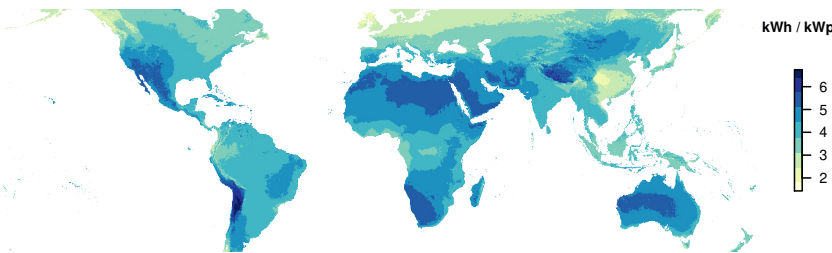
## 1.1 Why Photovoltaics?

**Abundance.** The total solar irradiance hitting the outer Earth atmosphere is around  $1361 \text{ W m}^{-2}$  [5], which, considering our planet cross section area, makes  $1.6 \times 10^{17} \text{ W}$ . Nature conveys this energy in plenty of ways, including the generation of every renewable and most of non-renewable energy sources. Solar energy is effectively the primary energy source for our planet's ecosystem, so it is the most interesting source of energy for human usage.

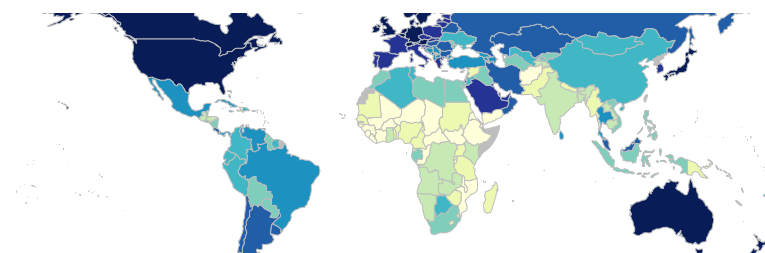
**Availability.** The ubiquitous availability of solar power can be the leverage for an economical power levelling across different regions of the planet. Indeed, the abundance of solar irradiation (represented in fig. 1.1a) is quite high in most of the regions where life quality is seriously affected by economical situation (represented in fig. 1.1b by the Human Development Index).

**Resilience.** The usage of photovoltaic energy is compatible with a distributed and decentralized network model. Such a power network can be much more resilient than the fossil fuels based system, with the only single-point-of-failure being the climate variability. Combined with accumulation (needed for night time usage) and with other energy sources, it can be the pivot of an extremely reliable electric energy provisioning system.

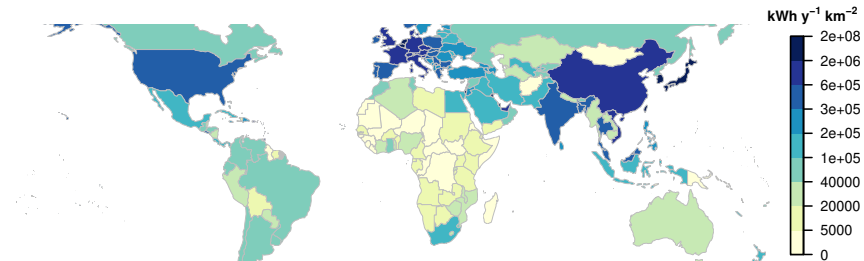
**More energy is not enough.** It is intuitive that increasing the energy production is a high-price solution to the growing energetic demand. Indeed, in some regions a decrease in the electricity consumption has to be included for a long-term solution. For example, a study [10] reports that if every rooftop (not considering utility-scale solar facilities) in United States of America was covered with solar panels, just the 39 % of its nowadays national consumption would be covered. In fig. 1.1c we can see how electricity consumption density is greatly inhomogeneous and comparing with the photovoltaic potential map in fig. 1.1a, it is evident that such a problem is shared with many other poorly insulated but energy eager regions. Both an increase in machinery's efficiency and a change in life-style can be part of the solution, following the example and thinking at life-style, in USA the *per capita* energy usage is more than twice the European average, and five times the Latin America average [11].



(a) Daily photovoltaic electricity potential



(b) Human development index by region



(c) Yearly electricity consumption over region land area

**Figure 1.1: Geographical distribution of development, sunlight and consumption.** Data in (a) represents the photovoltaic electricity potential: considering a photovoltaic module installed in a region, is the ratio between the average daily produced energy, in kWh, and the nominal power, or nameplate capacity, of the installed module [6]; data in (b) represent the human development index: “a summary measure of average achievement in key dimensions of human development: a long and healthy life, being knowledgeable and have a decent standard of living” from UNDP [7] (missing data in grey); data in (c) represents the yearly electricity consumption [8] (comparing total electricity generated annually plus imports and minus exports) on a country scale divided by country land surface [9], expressed in kilowatt-hour per year and per square kilometre.

**And more research is needed.** Every source of electrical energy we can think of works via the conversion of motive power (a flow of steam, wind, or water, waves, tides...) to electricity, which relays on the well established electric generator. Except photovoltaic energy. This very simple difference already hints for the huge conceptual and technological step required by photovoltaics as compared to other electrical energy sources.

## 1.2 Relevant Physics for Stacked Semiconductor Thin Films

### 1.2.1 Energy Levels and Occupancy

**HOMO and LUMO.** The energy that an electron can have when it is bound in a nanometric volume (like a molecular bond) is quantized, the possible energies are represented in fig. 1.2. The lowest levels represent the ones actually occupied with electrons and their energy is defined as the energy that can be provided to a neutral isolated molecule at its ground state which result in one electron being separated from it at an infinite distance and zero kinetic energy. The minimum of these ionization energies, is the highest-energy occupied molecular orbital (HOMO) energy. The upper levels are virtual ones and represent the energies that can be released when an unbound electron gets bound to a isolated molecule

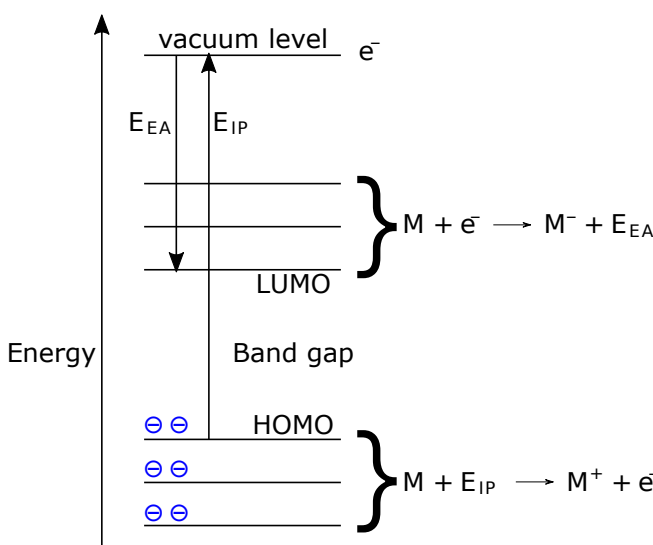


Figure 1.2: Representation of HOMO and LUMO levels. Each horizontal line represents the energy of a molecular orbital in a neutral molecule at ground state. So the bottom group are the occupied orbitals while the upper group are the virtual ones.

which was neutral and at its ground state. The maximum of these electron affinity energies, is the lowest-energy unoccupied molecular orbital (LUMO) energy. The difference between HOMO and LUMO energies is named band gap. After these electronic processes, the molecule will geometrically change and release some reorganization energy, but this is not included in the HOMO and LUMO definition (*i.e.* a vertical transition is considered).

**Valence and conduction bands in crystalline solids.** As we saw, for an isolated molecule the energy levels are discrete values. On the contrary, for materials where electrons are delocalised in a periodic potential (*e.g.* in a crystal structure) we have continuous bands (ranges) of allowed electronic energies separated by energy gaps [12]. For a 3D crystal, the density of states can be approximated to be the density of states (DOS) of a free electrons gas where it grows with the square root of the energy, as represented in fig. 1.3 [13, p. 140].

**Valence and conduction bands in amorphous solids.** In amorphous solids, the allowed electronic energy is still composed by bands but localised states can appear inside the band gaps and the band edges are less defined. These tails of the edges are usually composed by localised states whose mobility is low, for this reason in amorphous solids the mobility gap is wider than just the band edges separation [14, p. 213].

**Boltzmann and Fermi-Dirac statistics.** For a system with defined temperature and total energy but various possible states at different energies, Boltzmann distribution gives the probability of finding it in a specific state. For example, considering electrons as non interacting particles we can estimate the conduction band population with:

$$n_{\text{CB}} = n_{\text{DOS}} \exp \left[ \frac{\bar{\mu} - E_{\text{CB}}}{k_{\text{B}}T} \right] \quad (1.1)$$

where  $n_{\text{DOS}}$  is the density of states representing the energy state degeneracy,  $q$  is the elementary charge,  $\bar{\mu}$  is the electrons electrochemical potential (Fermi or quasi-Fermi level energy of electrons including the electrostatic contribution), and  $E_{\text{CB}}$  is the conduction band energy including the local electrostatic potential. For low temperature or high electron density cases, the interactions between particles cannot be ignored. The consideration of Pauli exclusion principle for fermions modifies the Boltzmann distribution into the Fermi-Dirac distribution, which has not been used for the

## 1.2. RELEVANT PHYSICS

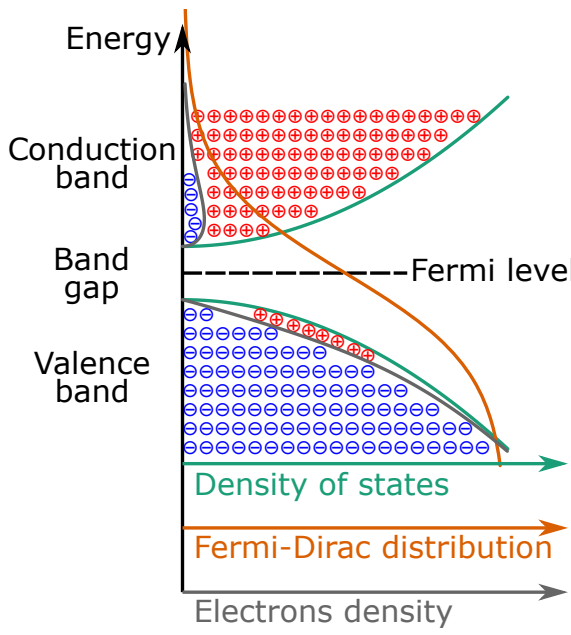


**Figure 1.3:** Schematic representation of the density of states, Fermi-Dirac distribution, and electronic population for a crystalline intrinsic semiconductor. The green line indicates the density of states in a 3D crystalline solid, the two bands have been drawn with the same shape for simplicity, in general this could not be the case. The orange line is the Fermi-Dirac distribution for the electrons population. The grey line is (approximatively) the product of the two aforementioned lines representing the electronic density energy distribution.

simulations performed in this thesis:

$$n_{CB} = \frac{n_{eDOS}}{\exp[(E_{CB} - \bar{\mu})/(k_B T)] + 1} \quad (1.2)$$

where  $n_{DOS}$  has been replaced with the effective density of states  $n_{eDOS}$  which considers the effective mass for interacting particles.

**Fermi level.** Fermi level is an imaginary level (disregarding the actual states present in a system) defined for systems in thermodynamic equilibrium (no macroscopic particles or energy fluxes, neither internal nor from other systems) having an energy such that its occupancy probability is 50 %. For example, considering the 3D crystalline system represented in fig. 1.3, if the Fermi level approaches the conduction band edge, the population at that edge state can be estimated using eq. (1.2):  $\frac{n_{eDOS}}{\exp[(E_{CB} - E_{CB})/(k_B T)] + 1} = n_{eDOS}/2$  so it will be half full, while the valence band will be close to completely full (many electrons, very few holes). This level is ultimately the relevant potential for the charge carriers for a system in thermodynamic equilibrium, so if carriers can migrate through the system the Fermi level will have the same energy in every location of it.

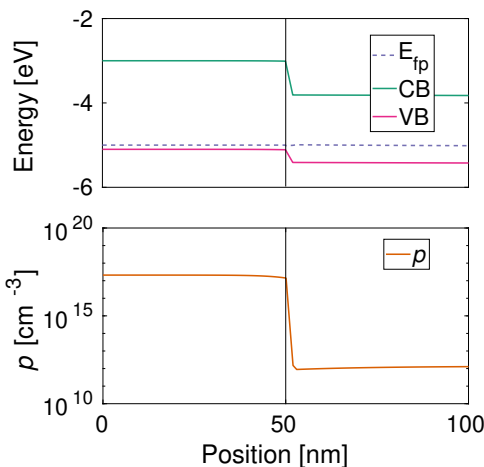


**Figure 1.4: Representation of the relation between quasi-Fermi level distance from respective band and carriers concentration.** Simulation of an heterojunction. Notice how the  $\bar{\mu}_{VB}$  (valence band quasi-Fermi level) distance from the valence band (top plot) relates to the holes concentration (bottom plot).

**Doping.** A perfect crystal semiconductor (no defects, no added dopants) is intrinsic, which means that its Fermi level is in the middle of the band gap and that the electron density in the conduction band is equal to the holes density in the valence band, as represented in fig. 1.3. In the example of the previous paragraph, where the Fermi level was close to the conduction band, the concentration of electrons greatly exceeds the holes density. This situation can happen in “extrinsic” or “doped” semiconductors, where the presence of, for example, positive ionic Schottky defects or oxidised species can compensate the charge of the high electrons concentration and result in a charge neutral material, as represented in fig. 1.6a. It can also happen that the material, or a part of it, is just charged, for example due to the application of an electric field or in a space charge layer as will be seen further.

**Quasi-Fermi level.** For a system out of thermodynamic equilibrium the Fermi level is not defined any more. For example, if a constant illumination hits the system plenty of electrons will be promoted from the valence band to the conduction band and the occupancy described by eq. (1.1) or eq. (1.2) does not hold. In order to keep using the same convenient concepts, two quasi-Fermi levels are introduced, where the electronic population in the conduction band and in the valence band are described separately, with two different electrons electrochemical potentials, as if they pertained to different systems in thermodynamic equilibrium. In order to have a meaningful definition of these new levels, the system condition has to vary slowly enough to allow the carriers to thermalise within an energy band. For simplicity, the quasi-Fermi level relative to the

valence band is usually referred to the holes concentration rather than to the electrons. As the system is not in thermodynamic equilibrium, macroscopic particle currents can be present and this means that the energy of this level is location dependent, and can also be time dependent. Clearly, at thermodynamic equilibrium both the holes and the electrons quasi-Fermi levels coalesce into the Fermi level.

**Quasi-Fermi level and occupancy.** When observing a band diagram, like the one reported in fig. 1.4, it is very easy to have an idea of the carriers concentrations observing the distance between the quasi-Fermi levels and the band edges. For example, in fig. 1.4 we can see that the closer the  $\bar{\mu}_{VB}$  (quasi-Fermi level relative to the valence band) gets to the valence band, the higher the holes concentration in it.

**Quasi-Fermi levels and current.** Coherent with the Fermi level concept, quasi-Fermi levels are the relevant potentials for the migration of holes in the valence band and electrons in the conduction band, treated separately. The quasi-Fermi level considers both the internal chemical potential  $\mu$  and the electrostatic potential  $V_E$  and, as we will see below, these two quantities determine respectively the diffusion and the drift current. For this reason, a gradient in the valence or conduction band quasi-Fermi level ( $\bar{\mu}_{VB}$  or  $\bar{\mu}_{CB}$ ) always indicates the presence of a current respectively of holes or electrons. The local value of this current will be proportional to the local quasi-Fermi level gradient and to the respective particle local concentration.

### 1.2.2 Electrostatics

Electrostatics refers to all electronic phenomena which does not intrinsically require a time varying quantity.

**Charged particles drift.** The electric field acts a Lorentz force on the charged particles. The movement of these particles due to the field is named “drift”. The velocity is proportional to the electric field intensity and the mobility (characteristic of material and type of charge). As represented in fig. 1.5a, in a typical energy diagram electrons drift downhill and holes drift uphill.

**Particles diffusion.** For all the non-fixed particles, part of the thermal energy is translational energy, regardless of their charge. This means that

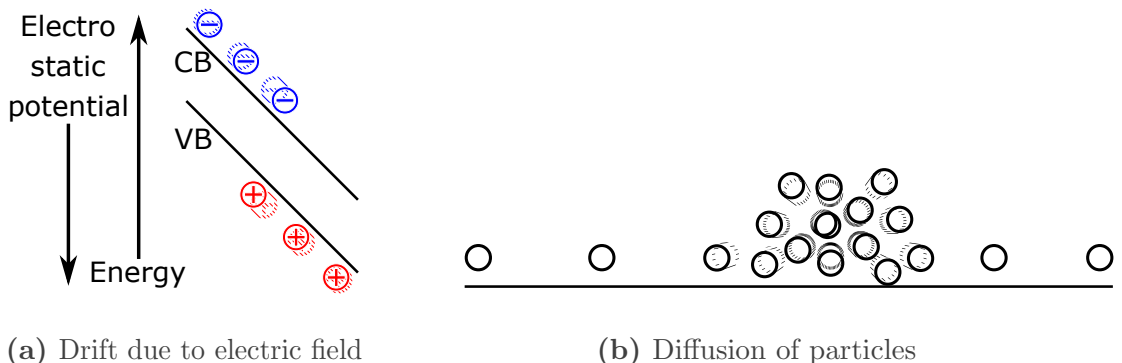


**Figure 1.5: Representation of drift and diffusion of charged particles.** In (a) the drift of holes in the valence band and electrons in the conduction band due to an electric field is represented. In (b) the diffusion of generic particles due to differences in concentration is represented.

the particles move in random directions, like in a Brownian motion for gases or in Drude model for classical description of electrons bouncing around. The disordered motion statistically compensate differences in concentrations. If the net diffusion flux is considered, this is proportional to the concentration gradient and to the diffusion coefficient (which is proportional to the mobility, as described by Einstein relation). As represented in fig. 1.5b, particles in highly concentrated zones tend to move towards less densely occupied ones. Concentration of particles is the main contribution to the internal chemical potential  $\mu$ .

**Poisson equation.** The net charge in a location is related to the “curvature” (second derivative) of the electrostatic potential (i.e. the vacuum level) by the Poisson equation:

$$\nabla^2 V_E = \nabla \cdot E = -\frac{\rho}{\epsilon_0 \epsilon_r} \quad (1.3)$$

where  $V_E$  is the electrostatic potential (defined as the energy for adding a positive elementary charge),  $E$  is the electric field,  $\rho$  is the net charge obtained summing up all the charged particles concentrations in the location, and  $\epsilon_0 \epsilon_r$  is the permittivity. For easing the understanding of the band diagram, the scheme in fig. 1.6b can be handful. As can be seen, in the zones where a net charge is present (space charge layers, depletion layers in the represented case) the second derivative of the electrostatic potential or of the vacuum level depends on the sign of this

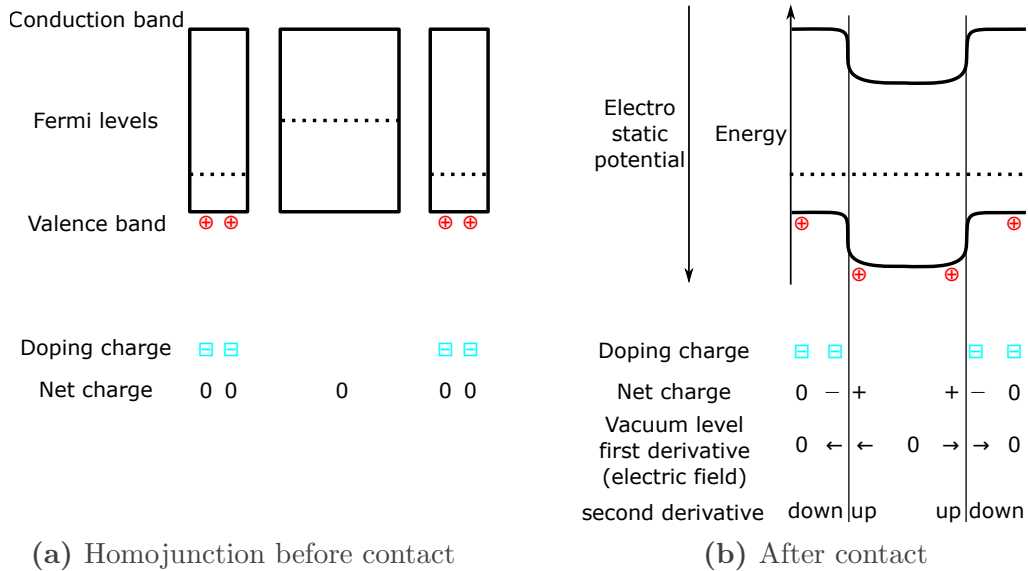


**Figure 1.6: Schematics of a  $p$ - $i$ - $p$  homojunction, with emphasis on depletion layers and representation of Poisson equation.** In (a) three layers of the same material when doped to be respectively  $p$ -type, intrinsic (non doped), and  $p$ -type are represented. In order to compensate the fixed charges introduced by dopage and maintain the net charge neutrality, the  $p$ -type layers have the valence band rich in holes (clearly also the populations on the conduction band is affected by the doping, but not represented for simplicity). In (b) the three layers are brought in contact forming an homojunction. The holes flow through the interfaces following the Fermi level gradient, until it gets flattened. This generates space charge layers at the interfaces, where a net charge is present (the thickness of it is expected to be thicker in the intrinsic layer rather than in the doped ones, as described in page 12). To easily understand the bending direction of the layers due to the net charge, the Poisson equation tells us that a positive charge means a positive vacuum level second derivative.

net charge: upwards for positive charge and downwards for negative one. A material with a different permittivity will need a different amount of net charge in order to have the same “curvature” of the vacuum level: the higher the permittivity, the more the charge needed for obtaining the same electrostatic potential profile.

**Space charge layers and electric field screening.** As represented in fig. 1.6, when two materials with different Fermi levels are brought into contact their free charges migrate until when the Fermi level is flattened. This generates non-neutral zones, where a net charge is present,

denominated space charge layers. When this involves the majority carriers (e.g. holes for a *p*-type material) exiting a material and leaving behind the charge from the doping species (fixed negative species for a *p*-type material), this is named a depletion layer and is the case represented in fig. 1.6b. This space charge layer generates a strong electric field at the interfaces. A space charge layer can also arise due to the presence of an external electric field, simply because of the force that this field exerts on the mobile charges. These space charge layers will cause an opposite electric field which will completely eliminate the field in the bulk of the material. Extending this concept to the aforementioned example of semiconductors in contact, it is easy to see that far from the interfaces the electric field is zero, or “screened” by the charged layers, as represented in fig. 1.6b.

**Debye length.** In each layer, the thickness of this space charge region is related to a material’s property: the “Debye length” or “Thomas-Fermi screening length”. The density profile and thickness of the space charge layer depends on the establishment of a dynamic equilibrium of drifting and diffusing charges in this region. Taking as a reference the charges shown in fig. 1.6b, the holes in the bulk of the *p*-type material (leftmost and rightmost) will diffuse towards the interface, just because of the concentration gradient (close to the interface the material is depleted of holes). In the opposite direction, the holes in the intrinsic material (in the middle) will drift towards the *p*-type material due to the electric field. The steady state of this equilibrium, and so also the Debye length, depends upon the carriers concentration (which in turn depends on the doping density) and the material permittivity [15]. For example, in a material with high permittivity the polarization will decrease the efficacy of the charges and a thicker layer will be needed. Another example, in an intrinsic material there are few free charges and the space charge layer will be much thicker, as in fig. 1.6b. If the material layer is thinner than the Debye length, the electric field will be screened just partially and no region will be completely field free.

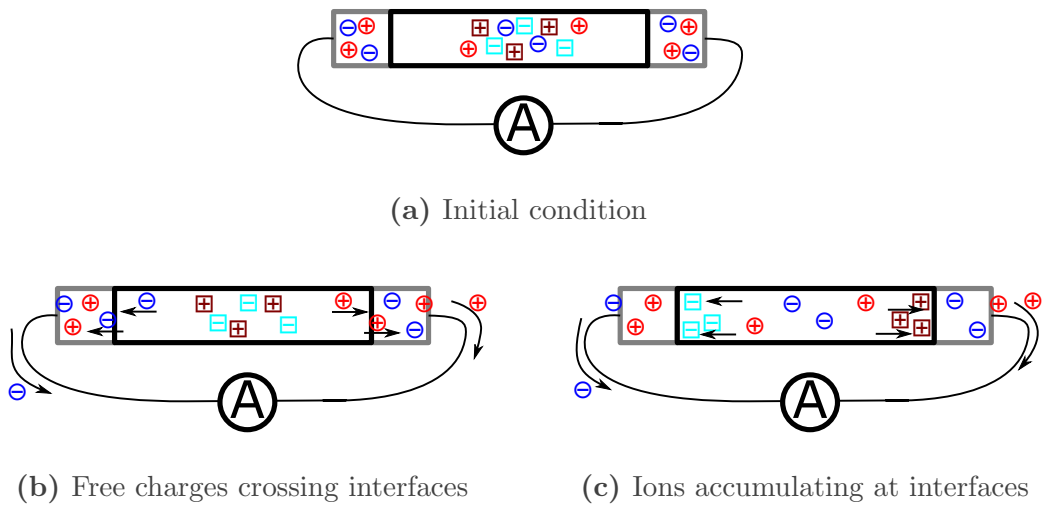


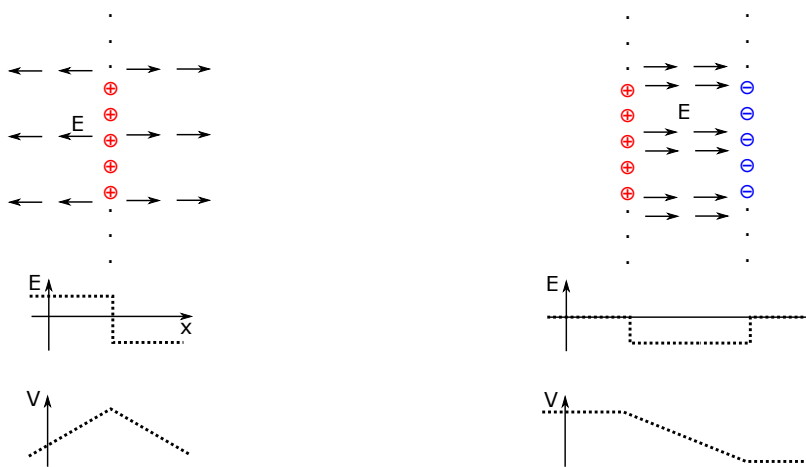
**Figure 1.7: Representation of current and displacement current.** In (a), a mixed ionic-electronic conductor material layered between two layers of electronic conductor material. In (b), the electronic charge can cross the material's interfaces. In (c), ionic charge cannot be transferred to the electrodes, still a displacement current due to the ionic migration is generated and can be measured in the amperometer.

### 1.2.3 Electrodynamics

Electrodynamics refer to all the phenomena intrinsically time-dependent, which varies with time.

**Displacement current – definition.** The displacement current  $J_D$  appears in the fourth macroscopic Maxwell's equation as  $\partial D / \partial t$  for describing the contributions to magnetizing field not originated by a current of free charges  $J_f$ :  $\nabla \times H = J_f + \frac{\partial D}{\partial t}$ . The displacement electric field  $D$  includes contributions from the electric field intensity  $E$  and the polarization  $P$ :  $D = \epsilon_0 E + P$  which can also be written in terms of relative permittivity  $\epsilon_r$  as:  $D = \epsilon_0 \epsilon_r E$ . So its time derivative defining the displacement current is:  $\frac{\partial D}{\partial t} = \epsilon_0 (\epsilon_r \frac{\partial E}{\partial t} + E \frac{\partial \epsilon_r}{\partial t})$ . For the scope of this thesis we are interested in the first term and we are going to ignore the second one considering the relative permittivity as a material dependent constant.

**Displacement current – interpretation.** So the displacement current accounts for the charge movements not identifiable as current and for their effect on the surrounding circuitry. An example is represented in fig. 1.7c:



(a) Infinite plane of charge

(b) Two infinite planes of opposite charge

**Figure 1.8: Electric field by two planes of opposite charges.** (a) an infinite plane of charged particles is represented, the electric field is constant on the two sides, with a discontinuity in the plane. (b) adding a second plane with the same concentration of charges of the opposite kind, the electric field out of the sandwich cancels out. What is present outside of the sandwich is just an electrostatic potential difference.

the amperometer can measure a current even if no charge crossed the perovskite/electrode interface, this is a displacement current caused by the creation of a dipole inside the central layer due to the ionic accumulation at the interfaces. One can imagine the resulting current as needed for maintaining the zero potential difference between the two contacts. It is not, as one could erroneously and instinctively think, the effect of an electric field generated in the contacts by the moving charge in the perovskite layer (with related Coulomb force and image charges) as out of the two two-dimensional planes of opposite charges no electric field is present. This can be understood thinking that the electric field intensity generated by a large plate of charges has a constant magnitude at distances much smaller than the plate dimensions (which is always true in our solar cells considering the thickness  $\approx 1 \mu\text{m}$  to area  $3 \times 3 \text{ mm}^2$  ratio, except at electrode edges). The concept is represented in fig. 1.8. In page 148 we will use the displacement current concept for simulating the current caused in the electrodes not by a net flux of charges through a device section but by the rearrangement of charges which not necessarily leave the device, like the ionic migration in perovskite material.

**Continuity equation.** The continuity equation has a very intuitive meaning: the concentration of a species in a specific volume can increase due to generation  $g$ , can decrease due to recombination  $U$  or can change due to a speed change of a charge flow passing by. This last contribution can be understood with the following example: a red traffic light stops the cars flow and causes the increase of their concentration. For an electron concentration  $n$ :

$$\frac{\partial n_x}{\partial t} = \frac{1}{q} \nabla_x \cdot J_n + g_{n,x} - U_{n,x} \quad (1.4)$$

### 1.2.4 Charge Recombination

**Primary geminate recombination.** This kind of recombination happens with the annihilation of a photo-generated exciton prior to the free charges separation. This is independent from the illumination intensity, so it can be considered as having a reaction order of zero. Lead halide perovskite have quite a high static permittivity [2] and a small electron effective mass [16] which means a high holes and electrons mobility [17], this implies that, at room temperature, the exciton binding energy (described in page 19) is even smaller than  $k_B T$  [18–20] and the direct generation of free charges occurs. So this kind of recombination is negligible in perovskite solar cells [21].

**Radiative recombination.** This is an unavoidable form of recombination, which finds its origin in the detailed balance principle describing that, at thermodynamic equilibrium, all the absorbed thermal photons, coming from the surroundings of the cell, have to be re-emitted as black body radiation. From this parallelism it can be understood that this recombination is larger for materials with high absorptivity [22] like the ones used for thin film solar cells [20]. An indirect bandgap disfavours the radiative recombination: in these materials the recombination involves a large momentum variation, while the photon emitted due to the recombination can take just a small momentum and the rest of it should be released as an additional phonon (lattice vibrations). Radiative recombination involves the collision of two opposite free charges, so it can be considered as having a reaction order of 2 when electrons and holes concentrations are similar,  $n \approx p$  (in intrinsic semiconductors out of depletion layers or, in intrinsic perovskites, once ionic profile screened the electric field), while in case of uneven concentrations (in doped semiconductors or within depletion layers) the limiting reagent is the minority carrier (electrons in

*p*-type and holes in *n*-type materials) and the reaction order is 1. The expression used for modelling is:

$$U_{\text{rad}} = k_{\text{rad}}(np - n_{\text{eq}}^2) \quad (1.5)$$

where  $n_{\text{eq}}$  is the equilibrium carrier density as obtained from Boltzmann distribution for an intrinsic semiconductor, it is just introduced in the equation in order to account for the thermal generation. The dependency from  $np$  indicates that this recombination type depends on the quasi-Fermi levels splitting [23]. This type of recombination is present in perovskite solar cells, indeed some of the most efficient perovskite solar cells can be used as light emitting diode (LED) taking advantage of their radiative recombination [24].

**SRH trap mediated recombination.** Shockley-Read-Hall recombination [25] happens in two steps: a free carrier decays from the respective band into an empty localised state with energy in between the valence and the conduction bands, a trap, after this event, a free charge of the opposite sign reaches the trapped charge location and recombine with it. Usually both the momentum difference and the chemical energy is released via phonons, so no radiative emission is involved. When the trap is empty and/or when it is occupied, it will have a net charge which will ease the capture of a free carrier through Coulomb force (partially screened by the material's permittivity) [26, 27]. As aforementioned, in an indirect band gap material the radiative recombination is disfavoured, but the presence of a trap state can divide in two easier steps the charge recombination process. This recombination type can have reaction order of 1 or 2 depending on how many of these steps constitutes a bottleneck [28]. In case of mid-gap traps (with energy in the middle of the bandgap), these states will be rather saturated and the process of trapping a free charge will be slow as an empty trap has to be hit, then the actual recombination is fast, so the reaction order is 1. In case of shallow traps, the first step could or could not be a bottleneck, this time depending on the availability of free charges to trap: in doped semiconductors this could be a limiting factor, and the reaction order would be again 1; in intrinsic semiconductors there will be plenty of free charges of both types, and the reaction order can get close to 2. The expression used for modelling is [22, 25]:

$$U_{SRH} = \frac{np - n_{\text{eq}}^2}{\tau_n(p + p_t) + \tau_p(n + n_t)} \quad (1.6)$$

where  $\tau_n$  and  $\tau_p$  are constants describing the trap capture cross section (which can be different for electrons and holes) and the traps density while  $n_t$  and  $p_t$  are the carrier densities that would be present with a the Fermi level equal to the traps energy. For a doped semiconductor with similar  $\tau_n$  and  $\tau_p$  constants, the expression can be simplified, for example in a *p*-type material we can use [22, p. 108]:

$$U_{SRH} \approx \frac{n - n_0}{\tau_n} \quad (1.7)$$

so, the more the material is densely doped, the smaller the minority carriers density and the less important is this kind of recombination. For lead halide hybrid perovskite materials, this kind of recombination is or is not important depending on the presence of mid-gap states, which in turn depends on the material composition and stoichiometry.

**Surface recombination.** Also known as interfacial recombination, refers to the annihilation of two opposite charges happening at the boundary of a material block: an interface. An interface can form between grains of the same material or between different materials. At the boundary of a crystal, the well ordered structure is interrupted creating various localised states which can act as traps for Shockley-Read-Hall recombination (SRH) recombination. Additionally, the impurities tend to accumulate to the crystalline grain surface, external contamination is likely to occur at the material surface, chemical reactivity can vary the composition of two materials' interface, and mid-gap states could be already present in one of the two interfacing materials. Recent reports indicate that also the LUMO of an hole transporting material (HTM), even if it is out of the perovskite's band gap, can efficiently mediate the recombination of hot electrons [29, 30]. In this thesis, I will consider the surface recombination as a case of SRH recombination. Considering the interface between two different materials, for example, *p*-type HTM and close-to-intrinsic perovskite, the surface recombination will involve the majority carrier, holes, in the *p*-type material and electrons in the intrinsic semiconductor. As the doped semiconductor has abundance of majority carriers, the limiting factor will be the concentration of “minority” carriers on the other side of the interface, which will depend on mobility and electric field in the intrinsic. So the reaction order should be 1 for this case. In efficient perovskite solar cells, this is the most important recombination pathway [23, 28, 31], at least for aged devices [32, 33].

**Auger recombination.** When a free charge gets in contact with another of the same kind, it is possible that one of these decays and the other absorbs the just released energy as kinetic energy. Additionally to the two free charges of the same kind, it also requires a free charge of the opposite kind for the decay to be possible, so it can be considered as having a reaction order of three. This recombination is important in materials with high free carriers densities or at high photo-generation conditions. These high charge densities are unlikely to happen in perovskite solar cells at maximum power point working conditions while they could happen at open circuit under illumination.

### 1.2.5 Charge Generation

Thanks to microscopic reversibility, each of the mentioned recombination processes has an identical but opposed generation process [22, p. 81]. These generation processes require some energy in input, which can be thermal (phonons, *i.e.* lattice vibrations) for the generation associated to the non radiative processes or radiative for the reverse of the radiative recombination. This last case, named photogeneration, is the most interesting for photovoltaics.

**Light absorption.** Photons passing through a material can be absorbed depending on their energy. This is closely related to the material polarizability (permittivity): imagine a molecule like a metallic stick and the incoming photon as its associated electric field wave. The electric field would cause the electrons and the holes inside the metallic stick to accumulate at its two opposite extremities, increasing its internal energy. The energy gained by the stick would absorb all the energy of the incoming electric field, causing the annihilation of the photon. Passing to consider a molecule, the photon would be absorbed just if it matches the energy difference between the fundamental (fig. 1.9a) and an excited molecular state (and just if a transition dipole moment is not zero and other selection rules). As we ultimately want to extract free charges from the material, we will consider just the transitions of electrons between molecular orbitals or bands. After the photon absorption, a previously occupied energy level is now missing one electron which has been promoted to a previously unoccupied virtual state. This is represented in fig. 1.9b for a high energy photon generating a hot excitation  $M^{*h}$  (which later can result in a hot exciton and a hot carrier, not treated in this thesis) or in fig. 1.9c for a photon with just enough energy to generate an excitation  $M^*$ . Photons

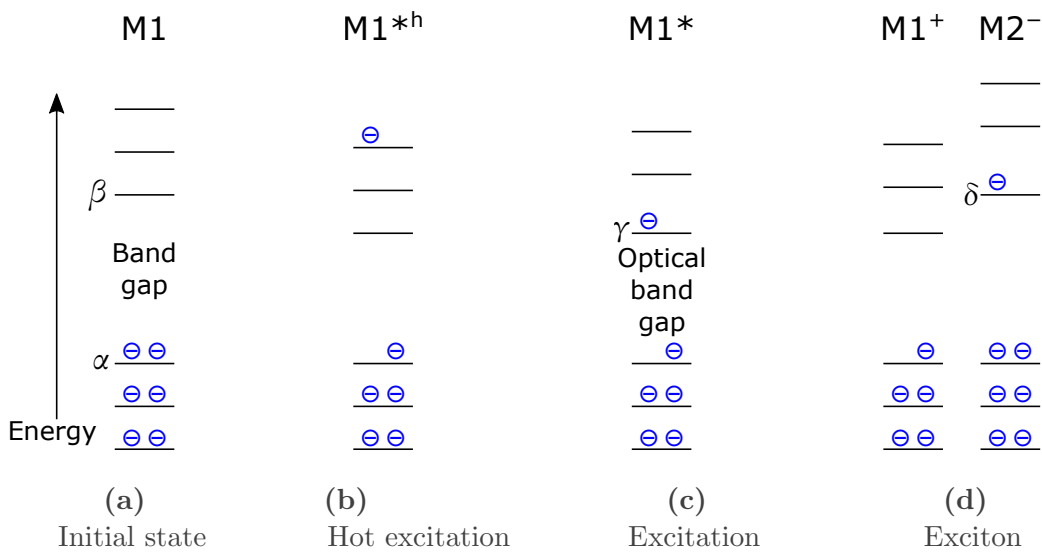


**Figure 1.9: Representation of absorption and generation of an exciton.** In (a) the fundamental molecular electronic configuration is represented, for the meaning of the levels refer to fig. 1.2. In (b) a photon with high energy excited an electron from the HOMO to the LUMO+2, equivalently also other levels can be involved e.g. HOMO-1. In (c) a photon with just enough energy has promoted an electron. Please note that the final state of the electron (a singly occupied molecular orbital (SOMO)) has a lower energy than the LUMO, as explained in the text. In (d) the excited electron in the SOMO has been transferred to the LUMO of an adjacent molecule.

with energy smaller than the optical band gap can also be absorbed by different processes like valence band to empty mid gap localised state, occupied mid gap localised state (trapped charge) to conduction band, localised states caused by structural disorder or thermal motion in crystals (Urbach tails) but they will not be considered in this thesis.

**Exciton and exciton binding energy.** The starting state of the electron involved in the radiative excitation is the HOMO of the molecule M, marked in fig. 1.9a with  $\alpha$ . When an electron is removed from the HOMO, the energy of the LUMO decreases, as it now refers to a different electronic configuration, where the underlying orbitals are not fully balancing the nuclei positive charges any more. So the arrival state of the excited electron, marked with  $\gamma$  in fig. 1.9c, is at a lower energy than the initial state LUMO ( $\beta$ ) and the optical band gap (which can be measured from absorbance spectrum via a Tauc plot) is smaller than the band gap (difference between

the electron affinity and the ionization potential represented in fig. 1.2). Additionally, these energies can be influenced by the polarisability of the surroundings (e.g. solvent permittivity) which can have different energetic contributions to  $M$ ,  $M^-$ , or  $M^*$ ; by intermolecular interactions; and by the molecular geometry which also depends on the solvent or solid state. Next to the excitation, an electron can either go back (recombine) or start getting apart from the original location, as represented in fig. 1.9d where it has been transferred to an adjacent molecule. As a final step for generating a free carrier, the Coulomb force caused by the electron on  $M^-$  and the “hole” on  $M^+$  has to be overcome. Both the aforementioned energy difference between  $\gamma$  (upper SOMO of the excited molecule) and  $\delta$  (LUMO), and the energy needed for taking the charges apart breaking the electrostatic attraction of the exciton contribute to the exciton binding energy. For most of the crystalline materials with delocalised orbitals, electron binding energy is smaller than the ambient thermal energy  $k_B T$  so a direct generation of opposite and independent free charges is observed.

### 1.2.6 PhotoVoltaic Effect

The charge generation causes an increase of the concentration of both electrons in the conduction band and of holes in the valence band. This can be represented with the position of the quasi-Fermi levels as they approach to the respective band edge ( $\bar{\mu}_{CB}$  towards conduction band and  $\bar{\mu}_{VB}$  towards valence band).

**Charges reaching the interfaces *via* diffusion.** In the absorber layer, the charges concentration increases thanks to the photogeneration, this causes a gradient of concentration that drives a diffusion current (see page 9) towards the non-absorbing layers. At the interface with the contacts, the carriers’ concentration is often smaller than in the bulk and this keeps up the diffusion current. This happens either due to recombination processes at the interfaces (e.g. when an electron reaches the holes rich *p*-type HTM) or to the charges collection through the interfaces as described in the next paragraph. As we will see, in perovskite solar cells the electric field in the bulk is mostly screened, and the transport *via* diffusion is very important. In the example reported in fig. 1.10 bottom, the gradients in the charges’ concentrations cause diffusion currents.

**Charge collection due to drift.** In regions where an electric field is present, e.g. close to the interfaces in a perovskite solar cells, the free

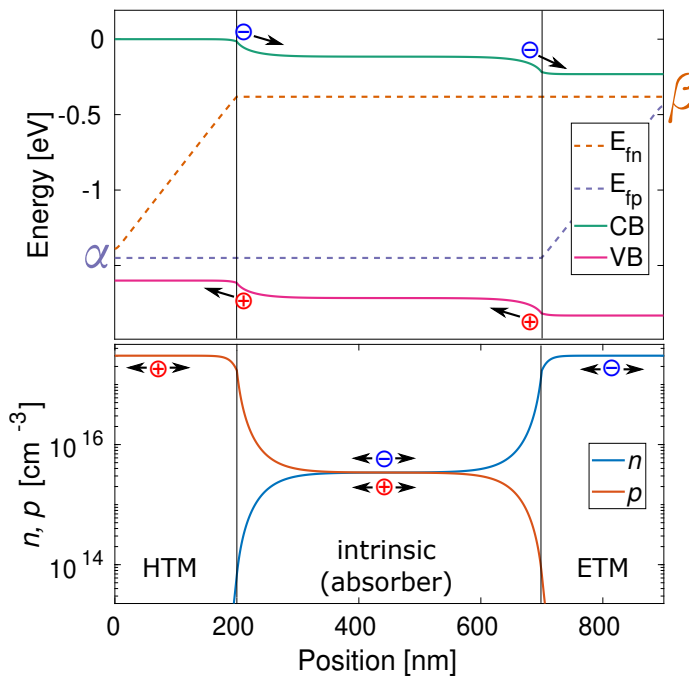


**Figure 1.10: Simulation of a  $p$ - $i$ - $n$  homojunction device illuminated at open circuit.** From left to right:  $p$ -type material, intrinsic semiconductor where generation occurs,  $n$ -type material. Low permittivity in the central layer was employed in order to represent also an electric field free zone. In top figure, the band diagram is represented. Single arrows indicate drift due to the field. The observable gradients of the quasi-Fermi levels just represent the minority carriers recombination current. The values of  $\bar{\mu}_{VB}$  in the location marked with  $\alpha$  and of  $\bar{\mu}_{CB}$  in  $\beta$  are the relevant ones for the open circuit voltage. In bottom figure: the charges' concentrations. Double arrows represent charge diffusion.

charges are pulled by the Lorentz force as seen in page 9. In the example reported in fig. 1.10 top, the curvature of the bands indicates the presence of electric field driving the charges' drift.

**Current.** As seen above, the photogenerated electrons get collected in the electron transporting material (ETM) and the holes in the HTM. If an external electrical circuit connects the two electrodes of our solar cell, optionally including a load, the accumulated carriers will discharge through this circuit and we will be able to measure a current and to extract a power.

**Voltage.** The quasi-Fermi splitting induced by the photogeneration of charges gets reflected in a shift of these levels also in the contacts. In doped contacts, the concentration of the minority carrier should become negligible due to the recombination with the abundant majority carrier (e.g. the electronic concentration in a *p*-type contact will decrease until where, in the bulk of the material, its respective conduction band quasi-Fermi level coalesce with the valence band quasi-Fermi level related to the majority carriers). Further, as in the metallic contacts there is no conduction nor valence band (and very fast recombination), the quasi-Fermi level related to the majority carrier ( $\bar{\mu}_{VB}$  in the HTM or  $\bar{\mu}_{CB}$  in the ETM) is the one ruling the Fermi level in the metal. So the difference between the holes'  $\bar{\mu}_{VB}$  at the HTM/electrode interface ( $\alpha$  in fig. 1.10) and the electrons'  $\bar{\mu}_{CB}$  at the ETM/electrode interface ( $\beta$  in fig. 1.10) gets reflected into the electrodes Fermi level, which ultimately can be measured as a voltage.

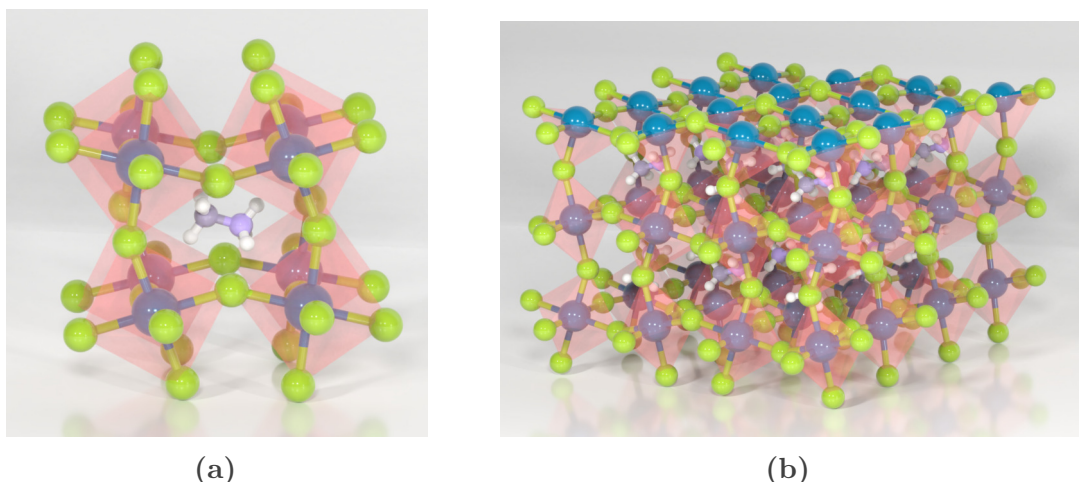


**Figure 1.11: Crystal structure of  $\text{MAPbI}_3$  perovskite.** In (a) the methylammonium cation is between  $\text{PbI}_6$  octahedra. In (b) the bulk structure is represented. These graphics, created with Vasp and Blender software, are courtesy of Edvin Fako <[efako@iciq.es](mailto:efako@iciq.es)>.

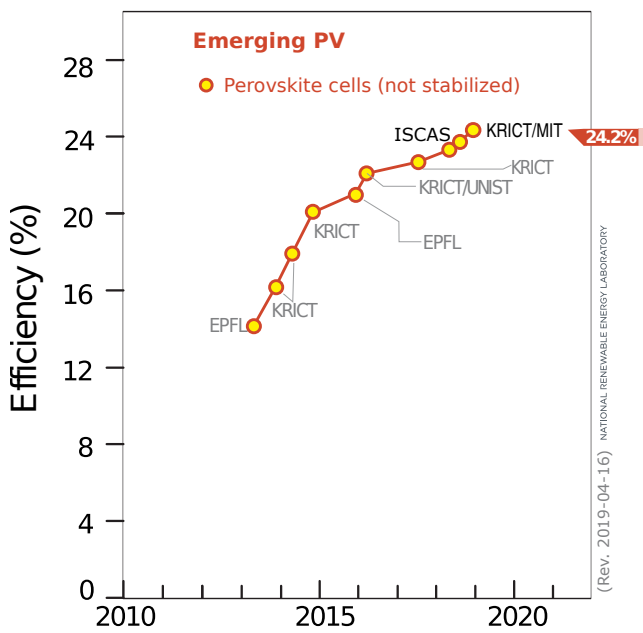


**Figure 1.12: NREL chart of “Best Research-Cell Efficiencies”** Just the perovskite solar cells (not stabilised) results have been reported.

## 1.3 Perovskite Solar Cells

*“That’s yogurt science!”*

Inorganic lead perovskites are known since at least 1958 and first reported in Møller [34]. Hybrid inorganic-organic lead halide perovskites have been first reported in 1978 by Weber [35] and one of the published structures,  $\text{MAPbI}_3$ , is represented in fig. 1.11. Just recently, in 2009, it has started to be used as absorber for solar cells (started by the research groups Miyasaka [36], Park [37, 38], and Snaith [39]). Perovskite solar cells evolved from the dye sensitized solar cells (DSSC) tradition, where an absorber dye is in contact with a titania ETM and different kinds of HTM. Here the absorber dye is substituted by a hybrid organic-inorganic lead halide perovskite semiconductor and both the ETM and the HTM can be composed of solid organic or inorganic materials. Thanks to the enormous research effort, these kind of devices reached a record stabilised efficiency of 20.9 % [40] with reports of even higher non-stabilised efficiencies (23.7 % [40, 41]) in relatively short time, as represented in fig. 1.12.

**Perovskite Absorber Synthesis.** The preparation of this hybrid semiconductor via spin coating and annealing at low temperature is extremely easy and convenient for small-scale research purposes. Nevertheless, this fabrication process is affected by a low reproducibility, likely due to the sensibility of the drying and crystallization step. This factor clearly slows down the research in perovskite solar cells. In literature, various reports of completely different results obtained from supposedly identical synthesis can be found [42, 43]. This issue is being addressed recently with the publication of more reliable and detailed fabrication procedures [44].

**Recombination mechanisms.** The non-radiative recombination inside the perovskite material is surprisingly low for a low temperature processed material. This is demonstrated by the large diffusion length in isolated crystals [21, 45–49]: for the CsFAMAPbIBr it is reported being  $\approx 140\text{ nm}$  for the electrons and  $\approx 1.9\text{ }\mu\text{m}$  for holes [50]. This is confirmed by the fact that once a thin layer ( $\approx 500\text{ nm}$ ) of the material is layered between an ETM and an HTM the photoluminescence lifetime is dramatically reduced [49, 51] indicating that the free charges can diffuse at least over the layer thickness. Even if not always the case [32, 52, 53], it is often reported that at open circuit conditions, the predominant recombination pathway in perovskite solar cells is identifiable as the surface recombination at the perovskite/selective contacts interfaces [3, 23, 28, 54–57]. This recombination is important in perovskite solar cells also due to the high minority carriers concentration close to the contacts, which is a result of the screening of the electric field in the bulk of the perovskite material.

**Open circuit voltage.** The open circuit voltage of a perovskite solar cell depends on many contributions and has a hard upper limit dictated by the perovskite band gap and the radiative recombination [58, 59]. This recombination is unavoidable as it originates by the detailed balance for a strongly absorbing material [22, p. 24] As just mentioned and as we will confirm in chapter 3, the surface recombination rate is one of the other contributions. Such non-radiative recombination has been predicted to have influence on the open circuit voltage ( $V_{\text{oc}}$ ) of perovskite solar cells when the carriers' lifetime is smaller than  $10\text{ }\mu\text{s}$  [27, 58]. A contact material having mid-gap states will favour the surface recombination, but also its additives (e.g. dopants, dispersants...) can introduce such trap states [56]. Additionally, a different material employed as ETM and HTM will result in a different built-in voltage (difference in contacts' Fermi levels energies), which constitutes a limit for the the open circuit voltage [3, 60] in case the

surface recombination is the main loss mechanism [58]. The presence of ionic accumulation in perovskite solar cells have been reported to reduce the influence of the  $V_{OC}$  from the built-in voltage [61]. Even a different molecular ordering in the selective contacts can influence the  $V_{OC}$  through the variation of the DOS width, and by consequence the energetics of the band edges [55]. Rather than a hard limit, the built-in voltage represents the applied voltage that saturates the depletion layers in the contacts, which implies a large charge density at the materials interface and an important surface recombination [3, 27]. Indeed, it has been predicted that suppressing the surface recombination can allow a device to give a voltage higher than the built-in voltage [27]. A large absorber band gap will have the excited charges thermally relaxing to a more energetic band, allowing the solar cell to achieve a higher  $V_{OC}$ . The perovskite band gap can be easily tuned changing its stoichiometry, for example partially replacing iodine with bromine [62–64] or using different organic cations [49]. For perovskite solar cells, the record reported *bandgap-voltage offset* are already much smaller than the voltage losses reported for organic solar cells (OSC) [20]. Also the morphology and composition of perovskite material can have an impact on the  $V_{OC}$ : non-passivated perovskite surface states which can act as traps [65] thanks to the easier deformation of the broken crystal cell, favouring the electron-phonon coupling needed for indirect transitions [66]; inhomogeneous perovskite layer can lead to pinholes and direct recombination between the two contacts [67–70]; accessible grain boundaries due to non-compact perovskite layer causes the presence of more recombination centres [71]; the presence of secondary phases with in-gap energies which can be reduced modifying the perovskite composition [24]. If we consider the possibility of stabilising the hot carriers (free charges generated by a photon with energy larger than the band gap, can be stabilised hindering the generation of phonons needed for their thermalisation) and of collecting them to the contacts before their thermal relaxation to the band edge, also a  $V_{OC}$  larger than the absorber band gap could be achieved and might, at least theoretically, break the Shockley-Queisser efficiency limit [72].

**Ionic defects.** A Schottky defect is the lack of a ion and its counter ion from an otherwise perfect crystal structure. This is commonly observed in ionic solids with weak lattice energy. Taking as an example the  $\text{MAPbI}_3$  lead halide perovskite, the formation of the Schottky defect  $\text{V}_{\text{MA}}' + \text{V}_\text{I}^\bullet$  (a methylammonium cation and a iodine anion leaving the crystal) is expected to be rather easy as these ions leaves behind vacancies with just charge  $\pm 1$

and the product,  $\text{CH}_3\text{NH}_3\text{I}$  can further decompose in volatile compounds like methylamine and hydrogen iodide. Indeed, the enthalpy of formation of this defect has been calculated to be only 0.08 eV, which at room temperature means that  $\approx 4\%$  of the  $\text{MA}^+$  and  $\text{I}^-$  sites in  $\text{MAPbI}_3$  are vacant [73, 74]. This specific defect can be avoided with small variations of the stoichiometry but other kind of defects will become more likely (e.g.  $\text{V}_{\text{Pb}}'' + 2\text{V}_{\text{I}}^\bullet$ ), and the minimum defects' concentration achievable with  $\text{MAPbI}_3$  perovskite has been reported to be around  $\approx 8 \times 10^{17} \text{ cm}^{-3}$  ( $\approx 0.02\%$ ) [73]. A iodine vacancy can also be originated by a Frenkel defect where a iodine migrates from its site to an interstitial one  $\text{V}_{\text{I}}^\bullet + \text{I}'_i$  and some studies support this as the origin of defects in perovskite materials [75–79]. Frenkel defects are expected to constitute shallow or deep traps in the perovskite band gap while Schottky defects should not present energies inside the band gap [74, 80–82].

**Ionic migration.** Ionic conductivity in halide perovskite materials has been pointed out more than 35 years ago [83–85]. In  $\text{MAPbI}_3$ , the presence of mobile ionic species has been directly observed from the slowly evolving work function or a lateral device using Kelvin probe force microscopy (KPFM) [75, 76]. In a generic  $\text{ABX}_3$  perovskite, it has been shown that both the A cation and the X anion can migrate through the crystal [86]. For  $\text{MAPbI}_3$  perovskite, the majoritarian mobile species has been identified as iodine vacancy  $\text{V}_{\text{I}}^\bullet$  [87, 88] and this is supported by a small simulated migration activation energy [89–93]. Instead, a significant contribution from methylammonium ions migration has been excluded [88, 90, 94]. In complete perovskite solar cells, the ionic migration is one of the factors causing hysteretic low frequency current-voltage behaviour [90, 95–97]. Still, the presence of ionic motion has been demonstrated even in non-hysteretic devices [98–100].

**Field free absorber.** The high density of ionic defects causes the equilibrium free charge concentration to be low [73] and the electric field inside the absorber to be completely shielded within few nanometres from the interfaces [97, 101].

**Diffusion as the main transport mechanism.** As we saw, most of the absorber layer in a perovskite solar cell will be electric field free. In this region, no drift will help with the charge collection and the photogenerated free charges will have to approach the contacts via diffusion. This is possible in perovskite thanks to its excellent electron and holes mobility

[16, 17] making possible diffusion lengths in the micrometre scale [21, 45–50].

**Hysteresis.** Hysteretic behaviour in current-voltage sweeps, while not often observed in other kind of solar cells, it is frequent in perovskite solar cells. Still, many reports of hysteresis-free perovskite solar cells can be found, especially for top cathode or for high performances bottom cathode devices. As we saw above, the presence of mobile ionic species is widely accepted for most of the hybrid lead perovskite materials and this has been indicated as one of the causes of the hysteresis [95, 96]. Considering that the recombination and collection of free charges is affected by the ions-modulated electric field [102], this is enough to explain the presence of hysteresis [97, 98] via the modulation of interfacial energy barriers [2]. Additionally, adsorption or chemical reaction of perovskite ionic defects with the selective contact surface (e.g. with titanium oxide [103–105]) could be important and can explain why [2], bottom cathode cells with inorganic contacts usually present hysteresis while top cathode with all-organic contacts usually does not.

**Characterisation.** The characterisation techniques for perovskite solar cells and the relative interpretation evolved from the techniques and theory built around OSC and DSSC [106]. This pre-existing framework has been widely used in literature for perovskite solar cells by various research groups [3, 31, 55, 107, 108]. Unfortunately, perovskite solar cells are different enough from OSC and DSSC to doom the utility of most of these observations. Moreover, while an acceptable agreement between different characterisation techniques was often observed in OSC [109–111] and DSSC [106], in perovskite solar cells we often observe hard-to-explain discrepancies [108]. In the past few years, the theoretical framework has been expanded and should finally enable the perovskite community to re-interpret and re-design the solar cells characterisation techniques. In chapter 3 the reader can find some of the accepted concepts and some novel proposals about the interpretation of the classical characterisation techniques when used on perovskite solar cells.

**Stability.** The stability of the perovskite solar cells is the number one blocker to commercialisation [112]. Its keystone has still to be identified. The inclusion of self-assembly mono layers at the materials’ interfaces helps the device stability passivating surface states [113, 114]. Usage of organic contact layers is also a source of instability, for example due to the

slow crystallisation of spiro-OMeTAD [115] (due to its low glass transition temperature of 126 °C [116]) and metallic oxides might be used instead [114]. Also fine tuning the stoichiometry and using a mix of cations (e.g. adding cesium salts) can lead to a more ordered crystalline phase and reduce ionic defects concentration and mobility, both these contributions helps the stability of the devices [112]. An interesting investigation is being carried on by Dr. D. R. Ceratti and Prof. D. Cahen (unpublished) regarding the release of a proton by methylammonium cation. So, when this cation gets in contact with non-acidic materials it can release its proton and leave the perovskite crystal structure as methylamine. This could explain the reports about the beneficial addition of acids in perovskite precursors solution, mainly by Snaith group [117–119]. Additionally, various other reactions can happen inside the material or at its interfaces, for example the formation of metallic lead [76, 120], of molecular iodine [77], of lead iodide [73, 121], of methylammonium iodide [73]. Some of these degradation pathways are further favoured by contact with moisture [122–125] (which if not too much, can be reversed [126]), with oxygen in combination with light [127, 128] (as described in page 48), with UV light [129], with temperature [130, 131], with spiro-OMeTAD [105, 132, 133], with PC<sub>60</sub>BM [134], with the metallic electrodes due to chemical reactivity [134–138] or intermixing [139].

## 1.4 Motivation and Aims

*“To begin with, we want everything.”*

autistici / inventati

The objectives of this thesis are:

- synthesise different kinds of lead perovskite absorbers (e.g.  $\text{MAPbI}_{3-x}\text{Cl}_x$ ,  $\text{MAPbI}_3$ , FAMAPbIBr, CsFAMAPbIBr);
- fabricate solar cells with different structures (e.g. top and bottom cathode);
- test different materials for selective contacts, either known (e.g. flat or mesoporous titania, PC<sub>70</sub>BM or plain fullerene) or novel materials obtained via collaborations (e.g. TAE-1, TAE-3, TAE-4);
- optimisation of the devices fabrication in order to get close to the state of the art devices;
- characterisation of the prepared devices using the existing routine techniques (e.g. current-voltage sweeps);
- characterisation using advanced small perturbation techniques;
- optimisation of the characterisation methods, data acquisition, and data processing;
- obtain information on the charge accumulation and charge dynamics from the characterisation output;
- model perovskite solar cells and compare the expected theoretical output with the experimental one;
- where the simulation matches the experiment, take advantage of the additional insight obtainable from the modelling.



# Chapter 2

## Experimental Methods

*“When it’s a humid day, we  
don’t fabricate cells”*  
*“But... don’t you fabricate them  
in a glovebox?”*  
*“Of course.”*

**Abstract.** The experimental methods are described here in detail, mixed with comments and warnings to the reader, trying to underline the critical points spotted over my PhD. Needless saying, the critical points in fabricating a complex electronic device such as a perovskite solar cells are many and neither a proper description can assure reproducibility.

---

**Table of Contents**

---

**Materials****Equipment****EQUIPMENTS FOR FABRICATION**

Ultra-violet ozone cleaning system, 34 • Spin coater in air atmosphere, 34 • Muffle oven, 34 • Titanium hotplate, 34 • Glovebox, 34 • Spin coater in inert atmosphere, 35 • Precision hotplate, 35 • Thermal evaporator, 35

**EQUIPMENTS FOR MATERIALS CHARACTERISATION**

Optical microscope, 35 • UV–Vis–NIR spectrophotometer, 35 • PhotoLuminescence spectrophotometer, 35 • Time Resolved PhotoLuminescence spectrophotometer, 36 • X-ray diffractometer, 36 • ESEM and ESEM-EDX microscopes, 36 • AFM microscope, 37 • Profilometer, 37

**EQUIPMENTS FOR DEVICES ELECTRICAL CHARACTERISATION**

Devices holder, 37 • Solar simulator, 37 • Programmable digital multimeter, 38 • White LED illumination, 38 • Pulsed illumination, 38 • Oscilloscope, 38 • Switch for transient measurements, 39

**Synthesis, Handling and Purification****MAI SYNTHESIS****LEAD SALTS HANDLING****DENSE TITANIA PRECURSORS SOLUTION****MAPbI<sub>3-x</sub>Cl<sub>x</sub> PEROVSKITE PRECURSORS SOLUTION****CsFAMAPbIBr PEROVSKITE PRECURSORS SOLUTION****SPIRO-OMETAD AND OTHER HTM SOLUTIONS**

Additives mother solution, 41 • Spiro-OMeTAD, 41 • TAE-\*, 41 • Oxidation control, 41 • PEDOT:PSS, 41

**Perovskite Solar Cell Fabrication****TOP CATHODE PEROVSKITE SOLAR CELLS**

Anode and HTM substrate reparation, 43 • MAPbI<sub>3-x</sub>Cl<sub>x</sub> perovskite one step fabrication, 44 • MAPbI<sub>3</sub> perovskite two step fabrication, 44 • ETM and cathode deposition, 45

**BOTTOM CATHODE PEROVSKITE SOLAR CELLS**

Cathode and ETM substrate preparation, 46 • CsFAMAPbIBr perovskite one step fabrication, 47 • HTM and cathode deposition, 47

**HANDLING AND PRESERVATION**

Oxidative doping of HTM, 48 • Degradation due to oxygen and illumination, 48

---

## 2.1 Materials

Dust free cloths Super Polx 1200A  $23 \times 23$  cm were bought from Berkshire.

Patterned FTO substrates with sheet resistance of  $7\Omega\Box^{-1}$  (TEC7) on 2.2 mm thick and  $14.8 \times 14.8$  mm wide Pilkington glass were bought from Xinyan Technology Ltd.

Patterned ITO substrates with sheet resistance of  $15\Omega\Box^{-1}$  on 1.1 mm thick and  $15 \times 15$  mm wide glass were bought from Xinyan Technology Ltd.

All anhydrous and non-anhydrous solvents had a reagent grade purity; were purchased from Sigma-Aldrich and used without any additional treatment.

Titanium(IV) isopropoxide (97 %), acetylacetone, and bis(trifluoromethane)sulfonimide lithium salt (LiTFSI) were bought from Sigma-Aldrich.

PEDOT:PSS Clevios P VP.AI 4083 was bought from Heraeus.

$\text{PbI}_2$  (99 %),  $\text{PbBr}_2$  (99.999 %),  $\text{CsI}$  (99.999 %),  $\text{PbCl}_2$  (98 %), anhydrous chlorobenzene, anhydrous DMF, and anhydrous DMSO were bought from Sigma-Aldrich and kept in a nitrogen-filled glovebox.

Methylamine in methanol (40 w/w%,  $\approx 9.8$  M) was bought from Tokyo Chemical Industry.

FAI, MABr and MAI were either synthesised (described in page 39) or bought from GreatCell Solar (unknown purity).

4-tert-butylpyridine and hydroiodic acid (57 w/w% in water) were bought from Sigma-Aldrich and kept in a fridge (the colour of both these reagents change with ageing when kept out of the fridge, indicating degradation).

Spiro-OMeTAD was bought from 1-Material and stored in a nitrogen-filled glovebox.

TAE-1, TAE-3, and TAE-4 molecules (subject of the study in chapter 4) were used as received from Dr. Inés García-Benito, Dr. Agustín Molina-Ontoria and Dr. Nazario Martín (IMDEA, Madrid). The synthesis of TAE-1 has been described in Cabau *et al.* [140] and Choi *et al.* [141]. The synthesis of TAE-3 and TAE-4 has been described in Gelmetti *et al.* [3].

## 2.2 Equipment

*“Bring magnets with you...”*

### 2.2.1 Equipments for Fabrication

**Ultra-violet ozone cleaning system.** Organic residuals removal was performed with a T10X10/OES UV/ozone cleaning system from UVOCS. Most common failure: insufficient gas extraction flow detected by differential pressure meter on the rear, it can be partially configured via a screw. It has been used for the treatment of FTO and ITO just prior to the deposition of titanium oxide precursors or PEDOT:PSS. For the latter, this process improves the PEDOT:PSS coverage increasing the support hydrophilicity.

**Spin coater in air atmosphere.** Spin coating depositions in the clean room were performed with a Laurell WS-400BZ-6NPP-LITE spin coater. It has been used for deposition of titanium oxide precursors, PEDOT:PSS, PC<sub>60</sub>BM, and PC<sub>70</sub>BM.

**Muffle oven.** Calcination was performed with a muffle oven Hobersal HD-230 controlled with a Fuji Electric PXR-4. Most common failure: misuse of the controller by the users can cause unexpected excessive heating. It has been used for calcination of just-deposited dense titanium oxide thin films.

**Titanium hotplate.** Calcination can be performed with a titanium hotplate Harry Gestigkeit PZ 28-3TD. Most common failures: controller failure and heating resistance breaks in a point, it can be unmounted and replaced. It has been used for calcination as an alternative to muffle oven.

**Glovebox.** Perovskite deposition and precursors storage was done in a nitrogen-filled glovebox MBraun UNILab.

**Spin coater in inert atmosphere.** Spin coating depositions in the nitrogen-filled glovebox were performed with a SPIN150 equipment (this model does not require a gas inlet, which would be troublesome in a glovebox) from SPS Europe where the transparent cap was removed from the lid for helping solvent vapours removal. For avoiding the accumulation of waste material, an aluminium foil was used for covering the deposition chamber and was replaced frequently. Most common failure: exhaustion of the supposedly 20 yr lasting non-volatile SRAM (integrated circuit BattRam DS1230Y-85+ DIP28, a perfect example of planned obsolescence). It has been used for depositing the perovskite precursors and the HTM selective contacts.

**Precision hotplate.** Annealing was performed with a highly homogeneous hotplate JP Selecta Plactronic. It has been used for annealing the just-deposited perovskite thin films.

**Thermal evaporator.** High vacuum ( $1 \times 10^{-9}$  bar) thermal depositions were performed with a MBraun vacuum deposition chamber connected with a scroll pump in series to a turbo pump. The deposition was controlled with an Inficom SQC310C unit (firmware version 6.44). The deposition rate was measured via two oscillating quartz sensors whose calibration tooling was performed yearly. The evaporation chamber was embedded in a MBraun MB200B glovebox module controlled by a MBraun MB20G. It has been used for depositing the metallic electrodes, usually gold or silver.

## 2.2.2 Equipments for Materials Characterisation

**Optical microscope.** Optical microscopy images were acquired with a Leica S6 D microscope. It has been used for studying the homogeneity of the deposited thin films.

**UV–Vis–NIR spectrophotometer.** Absorbance measurements were carried out on a Lambda 1050 PerkinElmer spectrophotometer equipped with a PhotoMultiplier Tube, InGaAs and PbS detectors system, double beam optics, double monochromator, D<sub>2</sub> and W light sources. It has been used for estimating the thickness of the deposited thin films.

**PhotoLuminescence spectrophotometer.** Fluorescence measurements were carried out on a Fluorolog Horiba Jobin Yvon spectrofluorimeter

equipped with photomultiplier detector, double monochromator, and Xenon light source. It has been used for the characterisation of molecules in solution.

## 2

**Time Resolved PhotoLuminescence spectrophotometer.** Photo-Luminescence lifetime measurements were carried out on a Edinburgh Instruments LifeSpec-II based on the time-correlated single photon counting (TCSPC) technique, equipped with a PhotoMultiplier Tube detector, double subtractive monochromator and picosecond pulsed diode lasers source. It has been used for comparing the radiative recombination lifetime in perovskite thin films with or without selective contacts.

**X-ray diffractometer.** X-ray diffraction (XRD) measurements were made using a Bruker-AXS D8-Discover diffractometer equipped with parallel incident beam (Göbel mirror), vertical  $\Theta - \Theta$  goniometer, XYZ motorised stage and with a GADDS (General Area Diffraction System). Samples were placed directly on the sample holder and the area of interest was selected with the aid of a video-laser focusing system. An X-ray collimator system allows to analyse areas of  $500\text{ }\mu\text{m}$ . The X-ray diffractometer was operated at 40 kV and 40 mA to generate Cu K $\alpha$  radiation. The GADDS detector was a HI-STAR (multiwire proportional counter of  $30 \times 30\text{ cm}$  with a  $1024 \times 1024$  pixel). We collected frames (2D XRD patterns) covering 15 to  $70^\circ 2\Theta$  from three different detector positions at a distance of 15 cm from the sample. The exposition time was 300 s per frame and it was chi-integrated to generate the conventional  $2\Theta$  versus intensity diffractogram. Identification of the materials was achieved by comparison of the XRD diffractogram with the ICDD data base (release 2007) using Diffracplus Evaluation software (Bruker 2007). It has been used for investigating the chemical composition of perovskite thin films after some months in contact with organic molecules.

**ESEM and ESEM-EDX microscopes.** Superficial and cross section environmental scanning electron microscopy (ESEM) images were acquired at low voltage (beam accelerated with 20 kV) and high vacuum ( $1 \times 10^{-8}\text{ bar}$ ) in a FEI Quanta 600 FEG microscope. The cut for cross section was performed mechanically: a small angle grinder (from Dremel) was used for furrowing a diagonal line on the substrate glass side (opposite to the FTO), then using two pliers the substrate was forced as if it was to bend the glass and opening further the furrow. It has been used for

studying the homogeneity of the thin film coverage both from the top view and from the cross section.

**AFM microscope.** The alternating current atomic force microscopy (AC-AFM) imaging was done via atomic force microscopy (AFM) (Pico SPM II) and processed with WSxM software [142]. It has been used for confirming the coverage of the deposited thin films and for measuring their roughness.

**Profilometer.** Thicknesses were measured furrowing layers with a hard object and measuring the elevation profile with an Ambios Tech. XP-1 profilometer. It has been used for measuring the thickness of the deposited layers thicker than 100 nm.

### 2.2.3 Equipments for Devices Electrical Characterisation

**Devices holder.** The devices holder is designed for holding 4 devices with 4 independent diodes each (the bottom electrode electrical contact is in common for all the diodes, the top electrodes contacts are independent) and consists in an airtight container topped with a quartz window. It was designed and fabricated by Ikerlan. The holder has at least one gold tip for each diode's electrode, the contact is ensured by springs pushing the tips towards the devices. A printed circuit board connects the gold tips to a coaxial connector via two rotatory selectors which allows to select the needed diode. It has been used for contacting the electrodes of the devices during all electrical measurements.

**Solar simulator.** The illumination with accurate solar spectra was provided by a Sun 2000 solar simulator (150 W) bought from ABET Technologies. The proper filters of the lamp were set to simulate the AM 1.5G solar spectrum. The light intensity at the measurement position was measured via the short circuit current of a small photodiode calibrated with a certified (NREL) silicon photodiode and regulated to  $1000 \text{ W m}^{-2}$ . When needed, the light intensity was reduced using neutral filters. Most common failure: the power supply providing high voltage to the lamp. It has been used for illuminating the devices during current-voltage sweeps.

**Programmable digital multimeter.** Currents and voltages were performed with a Tektronix Keithley 2400 (firmware revision C30) programmable digital source meter connected to a computer via a GPIB-USB-HS adapter from National Instruments, connected to the solar simulator for the shutter control via a RS-232 (Keithley side) to coaxial (solar simulator side), and connected to the device to measure via a coaxial (devices side) to 2 banana plugs (Keithley side). Most common failure: we observed sparks in the devices when connecting to the Keithley multimeter, so from our experience we recommend to manually set the Keithley in current measure mode with zero applied voltage, start the measure with the device not connected and finally connect the device. It has been used for registering the current-voltage sweeps.

**White LED illumination.** White illumination at tunable intensity was provided via a white light LED ring with LED from LUXEON Lumileds and powered by a Aim-TTi PLH120-P power supply. It has been used for background illumination for charge extraction (CE), transient photovoltage (TPV), or transient photocurrent (TPC) measurement.

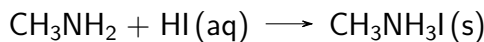
**Pulsed illumination.** Perturbation illumination for photophysical characterisation was provided by a nanosecond PTI GL-3300 nitrogen laser. The pulse was triggered with a Aim-TTi TG330 analog function generator generating a square wave pulse. The pulse duration is around 1.5 ns. The wavelength was selected using the absorption and emission of a dissolved molecular dye. The pulse intensity was attenuated with a semi-transparent glass for ensuring the small perturbation regime. The equipment can output up to 20 pulses per second, but due to the oscilloscope internal memory speed we are limited to 1 pulse per second. It has been used for providing the illumination perturbation in TPV characterisation.

**Oscilloscope.** The voltage transients for photophysical characterisation were registered with a Yokogawa DLM2052 oscilloscope with an internal resistance of  $1\text{ M}\Omega$ , connected to the device holder via coaxial cable and to a computer via an USB2 port (the transfer speed could be better if an Ethernet connection were used). For each registered transient, 12 500 points were saved (the maximum record length for this oscilloscope is 125 Mpoints and the maximum sampling rate is 2.5 Gpoints/s). It has been used for measuring the voltage transients for the transient photovoltage (TPV), transient photocurrent (TPC), and charge extraction (CE) measurement.

**Switch for transient measurements.** An equipment built in-house was used as a switch for opening and closing connections based on the input from a Aim-TTi TGP110 pulse generator. It has been used for simultaneously shutting down the white LED ring and short the devices during the CE measurements.

## 2.3 Synthesis, Handling and Purification

### 2.3.1 MAI Synthesis



The synthetic method was inspired by [37]. In a 500 ml one-necked flask (over-dimensioned for easing the drying step) opened at air, 14 ml of a methylamine in methanol (40 w/w%,  $\approx 9.8 \text{ M}$ ) were introduced. While stirring and cooling at  $0^\circ\text{C}$ , 15 ml of hydroiodic acid in water (57 w/w%) was added drop-wise. The cooling was interrupted and the mixture was continuously stirred at room temperature. Then the vessel was left still overnight. The solution was evaporated in a vacuum-assisted rotatory evaporator at  $60^\circ\text{C}$ . The obtained white solid was scraped and transferred on a funnel with membrane filter (Sartorius, PTFE). It was washed with diethyl ether and the diethyl ether discarded. The solid was dissolved with ethanol, using as little volume as possible and vacuum was used for forcing the ethanol through the filter. The solid was recrystallised pouring abundant diethyl ether, then filtered, washed with diethyl ether and dried at vacuum overnight.

### 2.3.2 Lead Salts Handling

Lead iodide and bromide bottles have to be opened in a nitrogen-filled glovebox. The failure in keeping the lead containing precursors away from oxygen causes the formation of insoluble derivatives, likely lead oxide or metallic lead, which will have to be filtered away from the precursors solution.

### 2.3.3 Dense Titania Precursors Solution

The precursor solution for the dense  $\text{TiO}_2$  layer was prepared adding drop-wise 0.38 ml of acetylacetone to 0.65 ml of titanium(IV) isopropoxide and diluted in 5 ml of ethanol. Beware that the titanium-acetylacetone reaction is strongly exothermic. The solution can be used just for a few days after preparation. Some hydrolysed product can be present in the solution, so it has to be filtered (PTFE, 0.2  $\mu\text{m}$ ) just before the usage.

An alternative synthetic route has been recently employed, starting from the stable and commercially available titanium diisopropoxide bis-(acetylacetonate) as a convenient alternative: 220  $\mu\text{l}$  of  $\text{Ti}(\text{i-PrO})_2(\text{acac})_2$  in isopropanol (75 w/w%, 0.45 mmol) were diluted adding 1.28 ml of isopropanol and filtered (PTFE, 0.2  $\mu\text{m}$ ) just before the usage.

### 2.3.4 $\text{MAPbI}_{3-x}\text{Cl}_x$ Perovskite Precursors Solution

In a vial, 400 mg of MAI (2.52 mmol) and 230 mg of  $\text{PbCl}_2$  (98 %, 0.81 mmol) were weighted. Then 1 ml of anhydrous DMF was added and the solution was stirred at 65 °C for 1.5 h. The solution was not filtered and was used the same day of preparation.

### 2.3.5 $\text{CsFAMAPbIBr}$ Perovskite Precursors Solution

In a nitrogen-filled glovebox, 507 mg of  $\text{PbI}_2$  (99 %, 1.1 mmol), 73.4 mg of  $\text{PbBr}_2$  (99.999 %, 0.200 mmol), 172 mg of FAI (1.00 mmol) and 22.4 mg of MABr (0.200 mmol) were weighted and mixed in a 5 ml vial. For reducing the effect of static charging on the weighting process in the glovebox, a stainless steel weighing boat was specifically fabricated. The mixed solid precursors can show some darkening due to the formation of perovskite in a solid-solid reaction (also known as mechanosynthesis [143]), nevertheless this solid mixture can be stored in the glovebox for weeks.

The day of the deposition, 0.2 ml of anhydrous DMSO and 0.8 ml of anhydrous DMF were added to the solid mixture of precursors. The solution was vigorously stirred at room temperature (RT) for 1 h. Heating or storing the solution for days has been observed to result in a yellow perovskite layer when deposited and annealed, so some kind of detrimental transformation is evident to happen in the solution, hindering its storage for long time. Finally 42  $\mu\text{l}$  of a 1.5 M CsI solution in DMSO (63  $\mu\text{mol}$ ) were added to the previous solution. The solution was filtered (PTFE, 0.2  $\mu\text{m}$ ) just before its usage. The resulting stoichiometry is  $\text{Cs}_{0.06}\text{FAMA}_{0.2}\text{Pb}_{1.3}\text{I}_{3.2}\text{Br}_{0.6}$ .

### 2.3.6 Spiro-OMeTAD and Other HTM Solutions

**Additives mother solution.** A solvent with additives mix was prepared adding 197 µmol of 4-tert-butylpyridine (28.8 µl) to 1 ml of anhydrous chlorobenzene, then 32 µmol of bis(trifluoromethane)sulfonimide lithium salt (LiTFSI, 9.1 mg) were added. The presence of 4-tert-butylpyridine enables the solubility of LiTFSI in chlorobenzene (otherwise it would have to be dissolved in acetonitrile).

**Spiro-OMeTAD.** N<sup>2</sup>,N<sup>2</sup>,N<sup>2'</sup>,N<sup>2'</sup>,N<sup>7</sup>,N<sup>7</sup>,N<sup>7'</sup>,N<sup>7'</sup>-octakis(4-methoxyphenyl)-9,9'-spirobi[9H-fluorene]-2,2',7,7'-tetramine (spiro-OMeTAD) solution was prepared dissolving 59.0 µmol of spiro-OMeTAD (72.3 mg) in 1 ml of the aforementioned solvent with additives mix.

**TAE-\*.** Other HTM solutions for bottom cathode cells were prepared dissolving either 29.5 µmol of tetra{4-[N,N-(4,4'-dimethoxydiphenylamino)-]phenyl}ethene (TAE-1, 36.6 mg), 19.7 µmol of 3,3',6,6'-tetrakis[N,N-bis(4-methoxyphenyl)amino]-9,9'-bifluorenylidene (TAE-3, 24.4 mg), or 9.83 µmol of 3,3',6,6'-tetrakis(3,6-dimethoxy-9H-carbazol-9-yl)-9,9'-bifluorenylidene (TAE-4, 12.1 mg) in 1 ml of solvent with additives further diluted with chlorobenzene in a 1:1, 1:2, 1:5 ratio respectively, in order to preserve the HTM to additives molar ratio of the spiro-OMeTAD solution (roughly 3 eq of 4-tert-butylpyridine and 0.5 eq of LiTFSI). The lower concentrations were used due to the lower solubility of these HTM as compared to spiro-OMeTAD one.

**Oxidation control.** The spiro-OMeTAD, TAE-1, TAE-3, and TAE-4 solutions did not include chemical oxidising agents and were prepared in a nitrogen-filled glovebox in order to have control over the oxygen oxidation degree of the molecules.

**PEDOT:PSS.** Poly(3,4-ethylenedioxythiophene) poly(styrenesulfonate) (PEDOT:PSS) was used as received from the commercial supplier.

## 2.4 Perovskite Solar Cell Fabrication

*“Making good devices is an art”*

The “top cathode” (or “illuminated anode”, fig. 2.2) or “bottom cathode” (or “illuminated cathode”, fig. 2.3) naming refers to the cell orientation during fabrication, so the “bottom” layer is the one closer to the glass substrate, as shown in fig. 2.1b. Both the top and the bottom cathode solar cells were fabricated following the scheme reported in fig. 2.1c.

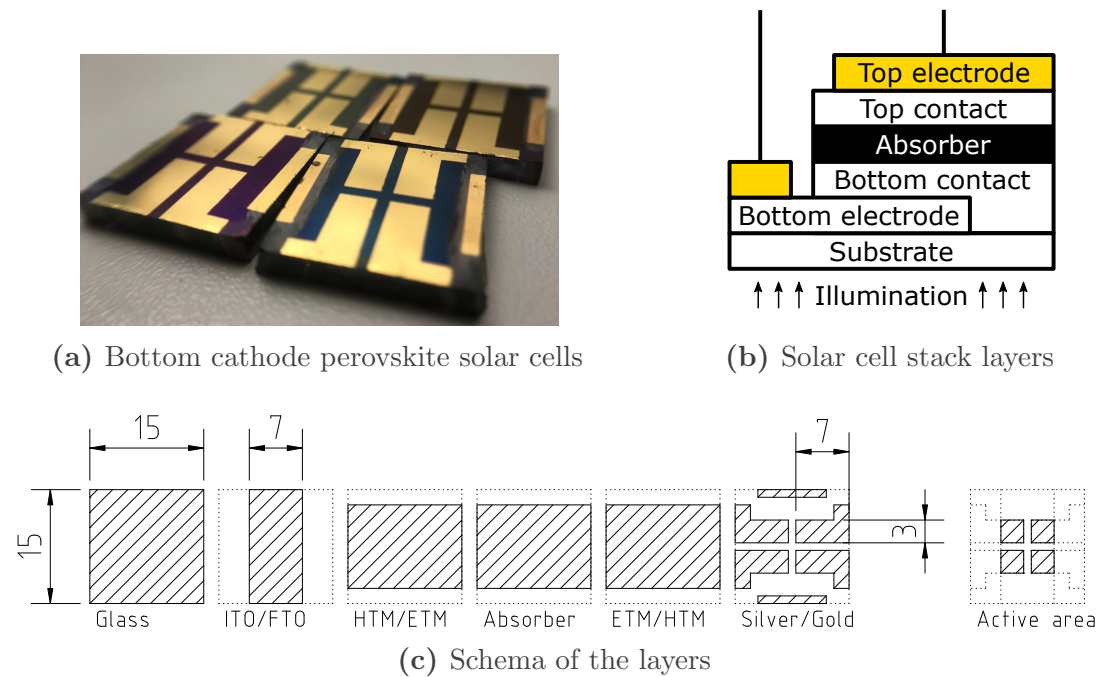


**Figure 2.1: Solar cells layers layout.** In (a) a picture of typical bottom cathode perovskite solar cells is reported, each cell have a different HTM [3]. In (b) “top and bottom” naming is represented. The layers are named in the fabrication order, from the substrate up. The selective HTM and ETM contacts are named “contacts” just for brevity. The non-selective electrodes used for the electric connections are referenced as “electrodes”. In (c) the shapes and dimensions of the utilised layers for top/bottom cathode solar cells are shown. From left to right: the glass substrate, the bottom transparent conducting oxide electrode, the bottom selective contact, the absorber, the top selective contact, the top metallic electrode. The active area is defined by the overlap of the ITO/FTO and the silver/gold layers, being  $9\text{ mm}^2$ .

## 2.4.1 Top Cathode Perovskite Solar Cells

**Anode and HTM substrate reparation.** This process was performed in a ISO 7 clean room. ITO coated substrates were cleaned in an ultrasound bath with acetone for 15 min, isopropanol for 15 min and rubbed with a dust-free cloth. Finally, an UV/ozone treatment was performed for 20 min. PEDOT:PSS was filtered on PES membrane ( $0.22\text{ }\mu\text{m}$ ) and deposited via spin coating (static dispensing,  $110\text{ }\mu\text{l}$ ) with a first step where the speeds regulates the thickness of the layer and a second step for removing the residual liquid accumulated at the substrate corners. The conditions are reported in table 2.1 and the thicknesses were obtained via absorbance

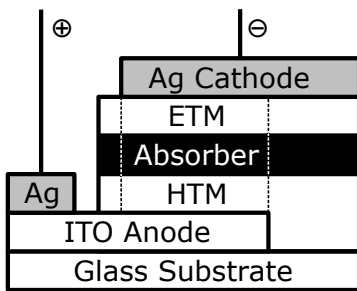


**Figure 2.2: Top cathode solar cell.** The stack of a top cathode (or illuminated anode) solar cell. The shapes dimensions does not relate to real thicknesses and areas. The dashed lines indicate the active area.

**Table 2.1:** PEDOT:PSS deposition conditions and resulting thickness

acceleration [ $\text{rpm s}^{-1}$ ]	1 <sup>st</sup> step		acceleration [ $\text{rpm s}^{-1}$ ]	2 <sup>nd</sup> step		thickness [nm]
	speed [rpm]	time [s]		speed [rpm]	time [s]	
1000	1000	60	2000	2000	3	65
1000	1600	60	2000	2000	3	45
1000	4500	30	500	3500	30	27

of light with wavelength 2150 nm calibrated to the a very thick layer measured with the profilometer. A rough relation between the thickness  $d$  and the spinning speed  $f$  (with 1000  $\text{rpm s}^{-1}$  acceleration) was found as  $d = \frac{1820}{\sqrt{f}}$ . Substrates were dried at 110 °C for 20 min and stored in a nitrogen-filled glovebox for avoiding moisture absorption.

**MAPbI<sub>3-x</sub>Cl<sub>x</sub> perovskite one step fabrication.** The deposition process was performed in a nitrogen-filled glovebox. The precursors solution (see page 40) was deposited via spin coating (80 µl, static dispensing, loading time 5 s) with an acceleration of 1000  $\text{rpm s}^{-1}$ , a speed of 1900 s for 40 s. The substrate was moved directly to a hotplate at 100 °C and annealed for 80 min, resulting in a 430 nm thick perovskite layer. The film is colourless just after deposition, then it turns to brown, yellow and finally black on the hotplate.

**MAPbI<sub>3</sub> perovskite two step fabrication.** This process was performed in a nitrogen-filled glovebox. A constant purge of glovebox atmosphere is needed during the whole deposition process. This reduces the DMF and DMSO vapours concentration avoiding damages to the

**Table 2.2:** MAPbI<sub>3</sub> two step deposition: conditions for the PbI<sub>2</sub> and MAI spin coating and resulting perovskite film thickness.

acceleration [rpm s <sup>-1</sup> ]	speed [rpm]	time [s]	thickness [nm]
2000	2000	90	440
4100	4100	90	320
8000	7500	90	230

formed perovskite layer and the poisoning of the glovebox oxygen removal catalysts. 460 mg of PbI<sub>2</sub> were dissolved in 1 ml of a 23:2 v/v blend of anhydrous DMF and anhydrous DMSO. This solution was stirred at 50 °C for 1 h. 50 mg of MAI were dissolved in 1 ml of a 3:1 v/v blend of anhydrous isopropanol and ethanol. A PbI<sub>2</sub> layer was deposited from the unfiltered solution via spin coating (static dispensing, 80 µl, loading time 5 s) with accelerations and speeds reported in table 2.2. After 60 s from the start of the spin coating, the MAI solution (100 µl) was dynamically dispensed on the centre of the spinning substrate with a 100 µl micropipette keeping it tilted and depositing an uninterrupted stream. The substrate was then moved directly from the spin coater to a hotplate at 100 °C and annealed for 15 min. The thicknesses reported in table 2.2 were measured using a profilometer.

**ETM and cathode deposition.** The solution was prepared in a ISO 7 clean room and the deposition process was performed in a nitrogen-filled glovebox. 30 mg of PC<sub>70</sub>BM were dissolved in 1 ml of anhydrous chlorobenzene and stirred at RT for 1 h. This solution was filtered (PTFE, 0.2 µm) and deposited in a nitrogen-filled glovebox via spin coating (static dispensing, 80 µl, loading time 5 s) with accelerations and speeds reported in table 2.3. The thickness was estimated by absorbance with monochromatic illumination at 378 nm calibrating the highest point with a profilometer measurement. A rough relation between the thickness  $d$  and the spin speed  $f$  was found as  $d = \frac{3930}{\sqrt{f}}$  when a concentration of 30 mg ml<sup>-1</sup> in chlorobenzene was used. ITO contact was cleaned on two edges using swabs slightly wet with chlorobenzene and then DMSO (the solvent vapours can damage the perovskite layer, so it is suggested to do this after HTM deposition which partially protects the underlying layer).

**Table 2.3:** PC<sub>70</sub>BM deposition conditions and resulting thickness, with a concentration of 30 mg ml<sup>-1</sup>

acceleration [rpm s <sup>-1</sup> ]	speed [rpm]	time [s]	thickness [nm]
1100	1100	80	120
2000	2000	60	90
4000	4000	40	60
8000	7500	20	40

Finally, 120 nm of silver were deposited by thermal evaporation in high vacuum ( $1 \times 10^{-9}$  bar). This resulted in four independent 0.09 cm<sup>2</sup> diodes for each substrate.

#### 2.4.2 Bottom Cathode Perovskite Solar Cells

**Cathode and ETM substrate preparation.** This process was performed in a ISO 7 clean room. Pre-patterned 1.5 × 1.5 cm FTO coated glasses were employed as substrate. The identification code was scratched with a diamond tip pencil. Initially the dust is removed with adhesive tape and rubbing with a dust free cloth. Then the substrates were cleaned with ultrasonication in water with Hellmanex soap, then in deionised water, and finally in isopropanol; dried rubbing with a dust free cloth and the organic residuals were removed with an UV/ozone treatment for 20 min. Dense (as opposed to mesoporous) TiO<sub>2</sub> layer was deposited (static dispensing, 80 µl) from the solution described in page 40 by spin-coating at 3000 rpm, 3000 rpm s<sup>-1</sup>, for 60 s ( $\approx$ 30 nm) over the previously cleaned FTO. The substrates were placed in a glass Petri dish kept slightly open (this helps

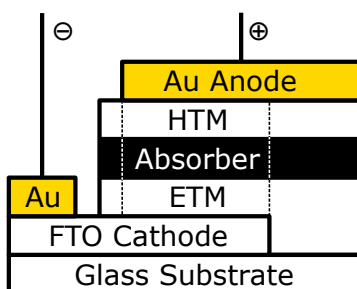


**Figure 2.3: Bottom cathode solar cell.** The stack of a bottom cathode (or illuminated cathode) solar cell. The shapes dimensions does not relate to real thicknesses and areas. The dashed lines indicate the active area.

the removal of the burnt organic residuals and manages to reduce the entrance of dust) and inserted in a muffle oven. The sintering can also be performed placing the substrates on a titanium hotplate, but the amount of dust on the deposited layer is greater. Then the substrates were sintered at 500 °C for 30 min and cooled down slowly for not breaking the Petri dish. Subsequently the substrates were immersed in a filtered (PES, 0.22 µm) 40 mM TiCl<sub>4</sub> solution in 9 % HCl in an oven at 70 °C for 20 min (this process erode the titania layer, so it is important to not exceed in the duration), cleaned with water, with isopropanol and calcined as aforementioned at 500 °C for 30 min. The usage of a thicker glass (2.2 mm) as compared to the one used for top cathode cells (1.1 mm) and the usage of FTO in place of ITO are needed for resisting the high temperature processing of the titania layer. Please note that FTO absorbs more in the infrared region than ITO and is more rough.

**CsFAMAPbIBr perovskite one step fabrication.** This process was performed in a nitrogen-filled glovebox while constantly purging with a nitrogen flow for reducing the DMF and DMSO vapours concentration. Perovskite precursor solution (see page 40) was filtered (0.2 µm, PTFE) and deposited by spin-coating (80 µl, static dispensing, first step 1000 rpm, 1000 rpm s<sup>-1</sup>, 10 s; second step 6000 rpm, 1000 rpm s<sup>-1</sup>, 20 s; fast crystallisation was induced dynamically dispensing 50 µl of chlorobenzene on the spinning substrate 5 s before the end of the second step) obtaining a 500 nm thick perovskite layer. The substrates were immediately transferred from the spin coater to a hot plate and annealed at 100 °C for 60 min. After removing from the hotplate, the devices were stored in a glass Petri dish for protecting from dust deposition. It was left partially open to avoid accumulation of vapours from solvent residuals.

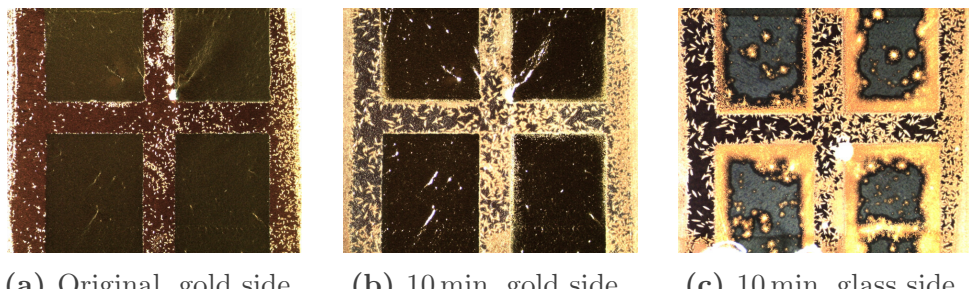
**HTM and cathode deposition.** The HTM solutions (spiro-OMeTAD, TAE-1, TAE-3, or TAE-4) were filtered (0.2 µm, PTFE) just before usage and deposited by spin-coating in a nitrogen-filled glovebox onto the perovskite layer (60 µl, static dispensing, spiro-OMeTAD at 4000 rpm, 4000 rpm s<sup>-1</sup>, for 30 s; TAE-1 and TAE-3 at 2000 rpm, 2000 rpm s<sup>-1</sup>, for 30 s; TAE-4 at 1000 rpm, 2000 rpm s<sup>-1</sup>, for 45 s) and similar HTM thicknesses were obtained ( $\approx$ 100 nm). FTO contact was cleaned on two edges scratching away the HTM and perovskite materials; then the edges were further cleaned rubbing them with swabs slightly wet with DMSO (the solvent vapours can damage the perovskite layer). Unless otherwise specified, in order to increase the oxidative doping of the HTM in a more

or less controlled way, the devices were kept 1 h in dark in a dry air chamber. Finally, 80 nm of gold was deposited by thermal evaporation in an ultra-high vacuum chamber ( $1 \times 10^{-9}$  bar, MBraun) using a shadow mask leading to 4 diodes for substrate each with an active area of 9 mm<sup>2</sup>.

### 2.4.3 Handling and Preservation

**Oxidative doping of HTM.** In case of bottom cathode cells, the oxidation of the HTM has been proven to improve the power conversion efficiency (PCE). The oxidation can be induced using dopants, for example FK 209 Co(III) TFSI salt[144] (this was not done in this thesis), or via oxygen exposure in dark.

**Degradation due to oxygen and illumination.** As explained in page 27, a synergic light and oxygen contribution on the perovskite layer degradation has been reported [127, 128]. In fig. 2.4 the degradation of a complete device exposed to continuous illumination for 10 min and ambient air conditions is shown. An analogous device kept in air but without illumination did not show any degradation as observable via optical microscopy. The presence of mesoporous titania in the photographed solar cell helps the permeation of oxygen allowing the degradation to occur in every zone of the device. Interestingly the degradation is more prominent at metallic contacts' edges, one could speculate the reason being the electrical field being higher at smaller curvature metallic edges. It could also be that the ionic profile of perovskite when holes quasi Fermi level is pinned at gold workfunction makes perovskite more sensible to degradation, and this is more evident at edges due to oxygen diffusion being blocked by the gold layer. Even if storage in dark and dry air should not be damaging for perovskite solar cells, usually the long-term storage happens in a nitrogen-filled glovebox.



(a) Original, gold side. (b) 10 min, gold side. (c) 10 min, glass side.

**Figure 2.4: Degradation due to oxygen and illumination combination.** A FTO/d-TiO<sub>2</sub>/mp-TiO<sub>2</sub>/CsFAMAPbIBr/spiro-OMeTAD/Au device upon 10 min illumination in air.



# Chapter 3

## Characterisation Techniques: Description and Interpretation

*“If I made it, I think everybody can do it.”*

**Abstract.** Characterisation of perovskite solar cells is a non-trivial subject, the techniques researchers successfully employed for OSC and DSSC needs to be re-validated for this new kind of solar cells. The presence of ionic migration in the absorber can be a game-changer for which special care has to be taken. In this chapter the employed characterisation techniques are described and critically assessed. Taking advantage of drift-diffusion simulations, some new hypotheses are thrown about the interpretation of the characterisation output.

---

**Table of Contents**


---

**Conventions and General Remarks**

## SIGN CONVENTION AND PARAMETERS DEFINITIONS

Fermi level, 54 • Cathode and anode, 54 • Voltage, 54 • Electrical power, 54 • Current and current density, 55 • Open circuit voltage, 55 • Short circuit current, 56 • Maximum power density, 56 • Power conversion efficiency, 56 • Fill factor, 56 • Forward and reverse bias, 56 • Forward and reverse scan, 56 • Ideality factor, 56 • Top and bottom of devices, 57

## USAGE OF SHADOWING MASK

## STABILITY DURING THE MEASUREMENT AND SMALL/LARGE PERTURBATIONS

Long lasting measurement, 58 • Large perturbations, 58

**Current-Voltage Sweeps**

Automatic scale, 60 • Scan speed, 60 • Noise, 61 • Shunt and series resistances, 61 • Solar cells parameters extraction from sweeps, 62 • Stabilized or dynamic current-voltage sweeps, 62

 **$V_{OC}$  and  $J_{SC}$  Dependence on Light Intensity** $J_{SC}$  versus  $\phi$ 

Interpretation, 63

 $V_{OC}$  versus  $\phi$  AND THE IDEALITY FACTOR  $n_{id}$ 

Transient Suns- $V_{OC}$ , 64 • Interpretation, 65

**Charge Extraction (CE)**

Concept, 66 • Procedure, 66 • Noise sources, 67 • Reduction of instrumental noise, 67 • Reduction of instrumental noise – subtraction of dark noise, 69 • Reduction of instrumental noise – integration of a fitting, 69 • Specific limitations for perovskite solar cells, 69

## INTERPRETATION OF CE SINGLE DECAYS

Charge extracted, 70 • CE time constant, 70 • CE time constant and TPV time constant – Corrections, 72 • CE time constant and TPV time constant – Correlation?, 73

## INTERPRETATION OF CE versus LIGHT BIAS WITHOUT MOBILE IONS

Exponential part and chemical capacitance in OSC, 73 • Linear part and geometric capacitance, 74 • Geometric capacitance voltage dependency, 75 • Energy levels point of view, 76

## INTERPRETATION OF CE versus LIGHT BIAS WITH MOBILE IONS

Linear part with mobile ions, 76 • Exponential part with or without mobile ions, 77

**Transient PhotoVoltage (TPV)**

Concept, 78 • Procedure, 79 • Noise treatment, 80 • Importance of stable steady state starting point, 80 • Small perturbations regime, 80

## INTERPRETATION OF TPV MONO-EXPONENTIAL DECAYS

Voltage transient and charge concentration relationship, 82 • Voltage re-equilibration dynamics, 82

## INTERPRETATION OF TPV BI-EXPONENTIAL DECAYS

At high background illumination, 83 • Mobility limited case, 85 • Inhomogeneous charge concentration profiles, 85 • At low background illumination – large perturbations, 85 • At low background illumination – ionic migration, 87 • At low background illumination – fast lifetime

plateau, 88 • At low background illumination – calculating ionic resistance, 89 • At low background illumination – slow lifetime plateau, 89

#### INTERPRETATION OF TPV versus LIGHT BIAS TREND

Lifetime versus light bias dependence, 90 • Diode-capacitor discharge could be the limiting time, 91

#### Transient PhotoVoltage Referenced to Charge Density (TPV-CE)

Concept, 92 • Procedure, 92 • Which charge from CE, 92 • From small perturbations lifetime to rate constant – first-order reaction, 92 • From small perturbations lifetime to rate constant – higher order reaction, 94

#### Transient PhotoCurrent (TPC)

Concept, 95 • Procedure, 95 • Small resistance and fast extraction, 96 • Dependency on background illumination, 96

#### Differential Capacitance (DC)

Concept, 98 • Procedure, 98 • Capacitance dependence on applied voltage, 99 • Small perturbations, 99 • Consideration on mobility limited case, 99 • Voltage peak value from TPV, 99 • Capacitance from voltage and current increase during the pulse, 101 • Comparison of charge from DC and from CE, 101

#### Voltage and Current Reconstruction

$J_{SC}$  reconstruction, 104 •  $V_{OC}$  reconstruction, 104

#### Impedance Spectroscopy

Concept, 105 • Frequency-domain, 105 • Stability, 105 • Interpretation, 106

---

## 3.1 Conventions and General Remarks

All the characterisation on complete devices was performed keeping them in an air-tight holder filled with nitrogen. The electrical connection from the cell electrode to the external end of the holder was obtained using gold tips connected via a printed circuit board to a coaxial cable.

### 3.1.1 Sign Convention and Parameters Definitions

3

**Fermi level.** The electrochemical potential of electrons, also known as Fermi level, for a body with a large number of electrons, is defined as the energy required for adding an electron to this body. In general, its definition is bound to the Fermi-Dirac distribution (see page 6): the Fermi level is a virtual level with an occupancy probability equal to 0.5. Its value depends on the electrostatic potential  $V_E$  in that position and on the internal chemical potential  $\mu$  which in our case mainly depends on the concentration of electrons (not related to their electric charge, similarly to the density of a gas). As the Fermi level is going to be used mainly for comparisons, its zero is not going to be defined thesis-wide, instead it will be defined to a convenient reference just where needed.

**Cathode and anode.** Considering a solar cell device at steady state under illumination and in open circuit conditions, its cathode is defined as the electrode where the electrons electrochemical potential  $\bar{\mu}$  (quasi-Fermi level of electrons including the electrostatic contribution) is the highest. By consequence the other electrode is the anode. In any illumination and applied voltage case, the naming of the two physical electrodes holds to the one just defined for the illuminated device at open circuit conditions.

**Voltage.** The voltage  $V$  is a relative value indicating a difference of electrons electrochemical potential in two different physical locations. It can be obtained subtracting the electrons electrochemical potential at the cathode position, from the one at the anode position. So in the aforementioned solar cell example, the voltage is positive. The unit is the Volt.

**Electrical power.** The electrical power  $P$  is defined as positive when the device absorbs electrical energy (incoming, passive element as a resistance) and negative when it generates energy (outgoing, active element as a solar

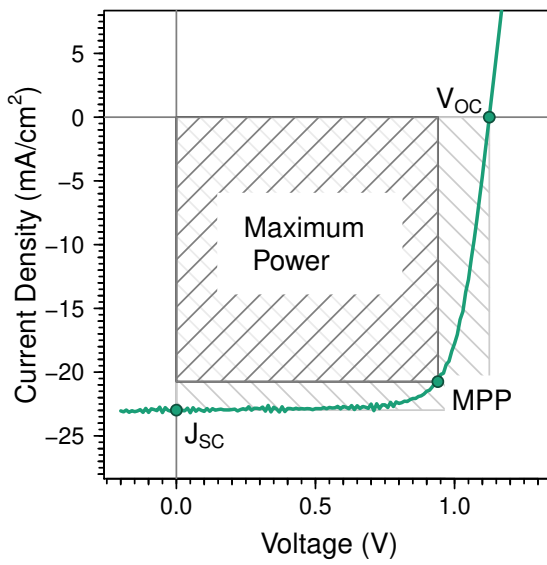


**Figure 3.1:** Solar cells parameters from current-voltage sweeps. A typical current-voltage sweep is represented. MPP stands for maximum power point, short circuit current ( $J_{SC}$ ) stands for short circuit current,  $V_{OC}$  stands for open circuit voltage. The ratio between the small and the large rectangles areas is the fill factor (FF).

cell in working conditions). It can be expressed in extensive form with power (Watt) unit or in intensive form “electrical power density” with power over active area unit (Watt over square centimetre).

**Current and current density.** The current  $J = P/V$  is measured through an external circuit and the sign is a consequence of the voltage and electrical power definition: a current (“conventional current”, flow of positively charged particles) being released from the device’s anode and being received from the cathode is defined as negative. The sign convention can be understood thinking that: inside the device, somehow, a positive charge was moved from the high Fermi level contact to the low Fermi level contact, increasing its electrochemical energy, the opposite to what would happen in a resistor, whose electrical power is always positive. In a solar cell device, the electrical power (and the related current) can be either positive or negative depending on the illumination and voltage conditions. It can be expressed in extensive form with current (Amperes) unit or in intensive form “current density” with current (Amperes) per active area (square centimetre) unit.

**Open circuit voltage.**  $V_{OC}$  parameter is defined as the voltage  $V$  at which the current is zero while the solar cell device is illuminated and in steady state (positive by its own definition).

**Short circuit current.**  $J_{SC}$  parameter is defined as the unsigned value of the current density flowing in an external circuit short circuiting (zero resistance) the solar cell device's contacts while illuminated and in steady state. When not specified, the reference illumination intensity is 1 sun. It is usually reported in current (milli Amperes) over active area (square centimetre) unit.

**Maximum power density.** The maximum power density is defined as the unsigned minimum of electrical power density which can be obtained by  $P(V) = J(V) \cdot V$ . It is usually reported using power (Watt) over active area (square centimetre) unit.

**Power conversion efficiency.** PCE parameter is defined as the maximum power density over the illuminating power density, which at 1 sun AM 1.5G is defined to  $100 \text{ mW cm}^{-2}$ . It is usually reported as a percentage.

**Fill factor.** FF parameter is defined as the ratio between PCE and the product of  $V_{OC}$  and  $J_{SC}$ . This parameter does not have a physical meaning, but it represents how much the series and shunt resistances affect the device efficiency. If resistances are negligible (series resistance very small and shunt resistance very large), the FF will be limited by charges' recombination processes. It can be represented either as a fraction of unity or as a percentage. In fig. 3.1, the FF can be graphically obtained from the ratio of the areas of the two rectangles.

**Forward and reverse bias.** Forward bias is a device condition where applied voltage is positive, reverse bias is the case where applied voltage is negative.

**Forward and reverse scan.** In current-voltage sweeps, a scan where the voltage is increasing over time is a forward scan, while a voltage variation in the opposite direction constitutes a reverse scan.

**Ideality factor.** An ideality factor  $n_{id}$  different from 1 describes deviations from the ideal photo-diode. The Shockley diode equation adapted for photogeneration becomes [28]:

$$J(V, \phi) = J_{ph}(\phi) - J_0 \left[ \exp\left(\frac{qV}{n_{id}k_B T}\right) - 1 \right] \quad (3.1)$$

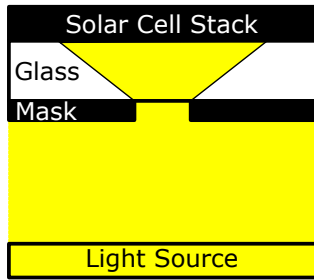


**Figure 3.2:** Illuminated area after a shadowing mask. This schema is just for explaining the concept described in the text, its dimensions are not realistic.

where  $J_{\text{ph}}$  is the total photo-generated current (negative sign),  $J_0$  is the dark diode saturation current (the current flowing in dark when applying a reverse bias, negative sign),  $q$  is the elementary charge,  $k_B$  is the Boltzmann constant, and  $T$  is the temperature. If recombination losses at short circuit are negligible (which can be measured either with  $J_{\text{SC}}$  versus  $\phi$ , see page 63, or with TPC, see page 95), the photo-generated current can be approximated with the short circuit current  $J_{\text{ph}}(\phi) \approx J_{\text{SC}}(\phi)$ . Clearly the reported equation just offers a simplified model. For example, it can be improved adding the contribution from the series resistance  $R_s$  and would become:

$$J = J_{\text{ph}}(\phi) - J_0 \left[ \exp\left(\frac{q(V + JR_s)}{n_{\text{id}}k_B T}\right) - 1 \right] \quad (3.2)$$

The function is now an implicit one, requiring numerical solving even for obtaining  $J_{\text{SC}}$ . Additionally, we can include the leakage current due to the internal shunt resistance  $R_{\text{sh}}$  [22]:

$$J = J_{\text{ph}}(\phi) - J_0 \left[ \exp\left(\frac{q(V + JR_s)}{n_{\text{id}}k_B T}\right) - 1 \right] + \frac{V + JR_s}{R_{\text{sh}}} \quad (3.3)$$

**Top and bottom of devices.** The point of view of the manufacturer is used for defining the physical top and bottom of a device: the bottom is the glass substrate and the top is the last deposited layer. This is opposite with the usage of a solar cell in the real world and with most of the solar simulators (but not all of them [145]).

### 3.1.2 Usage of Shadowing Mask

In literature is generally suggested to use a shadowing mask when measuring the solar cell devices in order to better define the illuminated area (e.g. in the obsolete [146] form by Nature publisher [147] or in [148]). Our active area is just  $0.09\text{ cm}^2$  so the mask aperture should be extremely small and its positioning troublesome. Additionally, the fact that the illumination reaches the mask from a wide angle (the illumination passes through spread lenses, whose size is not small compared to the lamp-cell distance) allows the light to spread through the substrate glass (2.2 mm for our FTO substrates) illuminating a large area on the active layer, as represented in fig. 3.2. In our solar simulator a linear widening of 8 % over 2 mm was estimated, this makes an illuminated area 16 % larger than the mask aperture. Even if the total incident power is determined from the mask aperture, the incident intensity is not 1 sun any more, compromising the validity of the measurement.

### 3.1.3 Stability During the Measurement and Small/Large Perturbations

Most of the reported hybrid lead halide perovskite materials can show rather impressive changes in their structure on long time scales, for example due to ionic migration [98], degradation [149], and self-healing [150]. This have to be taken into account for all the measurements techniques output which either takes too long time to be measured or employs large perturbations.

**Long lasting measurement.** An example of the first case is the impedance spectroscopy where during the long lasting measurement various phenomena can occur, like: a slow current evolution due to perovskite well known hysteretic behaviour prior to stabilisation; a degradation process changing the current; the heating of the device changing its properties. This slow current evolution can easily be misinterpreted for capacitive current [99], introduce artefacts like loops in the Nyquist plots [2], or even justify negative capacitance observations [151].

**Large perturbations.** Large perturbations regime means that the independent variable is changed by an amount large enough to cause the dependent variable to not adhere to the first term of its series expansion. For example, a too intense laser pulse in TPV could change the voltage by

a less-than-linear amount. In this case, the light pulse is not only probing the recombination, but it is adding some, so a large perturbation has to be avoided. This effect has been reported for DSSC in Barnes *et al.* [106]. Last example: in the time-resolved photoluminescence a laser pulse illuminates the otherwise unilluminated absorber layer. If mobile ions are present and if the absorber is in contact with other semiconductor layers generating a built-in voltage, this pulse induces some extent of ionic migration to a new profile [152] (just consider that the ionic profile for a solar cell in dark and at 1 sun is different, as the amount of electric field to screen is different). The extent of this migration will depend on the pulse intensity and duration. The fact that the relaxation time of the ionic migration (ms to seconds for the ions [99]) is usually much larger than the laser repetition rate ( $\mu$ s to ms for typical time-resolved photoluminescence (TRPL) lasers [153]) implies that the ionic profile variation slowly “builds up” pulse after pulse. As the ionic profile affects the free charges concentration profile and non radiative surface recombination, and these in turn affect the radiative recombination, the measurements of TRPL in contacted perovskite layer have to be done with extreme care as they are expected to strongly depend on laser intensity and repetition rate. An example of hysteretic behaviour observed with TRPL can be found in Motti *et al.* [154] and elsewhere [155, 156]. This is not expected to be a problem for perovskite in contact just with isolating layers.

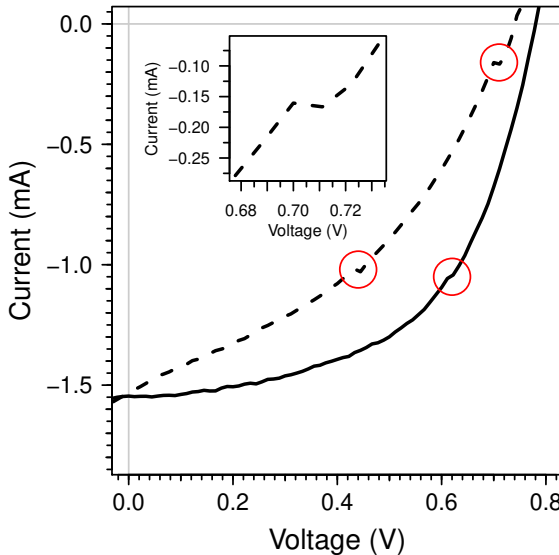


**Figure 3.3: Kinks in J-V sweep due to autoscale.** A current-voltage sweep of an hysteretic perovskite solar cell with Keithley autoscale active. Both the forward (dashed) and the reverse (solid line) present small discontinuities around 1 mA and 0.1 mA.

## 3.2 Current-Voltage Sweeps

After calibrating the light intensity in the solar simulator (see page 37), the devices were exposed to the illumination at open circuit for some seconds in order to have a stabilised open circuit voltage. Then the curves were measured with the auto-measure function of the PyPV software which measures the reverse scan and then the forward scan (see page 201).

**Automatic scale.** In literature one can easily find current-voltage curves with discontinuities or “kinks” [157–159] like the one reported in fig. 3.3, this is usually left unexplained. Disabling the auto-scale feature of the Keithley equipment the discontinuities disappear, so we can account these kinks to an hysteretic effect happening during the instrumental scale change.

**Scan speed.** The used sweep speed is  $500 \text{ mV s}^{-1}$ , which was arbitrarily chosen for avoiding bumps leading to currents higher than  $J_{\text{SC}}$ , like the one in fig. 3.4 (seldom reported in literature, like in figure S3 of [160] or for different speeds in [95, 97, 101, 161] and simulated with drift-diffusion in [162]). Our arbitrary choice allowed us to make fair comparisons between devices, but the absolute values should be considered as approximations. We wanted to underline that due to hysteresis phenomena, no scan speed, direction, or precondition is the correct one. Rather, a static measurement

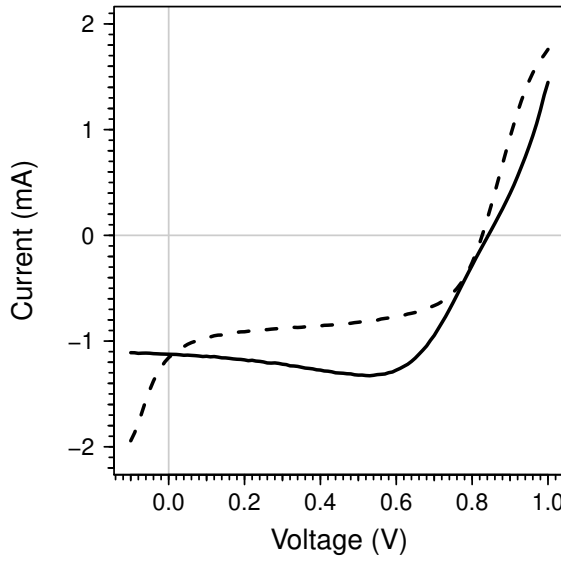


**Figure 3.4: Hysteretic current-voltage scan.** At the employed scan speed, the hysteresis phenomena causes the reverse (solid line) scan to reach currents higher than the  $J_{SC}$ .

or a maximum power point tracking (MPPT) should be used for obtaining a accurate and realistic result [163]. This comment regards also the so-called “hysteresis-free” perovskite solar cells, which can also present hysteretic phenomena on different time-scales [99, 160] or temperatures [100].

**Noise.** The noise often observed in current-voltage sweeps at high scan speeds in this thesis is mainly caused by oscillations in the solar simulator illumination intensity, as an example see fig. 3.1. For reducing the noise impact on the  $J_{SC}$  and  $V_{OC}$  parameters extraction, these values were extracted via a parabolic fitting.

**Shunt and series resistances.** The shunt and series resistances can be evaluated by the current versus voltage derivative of a dark current-voltage sweep [164]. The former from the current values at voltages close to zero and the latter from the current at high-enough voltage. Perovskite solar cell hysteretic behaviour can affect this measurement. An alternative could be to measure the stabilised current at a few voltage points: a couple of measurements close to zero voltage is enough for estimating the shunt resistance while two points at high voltages should be enough for estimating the series resistance. Still, the ionic profile would be different for the different applied voltages used for shunt resistance measurement, affecting the recombination barriers [2, 102]. So a transient measurement

similar to the one proposed for the ideality factor in [28] and explained in page 64 might be implemented for estimating the shunt resistance. Instead, for series resistance the transient method should not be needed, as the large employed voltage should be enough for flattening the ionic profile. The impact of these resistances on the PCE is paramount, as the FF strongly depends both on series and on shunt resistances.

**Solar cells parameters extraction from sweeps.** For the devices studied in this thesis, the reported values of  $V_{OC}$ ,  $J_{SC}$ , PCE and FF are extracted from a forward or reverse current-voltage sweep. This follows the tradition of solar cells reporting; but for hysteretic devices, like perovskite solar cells, a static measurement should be preferred. For measuring the  $V_{OC}$  or the  $J_{SC}$  a static measurement is experimentally straightforward. Instead, for the PCE, and by consequence the FF, a proper measurement is made difficult due to the cell evolution over time (hysteresis). This evolution involves a drift of the maximum power point over the time, so a static measurement is suboptimal. A MPPT system has to be employed in order to track the voltage evolution of this point [163]. Such a system is not trivial, as the process of localisation of the maximum power point involves a varying applied voltage, which can trigger some hysteresis, some attempts to achieve a working MPPT system are described in page 210.

**Stabilized or dynamic current-voltage sweeps.** One very appealing alternative to current-voltage sweeps are the so-called “stabilised current-voltage sweeps”, where at each voltage point a fixed stabilisation time is waited and the stabilised current is reported [95, 148, 165]. An improvement of this technique is named “dynamic current-voltage sweeps”, here the stabilisation step is of variable duration, until the current-time derivative falls below a threshold (e.g. 0.2 %/min) [166, 167].

### 3.3 $V_{OC}$ and $J_{SC}$ Dependence on Light Intensity

The solar simulator illumination intensity  $\phi$  is reduced via neutral density filters with transmittance of 0.05, 0.12, 0.25, 0.51, 0.81 and 1 (no filter). The values of  $V_{OC}(\phi)$  and  $J_{SC}(\phi)$  can be obtained from static measurements or from current-voltage sweeps. The static measurement of  $V_{OC}(\phi)$  at high light intensities is troublesome as it can easily damage the device. In this thesis, the used method is specified case by case.

#### 3.3.1 $J_{SC}$ versus $\phi$

The  $J_{SC}$  dependency on the light intensity  $\phi$  is close to linear and can be fitted with a power law:

$$J_{SC} \propto \phi^\alpha \quad (3.4)$$

where  $\alpha$  is a free fitting parameter. Its values usually range from 0.95 to 1.

**Interpretation.** An  $\alpha$  value lower than 1 indicates that not all the photo-generated charges get extracted, neither at short circuit conditions. This can happen due to recombination processes (non-geminate ones, for geminate recombination see page 15) at short circuit [168] or of other factors limiting the charge collection.

#### 3.3.2 $V_{OC}$ versus $\phi$ and the Ideality Factor $n_{id}$

Setting  $J = 0$ , which corresponds to open circuit conditions, in eq. (3.1) (without considering the series resistance correction) we can obtain a relation between  $J_{SC}$  and  $V_{OC}$ :

$$J_{SC}(\phi) = J_0 \left[ \exp\left(\frac{qV_{OC}(\phi)}{n_{id}k_B T}\right) - 1 \right] \quad (3.5)$$

This equation can already be used for obtaining the  $n_{id}$  and  $J_0$  values fitting the  $J_{SC}$  and  $V_{OC}$  measured at different light intensities  $\phi$  (also varying the temperature could be used for fitting the values, but it was not done during this thesis [169]). Solving for  $V_{OC}$  we obtain:

$$V_{OC} = \frac{n_{id}k_B T}{q} \cdot \ln\left(\frac{J_{SC}}{J_0} + 1\right) \quad (3.6)$$

Considering that the saturation current  $J_0$  (current in dark under reverse bias) is much smaller than  $J_{SC}$  for the light intensities we usually employ (down to 0.05 suns), we can approximate to:

$$V_{OC} \approx u_1 + \frac{n_{id}k_B T}{q} \cdot \ln(J_{SC}) \quad (3.7)$$

where  $u_1$  is a useless constant. Then if the  $\alpha$  value is close enough to 1, we can use eq. (3.4) and further approximate for plotting against light intensity  $\phi$ :

$$V_{OC}(\phi) \approx u_2 + \frac{n_{id}k_B T}{q} \cdot \ln(\phi) \quad (3.8)$$

This is the equation we commonly employ for fitting and obtaining an ideality factor value [22] as it conveniently uses a zero current measurement ( $V_{OC}$ ) so that series resistance can be completely ignored [170]. The shunt resistance will still affect the measurement [171]. The so-obtained ideality factor  $n_{id}$  is usually from 1 to 2. A light bias/illumination dependent ideality factor can also be measured either from a current-voltage sweeps in dark (which would be influenced by hysteretic behaviour) or from a derivative form of eq. (3.8) [28]:

$$n_{id}(\phi_0) = \frac{q}{k_B T} \left. \frac{dV_{OC}}{d \ln(\phi)} \right|_{\phi=\phi_0} \quad (3.9)$$

**Transient Suns- $V_{OC}$ .** A critical analysis of these methods and the proposal of a new “Transient Suns- $V_{OC}$ ” method can be found in Calado *et al.* [28]. In their work the authors propose to precondition the device in dark at an applied voltage bias roughly equal to the built-in voltage. After this stabilisation step the needed measurement conditions are applied (illumination is switched on and open circuit conditions are set) and the interesting quantity measured within a few milliseconds. The preconditioning step can increase the filling of the depletion layers in the contacts, which makes the ionic accumulation at the interface vanish through diffusion, or at least decrease. This is illustrated in fig. 3.5 where a simulation of an homojunction device is reported. While the ionic profile is flat through the perovskite layer, the electronic properties of the cell can be studied using the theory from OSC *i.e.* without the influence of ionic accumulation. Please notice that in the real case of a heterojunction device, where the two selective contacts have different band gaps, this flattening of the ionic profile could be impossible.

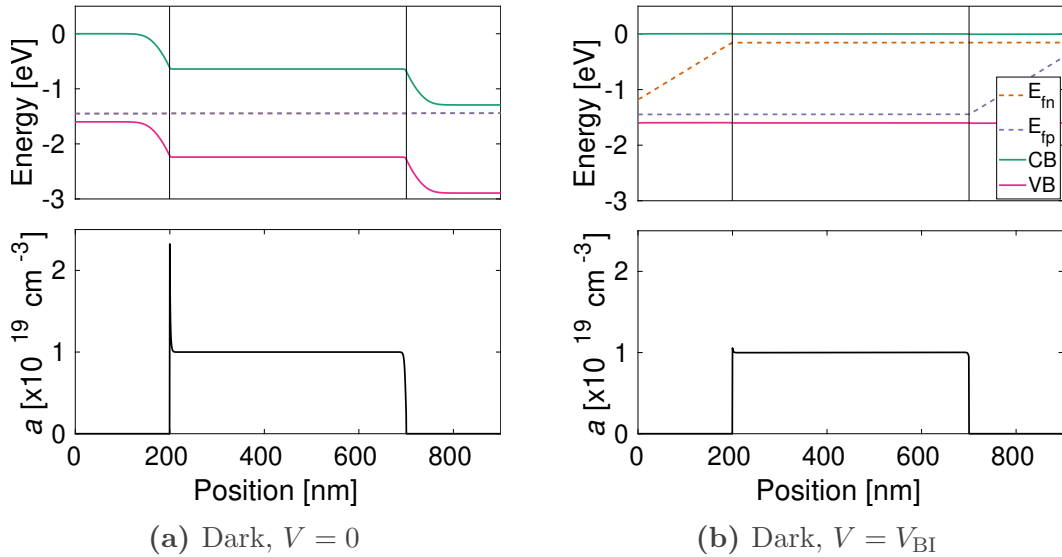


**Figure 3.5: Simulated effect on the ionic profile of the application of a voltage equal to the built-in voltage.** A  $p(200\text{ nm})-i(500\text{ nm})-n(200\text{ nm})$  homojunction device is simulated, above the energy levels are reported and below the ionic density profile is reported. In (a) the device is at equilibrium in dark. In (b) the device is in steady state in dark with an applied voltage equal to the built-in voltage  $qV = qV_{BI} = \bar{\mu}_{\text{cathode}} - \bar{\mu}_{\text{anode}} \approx \bar{\mu}_{\text{CB}}^{\text{ETM}} - \bar{\mu}_{\text{VB}}^{\text{HTM}}$ .

**Interpretation.** Pockett *et al.* [42] measured ideality factors of planar perovskite solar cells via stabilised  $V_{OC}$  obtaining, for some cases, values as high as 5. Also in organic [170, 172] and silicon solar cells [173] ideality factors greater than 2 has been observed and explained. According to Calado *et al.* [28] and Kirchartz *et al.* [170], the ideality factor, once obtained in the correct way, is 1 when studying most of the recombination types and 2 for mid-gap trap mediated recombination in regions where the electrons and holes concentrations are similar,  $n \approx p$ .

## 3.4 Charge Extraction (CE)

**Concept.** The charge extraction experiment has been designed to quantify the free charges available in a device [174, 175]. It works via the sudden extraction of the free charges in a solar cell illuminated at open circuit conditions. The measured charge has to be considered as a lower bound to the actually present excess charge, as part of it could recombine inside the device during the extraction time [176]. Performing this experiment at various light intensities, we can obtain a charge density *versus* light bias relationship.

**Procedure.** As represented in fig. 3.6, the device is kept under constant illumination by a white LED at open circuit conditions until stabilisation is reached. After stabilisation, the illumination is suddenly switched off and, at the exactly same moment, the device is short circuited through a small and known resistance ( $50\Omega$ ). In the first microseconds, most of the free charge flows through the resistor generating a current and a voltage drop across it. An oscilloscope in parallel to this resistance measures the transient voltage. The current flowing at any moment can be obtained from the measured voltage via Ohm's law:  $J = V/R$  where  $R$  is  $50\Omega$ . This transient current can be integrated over time to obtain the extracted charge. Then the light intensity is decreased and the experiment

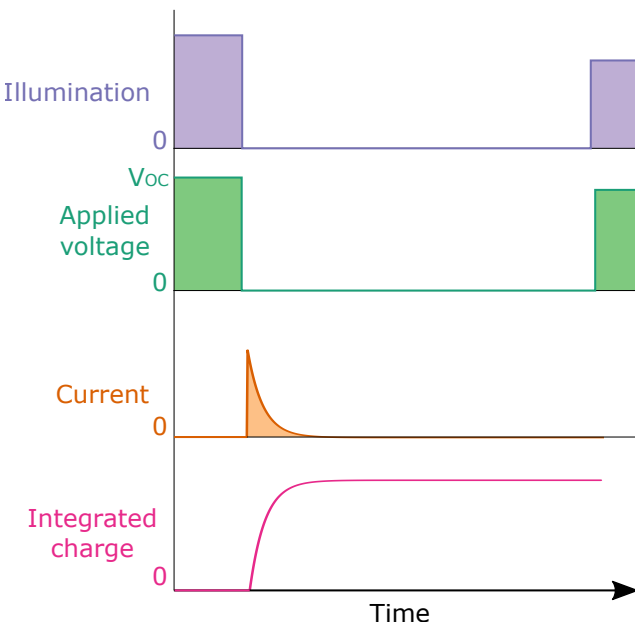


**Figure 3.6: Scheme of CE experiment.** A device is illuminated in open circuit conditions, then simultaneously the illumination is switched off and the circuit is closed through a small resistance. The current flowing gets integrated to obtain the extracted charge. Then the illumination is switched on at a different intensity and the measurement is repeated.

is repeated, from 1 sun down to dark (in dark no signal should be observed). A single decay is measured for each illumination point, over a few tens of different illumination intensities. The results are plotted as charge density versus light bias. The equipment switching off the illumination and setting the short circuiting includes two transistors (circuit designed and built by Dr. Javier Pérez Hernández) and gets activated by a square voltage pulse from a pulse generator, the pulse is, at least, as long as the measurement window. From my experience, I recommend to use a short dark period in order to save time for the following stabilisation step. 1 sun equivalent illumination is defined as the illumination at which a silicon photodiode gives the same  $J_{SC}$  as under calibrated 1 sun from the solar simulator. The LED-solar spectral mismatch affects slightly the measurement, but in no case a PCE is reported from any LED-illuminated experiment.

**Noise sources.** The lack of complete stabilisation of the device before the extraction of charge can introduce both an error in the measured  $V_{OC}$  and in the extracted charge. Regarding the  $V_{OC}$ , in perovskite solar cells it not only depends on the illumination intensity, but it also evolves slowly until the stabilisation at the steady state value, so a well defined stabilisation procedure is key for achieving reproducibility in CE experiments. Regarding the extracted charge, the ionic profile can influence the amount of accumulated charge, as shown for two extreme cases of presence/absence of ionic charges in fig. 3.14, so a reproducible procedure for device stabilisation will also improve the reproducibility of the integrated current amount. Additionally, the measurement equipment introduces some electronic noise whose effect can be mitigated through data post-processing.

**Reduction of instrumental noise.** Most of the observed short-time noise ( $<5 \times 10^{-7}$  s) observable in fig. 3.7a is related to the opening and closing of the transistor switches included in the home-made circuit. The characteristic frequencies of the observed noise are not small compared to the measurement window, so its time-integral does not necessarily sum to zero. In order to reduce its impact, various approaches have been tested and here described. The noise can be ignored in some cases, but it is a problem if the charge versus light bias ( $V_{OC}$  generated at a given illumination intensity) profile, reported on the right hand column of fig. 3.7, has to be studied in detail, as in chapter 4. In the mentioned case, just the exponential part of its linear plus exponential behaviour, reported

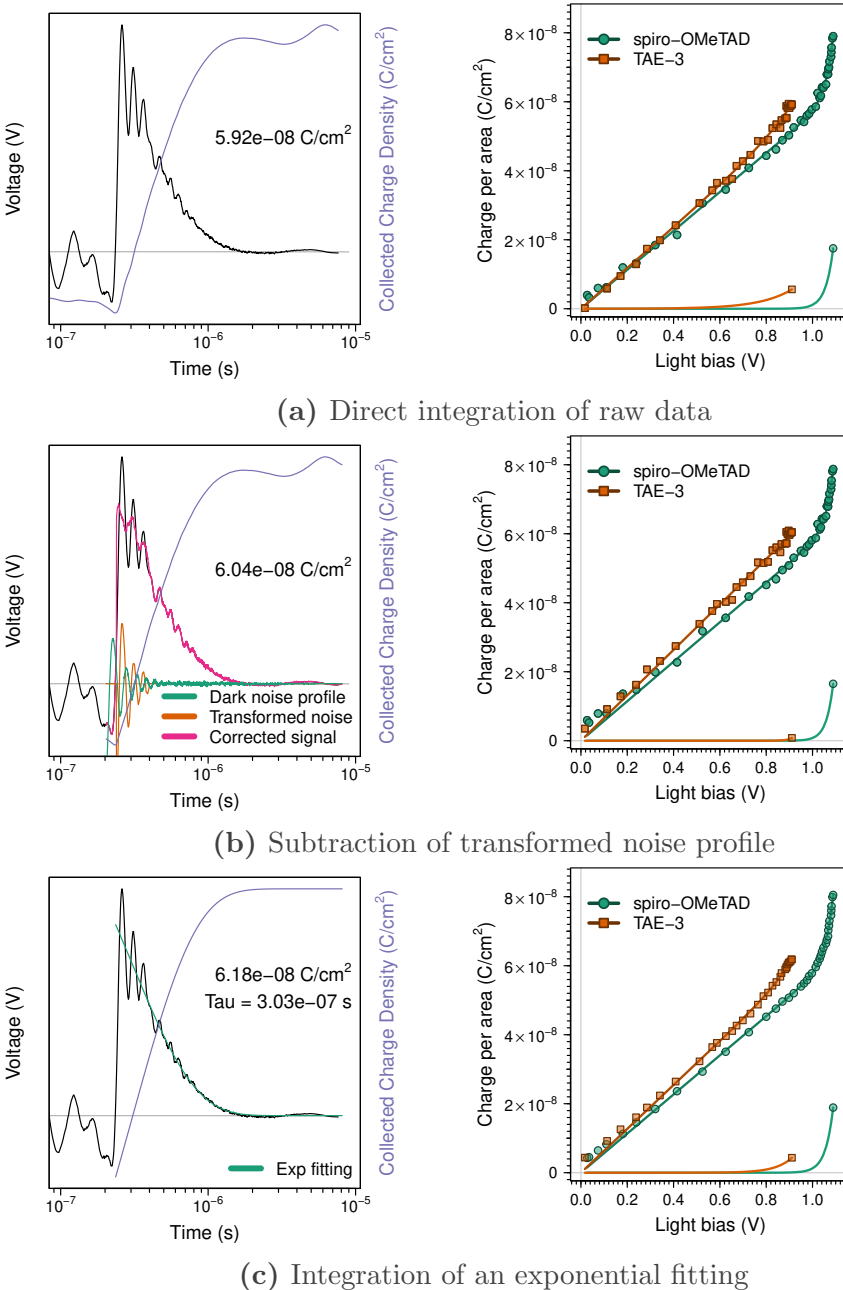


**Figure 3.7: Strategies for reducing the instrumental noise in a single CE integration.** On the left, single CE decays from a FTO/d-TiO<sub>2</sub>/CsFAMAPbIBr/TAE-3/Au device [3] is integrated without noise reduction in (a), adapting the noise profile from the dark measurement and subtracting it in (b), or fitting the decay and integrating the fit in (c). On the right, the charge versus voltage trends obtained applying the respective noise reduction methods.

in the bottom of each right hand figure, was of interest and it is evident that the employed noise-reduction method influences it heavily.

**Reduction of instrumental noise – subtraction of dark noise.** Annoyingly, the noise profile is characteristic of the cell and of the circuitry, so a simple average over many decays does not help in cancelling it. Based on this consideration, we tried to subtract a pure noise profile as obtained from a dark measurement (without any light bias). The operation was made more difficult by the slight variations of the noise profile with the light bias. A data-to-morphed-noise fit was implemented where the  $f(t)$  noise profile was transformed with:  $t' = u_3 + u_4 \cdot t + u_5 \cdot t^2$  and  $f'(t') = u_6 \cdot f(t') + u_7 \cdot t' \cdot f(t') + u_8 \cdot e^{-t'/u_9}$  where  $u_{3-9}$  are constrained fit variables. Then  $u_6$  was set to zero and the resulting profile was subtracted from the data and the result integrated. As can be seen in fig. 3.7b, this technique is working for most of the cases but it can fail if the noise profile changes in a more complex fashion.

**Reduction of instrumental noise – integration of a fitting.** Finally the decays were fitted with a bi-exponential formula (sum of two exponential) or, if the bi-exponential fitting was not converging, by a simple exponential and the integral of this fit was used. In both cases a robust fitting routine was employed [177].

**Specific limitations for perovskite solar cells.** When measuring the CE of a perovskite solar cell, additionally to the aforementioned limitations, one should also consider that the ionic profile update (from  $V = V_{OC}$  to  $V = 0$ ) causes a displacement current, as described in page 13. A simulation with Driftfusion has been performed for an homojunction device, the evolution of the energy levels is shown in fig. 3.8 and two well distinct processes are observed with the extraction of free charges over short times and the rearrangement of ionic defects over long times. In fig. 3.9b, we can see the fast extraction of the free charges in the short time region. Zooming in the long times region, shown in fig. 3.9c, we can see that a very weak but long lasting current appears and gives a relevant contribution to the integrated charge, this is caused by the slow ionic profile change (and the related displacement current). This will happen on very large time scales and it will not affect the short measurements used for the free charges estimation, so it is rarely reported [107]. The charge measured in the external circuit due to the ionic displacement current

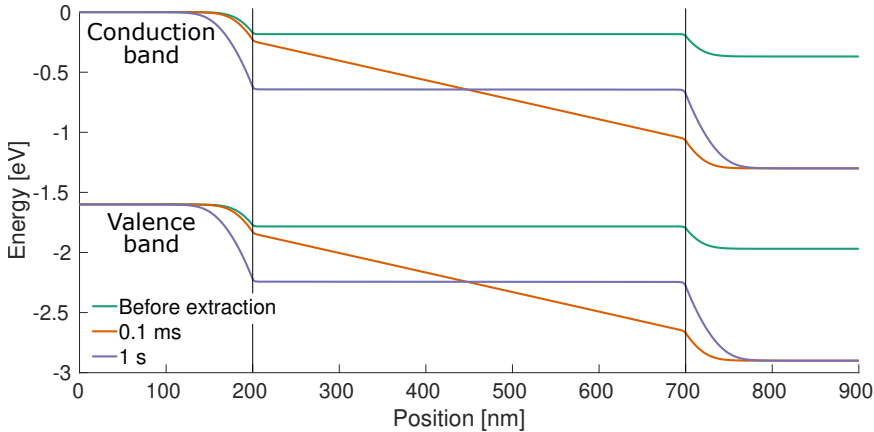


**Figure 3.8: Evolution of energy levels during CE.** A  $p(200\text{ nm})-i(500\text{ nm})-n(200\text{ nm})$  device is simulated and the energy levels evolution during a CE experiment are shown. At the beginning, the device is stabilised at open circuit conditions under 1 sun illumination, represented by the green lines. Then the illumination is switched off and the device is brought to short circuit. After  $1 \times 10^{-4}\text{ s}$ , the electronic charges have been extracted, leaving an electric field in the bulk of the perovskite layer. Subsequently, at long times ( $1\text{ s}$ ) the ions move for screening the mentioned electric field. CE simulation routines explained in page 187.

could be underestimated as the free charges rearrangements can also occur through the perovskite layer rather than through the external circuit.

### 3.4.1 Interpretation of CE Single Decays

**Charge extracted.** The integrated charge is assumed to include the excess free charges in the valence and conduction bands. With *excess* we refer to the difference between the charge concentration in the conditions of interest and the stabilised dark condition. For a non perfectly crystalline material, localised shallow traps constituted by the tails of the valence and conduction bands density of states inside of the so-called mobility gap [178] are not negligible and should also contribute to the extracted charge amount [160, 170]. On the contrary, charges trapped in deep traps contributing to SRH trap mediated recombination, with energies far from the band edges, should not be possible to extract in a CE experiment.

**CE time constant.** The free charges extraction time is related to the RC time of the  $50\Omega$  resistor and the capacitance of the solar cell device. We can see in fig. 3.10 a weak covariance (Pearson correlation coefficient

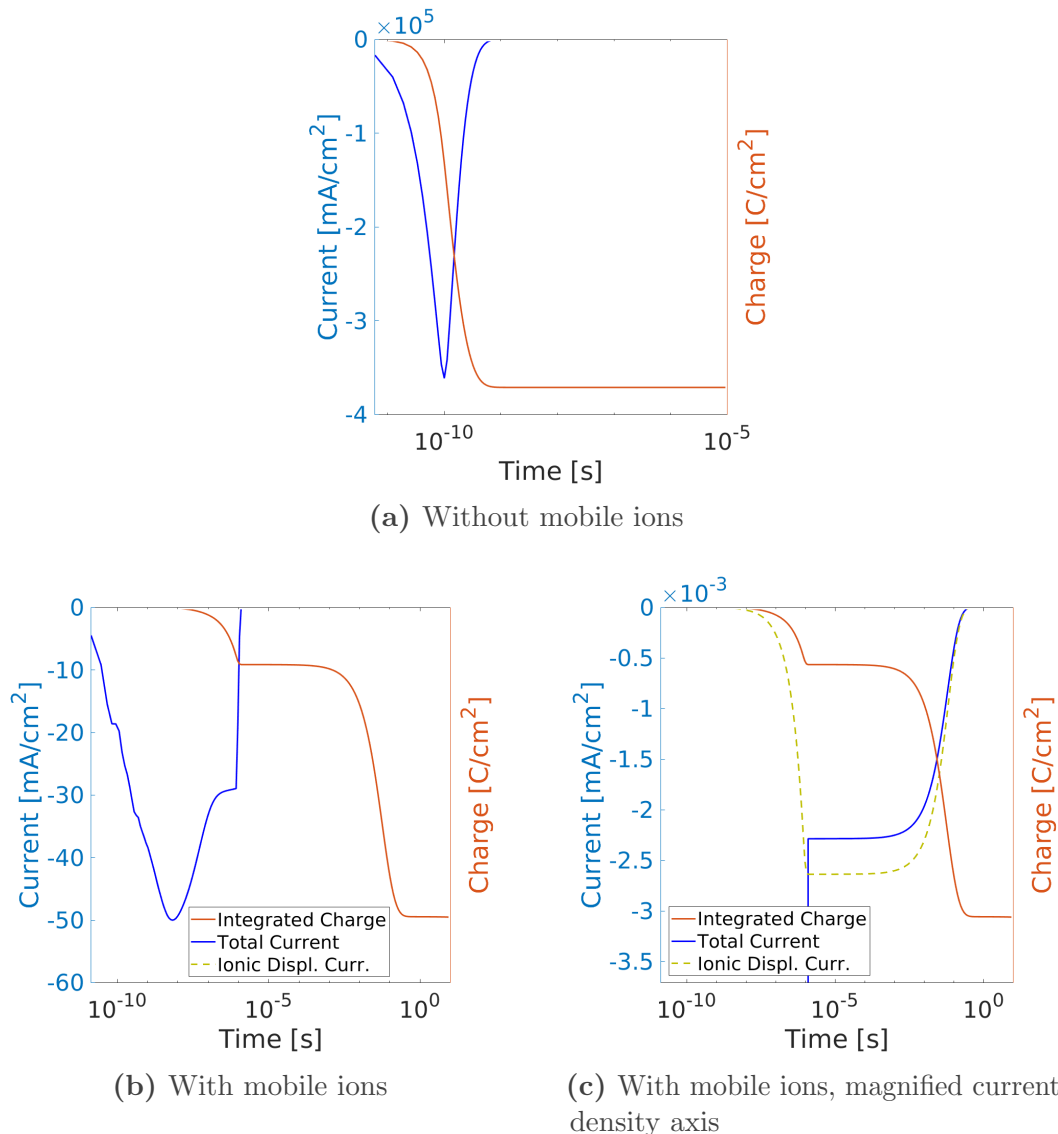


**Figure 3.9: Simulation of a single CE current profiles without or with mobile ions.** The current versus time profile of a CE simulated experiment is shown on the left axis just for the 1 sun illumination intensity. On the right axis the cumulative integration of the extracted charge. Clearly, the extraction is unrealistically quick as the resistance included in a real CE experiment was not included in the simulation. In (a) the measurement of a device without mobile ions is shown, we can observe just one current peak contributing to the integrated charge; in (b) the presence of the mobile ions introduces a long-times contribution to the extracted charge, the current causing this is very weak and long lasting, it can be better observed in the magnification in (c). CE simulation routines explained in page 187.

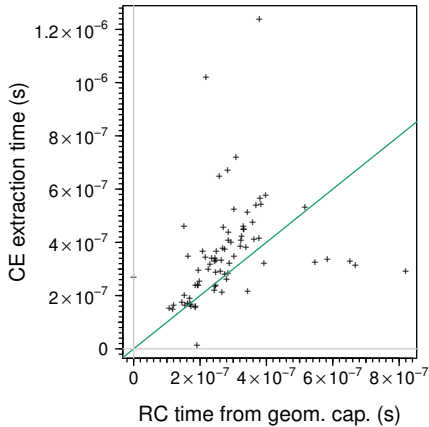


**Figure 3.10: Charge extraction time is related to a RC time.** Covariance of CE extraction time at low light intensity versus the expected time from geometric capacitance (as obtained from dark DC). Each point is a different device for a total of 78 devices, many different structures studied during my PhD are represented. The green line indicates the 1 to 1 relationship.

of 0.3) between the RC time obtained extrapolating the dark capacitance from differential capacitance (DC) (which is the geometric capacitance) and the extraction time (as obtained by an exponential fitting to a single CE current decay) at low light intensity (enough for having a signal but far from 1 sun light intensity). At higher light intensities, the correlation is weaker as the capacitance is less defined as the cell is in a transition between illuminated (high capacitance) and dark (low capacitance) status. Anyway, the extraction time does not change much between low light intensity and 1 sun with an increase from 1.1 to 2.4 times (first and third quartile). More discussion on this topic can be found on Montcada *et al.* [179].

**CE time constant and TPV time constant – Corrections.** During this time, and depending on its location in the device stack, some free charges can recombine. One could argue that a CE measurement is valid only if the extraction is faster than the recombination time as measured via TPV [180] or that the extracted charge should be corrected considering the recombination [168, 181]. Considering the charges accumulated in the depletion layers in the selective contacts, these will flow to the electrodes without crossing the perovskite/selective contacts interfaces, where has been reported that most of the recombination occurs [23, 54, 182]. So this part of the extracted charge, distinguishable as the linear part of the charge versus voltage plot, as represented on the right column of fig. 3.7 should not be corrected. Instead, regarding the charge accumulating in the perovskite layer, which we assume can be assigned to a chemical capacitance and can be recognized as the exponential part on the right

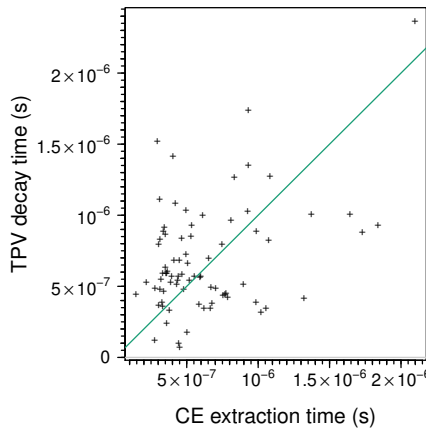


**Figure 3.11: Comparison between CE and TPV exponential decay times.** Covariance of CE extraction time at 1 sun light intensity versus the TPV mono-exponential decay time at 1 sun light intensity. Each point is a different device for a total of 79 devices, including many different structures. The green line indicates the 1 to 1 relationship.

column of fig. 3.7, it may be that a correction [183, 184] is needed, but this has not been attempted in this thesis.

**CE time constant and TPV time constant – Correlation?.** Some covariance (Pearson correlation coefficient of 0.4) can be observed in fig. 3.11 between the CE and the TPV time constants at 1 sun illumination. This is unexpected and weird as the two times change with very different trends with light bias (when changing the preconditioning light intensity, CE extraction time changes just slightly while TPV decay time varies over various orders of magnitude). In case a stronger proof of correlation is found, this could indicate that both processes, even if not of the same nature, are limited by the same diffusion process, for example the migration of free charges from all the absorber to the absorber/contacts interfaces.

### 3.4.2 Interpretation of CE versus Light Bias Without Mobile Ions

**Exponential part and chemical capacitance in OSC.** In OSC literature the charge versus light bias voltage trend is described simply as the exponential shape which describes a Maxwell-Boltzmann distribution for a two levels scenario, and fitted to an exponential growth. In a few publications, the shape is fitted to an error function [185]. For a common solar cell working conditions, the Maxwell-Boltzmann classical particles approximation should be valid as the distance between Fermi level energy and the band edges is expected to be always much larger than  $k_B T$ . This could be false for high applied voltages, where Fermi-Dirac distribution for fermions should be used. Thus, the expression for the conduction band

electronic density  $n$  obtained from the mentioned distribution is:

$$n(V) = n_{\text{DOS}} \exp\left(\frac{qV - E_g}{k_B T}\right) = n_{\text{eq}} \exp\left(\frac{qV}{k_B T}\right) \quad (3.10)$$

where  $n_{\text{DOS}}$  is the density of states which can be occupied by free charges,  $E_g$  is the material band gap, and  $n_{\text{eq}} = n_{\text{DOS}} \exp[-E_g/(k_B T)]$  prefactor is the equilibrium carrier concentration from a Boltzmann distribution of a two levels system. As the CE can just extract the excess charge  $n_{\text{CE}}$ , what we can measure is:

$$n_{\text{CE}}(V) = n(V) - n(0) = n_{\text{eq}} \cdot \left[ \exp\left(\frac{qV}{k_B T}\right) - 1 \right] \quad (3.11)$$

now the expression of  $n_{\text{CE}}$  evaluated at zero voltage gives zero extra charge as expected. In some cases an ideality factor  $m$  is introduced [170], which can help to account for the shape of the density of states of the conduction band, so the expression can be found as:

$$n_{\text{CE}}(V) = n_{\text{eq}} \cdot \left[ \exp\left(\frac{qV}{mk_B T}\right) - 1 \right] \quad (3.12)$$

For perovskite solar cells, an alternative interpretation can be found indicating that the exponential trend reflects the extraction from exponential subgap states, *i.e.* shallow traps [160]. This can be used for explaining values of  $m$  greater than 2, which would be indicative of the exponential tail width as shown for OSC by Kirchartz *et al.* [170]. Moreover, in OSC has been shown that an inhomogeneous carriers concentration profile through the device thickness, likely to happen in thin films, would also cause high  $m$  values [170] especially for low doping levels resulting in drift-driven solar cells [186, 187].

**Linear part and geometric capacitance.** With the introduction of selective contacts, a linear contribution starts to grow in importance summing up to the exponential part. It has been observed both in OSC [180, 181, 188] and in perovskite solar cells [1, 64, 160]. This linear trend accounts for the accumulation in the selective contacts' depletion layers and in the electrodes, in a parallel plate capacitor fashion:  $n = C_g \cdot V = \frac{\epsilon_0 \epsilon_r A}{d} \cdot V$  where  $C_g$  is the geometric capacitance,  $A$  is the active area,  $d$  is the thickness of the dielectric,  $\epsilon_0$  is the electric constant, and  $\epsilon_r$  is the relative permittivity. This carriers accumulation in the contacts can be visualized

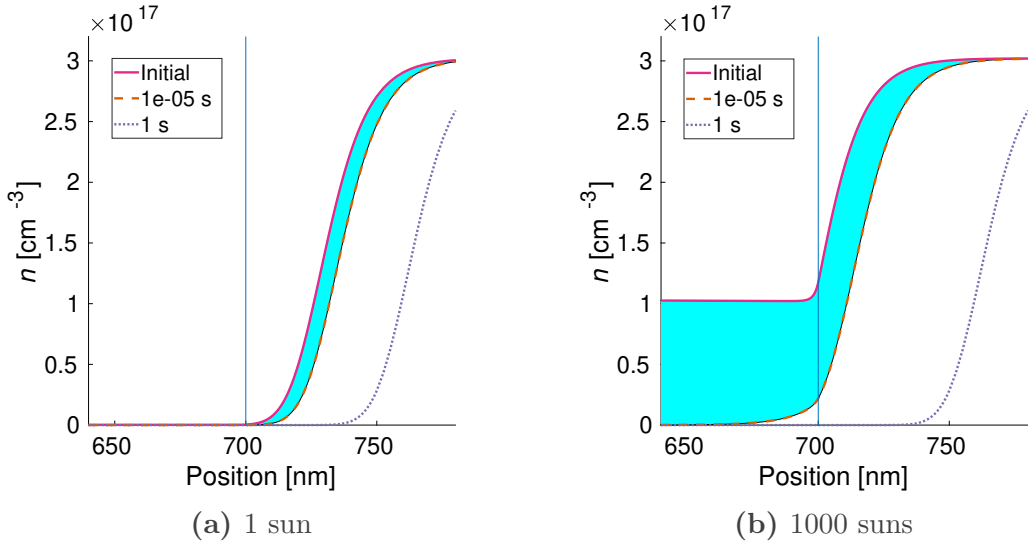


**Figure 3.12: Simulated electron density profile during a CE experiment.** The electron density profile of a homojunction cell with mobile ions is plotted at the interface between perovskite (position <700 nm) and ETM (position >700 nm) at different times during a CE experiment. The green solid line represent the situation as stabilised at open circuit conditions, before the CE experiment. Corresponding energy levels for (a) in fig. 3.13b and for (b) in fig. 3.13c. The dashed orange line represent the profile at short times, after the extraction of the free charges but before the reorganization of the mobile ions. The light blue area represents the extra charge extracted during a typical CE experiment. In (a) the device is stabilised at 1 sun light intensity before performing the charge extraction, in this case most of the extra charge is accumulated in the contacts. In (b) the device is stabilised at 1000 suns, in which case the charge is mainly accumulated in the perovskite layer. The dotted violet line is the final electronic profile, at long times after the mobile ions migration, which is identical for (a) and (b) cases. Corresponding energy levels in fig. 3.13a. CE simulation routines explained in page 187.

with the simulation reported in fig. 3.12a. Extending eq. (3.12), the complete equation becomes:

$$n_{\text{CE}}(V) = C_g \cdot V + n_{\text{eq}} \cdot \left[ \exp\left(\frac{qV}{mk_B T}\right) - 1 \right] \quad (3.13)$$

**Geometric capacitance voltage dependency.** More exactly,  $d$  is the distance between the regions where the opposed charges are getting accumulated, which is the space charge layers (usually depletion layers) in the contacts. So this value can be somewhat wider than just the

distance separating the two perovskite/contacts interfaces. By consequence,  $\epsilon_r$  should be considered as a thickness-weighted mean of the relative permittivities of each material between the two accumulation zones. Moreover, as the depletion layers fill up they widen and shrink, so this capacitance can vary as happens for the junction capacitance (*i.e.* transition capacitance) of a *p-n* junction. A voltage dependent geometric capacitance can be obtained from dark CE measurements applying reverse voltage biases [108] or via impedance spectroscopy in dark with a constant voltage bias [42, 189]. While this dependency cannot be ignored in silicon solar cells or in OSC, where the *n* and the *p*-type materials are in close contact, it is likely negligible in perovskite solar cells as the change of depletion layers thickness, happening in the contacts, is negligible when summed to the perovskite layer thickness.

**Energy levels point of view.** As we mentioned, the linear trend is related to the accumulation in the contacts depletion layers (or, generically, space charge layers), this can be seen from the decrease of the perovskite-contacts conduction band offset between figs. 3.13a and 3.13b. Increasing the light illumination at open circuit conditions, the quasi-Fermi levels splitting approaches the built-in voltage represented by the contacts' band edges:  $qV_{BI} = \bar{\mu}^{\text{cathode}} - \bar{\mu}^{\text{anode}} \approx \bar{\mu}_{CB}^{\text{ETM}} - \bar{\mu}_{VB}^{\text{HTM}}$ . This means the depletion layers are close to saturation, like in fig. 3.13c where 1000 suns illumination was simulated, and the charge accumulates in the perovskite layer, as shown in fig. 3.12b, and the exponential trend gains importance.

### 3.4.3 Interpretation of CE versus Light Bias With Mobile Ions

**Linear part with mobile ions.** The presence of mobile ions in perovskite materials which can accumulate at the perovskite/contacts interfaces, adds an additional capacitance  $C_{\text{ion}}$ , which replaces the geometric capacitance  $C_g$  at low frequencies or long time scales, as we showed in Moia *et al.* [2]. Comparing the initial electrostatic potential profile with the electrostatic potential at long times, after the ionic migration, we can see that there is no electric field in the bulk of the perovskite layer neither at the beginning neither at the end of the measurement. This means that the capacitance we can observe at long times or slow frequencies is not the geometric one, but rather the ionic one across each of the interfaces which is expected to be independent on the device's thickness. Nevertheless, as pointed out in page 69, the CE measurements are never carried on for long enough to

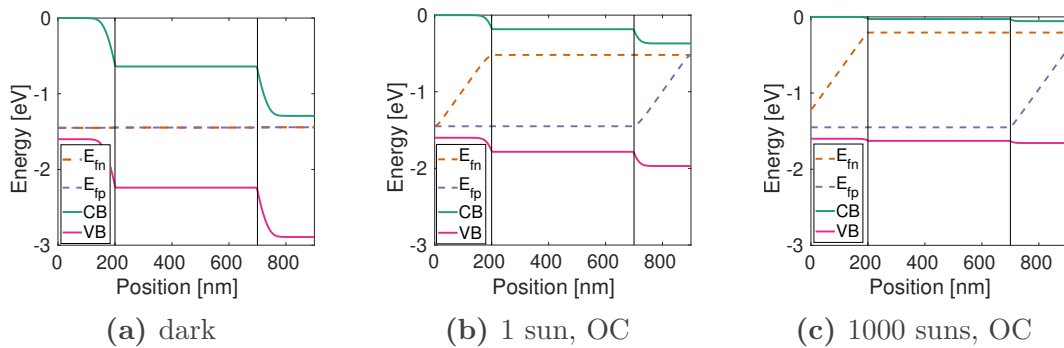


**Figure 3.13: Simulated energy levels in a homojunction device with mobile ions at open circuit conditions at different light intensities.** The simulated energy levels of a homojunction  $p(200\text{ nm})-i(500\text{ nm})-n(200\text{ nm})$  device with mobile ions in the intrinsic layer. In **(a)** the device is in dark, in **(b)** it is illuminated at 1 sun light intensity, and in **(c)** illuminated at 1000 suns.

include the ionic migration, and so also the ionic accumulation capacitance is not observed in our experiments. This can be visualized with the simulation reported in fig. 3.14 where the long timescale (where the current is monitored until complete stabilisation) and the short timescale (few tens of microseconds) CE experiment are compared. The difference between the short and long timescale extracted charges is the linear contribution by the ionic capacitance discharge, observable as electronic current thanks to the relative displacement current. A simulation with frozen ions (the ionic profile was stabilised at open circuit and frozen during the CE experiment) was also performed but not reported. For this case, the simulated extracted charge was identical to the reported short timescale extraction simulation in fig. 3.14.

**Exponential part with or without mobile ions.** As can be seen in fig. 3.14, the simulated geometric capacitance is similar to the one obtained from short time extraction with mobile ions but the exponential part is considerably different. This is caused by the very different free charge accumulation profile: the presence of an un-shielded electric field in the absorber layer causes the free carriers to accumulate close to the respective selective layer, in other words it keeps the charges away from the respective recombination centres (e.g. perovskite/HTM for electrons). This allows the simulated ions free device to store more charge at the same illumination intensity.

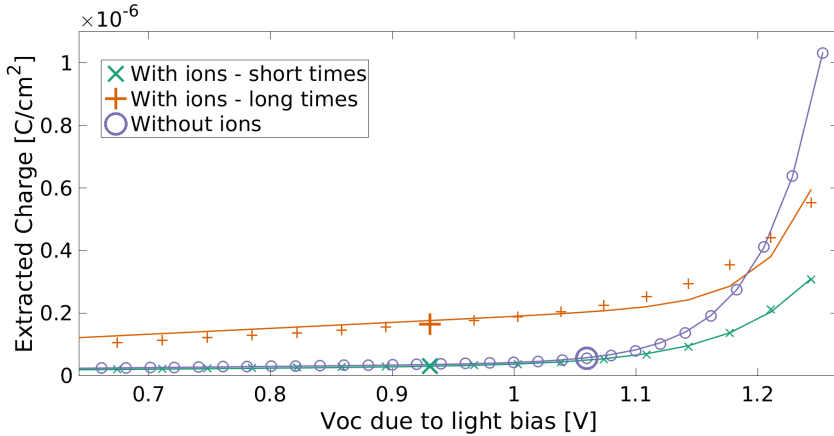


**Figure 3.14: Simulation of a complete CE experiment: charge versus light bias with or without mobile ions.** A simulation for a homojunction device up to 1000 sun illumination (rightmost point of each set) is reported, with three points for decade. For each set of points, the bigger size one indicates the 1 sun pre-illumination. The green crosses simulates the experimentally utilised conditions: the charge gets integrated over few microseconds, while the mobile ions did not have enough time to start migrating. The orange pluses considers the charge integrated until the device stabilisation, over various seconds, including also the ionic displacement current. The purple circles simulates a mobile ions free device. The solid lines represents the linear plus exponential fit crossing (0,0) obtained with the eq. (3.13)  $n_{CE} = C_g V + n_{eq} \{ \exp[qV/(mk_B T)] - 1 \}$  where  $C_g$ ,  $n_{eq}$ , and  $m$  are free fitting parameters whose meaning is described in the text. CE simulation routines explained in page 187.

### 3.5 Transient PhotoVoltage (TPV)

*“Imma firin mah lazor  
pewpew pewpewpew”*

**Concept.** This technique allows us to induce a perturbation to a solar cell at open circuit under illumination and observe how it behaves. The device at steady state is perturbed photo-generating an additional small amount of charge, then we observe the perturbed open circuit voltage dynamics. As represented in fig. 3.15, the  $V_{OC}$  originally at its steady state value, will increase due to the greater generation rate during the laser pulse. After the end of the short pulse, the  $V_{OC}$  will slowly go back to the steady state value relative to the constant illumination. The dynamics

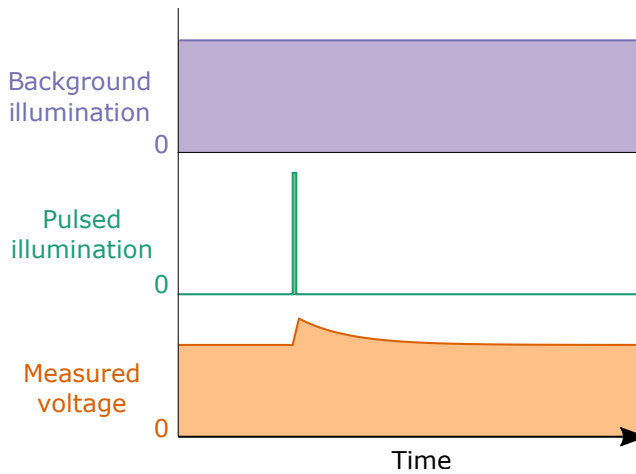


**Figure 3.15:** Scheme of TPV experiment. A pulsed illumination sums on the constant background illumination, the measured open circuit voltage dynamic shows an increase and a relaxation.

of this  $V_{OC}$  relaxation back to the steady state value is the focus of Transient PhotoVoltage experiments (also known as PhotoVoltage Decay experiments) which has been applied to OSC [190], to DSSC [176, 191, 192], and recently also to perovskite solar cells [193, 194]. From this kinetic profile, a charge lifetime can be obtained and plotted against the light bias due to the constant background illumination, as in the example of fig. 3.17a. This gives us information about the dominant recombination rate and its dependence on the light bias.

**Procedure.** The device is kept under constant illumination by a white LED ring at open circuit until stabilisation is reached. Failure to reach stabilisation of the ionic profile will affect the measurement results [107] and can cause unexpected negative TPV peaks [98]. Then an additional short illumination pulse is provided using a nitrogen laser. The pulse duration ( $\approx 1.5$  ns) is shorter than the oscilloscope resolution we usually employ, so we assume that the measurement happens when the pulse is already over. In the literature, this is not always the case as other research groups use a LED diode for the pulsed illumination [98]. Usually a wavelength of 590 nm is selected using a Rhodamine 6G solution [195], this wavelength illuminates in depth the perovskite layer (in contrast to a blue light where the illumination would be absorbed within the first hundreds of nanometres of the material [24, 196]). During all the process, the device is connected to an oscilloscope, registering the open circuit voltage profile (the  $1\text{ M}\Omega$  resistance of the oscilloscope is a good approximation of open circuit). The voltage profile gets averaged over a few tens of pulses in order to increase the signal to noise ratio. Initially the

light illumination is set to 1 sun and the laser pulse intensity is attenuated using a neutral filter so that the voltage perturbation remains smaller than 10 mV for ensuring the small perturbation regime. The measurement is repeated after decreasing the background light intensity and waiting a stabilisation time. The fitted small perturbation lifetime is plotted versus the light bias. The background illumination is decreased down to dark background illumination over a few tens different intensities. 1 sun equivalent illumination is defined as the illumination at which a silicon photodiode gives the same  $J_{SC}$  as under calibrated 1 sun from the solar simulator.

**Noise treatment.** Most of the observed noise ( $<2 \times 10^{-7}$  s) is due to the radiofrequency emitted by the spark in the nitrogen laser which gets received by all the non-coaxial cables (coaxial ones do not) and from the circuitry of the samples holder acting as an antenna. On the contrary to what happens for CE (see page 67), the short times noise does not follow a constant pattern, so averaging the measurement over a few repetitions (usually 30) manages to reduce the noise. This noise can affect the exponential or bi-exponential fitting, for this reason a robust fitting routine has been used, which gives a lower weight to outlier points. An example can be seen in fig. 3.16.

**Importance of stable steady state starting point.** The values extracted from TPV are strongly sensible to the surface recombination and electric fields in the absorber, which in turn vary during ionic profile stabilisation. Comparison of decay times with different stabilisation times can be found in O'Regan *et al.* [107], while in Calado *et al.* [98] even negative peaks are reported and explained with the presence of a residual electric field in the absorber previous to ionic profile stabilisation.

**Small perturbations regime.** The intensity of the laser pulse is attenuated using a variable neutral density filter (a partially reflecting wheel with different positions for different transmittivities) so that the voltage perturbation caused by the light pulse does not exceed 10 mV with 1 sun background illumination intensity. We consider this a “small-enough” perturbation with regards to the measured  $V_{OC}$  (see page 58 for a definition of small perturbation). For example, comparing the excess charge in a FTO/d-TiO<sub>2</sub>/CsFAMAPbIBr/spiro-OMeTAD/Au solar cell at  $V_{OC}$  and at  $V_{OC} + 10$  mV which can be obtained from the data in fig. 3.7c

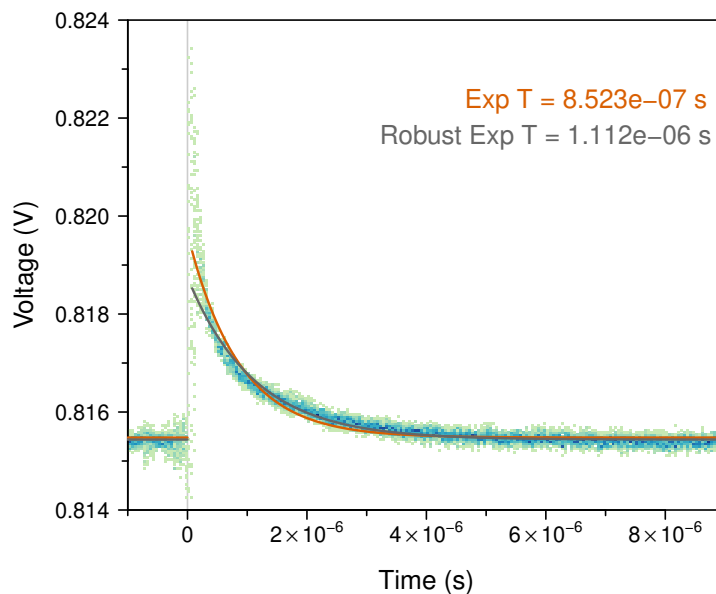


**Figure 3.16: Robust and normal fitting comparison.** Plot of a voltage profile from a single TPV decay. The 12500 voltage points are represented in a 2D histogram for avoiding the overplotting problem. The normal non-linear least squares fitting (in orange) is affected by initial noise (a faster decay if we consider this as a bi-exponential decay), outliers and characteristics not of interest by the model. The non-linear robust fitting (in magenta) manages to reduce the weight of these points. The studied device is a FTO/d-TiO<sub>2</sub>/CsFAMAPbIBr/TAE-4/Au [3] with 1 sun background illumination.

fitted with eq. (3.13) we can obtain respectively a value of  $8.2 \times 10^{-8}$  and  $8.9 \times 10^{-8} \text{ C cm}^{-2}$ . A smaller perturbation is not practically doable as we are limited to  $>3 \text{ mV}$  perturbations due to the strong noise observed in this transient measurement. Decreasing the background light bias, the laser light pulse intensity is kept constant even when it gets out from small perturbation regime, this is needed in order to be able to use the TPV data for calculating DC, as explained in page 99. This does not affect the parameter extraction from TPV as just the high illumination intensity points are considered, as seen in page 90, in order to study the device close to its expected working conditions.

### 3.5.1 Interpretation of TPV Mono-Exponential Decays

**Voltage transient and charge concentration relationship.** As we assume to be in the small perturbation regime, we can study the eq. (3.13) up to the first term of its series expansion:

$$\begin{aligned} n(V_0 + \Delta V) &\approx n(V_0) + \Delta V \cdot \frac{\partial n}{\partial V} \Big|_{V=V_0} \\ &= n(V_0) + \Delta V \cdot \left[ C_g + \frac{n_{\text{eq}}q}{mk_B T} \exp\left(\frac{qV_0}{mk_B T}\right) \right] \end{aligned} \quad (3.14)$$

Assigning the last addend to  $\Delta n$  we can see that the charge amount variation not only is linear with  $\Delta V$  (as we are in the small perturbation regime), but it also depends on the steady state voltage  $V_0$ . This relation is studied in the differential capacitance (DC) experiment, described further in this chapter.

**Voltage re-equilibration dynamics.** For what concerns a TPV experiment, we are just interested in the analysis of the time needed for re-equilibration to steady state conditions. As seen in eq. (3.14), the relation between  $\Delta V$  and  $\Delta n$  in small perturbation regime is linear, so the lifetime extracted from a  $\Delta V$  decay will have the same lifetime of the underlying  $\Delta n$ , which is the interesting quantity when speaking of recombination. This means that we can observe the variations in voltage for having a correct kinetic description of the charge amount variation. At steady state conditions, the time derivative of the amount of charge is zero  $\partial n_0 / \partial t = g(\phi) - U(n_0) = 0$  where  $g$  is the generation rate and  $U$  is the recombination rate. Considering the situation after the end of the light pulse, so while  $g$  is constant but  $n$  has been increased by  $\Delta n$ , and using a simplified expression for the recombination including just two contributions with reaction order 1 and 2 and rate constants  $k_1$  and  $k_2$  we can write:

$$\begin{aligned} \frac{\partial(n_0 + \Delta n)}{\partial t} &= g - U \\ &= g - k_1(n_0 + \Delta n) - k_2(n_0 + \Delta n)^2 \\ &= (g - k_1 n_0 - k_2 n_0^2) - (k_1 \Delta n + 2k_2 n_0 \Delta n) - (k_2 \Delta n^2) \\ &\approx -(k_1 + 2k_2 n_0) \Delta n \end{aligned} \quad (3.15)$$

where the zeroth order term is the steady state value, so it is zero, and the second order term can be neglected (if  $\Delta n \ll n_0$  then

$k_2\Delta n^2 \ll k_2n_0\Delta n$ ). So the rate equation is a simple pseudo first order reaction, and the kinetic behaviour follows an exponential description like:

$$n(t) = n_0 + \Delta n_0 \cdot e^{-(k_1+2k_2n_0)t} = n_0 + \Delta n_0 \cdot e^{-t/\tau} \quad (3.16)$$

where  $\tau = (k_1 + 2k_2n_0)^{-1}$  is the small perturbation lifetime. For a single recombination with a generic recombination reaction order  $\Phi$  we can generalize to [190]:

$$\tau \approx (\Phi k n_0^{\Phi-1})^{-1} \quad (3.17)$$

where  $k$  is the dominant recombination rate constant.

### 3.5.2 Interpretation of TPV Bi-Exponential Decays

**At high background illumination.** In our simulation, at high illumination intensity we observe just mono-exponential voltage decays both without (fig. 3.19a) or with mobile ions (fig. 3.19b). Experimentally, for some devices rather than an exponential decay, a bi-exponential voltage decay is observed, like the one reported in fig. 3.17c. This is more frequent in bottom cathode devices including mesoporous titania layers [31, 107, 197] but has also been reported for silicon solar cells [108]. With *bi-exponential* decay we refer to the sum of two exponential decays with two different half-life times, like:

$$V(t) = V_0 + \Delta V_a \cdot e^{-t/\tau_a} + \Delta V_b \cdot e^{-t/\tau_b} \quad (3.18)$$

where  $\tau_a$  and  $\tau_b$  are two distinct lifetimes while  $\Delta V_a$  and  $\Delta V_b$  are the respective amplitudes of the contributions to the measured decay. The presence of two different recombination processes is not enough for justifying a bi-exponential decay. This is clear looking to eq. (3.16), where considering two recombination processes with two different reaction orders we obtained a simple exponential decay. What we have to remember here, is that eq. (3.16) was obtained for a zero dimensional case, like what would happen in a homogeneous chemical reaction. In our case, the multiple recombination centres could be spatially separated. If the charge concentration in the two centres is dis-entangled (is not identical at any time), the sum of two exponential decays can be expected rather than a simple exponential. This dis-entanglement is possible if the time needed for the free carriers to migrate from a recombination centre to the other is larger than the shorter recombination lifetime. This can happen thanks to a large-enough distance between recombination centres together with a slow free carriers mobility [4]. For example for recombination centres at

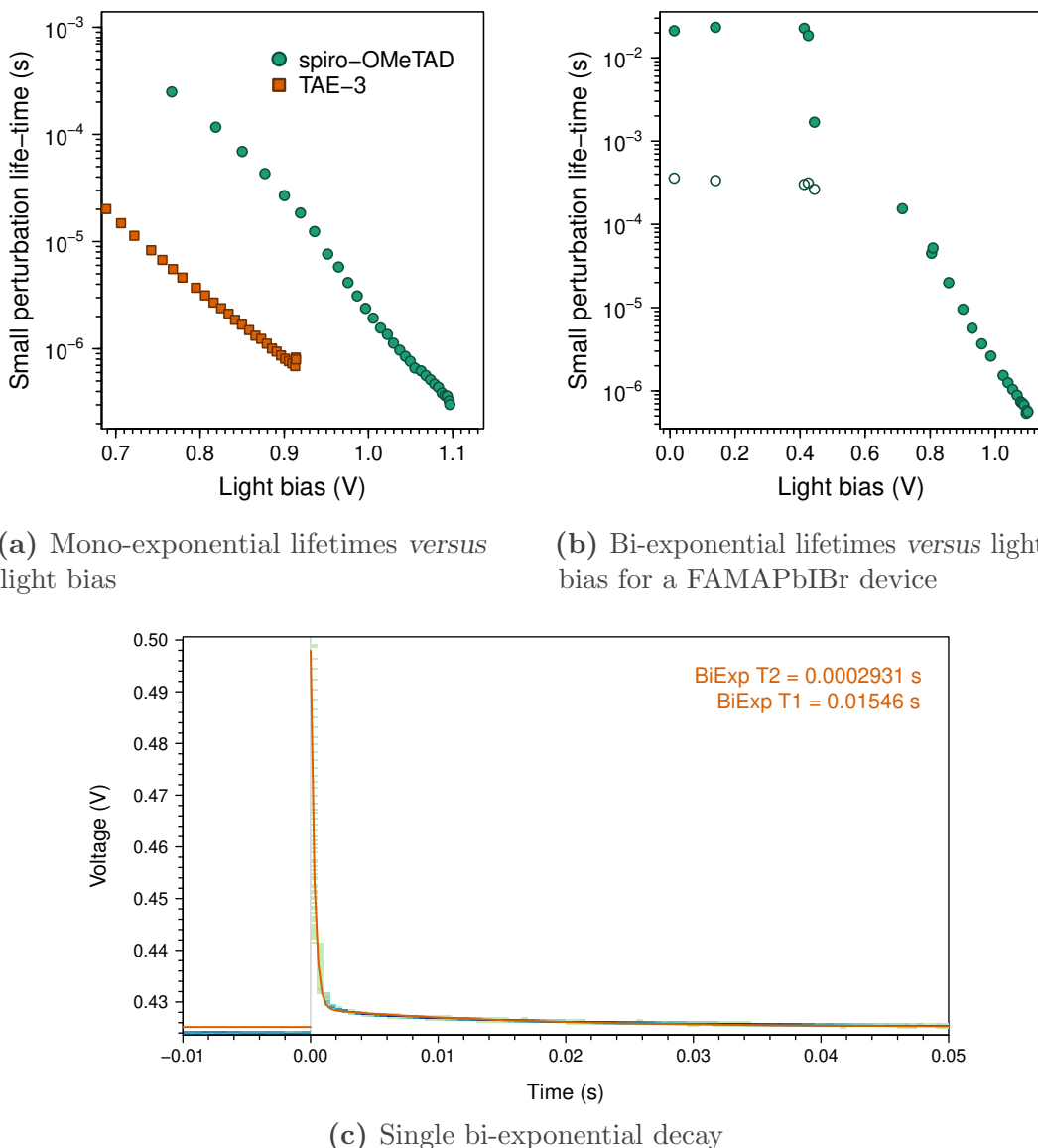


**Figure 3.17: Example of lifetimes versus light bias plot obtained from a TPV experiment.** In (a) the small perturbation lifetimes obtained from robust mono-exponential fitting are plotted against light bias for FTO/d-TiO<sub>2</sub>/CsFAMAPbIBr/HTM/Au devices [3]. In (b) the lifetimes of a FTO/d-TiO<sub>2</sub>/FAMAPbIBr/spiro-OMeTAD/Au device as obtained from a robust bi-exponential fitting for low light bias, where the decays are clearly biphasic, and mono-exponential for higher illuminations. In (c) the full data for the point at 0.42 V from (b) is reported.

different depths in the solar cell stack, like at the two perovskite/contacts interfaces. The fact that the presence of mesoporous structures are often present when bi-exponential decays are observed can be understood by the smaller mobility of perovskite when intercalated in such structures [17]. This have been reported also for laterally distanced recombination centres (e.g. pinholes *versus* well covered regions) by Montcada *et al.* [68].

**Mobility limited case.** As we just saw, the mobility is a crucial parameter for the TPV experiment. As a mental exercise we can imagine a case where the mobility is so slow that the free charges take a long time to diffuse (we consider diffusion as perovskite solar cells are assumed to be field-free in the absorber layer, but the same concept would hold with charges' drift) from the generation zone (in the absorber) to the recombination centre (e.g. at a contact/absorber interface). In such an extreme case the provisioning of charges to the recombination centres could become a bottleneck rather than the recombination itself. A drift-diffusion simulation of this can be found in Calado [4]. In this regime, a TPV experiment would be rather insensitive to actual recombination constants and even to light intensity, giving just information about mobility. As the observed TPV lifetimes are strongly light-intensity dependent, at least at high background illumination, we can exclude to be in this mobility-limited regime. This would have to be revised in case a strong illumination-dependent mobility in perovskite materials was demonstrated, as has been reported in OSC [187, 198, 199]. Also a slow trapping and de-trapping of the carriers can result in a reduced and illumination-dependent mobility [160].

**Inhomogeneous charge concentration profiles.** Due to the internal electric field, the free carriers concentration can be inhomogeneous. For the surface recombination, this implies that the average excess carriers concentration obtained from CE is not necessarily the carriers concentration at the recombination centre [170]. For the band-to-band recombination, this implies that the  $n \cdot p$  product, integrated over the device thickness, can be much smaller than an homogeneous carriers concentration [200]. These considerations are key for drift-driven OSC with low doping level materials [186, 187] but should be of smaller impact for the diffusion-driven, field free perovskite solar cells, at least at steady state when the internal electric field is mostly shielded by the ionic accumulation at the interfaces.

**At low background illumination – large perturbations.** While bi-exponential decays at high background illumination are often not observed,

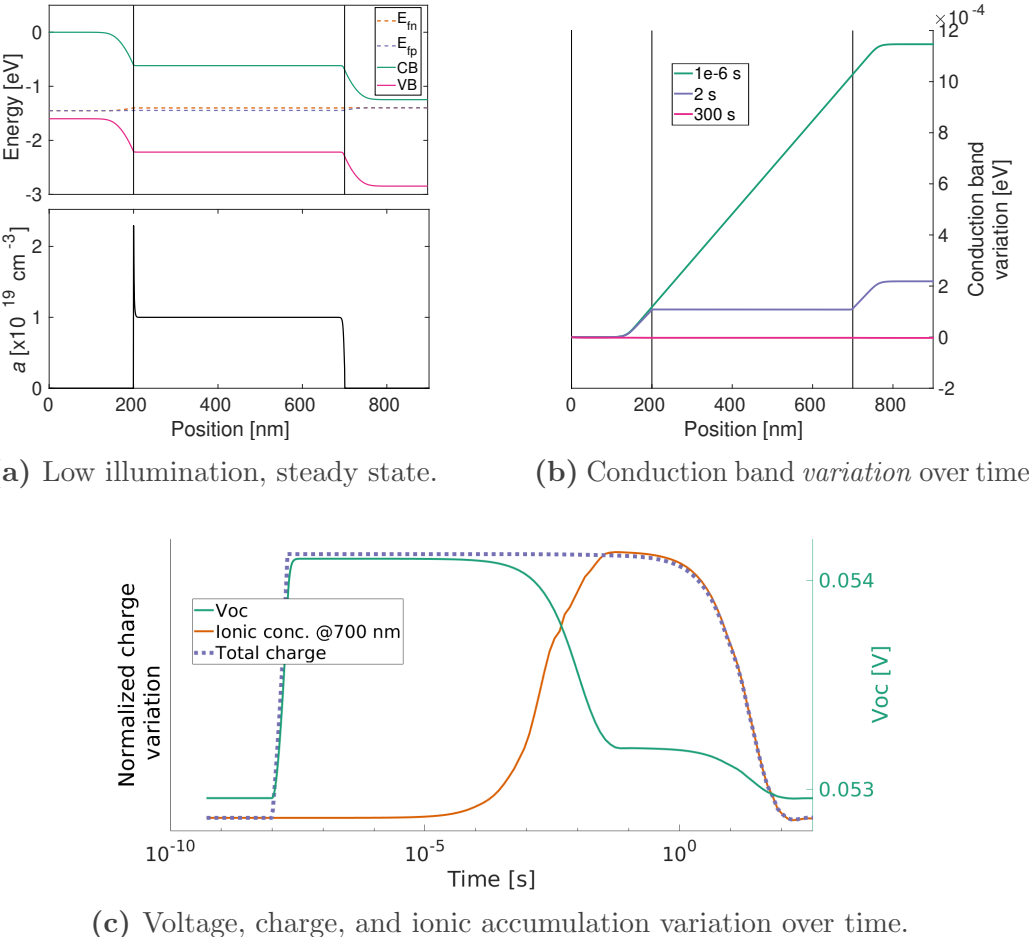
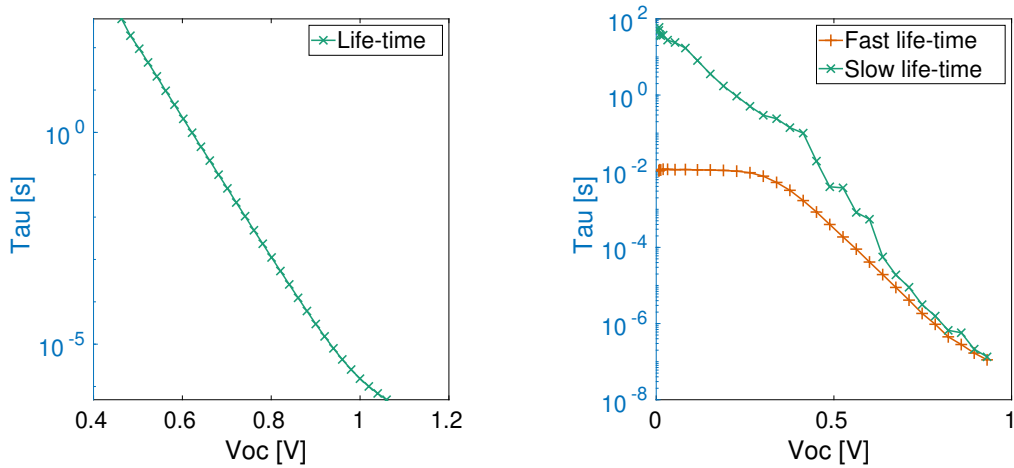


**Figure 3.18: Simulation of TPV at low background intensities with mobile ions.** A TPV experiment has been simulated on a  $p(200 \text{ nm})-i(500 \text{ nm})-n(200 \text{ nm})$  homojunction device with mobile ions in the absorber layer and at open circuit conditions. Low background light intensity  $1 \times 10^{-8}$  suns was applied, corresponding to a light bias of 53 mV. The illumination pulse was  $1 \times 10^{-8}$  s long and weak enough to cause a perturbation which can be considered small. In (a) the steady state energy levels and ionic profile is shown. In (b) the variation (the conduction band perturbation is too small for being plotted as in (a)), taking the steady state profile as zero, of the conduction band during a TPV experiment. In (c), over time I plotted: the bi-exponential voltage decay; the normalized total charge variation (the electronic profile integrated over the device thickness); and the ionic concentration variation at the perovskite/ETM interface, where the low ionic concentration temporarily increases during the transient. The represented data is interpreted in page 87. TPV simulation routines explained in page 188.

these are quite always present at lower background illumination, as in for the example reported in fig. 3.17b. Clearly, the aforementioned explanation for bi-exponential decays at high illumination are still valid for the low illumination case. Additionally, when studying a decay measured at very low background light intensity, we have to remember that we are out of the small perturbation regime and this could justify non-exponential decays in various ways. In our simulation, we ensured to be in the small perturbation regime, still we observe bi-exponential decays at low light biases as shown in fig. 3.19b, so another explanation has to be found.

**At low background illumination – ionic migration.** At low light intensity, the free carriers density can be very small, so that the recombination can be very slow. At these long times, another process of perovskite solar cells can be active: ionic migration. What we have observed, simulating a TPV experiment on a homojunction device with mobile ions in the absorber layer, is that ionic profile can update to the pulse-perturbed cell condition before the extra free charges recombine, in case this is very slow. In fig. 3.18a the steady state energy levels and ionic accumulation at the perovskite/contact interfaces is represented. In fig. 3.18b the variations of the conduction band profile are plotted. Here we can see that at  $1 \times 10^{-6}$  s the CB varies due to the new charges photo-generated by the laser pulse, the non-flat conduction band indicates the presence of an electric field in the perovskite layer. At the same times, we can see in fig. 3.18c the increase in the total amount of electrons in the device due to the laser photo-generation which is reflected also by the open circuit voltage increase, as expected for a TPV experiment. Then from  $1 \times 10^{-3}$  to  $1 \times 10^{-1}$  s, the ionic profile completely screens out the electric field. In fig. 3.18b this is visible as a flattening of the conduction band in the perovskite, this simple displacement of ions decreases the electrostatic potential at the ETM. In absence of changes in the charge density, a shift in the electrostatic potential in the ETM causes an identical shift in the quasi-Fermi levels in the ETM. As the voltage is defined as  $V = \bar{\mu}_{\text{CB}}^{\text{ETM}} - \bar{\mu}_{\text{VB}}^{\text{HTM}}$  this shift clearly gets reflected in a voltage change. In the same time span, in fig. 3.18c we can see how the ionic concentration at an interface changes and how this gets reflected on the open circuit voltage, without any change in the total charge concentration. Finally, at longer times the laser-generated free charges slowly recombine (the ionic profile just catches up this free charges variation), the CB returns to its steady state profile and a second decay is observed in the open circuit voltage. So, in this case, only the slow decay is actually related to charge



(a) Without mobile ions, mono-exp. fit      (b) With mobile ions, bi-exp. fit

**Figure 3.19: Simulated TPV without and with mobile ions.** The TPV of a homojunction solar cell is simulated, with background illumination from  $1 \times 10^{-10}$  to 1 suns (respectively the leftmost and the rightmost points) with 3 points per decade. The pulse intensity was regulated in order to not exceed 8 mV of perturbation. In (a) a device without mobile ions is simulated, the resulting decay is a simple exponential, so the lifetime of an exponential fit is reported. In (b) a device with mobile ions in the absorber layer is reported, the resulting decay is a simple exponential at high light biases but a bi-exponential at lower background illuminations, so the two lifetimes from a bi-exponential fitting are reported. TPV simulation routines explained in page 188.

recombination, while the fast one is due to the ionic profile update. This means that, if the simulation is correct, at low background light intensities we can obtain information on the ionic mobility and concentration from the fast component of bi-exponential TPV decays.

**At low background illumination – fast lifetime plateau.** Both the fast and the slow component of bi-exponential decays hit a maximum value (plateau) at very low light intensities. Looking at the fast component, assigned to the rearrangement of the ionic profile, we usually observe a constant lifetime. This suggests the presence of a background light insensitive ionic rearrangement time constant, which implies a light insensitive ionic mobility. This should be further studied considering the report of illumination-dependent ionic conductivity by Maier’s group in Kim et al. [201].

**At low background illumination – calculating ionic resistance.**

We can consider this fast component's lifetime as a RC time due to ionic motion. So, from this time and from the ionic capacitance (easy to obtain from impedance spectroscopy, see page 155), we can obtain the ionic resistance (which is proportional to ionic mobility and to ionic concentration) as:

$$R_{\text{ion}} = \frac{\tau_{\text{ion}}}{C_{\text{ion}}} \quad (3.19)$$

**At low background illumination – slow lifetime plateau.** The slow decay component at very low background light intensity has been assigned to the electronic recombination. In drift-diffusion simulations, the lifetime does not show a maximum value and grows as the light intensity is decreased. But in the actual experiment setup, decays lifetimes are limited at long times by the discharge of the through the oscilloscope resistance and through the device shunt resistance, whatever is the fastest. This happens with an RC time of the circuit composed by the capacitance of the device (which can be obtained via a DC experiment) and the  $1 \text{ M}\Omega$  resistance of the oscilloscope or the internal device shunt resistance [171]. The oscilloscope resistance could be varied using an attenuating probe (usually 10X or 100X) or a high impedance amplifier. This limit is often observed at low light intensities as a plateau in the TPV lifetime versus light bias graph [171]. Indeed, in Kiermasch *et al.* [108], where a  $1 \text{ T}\Omega$  input impedance amplifier is used, the plateau is observable from  $1 \times 10^{-1}$  to 1 s, *i.e.* three orders of magnitude higher than what we observe with our  $1 \text{ M}\Omega$  oscilloscope. This affirmation is corroborated by the correlation observable in fig. 3.20. For mid-illumination intensities, the measured lifetime can be corrected considering the contribution from the RC time [181].

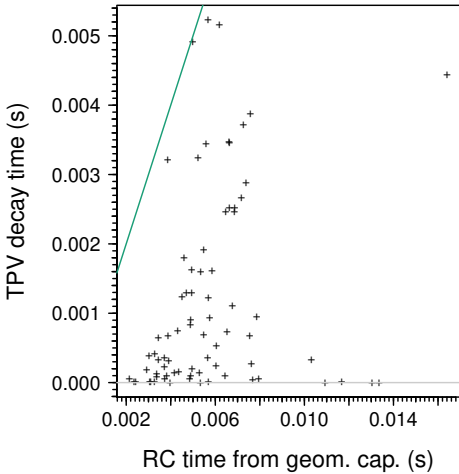


**Figure 3.20:** TPV time has an upper bound due to discharge through oscilloscope. Dark TPV time (from a robust exponential fit) versus RC time derived from the geometric capacitance from DC and the  $1\text{ M}\Omega$  of the oscilloscope. Each point is a different device for a total of 76 devices, including many different structures. The green line indicates the 1 to 1 relationship.

### 3.5.3 Interpretation of TPV versus Light Bias Trend

**Lifetime versus light bias dependence.** Considering the small perturbation lifetime dependency from charge concentration due to a single dominant recombination mechanism from eq. (3.17) and substituting the charge with the expression for the charge from eq. (3.13) we can obtain a relation between the lifetime and the  $V_{\text{OC}}$ . The main recombination mechanism in perovskite solar cells at open circuit conditions is the surface recombination (see page 24) which, as described in page 17, can be considered as a first-order reaction with regards to the carriers in the perovskite layer. This carrier density is related to the chemical capacitance represented as the exponential component in eq. (3.13), so expanding  $n_0$  from eq. (3.17) we obtain:

$$\begin{aligned} \tau &\approx (\Phi k n_0^{\Phi-1})^{-1} \\ &= \frac{n_{\text{eq}}^{1-\Phi}}{\Phi k} \left[ \exp\left(\frac{qV_{\text{OC}}}{mk_B T}\right) - 1 \right]^{1-\Phi} \\ &\approx \frac{n_{\text{eq}}^{1-\Phi}}{\Phi k} \exp\left(-\frac{(\Phi-1)qV_{\text{OC}}}{mk_B T}\right) \\ &= \frac{n_{\text{eq}}^{1-\Phi}}{\Phi k} \exp\left(-\frac{qV_{\text{OC}}}{vk_B T}\right) \\ &= \frac{\tau_0}{\Phi} \exp\left(-\frac{qV_{\text{OC}}}{vk_B T}\right) \end{aligned} \quad (3.20)$$

where we used that  $qV \gg k_B T$  for all non-dark cases in order to neglect the  $-1$  addend. The pre-factor  $\tau_0 = n_{\text{eq}}^{1-\Phi}/k$  represents the thermal equilibrium

lifetime. As shown, the lifetime typically decreases exponentially with the light bias, as experimentally observed in the example of fig. 3.17a, with an ideality modifier of  $v = m/(\Phi - 1)$ . This relation is in accordance with equivalent studies on OSC [168, 190, 202].

**Diode-capacitor discharge could be the limiting time.** Similarly to the example we just considered, where RC times put a cap to the slow observable lifetimes, Kiermasch *et al.* [108] underlines that also the often-neglected diode-capacitor discharge could have the same effect [171, 203]. The relevant capacitance would be the geometric capacitance of the generated charges accumulating in the depletion layers and the diode would be the perovskite-contacts interfaces with the relative dark saturation current. Basically this represents a re-injection of the majority charges from the contacts back to the perovskite, this causes a voltage decrease without actually needing recombination: charges could just diffuse back. The lifetime observed in this regime would also decrease exponentially with the light bias [204]. In his PhD thesis, also Calado [4] observed and modelled this effect, named “thermionic emission”. All the authors agree that this effect is more important at low light intensity for thin devices (high capacitance) [108] while it could be negligible at high background illuminations. Also when performing full signal Open Circuit Voltage Decay dynamics measurement (OCVD) [205, 206], which has not been performed in this thesis, this limitation has to be taken in consideration [42, 102, 108, 171].

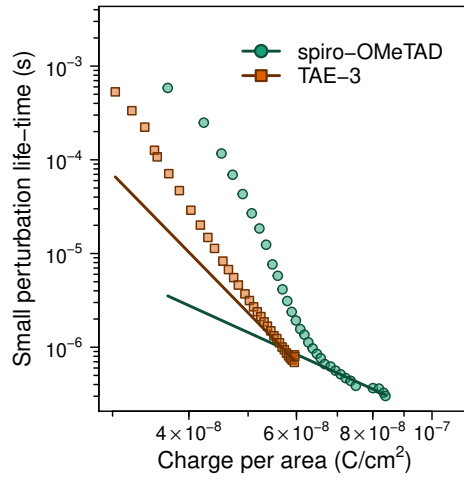
## 3.6 Transient PhotoVoltage Referenced to Charge Density (TPV-CE)

**Concept.** This is a meta experiment which combines the data from TPV and CE without needing any additional experimental step. Joining the information about charge lifetime *versus* light bias from TPV with the information about charge density *versus* light bias from CE, we obtain the relation of the charge lifetime *versus* charge density. This new relationship is more useful than the results from bare TPV, as it allows us to make a fair comparison between different devices.

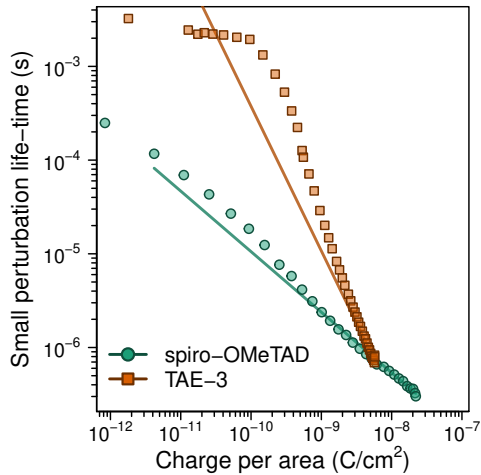
**Procedure.** The voltage dependency of the small perturbation lifetime  $\tau(V)$  obtained from TPV gets expanded with the  $V(n)$  relation which can be obtained inverting the fitted function of  $n(V)$  from a CE experiment for obtaining a  $\tau(n)$  relation. A reaction order  $\Phi$  can be obtained fitting the  $\tau(n)$ , this can be used for correcting the small perturbation lifetime to obtain a pseudo first order lifetime *i.e.* total carrier lifetime  $\tau_{\text{pfo}}(n)$  which can be compared between devices with different recombination mechanisms.

**Which charge from CE.** In OSC literature, where a simple exponential charge *versus* voltage is usually observed, the full  $n$  obtained by CE is taken. In perovskite solar cells, the charge from chemical capacitance is usually considered as the relevant charge density for surface recombination, as explained in page 90, so just the exponential addend is taken from the fit of CE data performed with eq. (3.13) [3, 64, 160]. As a reference, the figs. 3.21a and 3.21b can be compared where the full charge from CE is employed in the former while just the charge from chemical capacitance was used for the latter. Using eq. (3.17) for fitting the data, we can obtain physically unreasonable recombination orders when considering the full charge from CE (reported in fig. 3.21a). Instead, fitting data with the exponential component of CE only, the recombination orders obtained are between 1 and 2, which are the expected values (reported in figs. 3.21b and 3.21c).

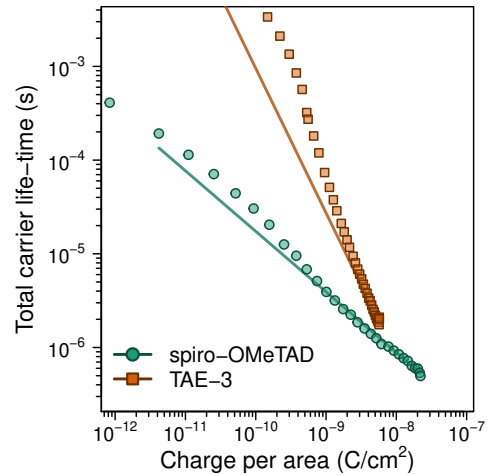
**From small perturbations lifetime to rate constant – first-order reaction.** Here we consider a simple case where just a first order or a second order recombination is present. From the eq. (3.17) it is clear that for the first-order reaction case it is easy to obtain  $k_1 = \tau^{-1} = \tau_{\text{pfo}}^{-1}$ . One



(a) Full charge from CE



(b) Exp. charge from CE

(c) Exp. charge from CE and lifetime corrected with  $\Phi$ 

**Figure 3.21: Example of TPV-CE processed in different ways.** Solid lines are the power-law fit with the formula  $y = k^{-1}x^{1-\Phi}$ . In (a) the charge used for the independent variable is taken from the full charge extracted in the CE experiment, including the charge stored in contacts and electrodes. The  $\tau_{pfo}$  lifetime as obtained from TPV is used as dependent variable. In (b) just the charge from chemical capacitance (exponential addend in eq. (3.13)) is used as independent variable. In (c) the  $\tau$  is corrected using the fitted recombination order  $\Phi$  to obtain the total carriers lifetime  $\tau_{pfo} = \Phi\tau$ . Data from FTO/d-TiO<sub>2</sub>/CsFAMAPbIBr/HTM/Au solar cells [3].

fact of eq. (3.17) for the  $\Phi = 1$  case have to be underlined: the small perturbations lifetime for a first-order recombination does not depend on the charge density, so it would appear as a plateau in the lifetime versus charge plot [108] which is not usually experimentally observed.

**From small perturbations lifetime to rate constant – higher order reaction.** For the second and higher order recombination cases, to obtain  $k$  is non-trivial as it is related to  $\tau$  via the charge density [207] and the reaction order [160, 175, 190, 208] as shown in eq. (3.17). From this equation we can notice that correcting the small perturbation lifetime  $\tau$  we can easily obtain a pseudo first order lifetime (total carrier lifetime)  $\tau_{\text{pfo}}$  as:

$$\tau_{\text{pfo}} = \Phi\tau = k^{-1}n_0^{1-\Phi} \quad (3.21)$$

where  $n_0$  is the excess carriers in the device. This simple correction allows us to make a meaningful graphical comparison between recombination rates at a given charge density, as represented in fig. 3.21c. The units of recombination constant  $k$  are rather unusual:  $\text{s}^{-1}\text{cm}^{2\Phi-2}$ . In order to obtain a more useful value, the lifetime extrapolated at zero applied voltage  $\tau_0 = n_{\text{eq}}^{1-\Phi}/k$  is often employed [64, 160, 170, 209] (as already used in eq. (3.20)):

$$\tau_{\text{pfo}} = \tau_0 \left( \frac{n_0}{n_{\text{eq}}} \right)^{1-\Phi} \quad (3.22)$$

where  $n_{\text{eq}}$  is the chemical capacitance prefactor obtained from eq. (3.13) indicating the intrinsic carrier density at equilibrium.

## 3.7 Transient PhotoCurrent (TPC)

**Concept.** This technique, applied to a solar cell at short circuit conditions, allows us to study the dependence of external quantum efficiency (EQE) on the light illumination intensity [191]. It gives approximatively the same information of the  $J_{SC}$  versus light intensity experiment explained in page 63. Usually, the actual value of EQE (generated charge over incident photons ratio) is not calculated, rather just the generated charge amount  $\Delta n$  for a given laser pulse intensity in measured.

**Procedure.** The device is short circuited through a  $50\Omega$  resistor and kept either at dark or under 1 sun illumination by a white LED ring until stabilisation is reached. Failure to reach stabilisation of the ionic profile will affect the measurement results [210]. Then, as represented in fig. 3.22, an additional illumination pulse is provided via a nitrogen laser and the voltage across the  $50\Omega$  resistor is monitored using an oscilloscope connected in parallel. This allows us to measure a potential drop across the resistor and to obtain the related current via Ohm's law  $J = V/R$ . Subtracting the constant current due to the background illumination and integrating the transient over time gives the charge photo-generated by the laser pulse. This process is repeated at 1 sun and at dark background illumination conditions, as shown in fig. 3.23. For each

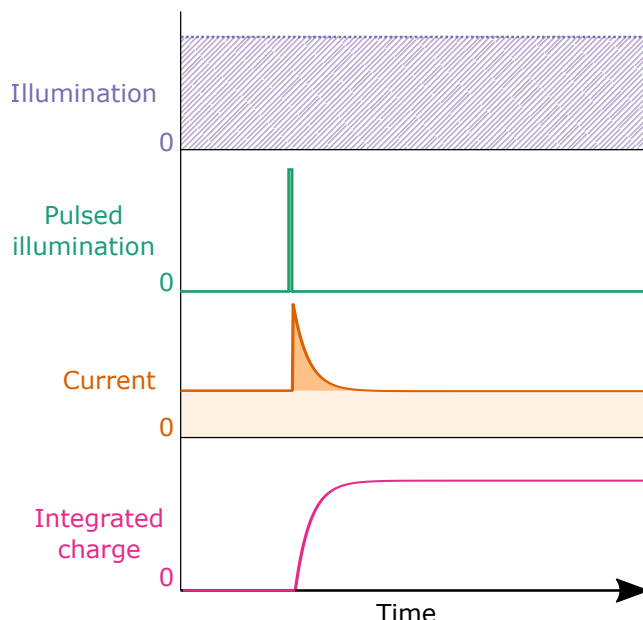


**Figure 3.22:** Scheme of TPC experiment. A device is illuminated while short circuited through a small resistance, then a short light pulse is added and the additional flowing current is integrated to give the photo-generated charge. The constant illumination intensity is changed and the measurement is repeated.

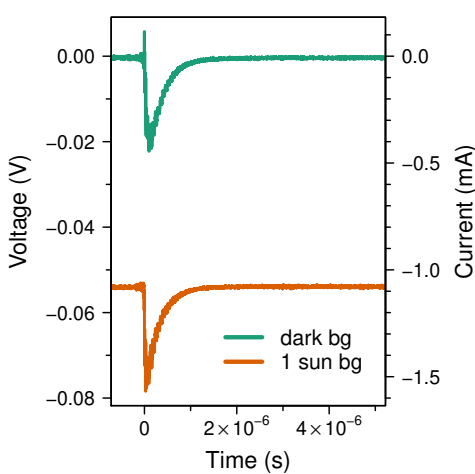


**Figure 3.23: Example of TPC experiment at dark and 1 sun background illumination.** The current profile of a FTO/d-TiO<sub>2</sub>-/CsFAMAPbIBr/TAE-4/Au solar cell [3] short circuited through a small resistance either in dark or illuminated with 1 sun and perturbed with a laser pulse. The voltage axis can easily be converted to the current axis dividing by the known small resistance of 50 Ω. The integrated peak resulted in 0.17 nC for the dark case and 0.14 nC for the 1 sun one.

illumination intensity, the reported decay is the result of averaging around 30 transients in order to increase the signal to noise ratio. 1 sun equivalent illumination is defined as the illumination at which a silicon photodiode gives the same  $J_{SC}$  as under calibrated 1 sun from the solar simulator.

**Small resistance and fast extraction.** The characteristic time of a TPC decay is often comparable with the small perturbation lifetime from TPV experiment at high background illumination. This not necessarily invalidate the TPC result, as the slow time could be due to the slow transport in the selective contacts. The TPC time can be limited by the RC time constant of the extracting circuit, in case a faster extraction is needed, a smaller resistance can be employed (clearly, the measure will be more noisy). Thanks to the short time of the measurement, both with or without background illumination, we can assume that the ionic migration is never observed in this measurement.

**Dependency on background illumination.** When measuring TPC at various background illumination intensities, a constant pulse-generated charge amount can be gathered for low illuminations that starts decreasing as the background illumination exceeds 1 sun (as reported for perovskite solar cells in fig. S5 of [160] and partially in fig. S9 of [64]). In OSC this was assigned to primary geminate recombination, which, as seen in page 15, is negligible in perovskite materials. The influence of the different electric field intensity on the absorption, explained in page 191, can be neglected as the field is screened in most of the absorber and anyway

the electro-absorbance phenomena (Franz-Keldysh effect) should have just a small contribution. Other kind of recombination can affect the extracted charge, even in short circuit conditions, if the charge extraction is not sufficiently quick. For this reason, in case of large discrepancies between the dark and the 1 sun background illumination measures, the dark one better describes the photo-generated free-charge (in case the dark and illuminated results were different, the first quartile of all TPC measurements was used).

## 3.8 Differential Capacitance (DC)

**Concept.** DC is a meta-measurement as it just combines the data from TPV and TPC without requiring any additional experimental step [110, 176, 181, 190, 192], sometimes also referred to as “differential charging”. From TPC we obtain how much charge  $\Delta n$  has been generated by the laser pulse and from TPV we obtain the voltage increase  $\Delta V$  due to the additional charge. Relating these two quantities, DC allows us to measure the capacitance of the solar cells at different light biases. Integrating this capacitance profile over voltage we can obtain the extra charge density versus light bias profile. This information is equivalent to the results from CE, with the advantage that this technique is a small perturbation technique, working on a stabilised device around its steady state conditions. Differently to CE, DC is an intrinsically short time-scale technique in which the ionic migration should never be observed. This technique has also been used for estimating the electronic band gap of the perovskite layer in Wheeler *et al.*, Credgington *et al.* [64, 181], considering that also for DC as seen for CE in page 76, the exponential trend is expected to gain importance as the quasi-Fermi splitting approaches the built-in voltage. For OSC, the consistency of this observation has been validated using ultraviolet photoelectron spectroscopy (UPS) in Credginton *et al.* [181].

**Procedure.** The laser pulse intensity has to be the same for the TPC and the TPV experiments. The needed value of  $\Delta V$  is the  $V_{OC}$  increase due to the laser pulse, prior to the decay to steady state, for each illumination intensity. The amount of charge photo-generated by the laser pulse  $\Delta n$  is obtained from TPC. In order to use the charge measured in TPC at short circuit for referencing the data from TPV at open circuit we have to assume that  $\Delta n$  is the same at open and short circuit conditions. In other words, we assume that the EQE does not depend on the applied voltage. Additionally, we have to assume that the EQE does not depend neither on the background illumination intensity for a device at open circuit conditions (used for TPV). This point was discussed for TPC in page 96. Adapting the definition of capacitance “the ratio of the change in an electric charge in a system to the corresponding change in its electric potential” [211] to an applied voltage dependent capacitance, we can write:

$$C(V) = \frac{\Delta n}{\Delta V'} \Big|_{V'=V} \quad (3.23)$$

where  $C$  is a light bias  $V$  dependent capacitance,  $n$  is the perturbed electron density, and  $V'$  is the perturbed voltage. So, the charge obtained from the TPC experiment is divided by an array of voltage increases  $\Delta V'(V)$  values obtained from TPV, one for each illumination intensity. The obtained capacitance value is plotted versus the steady state light bias  $V$ . The capacitance can be integrated over voltage for obtaining a charge density versus light bias relationship:

$$n_{DC}(V) = \int_0^V C(V') dV' \quad (3.24)$$

**Capacitance dependence on applied voltage.** The electrical capacitance of most of the commercial capacitors is independent on the applied voltage, as represented in fig. 3.24a where the capacitance was measured with a modified CE experiment where the pre-conditioning was done directly applying a voltage instead of applying a light bias. This means that the extracted charge is linearly proportional to the applied voltage. On the contrary, the electrical capacitance of a solar cell does depend on the applied voltage or light bias, as shown in fig. 3.24b.

**Small perturbations.** As mentioned in page 80, we measure TPV ensuring to be in the small perturbation conditions for high light bias illumination. But the perturbations are surely large getting close to dark illumination conditions. This happens because we are not changing the laser pulse intensity when decreasing the background illumination. This way, we can measure just one TPC for knowing the amount of generated charge, as we assume that it depends just on the laser pulse intensity. The measure of as many TPC as many laser pulse intensities would be too complex with our current experimental setup.

**Consideration on mobility limited case.** In order to have a meaningful voltage peak value, the charges have to equilibrate with the cell electrodes quickly compared to the recombination rate [181]. In a mobility limited case, as explained in page 85, the charges could recombine so quickly that the  $\Delta V$  value could be underestimated.

**Voltage peak value from TPV.** The  $\Delta V$  value can be obtained in various ways, the following methods were tested:

- The maximum voltage point, subtracting the steady state  $V_{OC}$  (fig. 3.25a). This is the classical way to obtain  $\Delta V$  but it is heavily

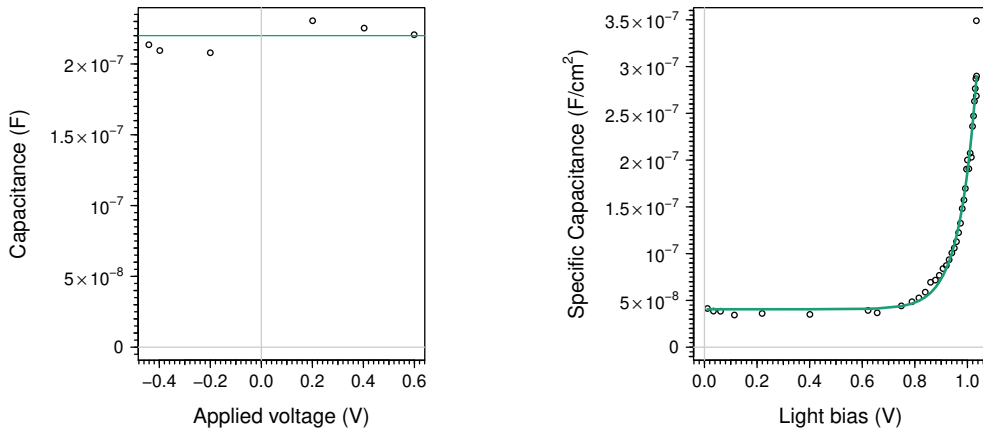


**Figure 3.24: Capacitance dependence on applied voltage.** In (a) the capacitance of a commercial capacitor is reported, it was measured using CE with applied voltage bias instead of the classical light bias used for solar cells. The capacitance is obtained as the extracted charge over the applied voltage prior to short circuiting. In (b) the typical capacitance versus voltage profile of a FTO/d-TiO<sub>2</sub>/CsFAMAPbIBr/TAE-1/Au device [3] is shown as measured by DC. In this case the indicated voltage is originated by various illumination intensities at open circuit prior to short circuiting.

affected by the aforementioned noise when a short time window is used.

- The linear factor  $\Delta V$  in an exponential fit  $V(t) = V_0 + \Delta V \cdot e^{-t/\tau}$  was used, but it can fail if the decay does not have a simple exponential shape (often a bi-exponential is observed, fig. 3.25b).
- In cases where the TPV decays have a bi-exponential behaviour, the sum of the two linear factors  $\Delta V = \Delta V_a + \Delta V_b$  in a bi-exponential fit as in eq. (3.18) could improve the previous method (fig. 3.25c). One have to carefully set boundary values to the fitting parameters for avoiding a fast exponential matching just some noise.
- The maximum value of a LOESS local regression was used, but this underestimates the value, especially when the peak top are just few points (when the measurement time window is large, fig. 3.25d).
- The average of the values registered starting from the maximum voltage point and during a specified time lapse. For selecting the

maximum voltage without interferences from the noise, a custom smoothing function is used (fig. 3.25e).

This last option is the one used in this thesis. The average was performed over 50 ns after the peak and this allowed us to get a reliable  $\Delta V$  value. As an example, we can compare the  $\Delta V$  obtained with the aforementioned criteria applied on the TPV decay in fig. 3.16: 16.5 mV from the maximum point; 4.2 mV from the simple mono-exponential fit; 3.3 mV from the robust mono-exponential fit ; 5.9 mV from the simple bi-exponential fit; 6.1 mV from the robust bi-exponential fit (see page 80 for discussion on robust fitting); 4.2 mV from the maximum of the LOESS; 4.6 mV using the average of the first points after the peak. To further illustrate the sensibility of DC from the  $\Delta V$  estimation, the capacitance of four devices from [3] has been reported in fig. 3.25. If the object of study is related to the presence of negative peaks, present in non-stabilised solutions as described in page 80, the data fitting code should be modified. A non stabilised ionic profile during the TPV measurement can lead to shifts in the DC profile [107]. The biphasic behaviour of TPV decays at low background intensity due to ionic migration, discussed on page 87, does not reduce the validity of the  $\Delta V$  value for capacitance determination, as at very short times the ionic profile is effectively frozen.

### **Capacitance from voltage and current increase during the pulse.**

In case a slow light pulse have to be employed, e.g. from a LED source, the voltage peak is too strongly affected by the ongoing recombination. An alternative method considering the plateau current of a TPC experiment *versus* the voltage grow rate from TPV has been reported [107, 192].

**Comparison of charge from DC and from CE.** The DC experiment has been demonstrated to output a very similar charge *versus* light bias profile as a CE experiment when used on DSSC [106, 176] and on OSC [183]. DC started to be employed in perovskite solar cells characterisation due to the excessively large charge amount sometimes measured by CE [64, 107]. Additionally, as explained in page 72, in cases where high charge recombination is present CE should be corrected while DC should be unaffected as it can be measured in shorter time scales. For obtaining the same parameters as when fitting CE data with eq. (3.13) we can either use that equation for fitting the integrated charge or use the following (which

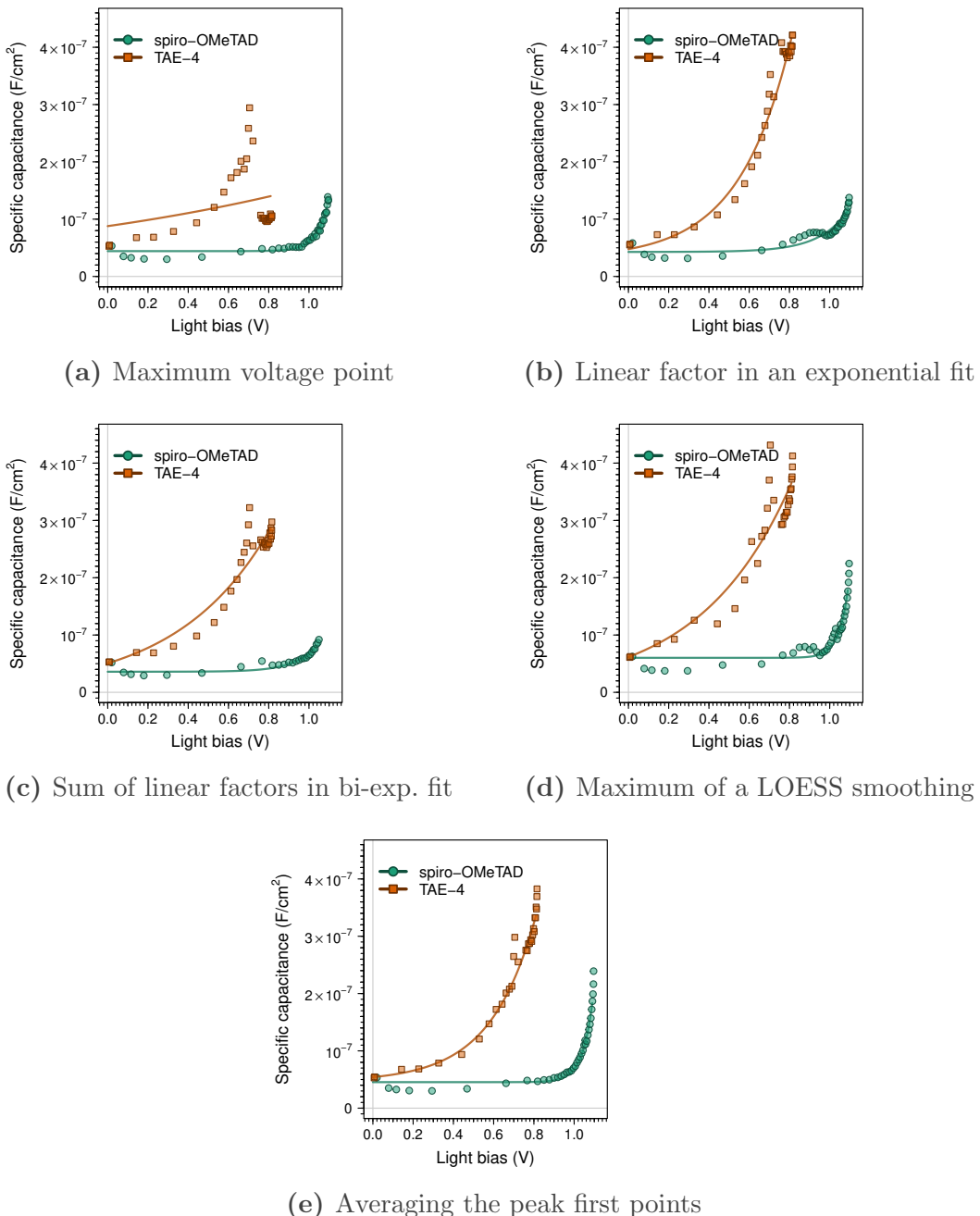


**Figure 3.25: Comparison of methods for obtaining DC experiments.** The capacitance obtained from DC experiment on FTO/d-TiO<sub>2</sub>/CsFAMAPbIBr/HTM/Au devices using different methods for extracting  $\Delta V$  value, as detailed in page 99.

is just the voltage derivative of eq. (3.13)) for fitting the capacitance:

$$C_{\text{DC}}(V) = C_g + \frac{qn_{\text{eq}}}{mk_B T} \cdot \exp\left(\frac{qV}{mk_B T}\right) \quad (3.25)$$

## 3.9 Voltage and Current Reconstruction

As a self consistency check for the photophysics techniques explained and for confirming that no important factor has been neglected, the performance parameters of the devices can be reconstructed from the fitted parameters from TPV, CE, and DC. The shown  $J_{SC}$  and  $V_{OC}$  reconstruction methods can be extended to obtain the whole current-voltage sweep [110].

3

**$J_{SC}$  reconstruction.** The recombination current  $J_{rec}$  can be described by the total carriers lifetime (or pseudo first order lifetime)  $\tau_{pfo}$  and by the excess charge  $n_{CE}$  with the following expression [64, 160]:  $J_{rec} = n_{CE}/\tau_{pfo}$ . At open circuit the photo-generated current has to match the recombination current (no external current means that these two, at least in steady state conditions, cancel out), so  $J_{rec} = J_{ph}$ . If losses at short circuit are negligible, photo-generated current can be approximated by the short circuit current  $J_{ph} \approx J_{SC}$  obtaining [107]:

$$J_{SC} = \frac{n_{CE}}{\tau_{pfo}} \quad (3.26)$$

**$V_{OC}$  reconstruction.** Expanding  $\tau_{pfo} = \Phi\tau$  with eq. (3.17) and neglecting the intrinsic charge density (consideration valid for non-dark cases) so that  $n_0 \approx n_{CE}$  we get:

$$J_{SC} = n_{CE} \cdot k n_{CE}^{\Phi-1} \quad (3.27)$$

Then considering just the chemical capacitance charge as relevant for recombination processes, so keeping just the exponential addend in eq. (3.13) we obtain:

$$J_{SC} = n_{eq}^\Phi k \exp\left(\frac{q\Phi V_{OC}}{mk_B T}\right) \quad (3.28)$$

again, we neglected  $-1$  from the additional intrinsic charge density. Then inverting the equation we obtain:

$$V_{OC} = \frac{mk_B T}{q\Phi} \ln\left(\frac{J_{SC}}{n_{eq}^\Phi k}\right) \quad (3.29)$$

The eq. (3.29) now contains just parameters which can be obtained from our photophysical measurements [64, 160, 208, 212].

## 3.10 Impedance Spectroscopy

*“One does not simply have a look at impedance spectroscopy data”*

Boromir

3

**Concept.** Impedance spectroscopy can be performed with easily available equipment: most of the electrochemical units used in the research labs for measuring cyclic voltammetry include this technique. An alternated voltage at frequency  $\nu = \omega/(2\pi)$  is applied to the two electrodes of the device and the resulting alternated current is observed in amplitude and phase. For an accurate phase estimation usually a lock-in amplifier is used. The in-phase component can be taken for calculating a resistance  $Z'(\nu)$  and the quadrature component for calculating the reactance  $Z''(\nu)$ . The sum of these two components give the complex impedance:  $Z(\nu) = Z'(\nu) + iZ''(\nu)$ . The voltage oscillation should be large enough for measuring a current profile without too much noise, usually amplitudes from 20 to 200 mV are employed. Repeating this on different alternating voltage frequencies, often from  $1 \times 10^{-2}$  to  $1 \times 10^7$  Hz, the spectra of impedance can be obtained. The impedance spectroscopy can be represented in various shapes: Nyquist plots where  $-Z''$  is plotted against  $Z'$ , Bode plots of phase,  $|Z|$ ,  $Z''$ , or  $Z'$  are plotted against the frequency  $\nu$  or, as a capacitance (or apparent capacitance, as we will see in chapter 6) defined as  $\omega^{-1} \operatorname{Im}(Z^{-1})$ .

**Frequency-domain.** The frequency-domain results should be related to the time-domain by the Fourier transform, so from frequency-domain techniques we should be able to extract the same information as from time-domain techniques, as the aforementioned ones (on this topic, see page 166). Nevertheless, frequency-domain techniques are more convenient for observing one by one all the different processes happening in a solar cell device, working at their characteristic frequency. On the other hand this also implies a much longer measurement, for which the device stability is paramount.

**Stability.** As the measurement of a complete impedance spectra is very time demanding, the device stability is of paramount importance. Moreover, degradation processes or stabilisation happening within the studied  $1/\nu$

time span (between hundreds of seconds and microseconds) will result in glitches which can be easily mistaken for interesting data [2, 99].

**Interpretation.** Due to the large amount of extracted data and the complex features usually observed when studying perovskite solar cells (e.g. multiple arcs in the Nyquist plot), the parameters extraction is usually done *via* fitting with an equivalent electrical circuit. A bad choice of the fitting circuit can doom the meaningfulness of the obtained information, so great care has to be taken in order to have a bijective relation between the circuit elements and the relevant physical processes.

# Chapter 4

## Comparison of HTMs in Bottom Cathode CsFAMAPbIBr Solar Cells

4

*“It’s so easy, can’t you see the shift?”*

**Publication.** Part of this chapter has been published in [3]: I. Gelmetti, N. F. Montcada, A. Pérez-Rodríguez, E. Barrena, C. Ocal, I. García-Benito, A. Molina-Ontoria, N. Martín, A. Vidal-Ferran, and E. Palomares. “Energy alignment and recombination in perovskite solar cells: weighted influence on the open circuit voltage”. In: *Energy & Environmental Science* 12.4 (2019), pp. 1309–1316. DOI: [10.1039/C9EE00528E](https://doi.org/10.1039/C9EE00528E).

**Abstract.** In this chapter, the well known spiro-OMeTAD, the previously reported TAE-1 and two novel molecules TAE-3 and TAE-4 were employed as HTM for fabricating perovskite solar cells. The lack of correlation between the molecules’ ionization potentials and the devices measured  $V_{OC}$  motivated us to deepen the investigation on the factors contributing to the cell voltage by means of transient optoelectronic techniques. We gained insight into the recombination process and the energy alignment at perovskite/HTM interface.

---

**Table of Contents**

---

**Introduction**

Design of the Experiment, 109 • Author contributions, 110

**Molecular Characterisation**

HOMO from cyclic voltammetry, 112 • Direct optical band gap, 112  
• LUMO and selectivity, 113 • Simulated energy levels, 113 • Other molecular characterisation, 114

**Thin Films Morphological Characterisation**

Atomic force microscopy, 114 • ESEM and EDX, 114 • X-Ray diffraction, 114

**Current-Voltage Sweeps**

Ideality Factor, 117

**Chemical Capacitance****Transient Lifetime****Work function of Stacked Materials****Conclusions**

---

## 4.1 Introduction

In perovskite solar cells, the absorber is usually sandwiched between two different contacts: the HTM and the ETM, with the role of extracting respectively the positive and negative free charges. Without this asymmetrical extraction of charges, the photogeneration would be of no use. The classical ETM from DSSC, mesoporous titania, is getting obsoleted by planar tin oxide [213]. On the contrary, the classical HTM from solid-state DSSC, spiro-OMeTAD, is still present in most of the record structures of CsFAMAPbIBr based solar cells [44, 214]. The huge explorative work done for finding a better performing HTM managed to find very few good alternatives [215]. Still, even if the performances are at par with spiro-OMeTAD, the commercial price of these alternative HTM is still too high for wide area applications. A better understanding of the HTM/perovskite interaction is needed for pinpointing the key characteristics to be looked for in the next HTM design. In this chapter, the devices fabricated using four different HTM have been compared in order to find a correlation with the HTM's chemical properties. Specifically we looked for the influence of the HTM on the device  $V_{OC}$ . For OSC, the correlation between the built-in voltage and the  $V_{OC}$  is well established [216–222]. For perovskite solar cells, some authors observed a weak correlation between the HTM ionization potential and the cell voltage [223–227] while others suggested a complex interplay of factors where the HTM HOMO just plays a marginal role [51, 56, 58, 61, 228, 229]. The tested HTM were: the classic spiro-OMeTAD (fig. 4.1a), the previously reported TAE-1 (CAS 1802982-22-4, fig. 4.1b, after the first report in [140], it has been used also by other research groups in [141, 227, 230, 231]) and two novel molecules: 3,3',6,6'-tetrakis[N,N-bis(4-methoxyphenyl)amino]-9,9'-bifluorenylidene (TAE-3, CAS 2055756-83-5, fig. 4.1c) and 3,3',6,6'-tetrakis(3,6-dimethoxy-9H-carbazol-9-yl)-9,9'-bifluorenylidene (TAE-4, fig. 4.1d).

**Design of the Experiment.** Differently from our previous report on TAE-1 [140], we decided to avoid the mesoporous titania layer decreasing the complexity of the stack. In order to compare different materials for the selective contact layer, we decided to avoid any modification to the layers underlying the absorber one in the solar cell stack, as these could heavily affect the perovskite crystallisation and morphology [232, 233]. Additionally, the HTM under comparison have been deposited under as similar as possible conditions (partially hindered by a different solubility),

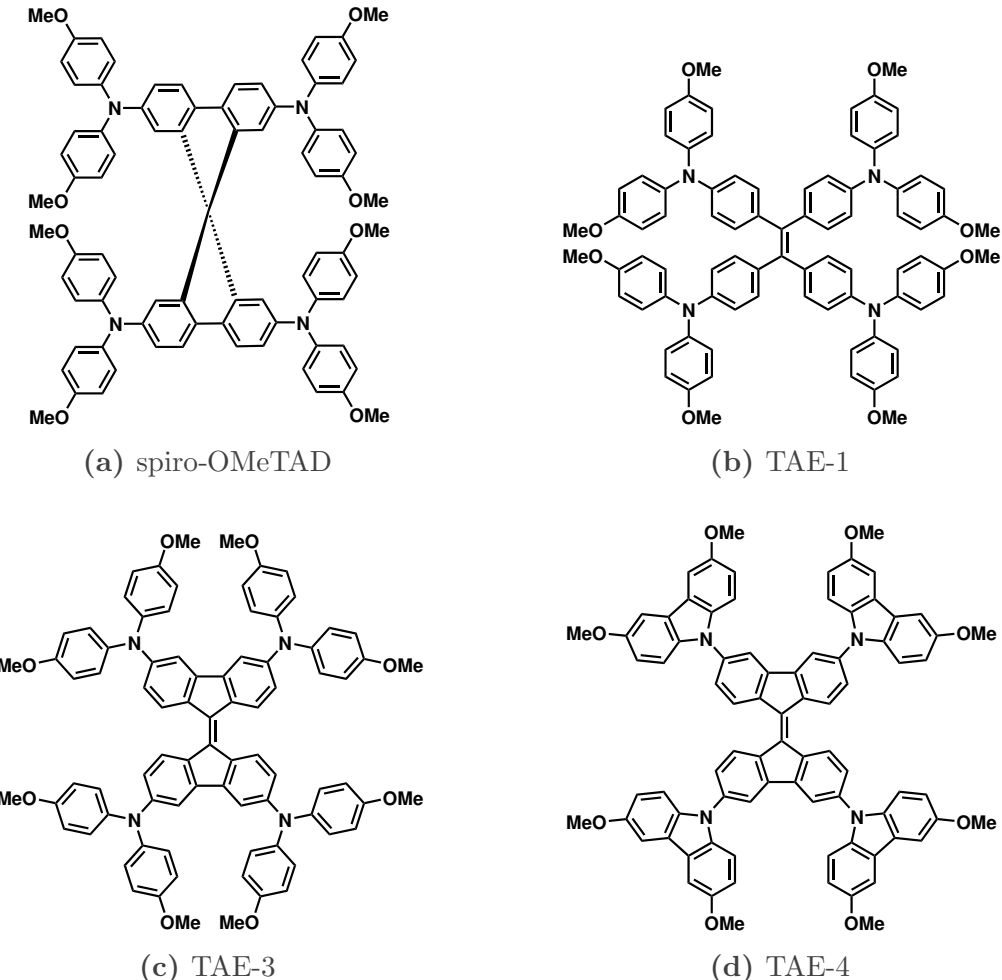


**Figure 4.1: Chemical structures of HTM utilised for bottom cathode solar cells.**

employing the same additives (with the same molar ratio with the HTM concentration, we used LiTFSI and 4-tert-butylpyridine) and thicknesses. For reducing the possible differences in DOS width, the chosen HTM have all very similar chemical structures.

**Author contributions.** The devices have been fabricated by me under the supervision of Dr. Nuria F. Montcada and Prof. Emilio J. Palomares Gil (fabrication described in pages 46 to 48). The current-voltage sweeps characterisation was performed by me and NFM. The transient electronic characterisation was performed and analysed by me using equipment

built by Dr. Javier Pérez Hernández. The electrochemical and optical characterisation (cyclic voltammetry, space charge limited current (SCLC), absorbance in solution, photoluminescence in solution) of the molecules was performed by NFM, Dr. Lydia Cabau, Dr. Agustín Molina Ontoria, and Dr. Inés García-Benito. These same co-authors calculated HOMO energies from cyclic voltammetry and hole mobilities from SCLC. Optical band gaps was calculated by me from absorbance in solution. Molecular simulations have been performed by Prof. Anton Vidal-Ferran. Dr. Agustín Molina Ontoria and Prof. Nazario Martín designed TAE-1, TAE-3, and TAE-4 molecules. The synthesis of these has been carried on by Dr. Inés García-Benito and reported in her PhD thesis [234] (there, TAE-3 is labelled as BF-1, and TAE-4 as BF-2) and in [3]. KPFM measurements has been performed and interpreted by Dr. Ana Pérez-Rodríguez, Dr. Esther Barrena, and Prof. Carmen Ocal at ICMAB-CSIC, UAB, Barcelona.

**Table 4.1: Molecular properties of tested HTM.** The values for spiro-OMeTAD and for TAE-1 were taken from our previous publication [140]. Hole mobilities  $\mu_h$  have been measured using SCLC fitted with Mott-Gurney law.  $E_{\text{onset}}^{\text{abs}}$  is the direct optical band gap obtained via Tauc plot.  $E_{\text{max}}^{\text{pl}}$  indicates the energy of the emission peak obtained exciting at 550 nm a solution of the molecule in THF.  $E_{\text{HOMO}}^{\text{exp}}$  is obtained from the cyclic voltammetry of the molecules dissolved in DCM and using ferrocene as reference.  $E_{\text{LUMO}}^{\text{exp}}$  is obtained adding the direct optical band gap  $E_{\text{onset}}^{\text{abs}}$  to  $E_{\text{HOMO}}^{\text{exp}}$  except for TAE-1 where the value from [140] has been taken.  $E_{\text{HOMO}}^{\text{sim}}$  and  $E_{\text{LUMO}}^{\text{sim}}$  have been obtained via a density functional theory (DFT) simulation.  $E_{\text{onset}}^{\text{sim,abs}}$  is the direct optical band gap obtained via Tauc plot of the absorbance simulated with time-dependent DFT.

HTM	$\mu_h$ $\text{cm}^2 \text{V}^{-1} \text{s}^{-1}$	$E_{\text{onset}}^{\text{abs}}$ eV	$E_{\text{max}}^{\text{pl}}$ eV	$E_{\text{HOMO}}^{\text{exp}}$ eV	$E_{\text{LUMO}}^{\text{exp}}$ eV	$E_{\text{HOMO}}^{\text{sim}}$ eV	$E_{\text{LUMO}}^{\text{sim}}$ eV	$E_{\text{onset}}^{\text{sim,abs}}$ eV
spiro-OMeTAD	$2.6 \times 10^{-4}$			-5.10	-2.09			
TAE-1	$5.9 \times 10^{-5}$	2.813		-5.32	-2.74	-5.61	-0.54	3.04
TAE-3	$8 \times 10^{-4}$	1.836	1.722	-5.00	-3.16	-5.54	-1.77	2.02
TAE-4	$7 \times 10^{-4}$	1.969	1.771	-5.53	-3.56	-6.14	-2.27	2.20

## 4.2 Molecular Characterisation

**HOMO from cyclic voltammetry.** The oxidation potential of each HTM has been measured via cyclic voltammetry in solution. Then the energy of HOMO, reported in table 4.1 and represented in fig. 4.2, has been obtained from the oxidation potential via the empirical linear relationship reported in D’Andrade *et al.* [235]. The obtained HOMO value is shallowest for TAE-3, then spiro-OMeTAD a bit above TAE-1 level, and finally TAE-4 being the deepest. Considering that these HTM gets doped by exposing the devices to dry air (see fabrication method in page 46, we did not add any chemical oxidiser, hopefully oxygen is enough for doping all the HTM even if their oxidation potential is quite variate), the Fermi level in these *p*-type materials should be rather close to the HOMO. The built-in voltage is defined in equilibrium as the Fermi level difference at the metallic electrodes in a complete device  $V_{\text{BI}} = (\bar{\mu}^{\text{cathode}} - \bar{\mu}^{\text{anode}})/q$  and can be approximated by the difference in Fermi levels of the isolated ETM (which is  $\text{TiO}_2$  in all cases) and HTM  $V_{\text{BI}} \approx (\bar{\mu}^{\text{ETM}} - \bar{\mu}^{\text{HTM}})/q$ . So, we expect the built-in voltage to follow the trend in  $\bar{\mu}^{\text{HTM}}$  and to be larger for the devices with TAE-4 and smallest for the TAE-3 ones. Please note that the value obtained from cyclic voltammetry in solution could be different from the HOMO energy in solid state film. This is expected to happen due to the different permittivity of the medium (e.g. the polarization of the surroundings can stabilise the cationic state), a different strain in solid state [236], intermolecular interactions [237], and an increased order [55]. Moreover, some chemical reactivity [105, 133], de-doping [132], or intermixing [139] could happen with the perovskite layer or the metallic electrode.

**Direct optical band gap.** We extracted the direct band gap value from the direct Tauc plot of the absorbance onset [238], an easy technique developed for crystalline and amorphous semiconductors [14] with delocalised orbitals but often employed also for small molecules. A closely related value can be obtained from the photoluminescence peak maximum, which is also reported in table 4.1 (but should not be used for estimating the band gap as the emission could happen from localised states with different energetics). The shape of the absorbance onset of an HTM, additionally to provide information on its optical band gap, can reveal the presence of mid-gap states (observable as an exponential Urbach tail) which would favour the surface recombination [171].

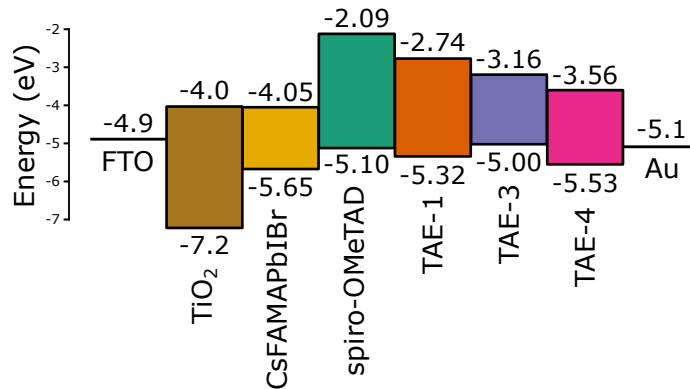


**Figure 4.2:** Representation of HOMO and LUMO energies for the materials composing the studied cells. The HOMO energy has been estimated from the oxidation potential obtained via cyclic voltammetry and the direct optical band gap from a Tauc plot, as described in the text.

**LUMO and selectivity.** The optical band gap has been employed for obtaining the LUMO values reported in table 4.1 and represented in fig. 4.2. The selectivity of HTM has been reported to be key for perovskite solar cells' Voc [23]. The often neglected position of the HTM LUMO has been reported to be relevant for the injection of hot electrons, thus favouring their recombination in a recent preprint by Jiménez-López et al. [29] and in Droseros et al. [30].

**Simulated energy levels.** The details of the molecular simulation are reported in the supplementary information of [3], shortly: geometry and energy levels of the fundamental state were obtained with DFT performed including the solvent effect via Polarizable Continuum Model simulating the presence of surrounding tetrahydrofuran; then a time dependent DFT using hybrid exchange–correlation functional (CAM-B3LYP) allowed us to obtain the absorption spectrum. As can be seen in table 4.1, the DFT simulated  $E_{\text{HOMO}}^{\text{sim}}$  manages to reproduce the trend of the experimental  $E_{\text{HOMO}}^{\text{exp}}$ , being the TAE-3 the shallowest and TAE-4 the deepest. Contrariwise, the simulated  $E_{\text{LUMO}}^{\text{sim}}$  values are rather distant from the experimental  $E_{\text{LUMO}}^{\text{exp}}$  ones, even if the trend is correctly reproduced. This can be understood considering that the  $E_{\text{LUMO}}^{\text{sim}}$  is simulated on top of the non-excited molecule, which is the molecule with a fully occupied HOMO level. This situation does not properly describe the final point of an excitation transition, where the HOMO is not full as one electron have been promoted to LUMO. The energetic difference between the two described configurations is an electron-hole interaction energy, which is the origin of the exciton binding energy described in page 19. The experimental

direct optical band gap  $E_{\text{onset}}^{\text{abs}}$  can be fairly compared with the value  $E_{\text{onset}}^{\text{sim,abs}}$  obtained from the onset of absorption spectra simulated with time-dependent DFT.

**Other molecular characterisation.** In the supplementary information of [3], the full data of: space charge limited current, hydrogen and carbon nuclear magnetic resonance, thermo gravimetric analysis, differential scanning calorimetry, high resolution mass via MALDI-TOF spectrometry, cyclic voltammetry, infrared spectroscopy, elemental analysis, absorbance and photoluminescence in solution.

## 4.3 Thin Films Morphological Characterisation

4

**Atomic force microscopy.** In order to verify that the various HTM gave an homogeneous coverage of the underlying layer, we performed alternated current AFM. As can be seen in fig. 4.3, all the layers have irregularities but seems that the coverage is complete. TAE-4 surface is the most rough one, showing grains which could represent some degree of crystallisation.

**ESEM and EDX.** The elemental analysis of the small features observed in spiro-OMeTAD in fig. 4.3a were further studied with ESEM-EDX, resulting in a composition no significantly different from the rest of the surface, data in the supplementary information of [3]. In order to further assuring the complete coverage of the perovskite by the tested HTM, a cross section image has been taken for each device kind and reported in the supplementary information of [3].

**X-Ray diffraction.** For excluding degradation of the CsFAMAPbIBr layer due to the contact with the HTM we performed an XRD analysis of complete devices aged for 8 months in a nitrogen filled glovebox. The usage of a collimator allowed us to observe the diffraction pattern in regions not covered by the gold top electrode. The diffraction patterns are shown in fig. 4.4 and no difference can be observed between the pristine and the covered perovskite layers structure. Due to the penetration of the beam, also the peaks from FTO and the bump from the glass are observed. The patterns perfectly match the reference Cs5 pattern from Saliba *et al.* [214].

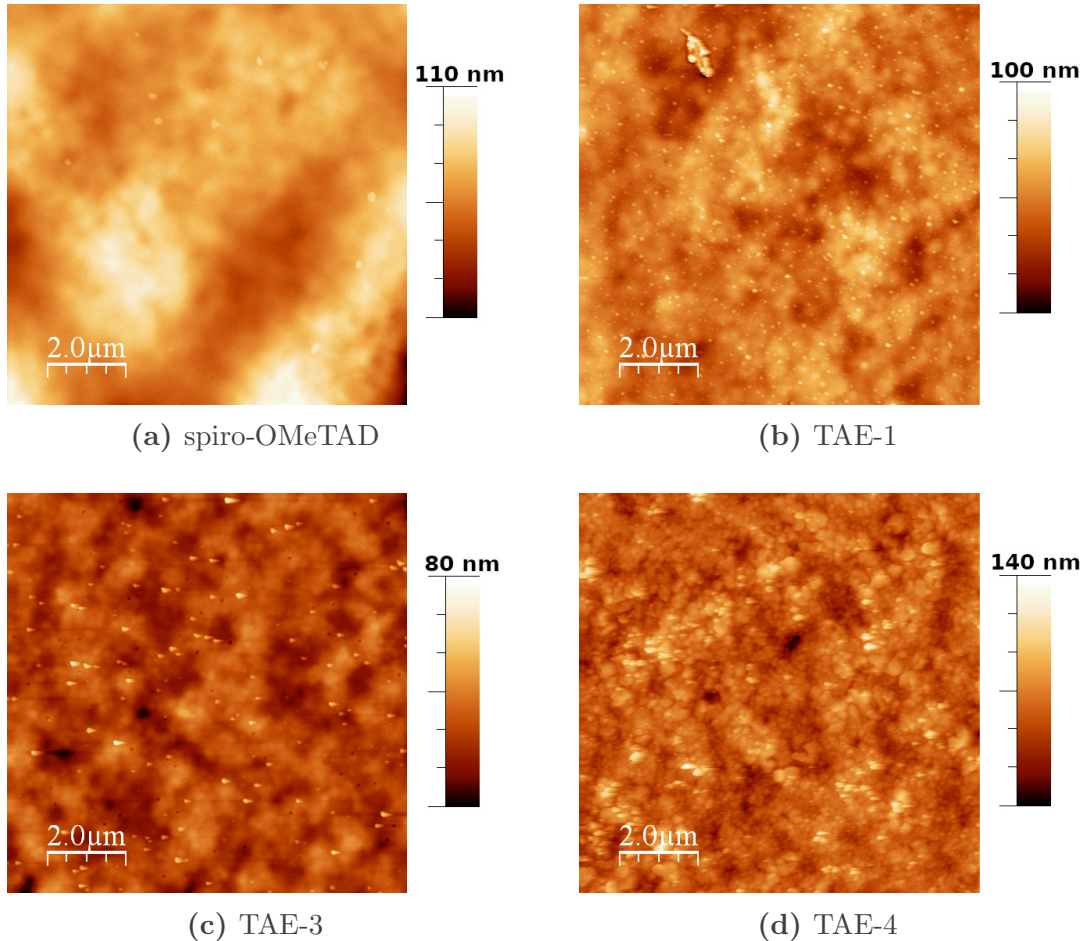


**Figure 4.3: Topography of HTM layered on top of perovskite, measured via AFM.** Morphology of the surface of different HTM deposited via spin coating on top of CsFAMAPbIBr perovskite layers. Larger scale images and phase data can be found in the supplementary information of [3].

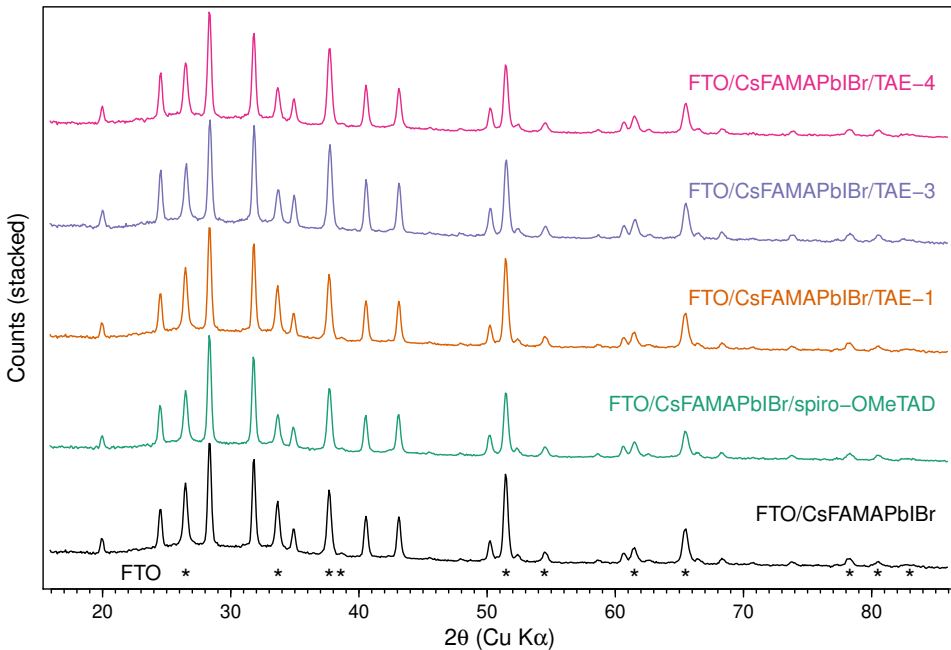


**Figure 4.4: X–Ray diffraction pattern for complete devices with different HTM.** All of the patterns matches perfectly the Cs5 reference from Saliba et al. [214]. Both the amorphous HTM and the thin TiO<sub>2</sub> layers are not observable. The gold peaks are not present as the usage of a beam collimator allowe us to avoid gold covered regions. The peaks marked with \* are assigned to FTO, it can be compared with the reference PDF No. 00-003-1114 of SnO<sub>2</sub>.

## 4.4 Current-Voltage Sweeps

As can be seen in table 4.2, the most significant differences in the performances of devices when changing HTM are observed in the  $V_{OC}$ . Spiro-OMeTAD allowed the devices to achieve the highest  $V_{OC}$ , while TAE-3 and TAE-4 gave the lowest voltages. Some minor correlation can also be observed in the other parameters, with spiro-OMeTAD and TAE-3 giving both slightly higher  $J_{SC}$  and FF. For all the measured solar cells, some hysteresis is observed in the  $V_{OC}$  and FF. Sweeps at different speeds are reported in the supplementary information of [3].

**Ideality Factor.** From  $V_{OC}$  versus light intensity we obtained the ideality factor, following the procedure described in page 63. The data is reported in [3]. The obtained values are 1.57 for spiro-OMeTAD, 1.44 for TAE-1,

**Table 4.2: HTM and related average performances of bottom cathode cells.** Tested HTM with *average* forward and reverse J-V sweep performances. The standard deviation for each value is indicated after the  $\pm$  symbol. For each reported result, at least 85, 23, 29 and 21 devices were averaged respectively for spiro-OMeTAD, TAE-1, TAE-3, and TAE-4 containing solar cells. The measurement conditions were 1 sun illumination, one minute light soaking,  $0.6 \text{ V s}^{-1}$  sweep speed. A boxplot representation of this data can be found in the supplementary information of Gelmetti *et al.* [3]. J-V curve for record devices are reported in fig. 4.5.

HTM	Sweep /	J-V sweep parameters			
		$J_{SC}$ $\text{mA cm}^{-2}$	$V_{OC}$ V	FF %	PCE %
spiro-OMeTAD	fwd	$21.2 \pm 1.6$	$0.97 \pm 0.05$	$60 \pm 9$	$12.4 \pm 2.4$
	rev	$21.4 \pm 1.6$	$1.07 \pm 0.06$	$68 \pm 11$	$15.6 \pm 3.1$
TAE-1	fwd	$20.1 \pm 0.9$	$0.91 \pm 0.05$	$50 \pm 10$	$9.2 \pm 1.6$
	rev	$20.2 \pm 0.9$	$0.98 \pm 0.03$	$60 \pm 10$	$11.9 \pm 2.1$
TAE-3	fwd	$22.4 \pm 2.0$	$0.76 \pm 0.02$	$63 \pm 5$	$10.7 \pm 0.9$
	rev	$22.5 \pm 1.9$	$0.89 \pm 0.04$	$71 \pm 6$	$14.1 \pm 1.4$
TAE-4	fwd	$21.0 \pm 1.9$	$0.81 \pm 0.03$	$54 \pm 10$	$9.3 \pm 2.5$
	rev	$21.0 \pm 1.8$	$0.90 \pm 0.05$	$61 \pm 9$	$11.6 \pm 2.8$

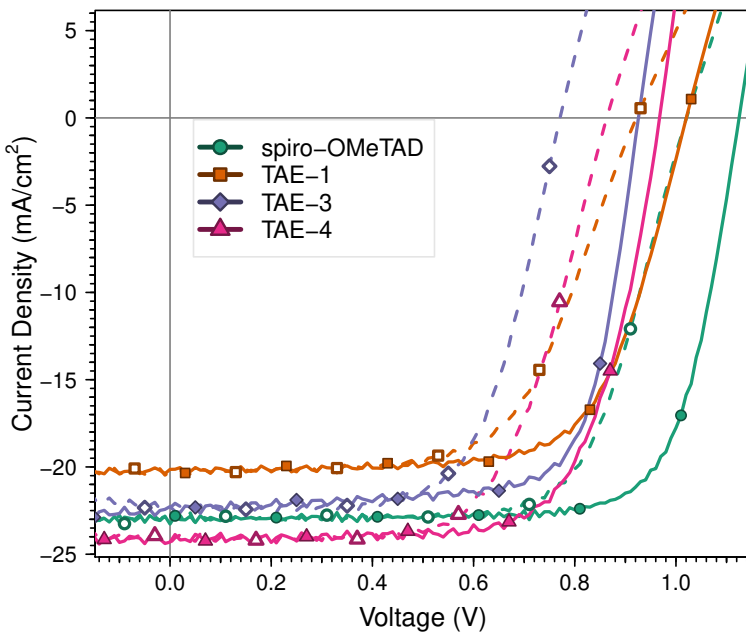


**Figure 4.5:**  
Current-voltage sweeps for champion devices with different HTM. The solid line with filled markers represents the forward scan, while the dashed line with hollow markers represents the reverse scan.

1.79 for TAE-3, and 1.83 for TAE-4. This data can be used for having some information on the trap level position inside band gap and on the Fermi level of the HTM [28]. With some caution (we employed the classical method, not the improved one described in page 64) we can state that trap levels close to the mid gap are present for all of the studied HTM.

## 4.5 Chemical Capacitance

Thanks to the very short measurement window ( $10\ \mu\text{s}$ ) we believe that no ionic displacement current (see page 13 and page 69) is included in our CE experiments. It is interesting to compare the light bias value (open circuit voltage originated by a light intensity) at which the chemical capacitance (exponential addend to the charge versus light bias relation, see page 73) gets relevant for the total charge. This growth of the chemical capacitance indicates that the quasi-Fermi levels splitting in the perovskite is approaching the built-in voltage of the device (see page 76) and can be used for estimating it. Both CE and DC show that the chemical capacitance gets relevant at lower light biasses for TAE-4, then TAE-3, TAE-1 and finally at high light bias for spiro-OMeTAD. This ordering corresponds to the one observed for the HOMO energies except for the TAE-3 case. The incoherence of the results from CE and DC for the TAE-4

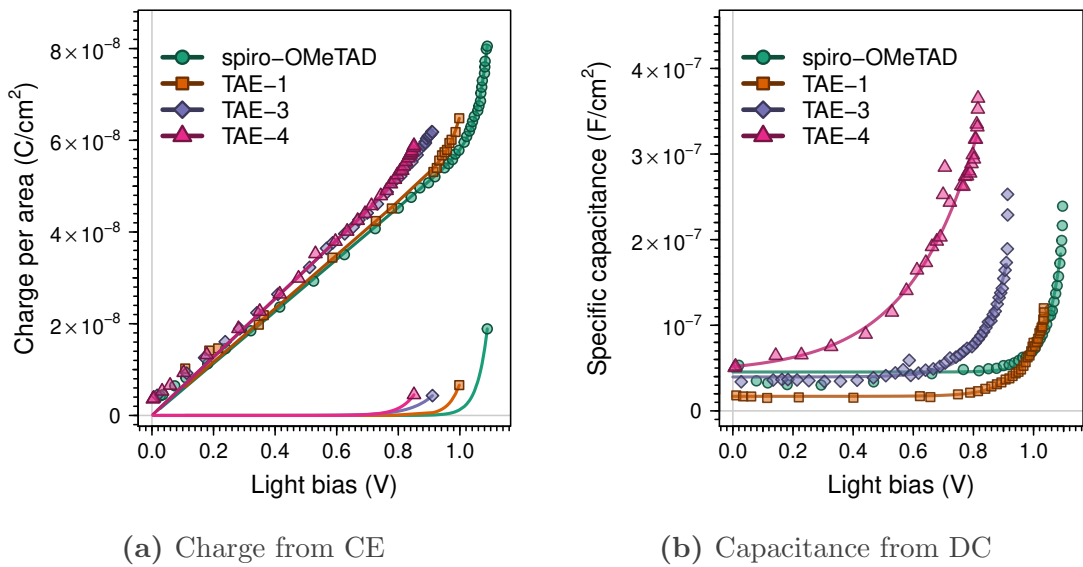


**Figure 4.6: CE and DC of devices with different HTM, highlighting the varying chemical capacitance.** In (a) the charge versus light bias as obtained from CE is reported. The dark solid line is an exponential fitting following eq. (3.13) while the light solid line is just its exponential part, ignoring the geometric capacitance. In (b) the capacitance dependence on light bias is reported as obtained from DC. The solid line indicates the fitting using eq. (3.25).

device have been confirmed on another device (not shown). Currently no explanation is available for explaining the deviation happening just when using this HTM.

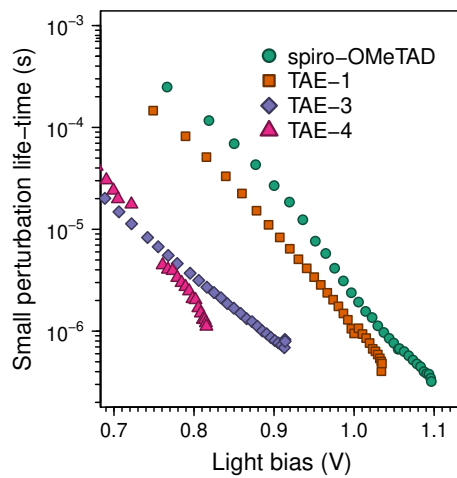
## 4.6 Transient Lifetime

As can be seen in fig. 4.7a, the small perturbation lifetimes at 1 sun illumination (for each device, the point at bottom right in the series) does not differ by much: from 0.3  $\mu s$  for spiro-OMeTAD to 1.1  $\mu s$  for TAE-4. This is exactly opposed to the expected trend, where spiro-OMeTAD giving the best performances should have shown the longest (small perturbation) lifetimes at 1 sun which would mean less recombination. A much more meaningful result can be obtained referencing the small perturbation lifetimes obtained from TPV to the chemical charge concentration (the charge stored in the perovskite layer, estimated from the exponential parts of fig. 4.6), and correcting the resulting data with the recombination order,

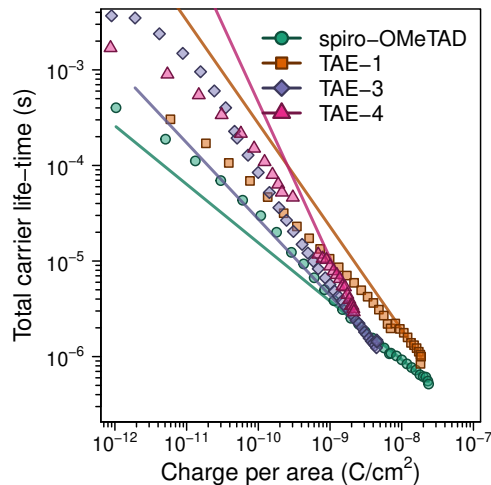
**Table 4.3: Parameters fitted from TPV, TPV-CE, and TPV-DC data, from devices with different HTM.** The experimental data reported in fig. 4.7 has been fitted using eq. (3.20) for TPV data (using a  $T$  of  $300\text{ }^\circ\text{C}$ ) and eq. (3.21) for TPV-CE and TPV-DC data.

HTM	TPV		TPV-CE			TPV-DC		
	$v$	-	$k$ $\text{s}^{-1}\text{ cm}^{2\Phi - 2}$	$\tau_0$ s	$\Phi$ -	$k$ $\text{s}^{-1}\text{ cm}^{2\Phi - 2}$	$\tau_0$ s	$\Phi$ -
spiro-OMeTAD	2.1		$9.0 \times 10^{-2}$	$1.6 \times 10^3$	1.7	$1.3 \times 10^{-9}$	$2.4 \times 10^3$	2.4
TAE-1	1.7		$1.2 \times 10^{-6}$	$4.3 \times 10^7$	2.1	$4.9 \times 10^{-21}$	$7.1 \times 10^7$	3.5
TAE-3	2.6		$3.4 \times 10^{-3}$	$3.5 \times 10^{-2}$	1.8	$5.2 \times 10^{-7}$	$4.1 \times 10^{-2}$	2.1
TAE-4	1.2		$9.5 \times 10^{-12}$	$3.7 \times 10^6$	2.6	$2.9 \times 10^{-81}$	$4.6 \times 10^6$	8.4

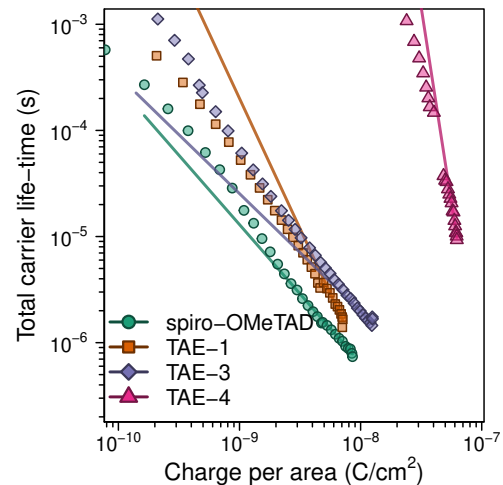
as explained in page 92. This way, the data points get closer indicating very similar recombination rates at the same excess chemical charge density (vertical comparison in fig. 4.7c data) being present for all the cases which thus are of no help for explaining the observed  $V_{OC}$  differences. The difference in lifetimes in TAE-4 devices when referencing to CE or DC is due to the large incoherence of CE or DC for this device, as shown in fig. 4.6.



(a) Mono-exponential lifetime from TPV



(b) Lifetime vs CE chemical charge



(c) Lifetime vs DC chemical charge

**Figure 4.7: Total carrier lifetime for devices with different HTM.** Four devices differing just for the employed HTM material has been compared by means of transient photophysical techniques. In (a) the plain TPV (small perturbation lifetime versus light-bias) is reported. In (b) the lifetime is plotted versus the exponential part of the charge from CE reported in fig. 4.6a and corrected using eq. (3.21) with the recombination order obtained from the power-law fit of the same graph. In (c) the lifetime is plotted versus the chemical charge from DC obtained subtracting the constant geometric capacitance from the data reported in fig. 4.6b and integrating it. The lifetime was corrected using eq. (3.21) with the recombination order obtained from the power-law fit of the same graph.

## 4.7 Work function of Stacked Materials

Further characterisation of the workfunction of the HTM surface when layered on top of FTO or  $\text{TiO}_2$  or CsFAMAPbIBr has been performed using KPFM. The measured contact potential difference (CPD) allowed us to study the impact the underlying perovskite layer can have on the HTM material. Perovskite Fermi level can depend on the underlying material workfunction [239, 240]. In our case, the different values between the FTO/ $\text{TiO}_2$  and the FTO/ $\text{TiO}_2$ /CsFAMAPbIBr surface workfunctions indicates that perovskite Fermi level is not pinned to the underlying layers. The value we observed for the CsFAMAPbIBr surface work function matches the reported one for  $\text{MAPbI}_3$  deposited on  $\text{TiO}_2$  [239]. Values for HTM on top of FTO/ $\text{TiO}_2$  have little deviations from the value for the uncovered substrate, with the exception of TAE-3. In the same way, the values measured for the organic layers deposited on top of FTO/ $\text{TiO}_2$ -/CsFAMAPbIBr are close to the value for the uncovered perovskite layer, also here with the exception of TAE-3. These measurements have been discussed in Dr. Ana Pérez-Rodríguez PhD thesis [241]. Within the rigid band model, the observation of such a large deviation for TAE-3 indicates that the equilibrium Fermi level of the substrate is out of the HTM band gap. This is expected to cause a strong interfacial dipole (identifiable as depletion layers) and a consequent vacuum level shift.

**Table 4.4: Work function of different HTM when deposited on perovskite.** The work function in eV is reported for the surface of different HTM either deposited on top of

Substrate	Substrate work function	Work function difference on top of spiro-OMeTAD	TAE-1	TAE-3	TAE-4
FTO/ $\text{TiO}_2$	4.81	+0.10	+0.04	+0.19	+0.11
FTO/ $\text{TiO}_2$ -/CsFAMAPbIBr	4.04	+0.04	-0.04	+0.20	+0.05

## 4.8 Conclusions

Comparing the  $V_{OC}$  obtained from solar cells having different HTM with the HOMO values of these, we noticed a discrepancy. For understanding the origin of this incoherence, the electronic band gap was measured using CE and DC, which was in accordance with the observed  $V_{OC}$  with exception of the inversion of TAE-3 and TAE-4 molecules order. This data indicates that the HOMO value measured in solution *via* cyclic voltammetry is quite different from the actual energy levels for the molecules in solid thin film. The analysis of the total carrier lifetimes using TPV referenced to chemical charge, has shown that the recombination rates at the same excess charge density are in the same order of magnitude regardless the employed HTM. The measurement of the work function of the HTM when layered on perovskite has shown the formation of a large dipole at the perovskite/HTM interface mainly for the TAE-3 case. This shift in the vacuum level could be the cause for the lower  $V_{OC}$  measured using this HTM and justify the incoherence with the observed electronic band gap in CE and DC.



# Chapter 5

## Insights into Charge Storage via Thickness Variation of Layers in Top Cathode MAPI Solar Cells

*“Let’s change as little as possible”*

5

**Publication.** Part of this chapter has been published in [1]: I. Gelmetti, L. Cabau, N. F. Montcada, and E. Palomares. “Selective Organic Contacts for Methyl Ammonium Lead Iodide (MAPI) Perovskite Solar Cells: Influence of Layer Thickness on Carriers Extraction and Carriers Lifetime”. In: *ACS Applied Materials & Interfaces* 9.26 (July 2017), pp. 21599–21605. DOI: [10.1021/acsami.7b06638](https://doi.org/10.1021/acsami.7b06638).

**Abstract.** All-organic contacts, solution processed, top cathode, two step perovskite deposition ITO/PEDOT:PSS/MAPbI<sub>3</sub>/PC<sub>70</sub>BM/Ag devices were fabricated and studied by means of current-voltage sweeps, CE, and DC. Small variations in each layer thickness were introduced, so that we could compare the effect of this change on the resulting device characteristics. Characterization via current-voltage sweeps and photophysical techniques allowed us to study the charge distribution in these devices. Specifically, we have measured devices’ capacitance under

illumination using photo-induced time resolved techniques and obtained indications about holes and electrons storage location.

---

**Table of Contents**

---

**Introduction**

Design of the Experiment, 128 • Author contributions, 128

**Varying MAPbI<sub>3</sub> Thickness (Absorber)**

Roughness and grain size, 129 • Current-voltage sweeps, 130 • Geometric capacitance from DC and CE, 132

**Varying PC<sub>70</sub>BM Thickness (ETM)**

Current-voltage sweeps, 134 • Geometric capacitance from DC and CE, 135

**Varying PEDOT:PSS Thickness (HTM)**

Current-voltage sweeps, 137 • Geometric capacitance from DC and CE, 137

**Conclusions**

---

## 5.1 Introduction

Many top cathode ITO/PEDOT:PSS/MAPbI<sub>3</sub>/PC<sub>70</sub>BM/Ag perovskite solar cells have been fabricated. The thickness of each of PEDOT:PSS (HTM), MAPbI<sub>3</sub> (absorber), and PC<sub>70</sub>BM (ETM) has been independently varied. All these layers were deposited by spin coating and the thickness was tuned via spin coating speed. These parameters where chosen so that their variation affect as little as possible the rest of the solar cell stack, so that we can unequivocally relate the observations to the changes. The champion device performances of each configuration are listed in table 5.1.

**Design of the Experiment.** Perovskite synthesis is a very easy and fragile process at the same time. When varying a fabrication parameter, for example during an optimization, it is quite likely to provoke a “butterfly effect” with the resulting device differing from the reference by much more than the characteristic under study. A principal component analysis of the fabrication parameters would be needed for a rational optimization, but such a complex procedure is further hindered by the difficulty of identifying all relevant contributions. In this study we vary a set of parameters that hopefully have a foreseeable relation with the resulting device structure: thickness of each layer, through the tuning of the spin coating deposition speed. This variation should just affect the thickness of one layer, having just a minor influence on the other layers and the rest of the device physical features. This will allow us to univocally relate the observations to the modifications.

**Author contributions.** The devices were fabricated and characterised by me under the supervision of Dr. Nuria F. Montcada, Dr. Lydia Cabau, and Prof. Emilio J. Palomares Gil (fabrication described in pages 43 to 46). The data was analysed by me and Dr. Nuria F. Montcada. The experiment was designed and the data interpreted by me, Dr. Nuria F. Montcada, and Prof. Emilio J. Palomares Gil.

## 5.2 Varying MAPbI<sub>3</sub> Thickness (Absorber)

**Roughness and grain size.** Using different spin coating speeds, devices with various MAPbI<sub>3</sub> thicknesses were obtained, as detailed in table 2.2. As a consequence to the different deposition conditions, the MAPbI<sub>3</sub> surface is more rough for the thick device than for the thin one, as can be intuited looking at ESEM image in fig. 5.1. Any way, measuring the roughness average with a profilometer, it resulted to be <10 nm for all the cases, so the 40 nm PC<sub>70</sub>BM layer should be enough for an homogeneous coverage. From the same ESEM image, we can measure the grain lateral size, which is not significantly different for the six observed samples (two per each MAPbI<sub>3</sub> thickness, data detailed in fig. 5.1 caption).

**Table 5.1: Layers thicknesses and related average performances of top cathode cells.** Explored thicknesses with *average* forward and reverse J-V sweep performances. The standard deviation for each value is indicated after the  $\pm$  symbol. For each reported result, at least 8, 8, and 4 devices were averaged respectively for MAPbI<sub>3</sub>, PC<sub>70</sub>BM, and PEDOT:PSS thickness exploration. ETM column indicates the PC<sub>70</sub>BM thickness, while HTM one refers to PEDOT:PSS thickness. The measurement conditions were 1 sun illumination, no light soaking, 1 V s<sup>-1</sup> sweep speed. A boxplot representation of this data can be found in Gelmetti *et al.* [1]. J-V curve for record devices are reported in figs. 5.2, 5.4 and 5.6.

Layers thickness			J-V sweep parameters				
MAPbI <sub>3</sub> nm	ETM nm	HTM nm	Sweep -	J <sub>SC</sub> mA cm <sup>-2</sup>	V <sub>OC</sub> V	FF %	PCE %
230	40	65	fwd	13.5 $\pm$ 0.5	1.03 $\pm$ 0.01	53 $\pm$ 3	7.3 $\pm$ 0.4
			rev	13.6 $\pm$ 0.5	1.02 $\pm$ 0.01	55 $\pm$ 3	7.7 $\pm$ 0.5
			fwd	13.9 $\pm$ 0.3	1.04 $\pm$ 0.01	57 $\pm$ 5	8.2 $\pm$ 0.6
			rev	14.1 $\pm$ 0.3	1.04 $\pm$ 0.01	55 $\pm$ 4	8.1 $\pm$ 0.5
440			fwd	16.3 $\pm$ 2.1	1.01 $\pm$ 0.04	58 $\pm$ 2	9.5 $\pm$ 0.8
			rev	16.5 $\pm$ 1.9	0.98 $\pm$ 0.07	50 $\pm$ 5	8.1 $\pm$ 1.4

continues...

... continues

MAPbI <sub>3</sub>	ETM	HTM	Sweep	J <sub>SC</sub>	V <sub>OC</sub>	FF	PCE
350	40	65	fwd	16.4 ±2.2	0.93 ±0.06	48 ±8	7.4 ±1.8
			rev	16.1 ±2.1	0.95 ±0.06	50 ±5	7.6 ±1.4
			fwd	13.2 ±1.1	0.99 ±0.04	47 ±6	6.2 ±1.1
			rev	12.8 ±0.7	0.98 ±0.05	47 ±5	5.9 ±0.8
	90	65	fwd	11.1 ±0.6	1.03 ±0.03	42 ±2	4.8 ±0.6
			rev	11.1 ±0.8	1.00 ±0.04	44 ±2	4.8 ±0.5
			fwd	7.7 ±1.6	1.02 ±0.04	18 ±2	1.4 ±0.4
			rev	7.6 ±1.6	1.01 ±0.04	18 ±2	1.4 ±0.4
	120	27	fwd	12.3 ±1.5	1.04 ±0.03	55 ±9	6.9 ±0.8
			rev	11.9 ±1.7	1.03 ±0.04	54 ±11	6.6 ±0.7
		45	fwd	12.2 ±1.7	1.04 ±0.01	58 ±4	7.3 ±1.2
			rev	11.8 ±1.7	1.00 ±0.09	53 ±7	6.2 ±0.9
		65	fwd	12.4 ±1.6	1.04 ±0.02	60 ±3	7.7 ±0.6
			rev	12.6 ±1.4	1.00 ±0.10	60 ±4	7.5 ±0.4

**Current-voltage sweeps.** In fig. 5.2 we can observe the current-voltage sweeps of the champion devices while in table 5.1 the averages and standard deviations are reported. The FF is not significantly different for the devices with different MAPbI<sub>3</sub> layer thickness. The only observable difference is the presence of a higher hysteresis (difference between forward and reverse scan) in this parameter for the thicker MAPbI<sub>3</sub> case. This could indicate a small change in the perovskite/PC<sub>70</sub>BM interface or just a change in the hysteresis characteristic time due to the increased ionic resistance in the thicker MAPbI<sub>3</sub> layer. Regarding the V<sub>OC</sub>, this value also

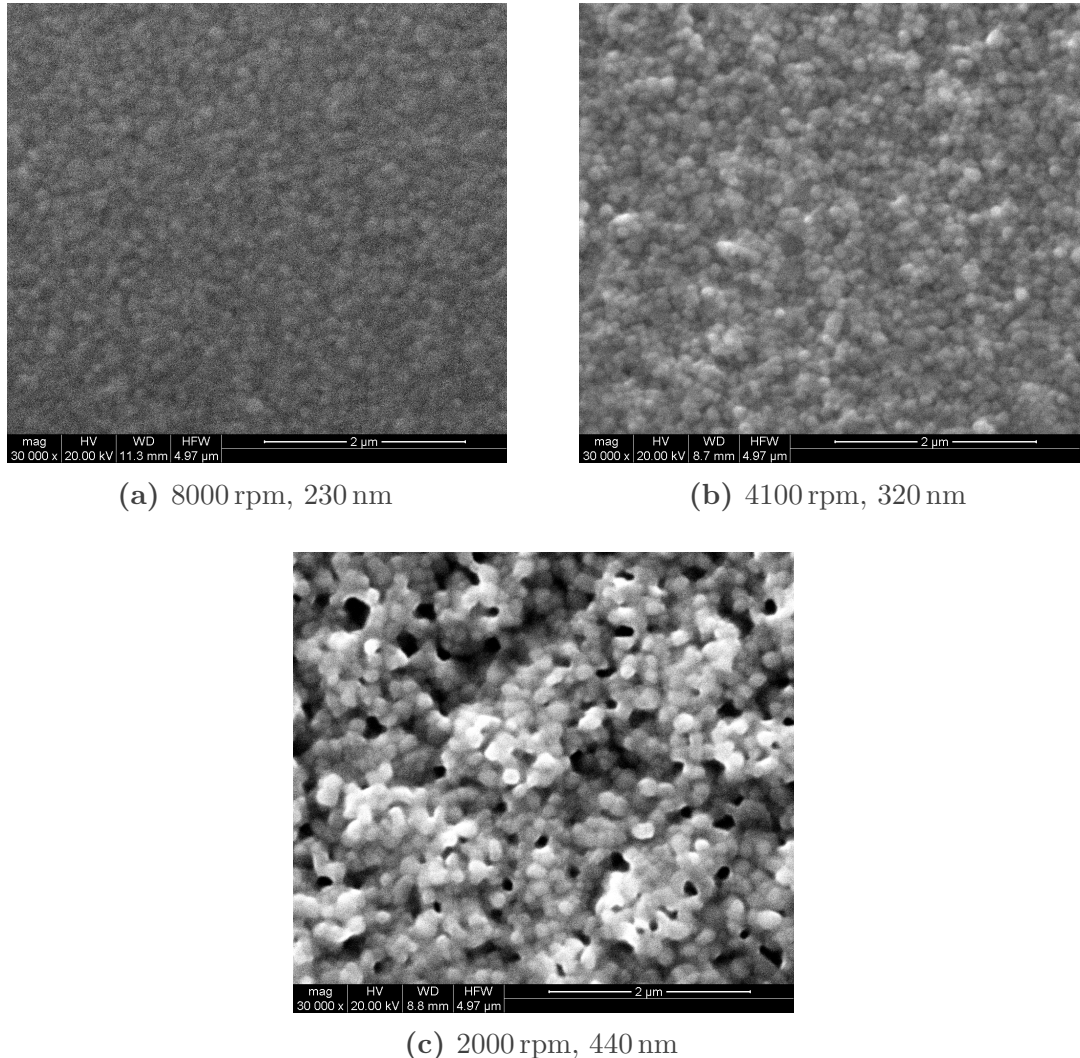


**Figure 5.1: Top view ESEM images of annealed perovskite layers with various thicknesses.** The surface of a thin perovskite layer is studied using FIJI/ImageJ [242] on images of two different devices for each deposition condition (just one reported here for brevity). The average domain diameter (and its standard deviation) is 182(25) nm for the thin 230 nm perovskite layer in (a), 190(34) nm for the medium 320 nm perovskite layer in (b), 189(23) nm for the thick 440 nm perovskite layer in (c).

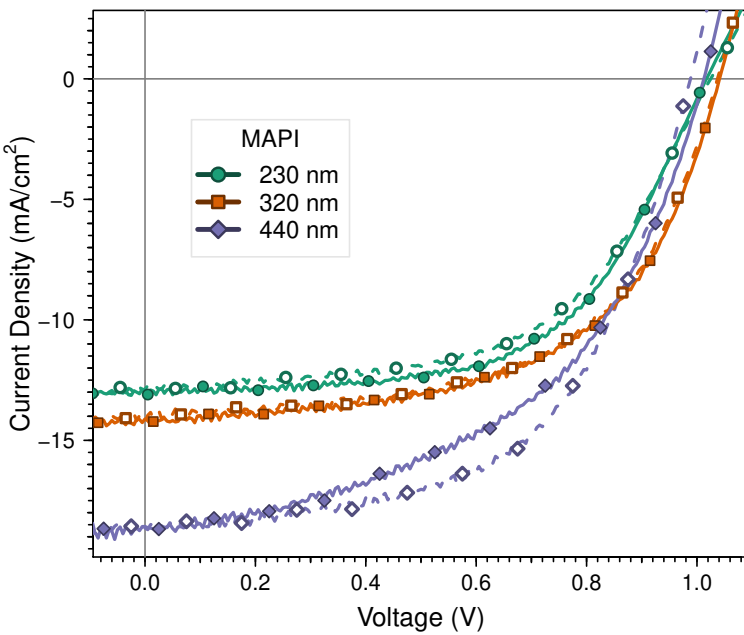


**Figure 5.2:**  
Current-voltage sweeps for champion devices with different MAPI thicknesses.  
The solid line with filled markers represents the forward scan, while the dashed line with hollow markers represents the reverse scan.

did not change with thickness, indicating that the same recombination processes and dynamics are present disregarding the absorber thickness. The higher deviation of this parameter for the thicker perovskite could be due to its higher roughness, causing some devices to have pinholes in the ETM layer. What is clear and expected is the  $J_{SC}$  increase. This is most likely due to the low EQE in the thin perovskite layer due to its far-from-zero transmittance. The increase in photogeneration rate is reflected in an increase of PCE.

**Geometric capacitance from DC and CE.** From the low and mid background light capacitance obtained from DC in fig. 5.3b and from the linear part of CE in fig. 5.3a we can obtain a geometric capacitance  $C_g$ , as explained in chapter 3. This capacitance arises from the accumulation of charges in the selective contacts' depletion layers, considering this as a parallel plates capacitor it is easy to foresee that the increase of  $\text{MAPbI}_3$  layer will increase the distance between the “plates” and cause a decrease in the capacitance. Please note that this is valid just if the CE is integrated over short times, so that the ionic displacement is negligible. Otherwise, as explained in page 76, the measured geometric capacitance would regard charges (ionic and electronic) accumulating on the two sides of each perovskite/contact interface (a junction capacitance rather than a

**Table 5.2:** Parameters fitted from CE and DC data, from devices with different layers' thicknesses. The experimental data reported in figs. 5.3, 5.5 and 5.7 has been fitted using eq. (3.13) for CE data and eq. (3.25) for DC data.

Layers thickness			CE			DC		
MAPbI <sub>3</sub> nm	ETM nm	HTM nm	$C_g$ nF cm <sup>-2</sup>	$n_{eq}$ C cm <sup>-2</sup>	$m$ -	$C_g$ nF cm <sup>-2</sup>	$n_{eq}$ C cm <sup>-2</sup>	$m$ -
230	40	65	85	$5.1 \times 10^{-21}$	1.4	64	$2.8 \times 10^{-12}$	4.4
320			78	$4.8 \times 10^{-27}$	0.97	55	$9.0 \times 10^{-13}$	4.1
440			71	$1.2 \times 10^{-27}$	0.91	50	$8.7 \times 10^{-15}$	2.6
350	40	65	76	$2.6 \times 10^{-20}$	1.4	55	$7.9 \times 10^{-15}$	2.5
			61	$9.0 \times 10^{-25}$	1.1	43	$9.3 \times 10^{-13}$	3.8
			44	$5.3 \times 10^{-29}$	0.85	34	$4.5 \times 10^{-11}$	6.0
300	40	27	64	$9.7 \times 10^{-15}$	2.9	46	$1.6 \times 10^{-15}$	2.4
		45	67	$6.4 \times 10^{-21}$	1.3	50	$4.6 \times 10^{-16}$	2.1
		65	64	$5.4 \times 10^{-32}$	0.68	50	$1.3 \times 10^{-16}$	2.0

geometric capacitance), being insensitive to the MAPbI<sub>3</sub> thickness. The fitted values of  $C_g$  are reported in table 5.2.

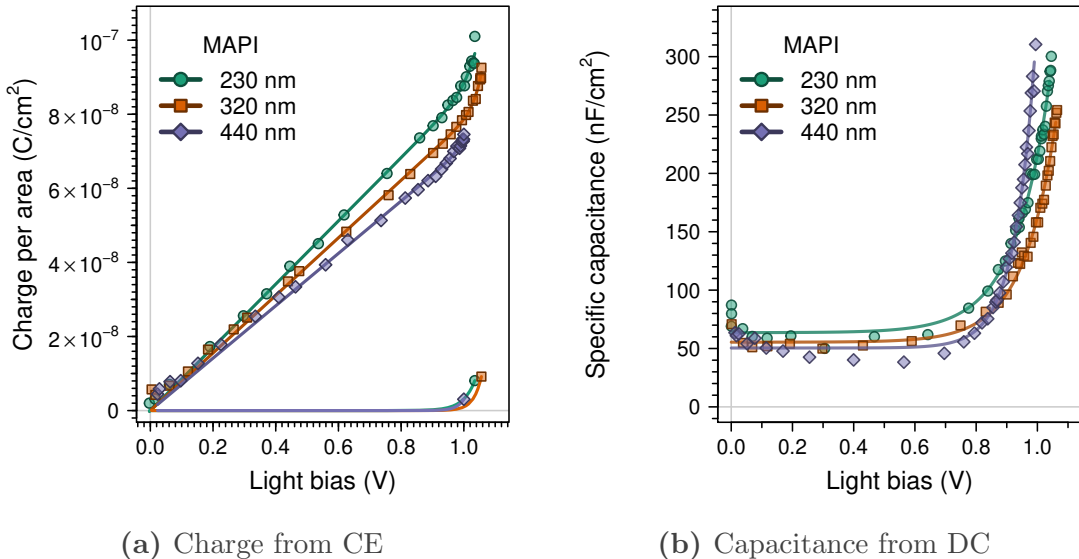


**Figure 5.3: CE and DC of devices with different MAPI thicknesses, highlighting the varying geometric capacitance.** In (a) the charge versus light bias as obtained from CE is reported. The upper solid lines are exponential fittings following eq. (3.13) while the bottom solid lines show just the exponential part, ignoring the geometric capacitance. In (b) the capacitance dependence on light bias is reported as obtained from DC. The solid line indicates the fitting using eq. (3.25). All the fitted parameters are reported in table 5.2.

## 5.3 Varying PC<sub>70</sub>BM Thickness (ETM)

Using different spin coating speeds, devices with various PC<sub>70</sub>BM thicknesses were obtained, as detailed in table 2.3. This was deposited on top of a rather thin layer of 350 nm of MAPbI<sub>3</sub>, which resulted to be smooth enough to allow the PC<sub>70</sub>BM to homogeneously cover it.

**Current-voltage sweeps.** In fig. 5.4 we can observe the current-voltage sweeps of the champion devices while in table 5.1 the averages and standard deviations are reported. The FF is heavily affected by the high series resistance of the thicker PC<sub>70</sub>BM layer. The S-shape observed close to V<sub>OC</sub> in the current-voltage sweep of devices with thick ETM layer is due to the poor mobility of electrons in PC<sub>70</sub>BM [243] which causes a charges collection bottleneck [212]. Interestingly enough, the V<sub>OC</sub> slightly increases when the PC<sub>70</sub>BM thickness is increased. If confirmed with a stronger statistics, the lower voltage for the thinner layer case could be

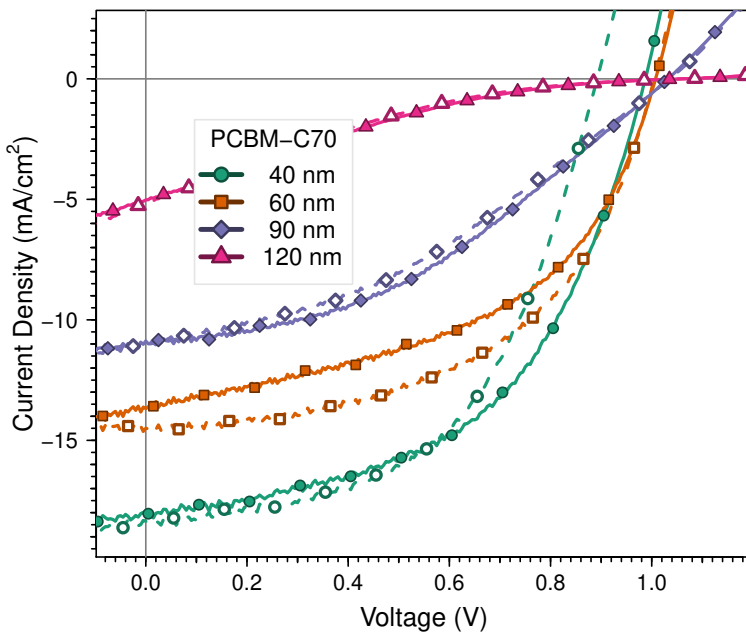


**Figure 5.4:** Current-voltage sweeps for champion devices with different PC<sub>70</sub>BM thicknesses. The solid line with filled markers represents the forward scan, while the dashed line with hollow markers represents the reverse scan.

explained by the presence of some uncovered perovskite area, causing a leakage current between the perovskite and the silver metal electrode. As also observed by Seo *et al.* [244], increasing the PC<sub>70</sub>BM layer results in a strong decrease of the  $J_{SC}$ . In Shao *et al.* [55], the same dependency is observed in disordered PC<sub>70</sub>BM films while it is not present if the layer is solvent annealed. Indeed, a very large series resistance, caused by the thick ETM layer, is expected to affect the short circuit current (this can be seen substituting  $V = 0$  in the implicit function in eq. (3.2)). This influence, together with the higher FF results in a much higher PCE for devices with a thin ETM.

**Geometric capacitance from DC and CE.** Also in the case of increasing PC<sub>70</sub>BM ETM thickness, the geometric capacitance diminishes (observed via CE in fig. 5.5a and DC in fig. 5.5b), coherently to what observed by Wheeler *et al.* [64]. Thinking within the parallel plate capacitor model (explained in page 74) where  $C_g = \epsilon_0 \epsilon_r A/d$ , this means that the distance  $d$  between the two charge storage locations is increasing. This is incompatible with what we expected: that the electronic charge gets stored in a thin depletion layer in the ETM on the perovskite layer side, as in this case the distance  $d$  would not change increasing the PC<sub>70</sub>BM layer. So, the main electrons storage location is either close to the ETM/Ag interface or

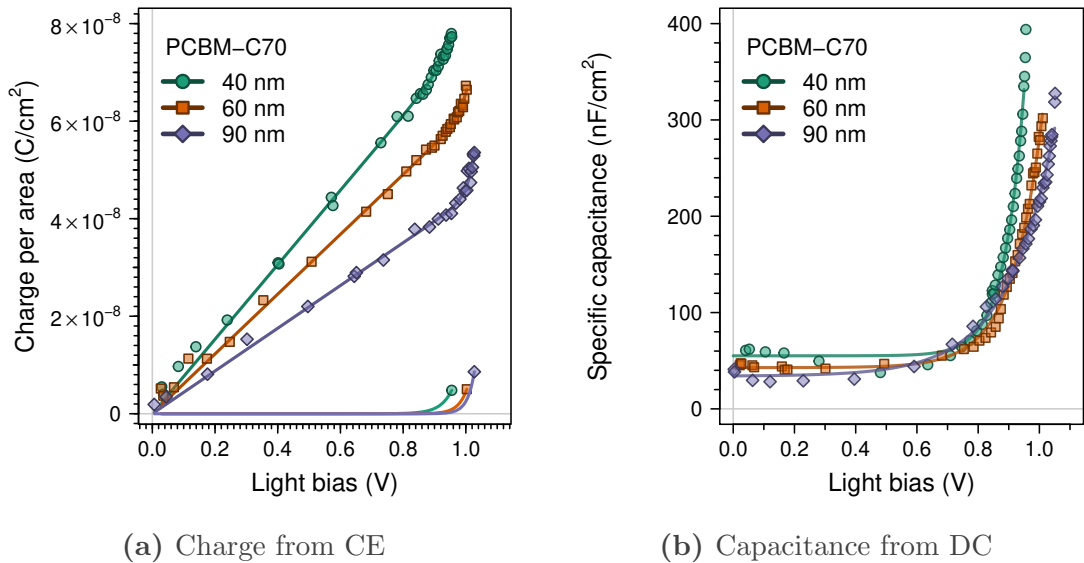


**Figure 5.5: CE and DC of devices with different  $\text{PC}_{70}\text{BM}$  thicknesses, highlighting the varying geometric capacitance.** In (a) the charge versus light bias as obtained from CE is reported. The upper solid lines are exponential fittings following eq. (3.13) while the bottom solid lines show just the exponential part, ignoring the geometric capacitance. In (b) the capacitance dependence on light bias is reported as obtained from DC. The solid line indicates the fitting using eq. (3.25). All the fitted parameters are reported in table 5.2.

within the whole ETM layer due to a Debye length (a.k.a. Thomas–Fermi screening length, is an indication of the depth inside a semiconductor layer at which an external electric field is completely screened, it depends on the permittivity and the doping density of the material, see page 11) larger than the  $\text{PC}_{70}\text{BM}$  thickness. So we can consider the  $\text{MAPbI}_3/\text{PC}_{70}\text{BM}$  stack as the inter-electrodes material of a capacitor.

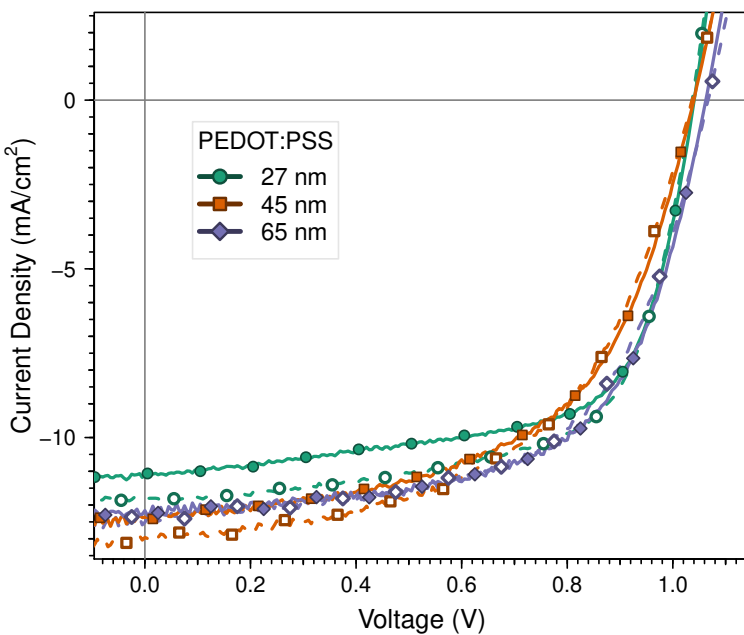


**Figure 5.6:** Current-voltage sweeps for champion devices with different PEDOT:PSS thicknesses. The solid line with filled markers represents the forward scan, while the dashed line with hollow markers represents the reverse scan.

## 5.4 Varying PEDOT:PSS Thickness (HTM)

Using different spin coating speeds, devices with various PEDOT:PSS thicknesses were obtained, as detailed in table 2.1. The ITO roughness is small enough to make us certain that even the thinner, 27 nm, PEDOT:PSS layer results in an homogeneous coverage.

**Current-voltage sweeps.** In fig. 5.6 we can observe the current-voltage sweeps of the champion devices while in table 5.1 the averages and standard deviations are reported. None of the current-voltage sweep parameters has shown a significant dependency on the PEDOT:PSS HTM thickness. Indeed, the high holes mobility of PEDOT:PSS [245] was expected to make this layer to be a non-limiting one.

**Geometric capacitance from DC and CE.** Changing the PEDOT:PSS HTM layer thickness did not affect the measured geometric capacitance values reported in table 5.2 and observable in fig. 5.7. This can either mean that no charge accumulates close to the ITO/PEDOT:PSS interface (e.g. in case the two materials have the same workfunction) or, considering the series of parallel plate capacitors model, that this layer's large capacitance does not influence the total measured capacitance.

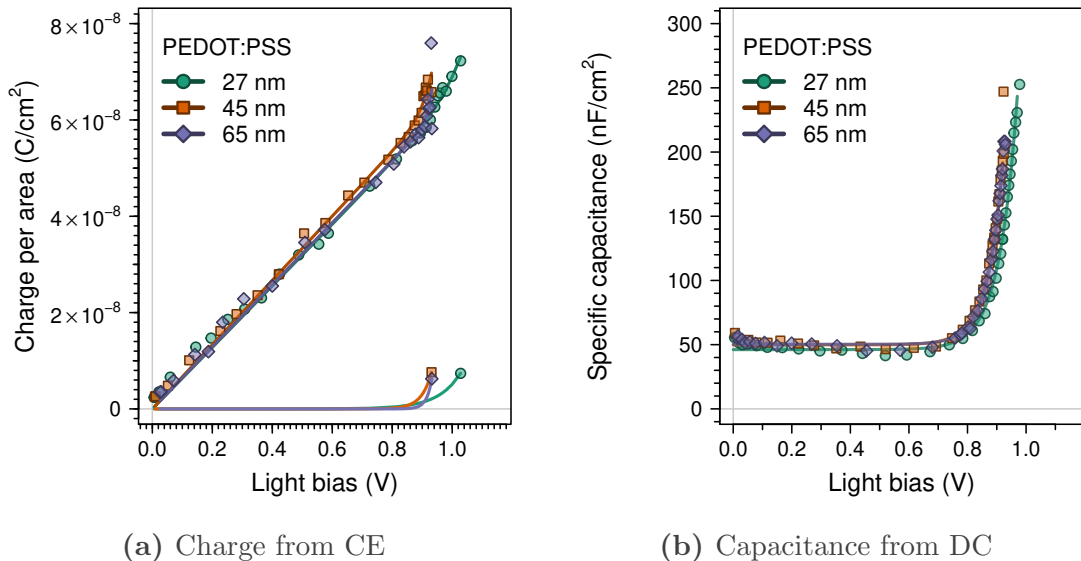


**Figure 5.7: CE and DC of devices with different PEDOT:PSS thicknesses, highlighting the varying geometric capacitance.** In (a) the charge versus light bias as obtained from CE is reported. The upper solid lines are exponential fittings following eq. (3.13) while the bottom solid lines show just the exponential part, ignoring the geometric capacitance. In (b) the capacitance dependence on light bias is reported as obtained from DC. The solid line indicates the fitting using eq. (3.25). All the fitted parameters are reported in table 5.2.

## 5.5 Conclusions

We fabricated various top cathode perovskite solar cells varying the thickness of each solution deposited layer. We measured the geometric capacitance of this set of devices using two independent characterisation techniques: CE and DC. From the obtained results, we gained insight on the storage location of the photogenerated charge at open circuit conditions. In our solar cell architecture, the holes are stored close to the PEDOT:PSS/MAPbI<sub>3</sub> interface, likely in a thin depletion layer in the HTM. Instead, the electrons does not get stored close to the MAPbI<sub>3</sub>/PC<sub>70</sub>BM interface but either through the whole ETM layer or at the PC<sub>70</sub>BM/Ag interface. Likely, this is simply caused by a space charge layer width (and the respective Debye length) larger than the ETM layer, due to the lack of doping in the PC<sub>70</sub>BM.

# Chapter 6

## Modelling the Influence of Ionic Migration on Impedance Spectroscopy

“We don’t see that plateau”

**Publication.** Part of this chapter has been published in [2]: D. Moia, I. Gelmetti, P. Calado, W. Fisher, M. Stringer, O. Game, Y. Hu, P. Docampo, D. Lidzey, E. Palomares, J. Nelson, and P. R. F. Barnes. “Ionic-to-electronic current amplification in hybrid perovskite solar cells: ionically gated transistor-interface circuit model explains hysteresis and impedance of mixed conducting devices”. In: *Energy & Environmental Science* 12.4 (May 2019), pp. 1296–1308. DOI: 10.1039/C8EE02362J. arXiv: 1805.06446.

**Abstract.** Driftfusion modelling platform allowed us to simulate the current evolution in a perovskite solar cell when applying an oscillating voltage in presence of constant illumination or voltage bias. From this simple simulation we could reproduce both the experimentally observed giant capacitance and negative capacitance gaining insight on their likely origin. The ionic migration in the perovskite layer behaves as a capacitive current of charges accumulating next to the interfaces with the contacts. The capacitive origin of this ionic current implies it happens out of phase with the applied oscillating voltage. We show that accumulation and

depletion of ionic charge at the interfaces modulates surface recombination and charge injection, causing respectively giant capacitance and negative capacitance (*i.e.* inductance).

---

## Table of Contents

---

**Introduction**

Design of the Experiment, 143 • Author contributions, 143

**Driftfusion software**

Homojunction, 144 • Recombination and generation, 144 • Boundary conditions, 145

**Simulating impedance spectroscopy**

Initial conditions, 145 • Applied voltage, 145 • Position and time grids, 145 • Oscillating stabilisation, 145 • Demodulation, 147 • Calculation of apparent capacitance, 148 • Calculation of ionic displacement current, 148 • Calculation of recombination current, 149 • Calculation of accumulation current, 150

**Simulated apparent capacitance spectra characteristics**

## VERY HIGH FREQUENCY

Dark case, 151 • Illuminated case, 153

## MID FREQUENCY

Dark case, 153 • Illuminated case, 153

## LOW FREQUENCY

Dark case, 155 • Illuminated case – Observation, 155 • Illuminated case – Not just accumulation, 155 • Illuminated case – Not just ions, 157 • Illuminated case – Recombination barriers without ions, 157 • Illuminated case – Recombination barriers with ions, 159 • Illuminated case – Minority carriers density point of view, 159 • Loops in the positive semi-plane and large perturbations, 161

**Comparison of simulated and experimental impedance spectra**

Lack of low frequency plateau, 162 • Short circuit, 164

**Further development**

Heterojunction, 164 • Complete simulation of ElectroAbsorbance, 164 • Implement other similar techniques, 166 • Faster simulation with voltage step, 166

**Implementation of impedance spectroscopy**

`ISwave_EA_single_exec` – Does a single impedance spectroscopy simulation, 168 • `ISwave_EA_single_demodulation` – Calculates phase and amplitude demodulating oscillating current data from impedance spectroscopy, 169 • `ISwave_EA_single_fit` – Calculates phase and amplitude fitting oscillating current data from impedance spectroscopy, 170 • `ISwave_single_analysis` – Calculate impedance and phase from impedance spectroscopy data, 170 • `ISwave_subtracting_analysis` – Calculates the time derivative of the total charge in the device, 171 • `ISwave_full_exec` – Simulates impedance spectroscopy at various frequencies on many provided solutions, 172 • `ISwave_full_exec_nonparallel` – Non parallelized version of `ISwave_full_exec`, 173 • `ISwave_full_analysis_phase` – Represents Bode plots of phase from impedance spectroscopy, 173 • `IS_full_analysis_impedance` – Represents Bode plots of impedance and apparent capacitance from impedance spectroscopy, 174 • `ISwave_full_analysis_nyquist` – Plots Nyquist graph for impedance spectroscopy, 174 • `fromISwaveEAStructToTxt` –

Exports single impedance simulation data to text files, 174 • `fromIS-waveResultsToTxt` – Exports data of a set of impedance simulations to text files, 175 • `examples_unit_test` – Runs unit testing on all the implemented experiments, 175

## Conclusions

---

## 6.1 Introduction

Impedance spectroscopy, introduced in page 105, is a powerful technique for characterising electronic devices in the frequency domain. The first information that can be directly extracted from impedance spectroscopy is a frequency-dependent capacitance [189]. When studying this in perovskite solar cells, the results are of difficult interpretation [246, 247]. A giant capacitance is always observed at low frequencies for illuminated devices [248, 249]. More rarely, also a negative capacitance (*i.e.* an inductance) has been observed in perovskite solar cell [250–252] and other kinds of solar cells [151, 253]. In order to extract the individual parameters, like transport and recombination constants, the data has to be fitted using an electronic equivalent circuit [254]. The components of the circuit should have a relation with the actually existing processes, so that we can relate the parameters of the electrical component with the solar cell specific internal mechanisms. Many complex circuits have been proposed in literature, some of them included inductors for matching the inductive behaviour [246, 250, 251]. Previous to 2018, these phenomena were interpreted as surface polarisation caused by a huge free charge accumulation at the interfaces due to the influence of ionic accumulation [251, 255] supported by drift-diffusion simulations [256, 257]. It has to be noted that any slow process causing a change in the flowing current could result in an apparent capacitance or inductance, this could happen with degradation processes or heating [151, 258]. When studying perovskite solar cells, we have to consider that the electrostatic potential arising from mobile ion redistribution controls electronic charge transfer barriers [102, 196]. In November 2017 we started modelling impedance spectroscopy using Driftfusion software and the modules already developed for Charge Extraction simulation. In May 2018 we uploaded to ArXiv a pre-print which was then published in Moia *et al.* [2] with an alternative interpretation for the giant capacitance: this influence of the ionic charge on the electronic processes such as recombination and can give rise to apparent capacitive behaviour. This effect does not involve an accumulation of an enormous amount of charge,

as it was expected by a giant capacitance, so it cannot be described by a capacitor in the equivalent electrical circuit. For the inductive behaviour (negative capacitance) we proposed that the same influence can affect the charge injection causing a negative apparent capacitance. Additionally, we also shown that the reaction or penetration of the perovskite's mobile ions into the contact materials can also explain some inductive behaviour. More or less at the same time, other research groups published similar interpretations [99, 259]. Moreover, in Ebadi *et al.* [259] the influence of ionic migration on the injection barrier is experimentally confirmed. We proposed that both of the effects (apparent capacitance and inductance) can be described by transistors element in the circuit, as represented in fig. 6.7f. This allows the charge to flow through an interface to not only depend on the applied voltage, like in a Schottky diode, but also on an external influence: the ionic density close to the interface. The influence of ionic migration on electronic transfer can be thought as an amplification of electronic current by ionic current. Our model not only works in the small perturbation regime employed in impedance spectroscopy, but can also explain hysteresis in current-voltage sweeps as shown in Fig.5 of Moia *et al.* [2]. The understanding of this mechanism allows the researchers to insightfully use impedance spectroscopy on perovskite solar cells and other ionic/electronic interfaces (e.g. electrochemical communication between neurons in the brain [260]) but could also be employed for designing new physical electronic components showing large and tunable apparent capacitance or inductance in a reduced volume.

**Design of the Experiment.** Impedance spectroscopy has been initially modelled studying the current evolution after a single voltage step. This first rough attempt should be polished using Kramers-Kronig relation and has not been published yet. In order to confirm the initial observations, the impedance spectroscopy has been implemented trying to match the actual experimental conditions. For this reason, the oscillating current obtained when applying an oscillating voltage has been studied separately for each frequency. This caused the simulation to be much slower but still doable with my laptop. Additionally, the phase and amplitude has been obtained mimicking the demodulation of a lock-in amplifier rather than with a sinusoidal fitting.

**Author contributions.** I implemented and run the impedance spectroscopy simulation on top of Driftfusion software developed by Dr. Phil Calado, Dr. Piers RF Barnes, Mohammed Azzouzi, Benjamin Hilton, and

myself. Dr. Davide Moia and Dr. Piers RF Barnes created the formalism and the electrical equivalent circuit. William Fisher and Dr. Davide Moia fitted the experimental data using fitting routines developed by Dr. Piers RF Barnes. Dr. Michael Stringer, Dr. Onkar Game, Yinghong Hu, Dr. David Lidzey, and Dr. Pablo Docampo provided excellently stable perovskite solar cells to be studied.

## 6.2 Driftfusion software

Driftfusion is a modelling platform for stacked semiconductors, mostly used for solar cells. It estimates the profile of electrostatic potential, free electrons, free holes, and mobile ions densities over one dimension (depth into the stack) and over time. The semi-classical transport, continuity, and Poisson's equations are solved using Matlab's built-in Partial Differential Equation solver for Parabolic and Elliptic equations `pdepe`. The simulation assumes static negative counter ions simulating Schottky defects [73] and positively charged mobile ions constrained into the absorber layer. This formalism is based on Nelson [22] and described in Calado *et al.* [98] and Calado [4]. All the mentioned functions, helper code and examples of impedance spectroscopy simulations have been released on <https://github.com/barnesgroupICL/Driftfusion/tree/2018-EIS>.

6

**Homojunction.** We employed the homojunction version of Driftfusion, which at the date of September 2017 was the stable and well tested release of Driftfusion. This means that in the presented simulations all the materials have the same band gap but can differ by other parameters: doping level (equilibrium Fermi level position), holes and electrons mobilities, permittivity, radiative and trap mediated recombination constants, traps relative energy inside the band gap, and thickness. This proved to be enough for simulating the influence of ionic current on the recombination current but was limited for studying their influence on the injection current.

**Recombination and generation.** High rates of recombination in the contact regions are used to simulate surface recombination. Even if an optical model was available in Driftfusion, an uniform generation through all the absorber proven to be enough for our purposes.

**Boundary conditions.** An arbitrary time dependent voltage can be applied with time-dependent boundary conditions.

## 6.3 Simulating impedance spectroscopy

**Initial conditions.** The solution of the electrons, holes, ions density and electrostatic concentration profiles of the device under steady state operating conditions was determined using Driftfusion core functions and the parameters listed in table 6.1. This solution provided the initial conditions for the simulated impedance spectroscopy. Most importantly, at this step we set the illumination intensity and the DC voltage  $V_{DC}$ , which usually are the explored parameters.

**Applied voltage.** The impedance spectroscopy simulations were performed by applying an oscillating voltage  $v$  superimposed on a background bias voltage  $V_{DC}$  boundary condition:

$$V = V_{DC} + v(t) = V_{DC} + v_{\max} \sin(\omega t) \quad (6.1)$$

$V_{DC}$  was set equal to the steady state voltage of the provided input solution (e.g.  $V_{OC}$  for the simulations at open circuit). Usually, a  $v_{\max}$  of 2 mV is employed. This value is much smaller than the experimentally used one but very similar results are obtained when using larger perturbations (simulations with a  $v_{\max}$  of 200 mV are mentioned in page 161). The small value allowed me to obtain a computationally fast simulation without being affected by too much numerical noise.

**Position and time grids.** In order to deal with the high gradients at the interfaces, a linear spatial mesh was used with a spacing of 0.55 nm within the approximate depletion regions of the device and 2.54 nm elsewhere. Even if the pdepe solver utilises an internal time grid, it outputs the data at the requested times array. All the stabilisations have been performed on a logarithmic time grid (`tmesh_type=2` in `meshgen_t`) while all the oscillating voltage simulations have been performed on a linear time grid (`tmesh_type=1` in `meshgen_t`). For the impedance simulations, 20 complete periods are simulated with 40 time points for each period.

**Oscillating stabilisation.** The change from steady state to oscillating voltage does require some complete periods before reaching a stable

**Table 6.1: Drift-diffusion simulation parameters.** These parameters were used for all the data simulated with the homojunction model. The meaning of each is described in detail in Calado *et al.* [98]. The 1 sun equivalent  $V_{OC}$  resulting from this parameters set is 0.931 V, the resulting  $J_{SC}$  is  $20.3 \text{ mA cm}^{-2}$ .

Parameter name	Symbol	<i>p</i> -type	Intrinsic	<i>n</i> -type	Unit
Layer thickness	$d$	200	500	200	nm
Band gap	$E_g$	1.6	1.6	1.6	eV
Built in voltage	$V_{BI}$	1.3	1.3	1.3	V
Relative dielectric constant	$\epsilon_r$	20	20	20	/
Mobile ionic defect density	$N_{ion}$	0	$1 \times 10^{19}$	0	$\text{cm}^{-3}$
Ion mobility	$\mu_a$	/	$1 \times 10^{-10}$	/	$\text{cm}^2 \text{V}^{-1} \text{s}^{-1}$
Electron mobility	$\mu_n$	0.02	20	20	$\text{cm}^2 \text{V}^{-1} \text{s}^{-1}$
Hole mobility	$\mu_p$	20	20	0.02	$\text{cm}^2 \text{V}^{-1} \text{s}^{-1}$
Donor doping density	$N_A$	$3 \times 10^{17}$	/	/	$\text{cm}^{-3}$
Acceptor doping density	$N_D$	/	/	$3 \times 10^{17}$	$\text{cm}^{-3}$
Effective density of states	$n_{DOS}$	$1 \times 10^{20}$	$1 \times 10^{20}$	$1 \times 10^{20}$	$\text{cm}^{-3}$
Band-to-band recombination rate coefficient	$k_{rad}$	$1 \times 10^{-12}$	$1 \times 10^{-12}$	$1 \times 10^{-12}$	$\text{cm}^3 \text{s}^{-1}$
SRH trap energy	$E_t$	$E_{CB} - 0.8$	/	$E_{CB} - 0.8$	eV
SRH time constants	$\tau_{(n p)}$	$5 \times 10^{-10}$	/	$5 \times 10^{-10}$	s
Generation rate	$g$	/	$2.5 \times 10^{21}$	/	$\text{cm}^{-3} \text{s}^{-1}$

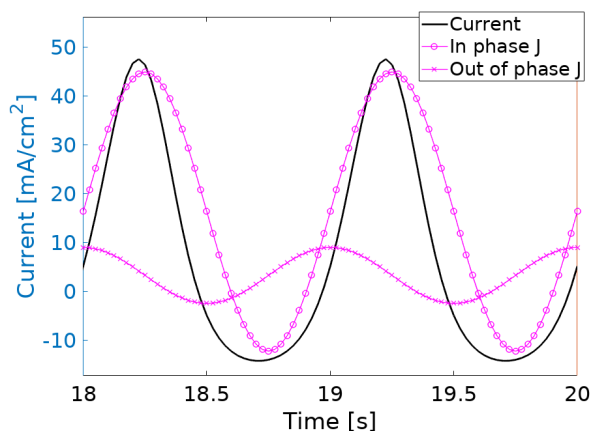


**Figure 6.1:** Example of demodulation on a large perturbation simulation. The applied voltage is not shown, it was a sinusoidal wave with frequency 1 Hz. Black line is the simulated oscillating current, the non sinusoidal shape is due to the large amplitude of the applied oscillating voltage. Pink lines are the output of the demodulation routine.

oscillation (where the current profile is identical from one period to the next). As represented in fig. 6.13, before analysing the oscillating solutions, the stabilisation is verified comparing the last time point profiles with the profiles at the half of the current simulation (so at the 10<sup>th</sup> period). In case the stability was absent, the last time point solution has been used as a starting point for 20 more periods, until when stabilisation was ensured. This is mostly important for large perturbation simulations (large  $v_{\max}$ ), where the time-averaged profiles are rather different from the steady state ones.

**Demodulation.** The amplitude and phase of the oscillating electronic current density was obtained via demodulation, mimicking the working principle of a two-phase lock-in amplifier [261]. As can be seen in fig. 6.1, this method works both with sinusoidal profiles obtained from small perturbation simulations and also for large perturbation signals including distortion by higher harmonics. It has been implemented in `ISwave_EA-single_demodulation` described in page 169. The current density profile  $j(t)$  was point-by-point multiplied by the voltage profile or the 90° shifted voltage profile normalised by  $v_{\max}$  and integrated over time (typically 10 periods):

$$X = \frac{\omega}{m\pi} \int_{t_0}^{t_0+2m\pi/\omega} j(t) \sin(\omega t) dt \quad (6.2)$$

$$Y = \frac{\omega}{m\pi} \int_{t_0}^{t_0+2m\pi/\omega} j(t) \cos(\omega t) dt \quad (6.3)$$

where  $m$  is the number of periods,  $t_0$  is the start of the integration time,  $\sin(\omega t)$  is the normalised voltage profile, and  $\cos(\omega t)$  is the  $90^\circ$  shifted one. Actually, for avoiding numerical problems (e.g. values close to the single-precision accuracy) the current profile constant bias is subtracted and the result is normalised. Amplitude  $j_{\max}$  and current phase  $\theta$  (which is the same as the impedance phase but with the opposite sign) are then given via:

$$j_{\max} = \sqrt{X^2 + Y^2} \quad (6.4)$$

$$\theta = \arctan\left(\frac{Y}{X}\right) \quad (6.5)$$

allowing the complex impedance to be determined via  $Z = v_{\max}/j_{\max} \exp(-i\theta)$ . The amplitude and phase obtained this way were confirmed by fitting  $j(t)$  with a sinusoidal function.

**Calculation of apparent capacitance.** The apparent capacitance  $C(\omega, \phi, V_{DC})$  can be calculated in a few different ways, maybe the most intuitive is from the amplitude of the out-of-phase (quadrature) component of the current  $Y$ :

$$C = \frac{Y}{2v_{\max}\omega} \quad (6.6)$$

The commonly reported formula is [2, 251]:

$$C = \frac{\text{Im}(Z^{-1})}{\omega} \quad (6.7)$$

But it was finally implemented as:

$$C = \frac{\sin(\theta)}{\omega|Z|} \quad (6.8)$$

**Calculation of ionic displacement current.** Various approaches have been tested in order to estimate the ionic migration contribution to the apparent capacitance. The most meaningful method is the calculation of the displacement current (see page 13) induced in the contacts by the changes in the ionic profile. The ionic accumulation at the interfaces will give a contribution  $E_{\text{ion}}$  to the electric field inside the perovskite material. This contribution can be calculated from the ionic profile  $a(x, t)$  with:

$$E_{\text{ion}}(x, t) = \frac{q}{\epsilon_0 \epsilon_r^{\text{prv}}} \int_{x_1}^{x_1+x} a(x', t) dx' \quad (6.9)$$

where  $x_1$  is the position of the HTM/perovskite interface. Actually, we are interested to the electrostatic potential  $V_{\text{Eion}}$  caused by this electric field, rather than in  $E_{\text{ion}}$  itself:

$$V_{\text{Eion}}(t) = \int_{x_1}^{x_2} E_{\text{ion}}(x, t) dx \quad (6.10)$$

where  $x_2$  is the position of the perovskite/ETM interface. For the sake of clarity, we consider the case in which the applied voltage does not vary, the obtained equation would be valid also for the case with varying voltage. So, for keeping the device voltage constant, this electrostatic potential variation caused by the ionic movement will have to be compensated by an accumulation of free carriers in the contacts (we will ignore the free carriers in the intrinsic, which for the dark and unbiased case has low density). So the compensating potential  $V_{\text{Edisp}}$  will be:

$$V_{\text{Edisp}}(t) = -V_{\text{Eion}}(t) = \frac{Q_{\text{disp}}(t) \cdot (p_2 - p_1)}{\epsilon_0 \bar{\epsilon}_r} \quad (6.11)$$

where  $Q_{\text{disp}}(t)$  is the free charge per area accumulating at the contacts,  $p_1$  and  $p_2$  are the positions of the depletion layers where the charges get accumulated, and  $\bar{\epsilon}_r$  is the average permittivity between  $p_1$  and  $p_2$ . If we consider the depletion layers to be thin,  $p_1 \approx x_1$  and  $p_2 \approx x_2$  we can also consider just the perovskite permittivity and write:

$$J_{\text{disp}}(t) = \left. \frac{dQ_{\text{disp}}(t')}{dt'} \right|_{t'=t} = -\frac{\epsilon_0 \epsilon_r^{\text{prv}}}{x_2 - x_1} \left. \frac{dV_{\text{Eion}}(t')}{dt'} \right|_{t'=t} \quad (6.12)$$

which is equivalent to the expression derived in page 13 if we consider that  $V_{\text{Eion}}(t)/(x_2 - x_1)$  is the average electric field in the perovskite due to the ionic accumulation.

**Calculation of recombination current.** The recombination current is the flow of charges getting annihilated due to the implemented recombination processes. It is evaluated simply calculating the radiative and the trap assisted recombination flux from the electrons and holes concentration in each position and integrating this over the whole device thickness.

$$J_{\text{rec}}(t) = q \int_{x_0}^{x_3} U_{x,t} dx \quad (6.13)$$

where  $x_0$  and  $x_3$  are the position of the beginning and the end of the simulated device.

**Calculation of accumulation current.** We refer with “accumulation current” to what is commonly considered the capacitive current: a flow of particles accumulating in the device rather than crossing it. As the aforementioned displacement current due to ionic movement is contributing to the accumulation of charges, it will also be included in this accumulation current. It can be calculated from the continuity equation eq. (1.4) integrated over the whole device thickness:

$$J_{\text{acc}}(t) = J(t) + qg \cdot (x_2 - x_1) - J_{\text{rec}}(t) \quad (6.14)$$

where we considered a constant photogeneration homogeneous through the whole absorber layer. Actually, it was implemented as the time derivative of the total electrons amount present in the device:

$$J_{\text{acc}}(t) = q \left. \frac{d \int_{x_0}^{x_3} n(x, t') dx}{dt'} \right|_{t'=t} \quad (6.15)$$

which gives the same information.

## 6.4 Simulated apparent capacitance spectra characteristics

As we can see comparing figs. 6.2a and 6.2b, when oscillating the voltage around  $V_{\text{OC}}$  on an illuminated solution or around the same values for a dark solution, the result is very similar. This behaviour is also observed experimentally, as reported in fig. 6.10d and elsewhere [97, 259]. All the parameters reported in table 6.1 are a very rough estimation of the reality. Because of this, some results can greatly diverge from the experimentally observed ones, for example all the time scales are expected to be incorrect. What we were looking for, was a qualitative description of the perovskite solar cell behaviour. In the newest versions of heterojunction Driftfusion, a better match to the actual solar cell characteristics is sought.

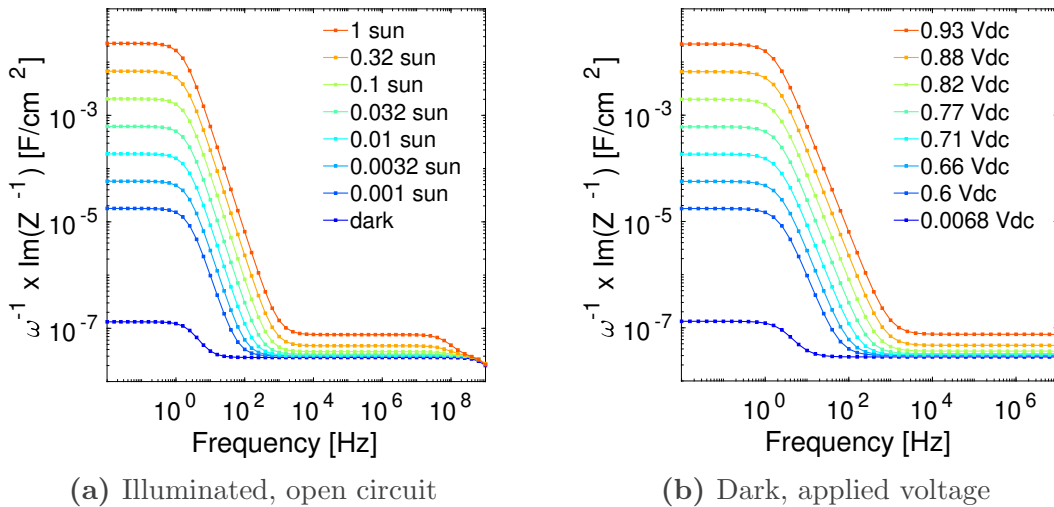
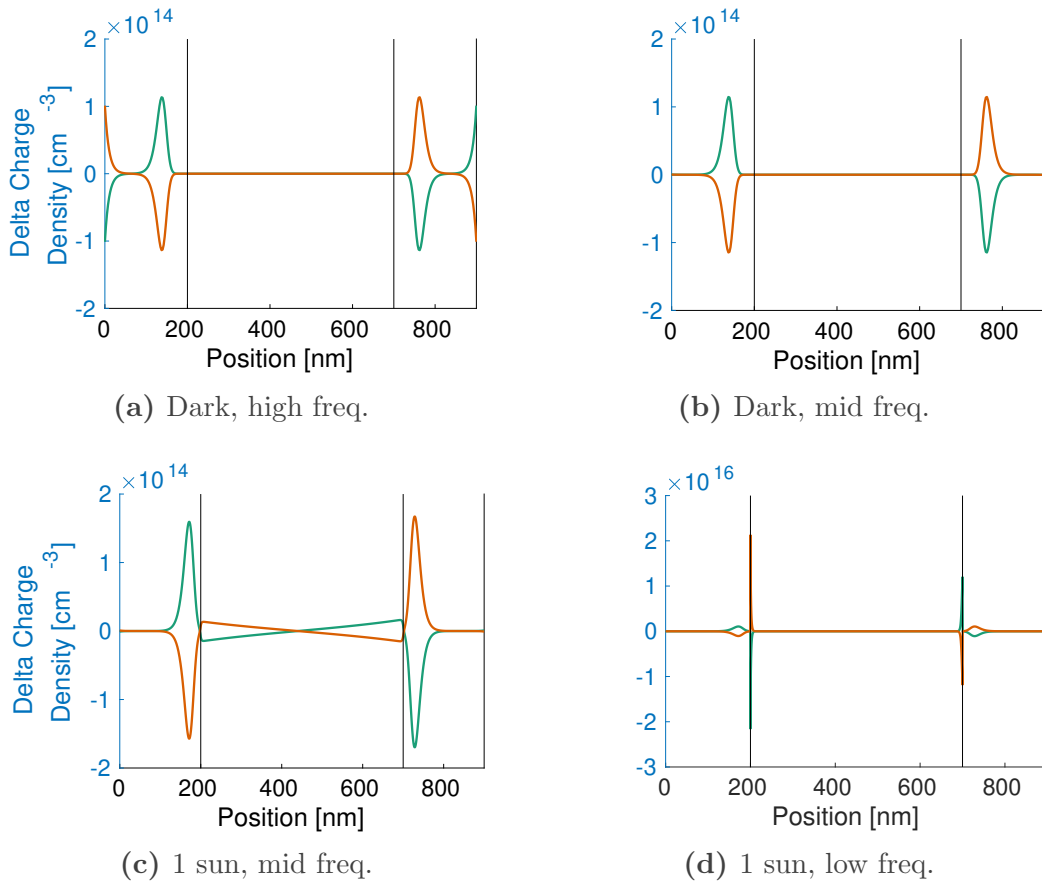


**Figure 6.2: Simulated apparent capacitance spectra of an illuminated perovskite solar cell at open circuit and dark applied voltage.** In (a) the simulation oscillates the voltage around the  $V_{OC}$  value induced by different light intensities at open circuit (light bias). In (b) the voltages from (a) are applied as constant voltage biases around which the applied voltage oscillates, in dark. Due to some unidentified numerical, in the dark case at 0 V there is a residual current. For eliminating this current, a voltage bias of 0.0068 V has been applied to the dark solution in (b).

### 6.4.1 Very high frequency

**Dark case.** In the simulation at frequencies above  $1 \times 10^7$  Hz in dark, the voltage change is too fast for the charges to migrate from the electrodes (in our simulation, the boundaries) to the depletion layers in the contacts. This can be seen in fig. 6.3a from the presence of net charge out of the depletion layers, at the electrodes/contacts interface (left and right simulation boundaries). This happens because the oscillation period is shorter than the RC time composed by the geometric capacitance of the device (a parallel plate capacitor having the imaginary plates at the depletion layers and the perovskite layer as dielectric) and the transport resistance in the HTM and ETM contacts. We can see this as a non 90° phase in the extremely high frequency region of fig. 6.6a and as a decrease of the apparent capacitance in fig. 6.2a. Experimentally, this is observed some times but lies close to the instrumental frequency limit (usually  $1 \times 10^6$  Hz).



**6** **Figure 6.3: Net charge profile variation in a period of oscillating voltage at high and mid frequencies.** A  $p(200\text{ nm})-i(500\text{ nm})-n(200\text{ nm})$  homojunction device is simulated. The space charge layers in the device (e.g. depletion layers in the contacts) have a net charge (unbalanced positive and negative charge densities). The net charge profile is obtained with  $\rho(x, t) = -n(x, t) + p(x, t) + a(x, t) + n_{\text{stat}}(x)$  where  $n$ ,  $p$ , and  $a$  are the electrons, holes, and ions density profiles and  $n_{\text{stat}}$  are the fixed charges profile, including the doping in the contacts and the fixed counter ions in the perovskite layer. The represented net charge variation is obtained as  $\Delta\rho(x, t) = \rho(x, t) - \rho(x, 0)$ . The green line indicates the additional net charge when the oscillating voltage is at its maximum, while the orange line indicates the situation at the voltage minimum. In (a) the device is in dark and the voltage oscillates at  $1 \times 10^9 \text{ Hz}$ ; in (b) it is also in dark but the frequency is lower:  $1 \times 10^6 \text{ Hz}$ ; in (c) the frequency is also  $1 \times 10^6 \text{ Hz}$  but the device is at 1 sun illumination and at open circuit conditions; in (d) the frequency is decreased to  $1 \times 10^{-2} \text{ Hz}$  so that the ionic migration is active.

**Illuminated case.** Looking at the phase in the high frequency region for 1 sun illuminated case in fig. 6.6a, we can see a trend similar to the one observed for the dark case. One small difference is represented by a bump at  $1 \times 10^8$  Hz, representing the characteristic time for the movement of the free charges in the perovskite layer. At frequencies lower than this point, the electrons and holes in the perovskite layer contribute to the screening of the electric field.

### 6.4.2 Mid frequency

At mid frequencies, approximatively from  $1 \times 10^3$  to  $1 \times 10^7$  Hz, a plateau can be observed in the apparent capacitance. In this region, the frequency is slow enough for the contacts' depletion layers population/depopulation and for the migration of the free carriers in the perovskite layer, as represented in fig. 6.3b.

**Dark case.** For the dark case, the observed capacitance of  $2.83 \times 10^{-8}$  F cm $^{-2}$  is just the geometric capacitance of the device. As explained in page 75, the parallel plate capacitor giving rise to this geometric capacitance has an inter plate distance slightly larger than the perovskite thickness (500 nm). The correct position of this imaginary plate is indeed in the contact's depletion layer, more precisely where the charge concentration varies when applying the oscillating voltage. This distance can be estimated from the distance of the peaks in fig. 6.3b as 625 nm. From this and from the materials' permittivity ( $\epsilon_r$  20 for all the layers, see table 6.1) we can predict a geometric capacitance of  $2.83 \times 10^{-8}$  F cm $^{-2}$  which is in accordance with the value obtained from the impedance.

**Illuminated case.** As can be seen in fig. 6.4, with an illumination, the apparent capacitance of the mid frequency plateau increases up to  $7.60 \times 10^{-8}$  F cm $^{-2}$  at 1 sun. This is caused by the large amount of free carriers in the perovskite due to illumination (or due to the voltage bias for the dark case reported in fig. 6.2b). As shown in fig. 6.3c, the free carriers drift inside of the perovskite layer causing a dipole. This partially screens the electric field allowing the device to accumulate more charges and effectively increasing its capacitance. From the parallel plate capacitor model point of view, these charges in the dielectric layer effectively increase its permittivity.

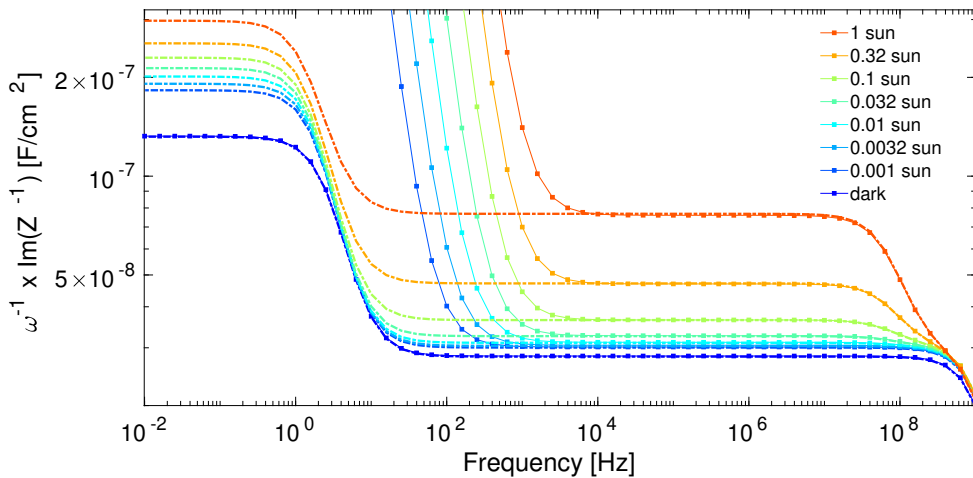
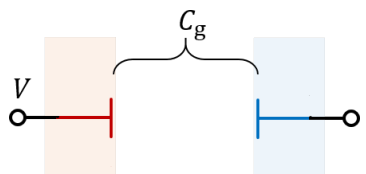
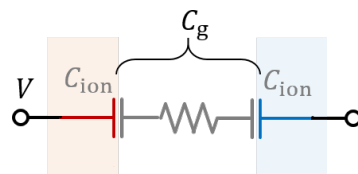


**Figure 6.4:** Simulated accumulation capacitance spectra compared with capacitance due to charge accumulation. Solid lines with dot markers represent the apparent capacitance, dash dotted lines show the capacitance calculated from the accumulation current obtained as explained in page 150. For the dark case, the apparent and the accumulation capacitances correspond at any frequency. With illumination, the high and mid frequency regions matches while the apparent capacitance is much larger for the low frequencies.



(a) Capacitance at mid frequencies



(b) Capacitance at low frequencies

**Figure 6.5: Capacitance representation with or without mobile ions.** The area in pink indicates the HTM and the one in blue the ETM. In (a) the geometric capacitance observable at mid frequencies is represented, where the charges accumulate in the contacts close to the perovskite interface. In (b) the ionic accumulation observable at low frequencies is represented as two additional capacitor plates and the ionic transport as a resistance between them.

### 6.4.3 Low frequency

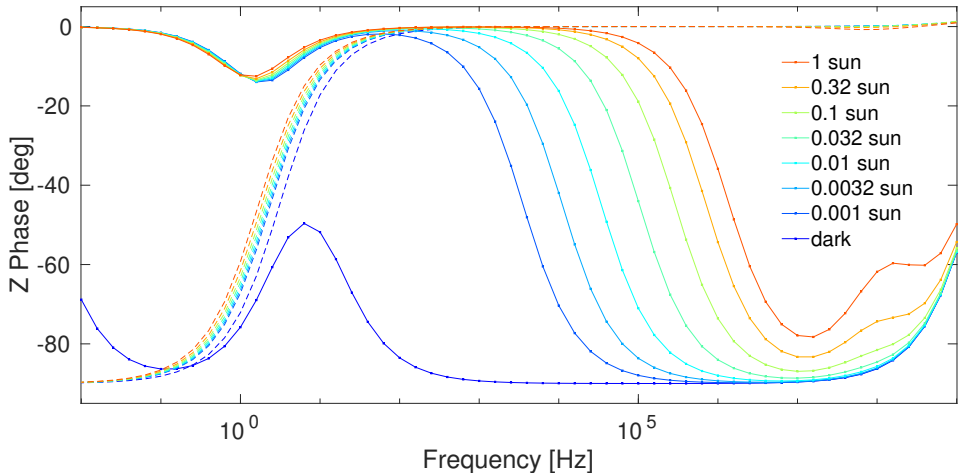
Up to now, we observed the charging and discharging of a geometric capacitance with the charge accumulation in the contacts and, in some cases, in the perovskite layer. This is represented by the capacitor in fig. 6.5a. We did not consider yet the ionic motion as at mid and high

frequencies it was effectively frozen: the slow ions did not have time to migrate. The activation of the ionic movement can be seen in the phase of ionic displacement current represented in fig. 6.6a. As we can see, once the ionic migration is active, the related current is purely capacitive ( $90^\circ$ ). This is expected as the ionic species can just accumulate or deplete at the interfaces of the perovskite layer with the contacts (simulations where ions could penetrate in the contacts have been performed but will not be reported in this thesis) screening the electric field, like in the capacitor represented in fig. 6.5b.

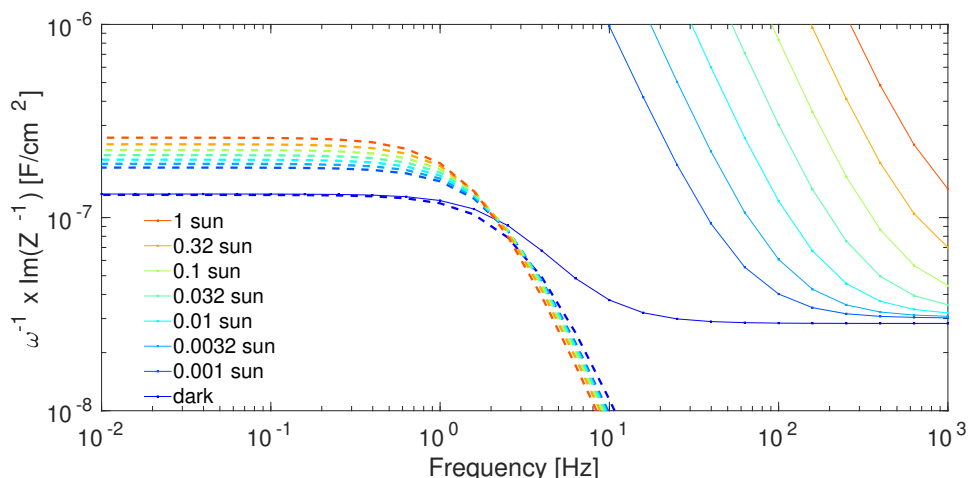
**Dark case.** Experimentally, a feature at frequencies  $<100\text{ Hz}$  is often observed in impedance of perovskite solar cells in dark [42, 248, 249, 251, 262]. This feature has been interpreted as a ionic influence on the dark capacitance by Yang *et al.* [87]. Indeed, calculating an apparent capacitance value from the ionic displacement current (see pages 13 and 148) we can see that it matches the apparent capacitance value in dark, reported in fig. 6.6b. Differently from the geometric capacitance observed at mid frequencies, this low frequency capacitance value is independent from the perovskite layer thickness, as it relates just to the interfacial region, neglecting any contribution from the perovskite bulk. In case the ionic capacitance is smaller than the geometric capacitance (e.g. if the ionic concentration is not high enough for screening the electric field or with a very thin device), no bump can be seen and just the geometric capacitance is observed at low frequency. As a concept, this ionic capacitance is similar to the “junction capacitance” or “transition capacitance” of the interface between a *p*-type and a *n*-type material but in this case one of the materials has ions rather than electrons or holes.

**Illuminated case – Observation.** Under illumination or dark but with constant voltage bias, the mentioned low frequency feature has been observed to become giant, increasing linearly with the light intensity [246, 248, 249, 255, 262]. The available explanations in literature relied on a very large accumulation of free charges at the interfaces caused by the ionic accumulation in the same zone. We were able to reproduce this behaviour without observing the expected huge charge concentration. The origin of our observation was the influence of the ionic accumulation on the interface energetics and, specifically, on the recombination barrier.

**Illuminated case – Not just accumulation.** As can be seen in the low frequency region of fig. 6.4, just the dark case can be explained by



(a) Ionic displacement current phase



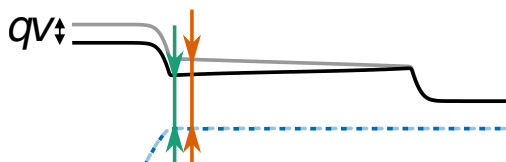
(b) Ionic displacement current capacitance

**Figure 6.6:** Simulated apparent capacitance and phase spectra compared with capacitance due to ionic migration. In (a) the phase of the impedance (solid lines, it is the same as the oscillating current phase but with the opposite sign) is plotted and compared with the phase of the ionic current (dashed lines, changed of sign for easing the comparison). In (b) the apparent capacitance spectra (solid lines) is compared with the capacitance calculated from the out-of-phase ionic current (dashed lines).

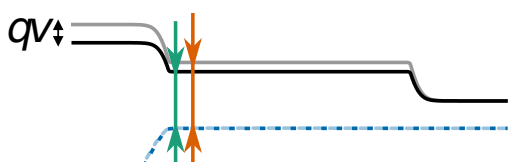
the accumulation capacitance resulting from the charges actually being stored in the device. When the an illumination or a voltage bias are applied, the accumulation capacitance increases by less than one order of magnitude, so the giant capacitance experimentally observed is not due to an accumulation of charges. This variation can be understood considering the different thickness of the depletion layers in the contacts depending on the voltage bias, as explained in page 75 for the voltage dependent geometric capacitance. Considering the parallel plates capacitor model, at low frequency we are observing one plate in the contact's depletion layer and the other contact in the perovskite at the interface, where we assume the ionic accumulation layer to be thin thanks to their abundance. Comparing fig. 6.3b with fig. 6.3c we can see how the different thickness of the space charge layers with different bias voltages (or dark versus 1 sun) implies that the charge variation happens at different distances from the materials' interface. This implies a higher accumulation capacitance at 1 sun, which means more charge getting accumulated and depleted in the space charges during the voltage oscillation.

**Illuminated case – Not just ions.** Looking at the low frequency region of fig. 6.6b, we can see how the ionic capacitance (so the amount of displaced ions) increases with the illumination or applied voltage. This is just due to the wider charge density variation in the contacts, as observed in the previous paragraph. Indeed the increase in ionic capacitance is more or less similar to the increase in accumulation capacitance, and neither this can itself explain a giant capacitance.

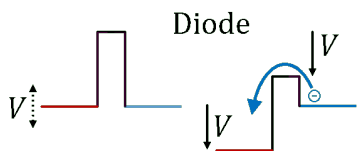
**Illuminated case – Recombination barriers without ions.** Let me go back to a “normal” solar cell with no mobile ions. In most of the solar cells and in the ions free systems, the recombination flux (the current of particles entering the device and annihilating either via radiative or trap mediated recombination) is expected to vary coherently with the applied voltage. In these cases, the device interfaces are usually considered like a *p-n* junction diode, where the energy barrier just depends on the voltage across it as represented in fig. 6.7c. When we simulate a perovskite solar cell at mid and high frequency we are in this same situation: the applied voltage is experienced as an electric field in the intrinsic layer and the recombination barrier represented in fig. 6.7a vary by the same amount and in the same moment as the applied voltage. So the recombination current (which depends on the recombination energy barrier) varies in-phase with



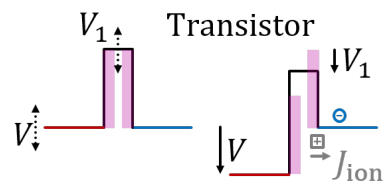
(a) Conduction band at high frequency



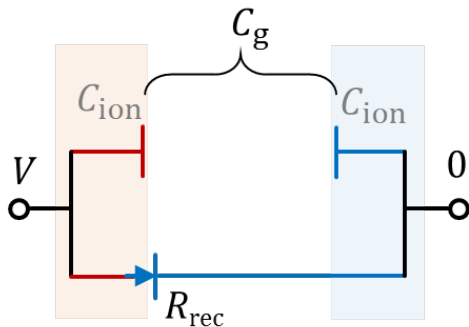
(b) Conduction band at low frequency



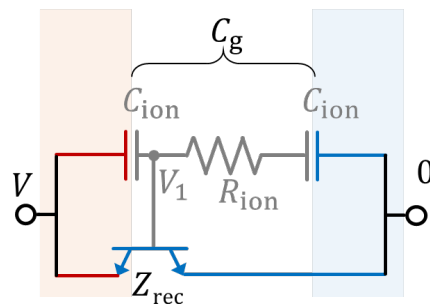
(c) Energy barrier in a diode



(d) Energy barrier in a transistor



(e) Equivalent circuit with diode



(f) Equivalent circuit with transistor

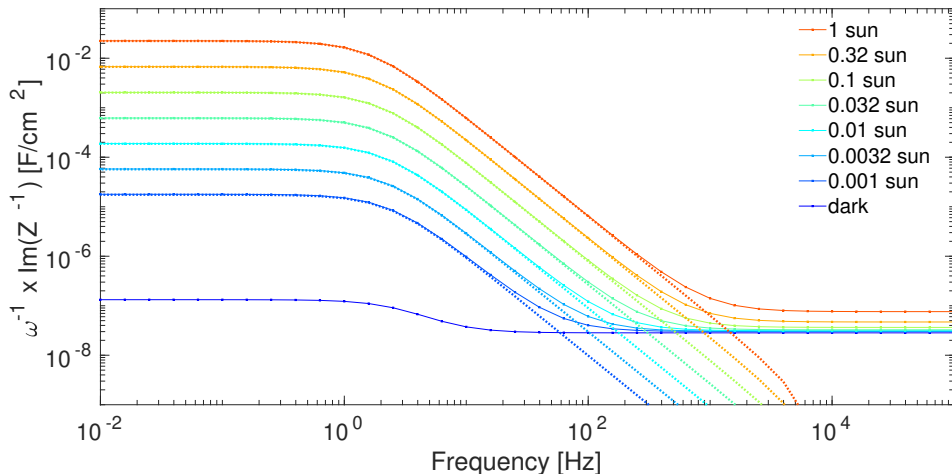
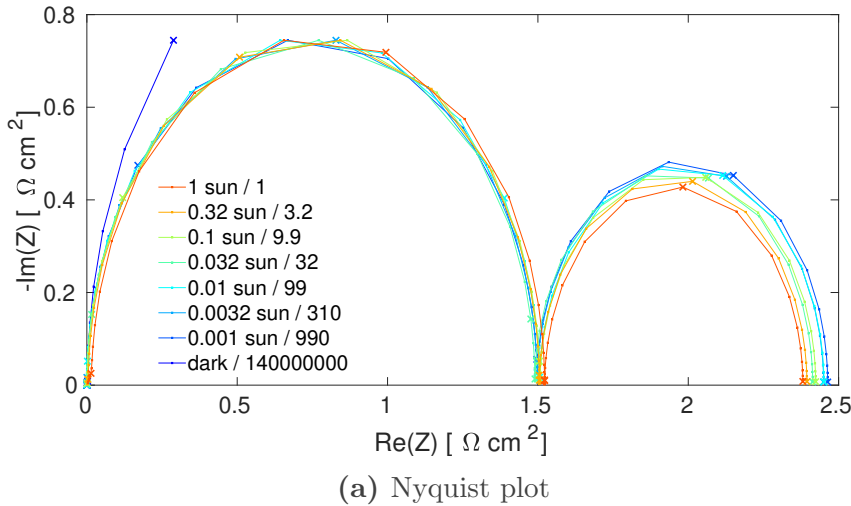
6

**Figure 6.7: Band diagram, energy barriers, and circuit representation of a diode or a transistor.** The conduction band (solid lines) and electron quasi-Fermi level (dashed lines) of a HTM (left) perovskite (centre) ETM (right) solar cell is represented as varied by an oscillating voltage at mid and high frequencies in (a) and at low frequencies in (b). The electrons recombination barrier is indicated in green for the minimum applied voltage and orange for the maximum one. In (c) the energy barrier (black line) in a diode with applied voltage  $V$  is represented. In (d) the energy barrier in a transistor is represented, with contributions from the applied voltage  $V$  and an external voltage  $V_1$ . Pink rectangles indicating the barrier for the non-biassed case are added as graphical reference. In (e) a classical circuit including the geometric capacitance and the Schottky junction diode is represented, it matches the perovskite solar cells behaviour at mid and high frequencies. In (f) the ionic accumulation is represented as a ionic capacitor, ionic transport as a resistance, the influence of ionic accumulation on the interfacial diode is made explicit by the inclusion of a transistor where the potential in ionic branch acts as a gate.

the oscillating voltage. The equivalent electrical circuit for this regime is represented in fig. 6.7e.

**Illuminated case – Recombination barriers with ions.** When we simulate in the low frequency regime, the ions accumulate and deplete close to the interface in a capacitive manner, as described in the previous paragraph and represented in fig. 6.3d. In our simulation, the ionic concentration was enough to screen the electric field inside the perovskite layer within a few tens of nanometres from the material's interfaces. In the low frequency, the ions have time for continuously screening the field induced by the varying voltage, as represented in fig. 6.7b. Contrariwise to what happened at mid and high frequencies in fig. 6.7a, we can see how at low frequency the variation of the recombination energy barrier is not just the applied voltage. The electrostatic contribution by the high concentration of ionic charge also contributes to this barrier. Checking the energy barrier in a transistor, as represented in fig. 6.7d, we can see how this circuit element can include the contribution of two different potentials: the applied voltage  $V$  and the ionic electrostatic potential  $V_1$ . In the equivalent electrical circuit, we can include the ionic capacitance as in fig. 6.5b and replace the interfacial diode with a transistor having the ionic potential as the gating potential, as represented in fig. 6.7f. So, now we know that the recombination current will depend both on the applied voltage and on the capacitive ionic current. The latter contribution, being capacitive, happens  $90^\circ$  out-of-phase with regards to the oscillating applied voltage. This key point means that the, otherwise in-phase, recombination current gains an out-of-phase component due to the ionic motion. This out-of-phase current, as pointed out in eq. (6.6), contributes to the apparent capacitance. Indeed, if we use the recombination current, calculated as described in page 149, for calculating an impedance and the relative apparent capacitance, we can see that this matches perfectly the simulated apparent capacitance, as reported in fig. 6.8b. This low frequency feature accounts for the arch on the right of the Nyquist plot represented in fig. 6.8a.

**Illuminated case – Minority carriers density point of view.** The same concept can also be understood thinking about carriers concentrations rather than energy barriers. As represented in fig. 1.4, the distance of the quasi-Fermi level from the corresponding band level indicates the density of the corresponding carrier. In figs. 6.7a and 6.7b the vertical arrows indicate the distance of conduction band quasi-Fermi level from conduction

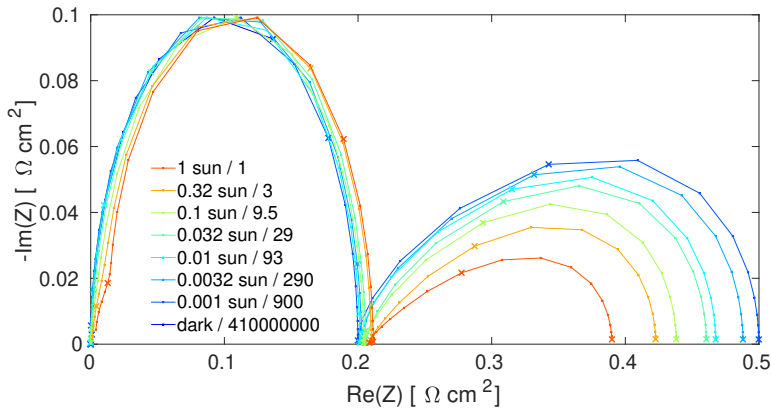


(b) Apparent capacitance from recombination current

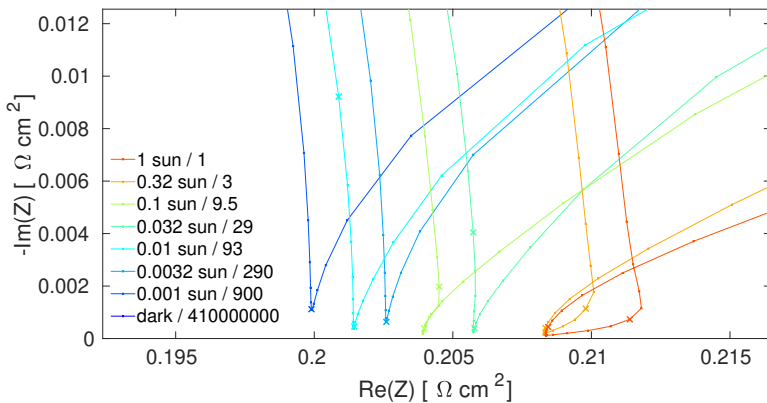
**Figure 6.8: Simulated apparent capacitance spectra and Nyquist plot compared with capacitance due to recombination current.** In (a) the normalised Nyquist plot is reported, the normalisation factor is reported in the legend. The cross markers indicate the even frequency decades (*i.e.* from right to left 0.01, 1, 100 Hz...) so that the mid frequency minimum of 1 sun curve is around 1000 Hz. In (b) the apparent capacitance spectra (solid lines) is compared with the capacitance calculated from the out-of-phase recombination flux (dotted lines).

band, the closer the higher the electrons concentration. The position of the arrows is the interface between the *p*-type and the perovskite layer, so it is the region where the surface recombination annihilates electrons in the perovskite with the holes majority carriers in the HTM. As we saw in page 17, the surface recombination is driven by the amount of “minority” carriers, that in this case are the electrons. The variation of the ionic species accumulation at the interface, simply due to ions electrostatic effect attracts or repels the electronic charges changing their concentration and ultimately modulating the surface recombination. It is important to remember that the recombination flux is always present, especially when no current is measured as it counterbalances the photogeneration. The ions accumulate and deplete at the interfaces following the applied voltage but with a delay, and this induces an out-of-phase component to the aforementioned recombination flux. So if the recombination flux is large, due to a high illumination intensity or a high applied voltage, also this component will be large and, if mistaken for a capacitive current, can explain the reports about giant capacitance.

**Loops in the positive semi-plane and large perturbations.** In Moia *et al.* [2] we showed that the failure in stabilising the device to the measurement conditions (temperature, background voltage, illumination) results in loops in the Nyquist plot positive semi-plane. Additionally, a large perturbation measurement, which is a wide sinusoidal voltage oscillation amplitude in impedance measurements, has been simulated to also cause loops in the Nyquist plot positive semi-plane, as represented in fig. 6.9. This observation comes merely from simulations, no experimental confirmation is available yet. The fact that a large voltage perturbation causes a non-sinusoidal current output is not a problem for the measurement itself, as the lock-in amplifiers are perfectly able to extract amplitude and phase of the signal’s first harmonic (as shown in fig. 6.1), ignoring the higher harmonics.



(a) Nyquist plot with large perturbations



(b) Zoom into mid frequency region

6

**Figure 6.9: Simulated Nyquist plot for large perturbations simulation.** In (a) the normalised Nyquist plot of a simulation with 200 mV wide oscillating voltage is represented. Normalisation factor is indicated in the legend. In (b) zoom at mid frequencies region of the same Nyquist plot, where loops can be observed in the high intensity curves.

## 6.5 Comparison of simulated and experimental impedance spectra

**Lack of low frequency plateau.** Simulating down to very low frequency we observe a plateau in the apparent capacitance, which, as shown in figs. 6.10c and 6.10d, experimentally is not usually observed [248] with

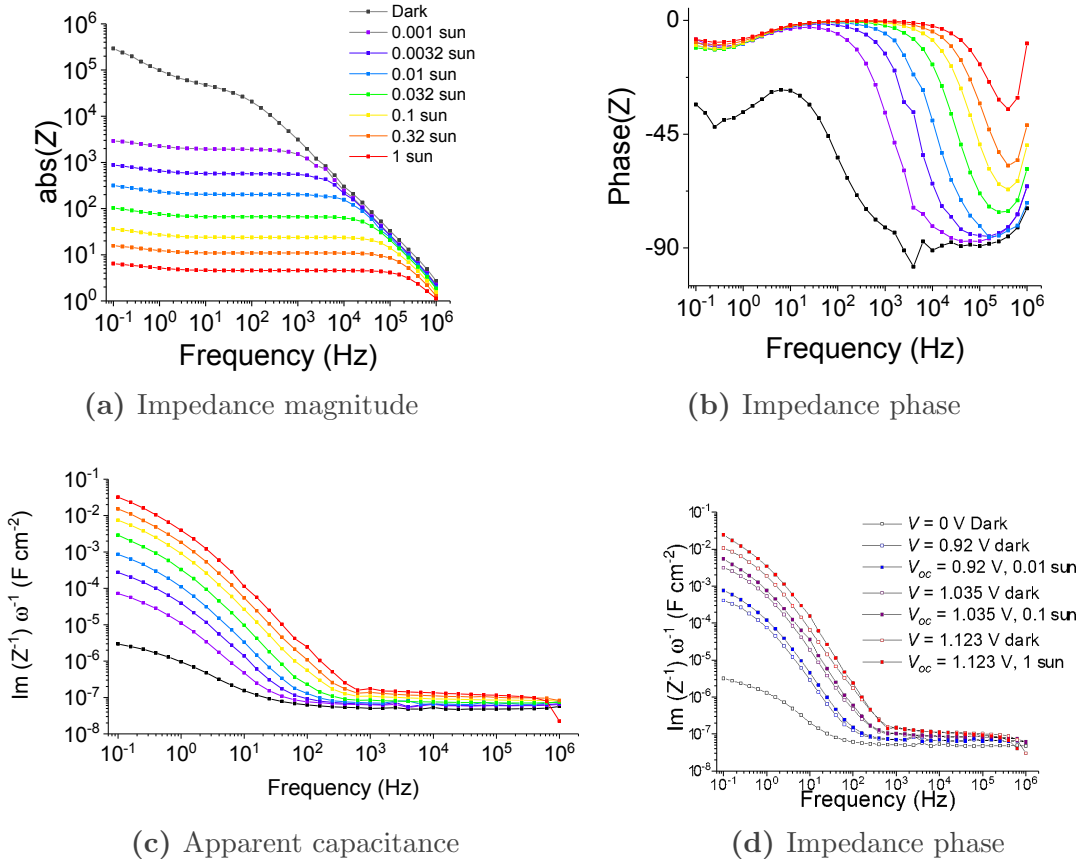


**Figure 6.10: Experimental data from impedance spectroscopy.** In (a) the absolute value of the experimental impedance of an illuminated perovskite solar cell at open circuit conditions is reported. In (b), for the same conditions, the phase of the experimental impedance is reported, it can be compared with simulated data in fig. 6.6a. In (c), for the same conditions, the experimental apparent capacitance is reported, it can be compared with simulated data in fig. 6.2. In (d) the apparent capacitance measured in the mentioned conditions is compared to the measurement performed in dark applying a voltage bias  $V_{DC}$  equal to the measured light bias. These experimental data are courtesy of Dr. Davide Moia and Dr. Piers Barnes.

a few exceptions [259]. The lack of a plateau has been interpreted by Jacobs *et al.* [99] with the presence of more than one mobile ionic species, which is quite likely as seen in page 26. Additionally, we hypothesized [2] that this effect could arise from the different ionic mobility in perovskite when infiltrated in mesoporous layers; dispersive transport in disordered material regions [263] where the mobility varies over time and position; or mostly diffusive transport of ions in the mesoporous layers which could

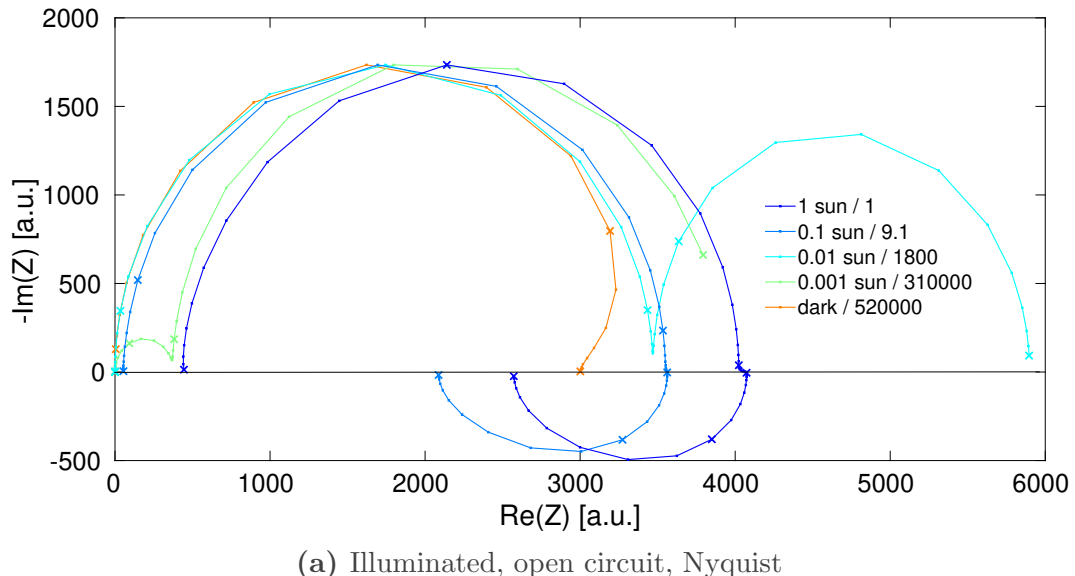
be better described by a Warburg diffusion element in the equivalent electrical circuit.

**Short circuit.** Both the simulation at open circuit with illumination or at dark with applied background voltage bias matches quite nicely the experimental data. On the contrary, the simulation at short circuit with illumination showed a low frequency apparent capacitance increase of just 30 times from dark to 1 sun, while experimentally a giant capacitance is also observed. This discrepancy is left unexplained, a closer look is needed in order to understand which physical phenomena is not implemented in the model or, more simply, which variable is far from the realistic value. Indeed, when using the more advanced heterojunction version of Driftfusion, an increase of  $\approx 50\,000$  times has been observed between the dark and the 1 sun case at low frequency (and no negative capacitance), which is closer to the experimental observation.

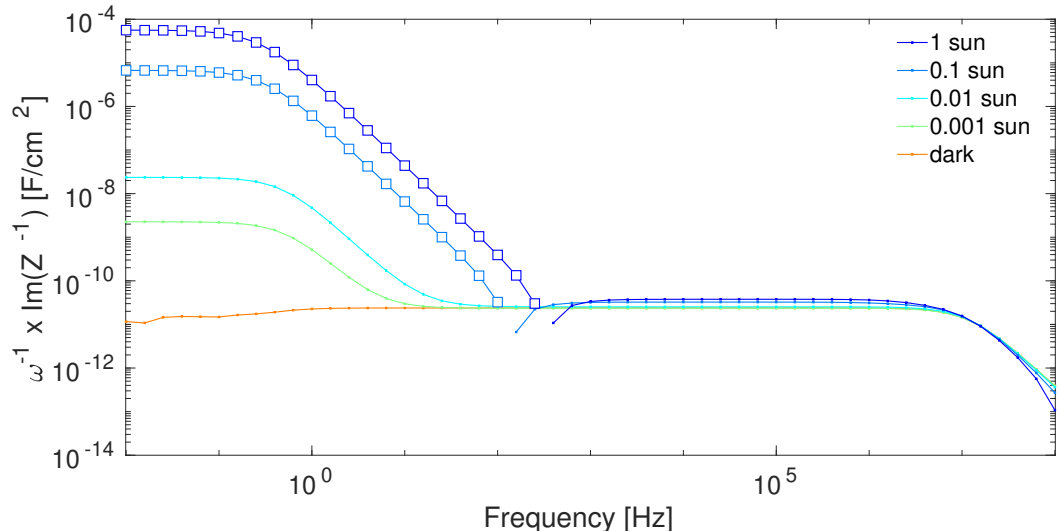
## 6.6 Further development

**Heterojunction.** The simulations shown here are all based on a *p-i-n* homojunction model, so a proper injection barrier could not actually be simulated and the negative capacitance we reported in Moia *et al.* [2] has been obtained playing with extreme values of the mobility and recombination parameters. An attempt of adapting the impedance scripts to the most recent heterojunction version of Driftfusion confirmed the presence of negative capacitance due to injection barrier modulation by ionic charge, as shown in fig. 6.11. This confirms that our hypothesis of the ionically modulated injection barrier can be used for explaining the experimentally observed negative capacitance [2, 250–252]. Further work is needed for completely adapting the impedance scripts to the upstream heterojunction core code.

**Complete simulation of ElectroAbsorbance.** We refer with the names of ElectroAbsorbance or Stark spectroscopy to the absorbance variation caused by an oscillating applied voltage, as described by the Franz-Keldysh effect. This effect stems from the higher absorptivity of a material in presence of an electric field. This simulation has already been implemented but the code release is waiting for the publication of the related work; the description of the modules is already available in page 191.



(a) Illuminated, open circuit, Nyquist



(b) Illuminated, open circuit, apparent capacitance

**Figure 6.11: Preliminary simulations of impedance on heterojunction model.** The filled symbols indicate positive capacitance values, the hollow symbols represents negative capacitance which was changed in sign in order to be plotted on the same axis.

**Implement other similar techniques.** Using some of the modules already implemented for impedance spectroscopy simulation, it should be easy to implement also other characterisation techniques like Intensity-Modulated Photovoltage/Photocurrent Spectroscopy (IMVS, IMPS) [42, 247] and Mott-Schottky capacitance analysis [264].

**Faster simulation with voltage step.** The first implementation of the impedance spectroscopy simulation done in November 2017 did not employ the complete description of the oscillating voltage. Just a voltage step was applied and the resulting current evolution was used for obtaining a rough approximation of the apparent capacitance spectrum. This approach is computationally much faster than a complete oscillating simulation and can give exactly the same results if properly treated for converting the time-domain data to frequency-domain using a Fourier transform. In the publication by Jacobs *et al.* [99], they used this approach for simulating impedance spectroscopy in perovskite solar cells. Our preliminary implementation needs to be refined and at this stage is not ready for being published. Following this approach, we can obtain frequency domain simulations for IMVS, IMPS, and impedance spectroscopy respectively from TPV, TPC, and current-voltage step small perturbations (see Supplementary Note 5 or Supplementary Note 4 for sweep large perturbation in Moia *et al.* [2]) simulations in time domain. For example, converting a bi-exponential decay in TPV to frequency domain through Fourier transform, we can obtain two arches in the IMVS Nyquist plot or from a bi-exponential current evolution after a voltage step we can obtain the impedance spectroscopy features (preliminary simulation performed by Dr. Piers Barnes) as shown in fig. 6.12. Ebadi *et al.* [259] also have shown how a device showing current transient with two opposite phases will also show a negative capacitance in impedance spectroscopy. Similarly, for current-voltage sweeps I suppose that the “bumps” (see page 60 and fig. 3.4) and the “negative hysteresis” (forward sweep giving a higher maximum PCE than reverse sweep) which can be observed for some perovskite solar cells at certain scan speeds are also indicative of the presence of negative capacitance in these devices.

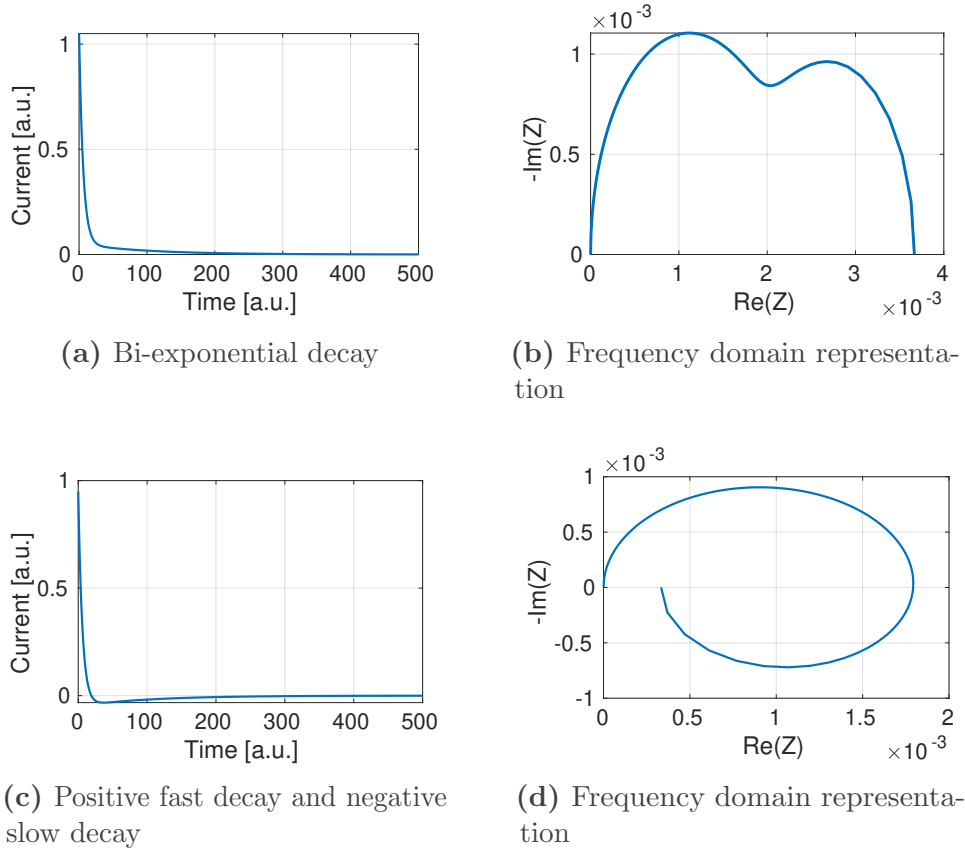


**Figure 6.12:** Example of Fourier transformation of bi-exponential current decays to impedance spectra. In (a) a bi-exponential decay is plotted, it can be thought as the output current profile after a voltage step. In (b) the corresponding Nyquist plot is reported as obtained via Fourier transform, we can see how the profile in (a) causes the presence of two arches. In (c) another kind of bi-exponential shape is represented, in which the slow exponential gives an increasing trend. In (d) the corresponding Nyquist plot shows that we can expect inductive effects for the case represented in (c). The employed code is courtesy of Dr. Piers Barnes.

## 6.7 Implementation of impedance spectroscopy

I choose to split the implementation in independent modules, so that some of them can be easily re-used for other kinds of simulations. The logical flowchart of a complete impedance spectra simulation has been represented in fig. 6.13.

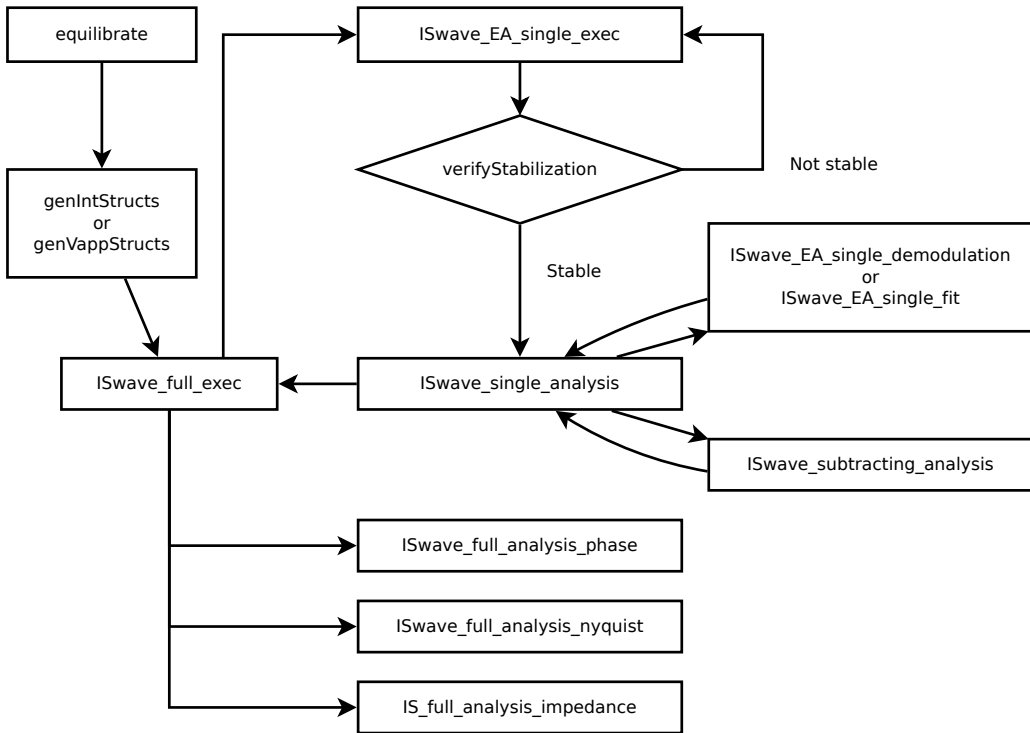


**Figure 6.13: Flowchart of impedance simulation modules.** The representation indicates the logical flow of the simulation, in some parts does not correspond to the actual calls. Also, some of the secondary pieces have been skipped for simplicity. `equilibrate` is part of Driftfusion core and generates stabilised solutions, while `genIntStructs`, `genVappStructs`, and `verifyStabilization` are described in pages 182 and 184.

**ISwave\_EA\_single\_exec – Does a single impedance spectroscopy simulation.** Starting from the last time point of the provided solution it applies a time-varying voltage. This voltage profile is the background voltage bias from the provided solution summed to a sinusoidally oscillating voltage.

**Inputs:** 1) a single asymmetric structure as created by `pindrift`; 2) voltage oscillation amplitude in volts; 3) voltage oscillation frequency; 4) number of periods to be simulated; 5) how many time points should the solution have for each period, suggested to use a multiple of 4; 6) logical, check if the oscillating solution reached a (oscillating) stabilisation, otherwise just use the result of the initial simulation. This can be useful when it is known that the starting solution is not stabilised, for example measuring with an unstabilised ionic profile; 7) logical, set to true when

performing ElectroAbsorbance simulation, this will skip the electrical current calculation; 8) starting relative tolerance of the `pdepe` solver, for example a value of  $1 \times 10^{-8}$  sets for a very precise simulation.

*Outputs:* a structure with a solution being perturbed by an oscillating voltage.

*Requires:* `pindrift`, `verifyStabilization`, `pinana`.

*Required by:* `ISwave_full_exec`, `ISwave_full_exec_nonparallel`, `EA_full_exec`.

*Example:* using `asymmetricize` (see page 183) the symmetric solution at 1 sun illumination and open circuit is broken in halves in order to be able to apply a custom voltage. Then this script simulates an oscillating voltage at 0.1 Hz and 2 mV of half peak to peak voltage amplitude, with a constant voltage bias equal to the device  $V_{OC}$ , 20 periods and 40 time points per period, taking care of reaching a stable solution, and using a starting relative tolerance of  $1 \times 10^{-8}$  and calculates also the electronic current needed by impedance simulations.

```
>> asymssol_i_1S_SR_is_100mHz_2mV =
    ISwave_EA_single_exec(asymmetricize(
        ssol_i_1S_SR), 2e-3, 1e-2, 20, 40, true, false,
        1e-8)
```

**ISwave\_EA\_single\_demodulation – Calculates phase and amplitude demodulating oscillating current data from impedance spectroscopy.** The current profile gets multiplied by the voltage profile and, separately, by the voltage profile with an additional  $90^\circ$  phase. The integrals of the resulting profiles are related to the phase. This simulates the working principle of a dual-phase demodulator often used by lock-in amplifiers. A phase close to  $90^\circ$  results in very small values of the in-phase integral which can have a wrong sign and result in a wrong phase of  $-90^\circ$ , in that case the simulation should be repeated with smaller `pdepe` relative tolerance.

*Inputs:* 1) a column with the time mesh; 2) a column with the value to be fitted, which in case of impedance simulation is the current versus time profile; 3) an anonymous function containing a constant bias, the amplitude of the sinusoid, its phase and the frequency; 4) an array with the parameters used for calculating the applied oscillating voltage in the provided anonymous function.

*Outputs:* an array with the values from the demodulation: constant bias, sinusoid amplitude, phase shift.

*Required by:* ISwave\_single\_analysis, EA\_single\_analysis.

*Example:* demodulate the components of the oscillating current.

```
>> ISwave_EA_single_demodulation(
    asymssol_i_1S_SR_is_100mHz_2mV.t',
    asymssol_i_1S_SR_is_100mHz_2mV.Jn, @(coeff, t)
    coeff(1) + coeff(2) * sin(coeff(3) + coeff(4) *
    t), asymssol_i_1S_SR_is_100mHz_2mV.p.
    Vapp_params)
```

**ISwave\_EA\_single\_fit** – Calculates phase and amplitude fitting oscillating current data from impedance spectroscopy. This is an alternative to ISwave\_EA\_single\_demodulation which can be used to confirm the demodulation results.

*Inputs:* 1) an array with the time mesh; 2) an array with the value to be fitted, which in case of impedance simulation is the current versus time profile; 3) an anonymous function to be used for the fitting, containing a constant bias, the amplitude of the sinusoid and its phase. The frequency is taken as it is from input, it is not fitted.

*Outputs:* an array with the values from the sinusoidal fit: constant bias, sinusoid amplitude, phase shift.

*Required by:* ISwave\_single\_analysis, EA\_single\_analysis.

*Example:* fits the oscillating current versus voltage data for a 200 Hz simulation.

```
>> ISwave_EA_single_fit(
    asymssol_i_1S_SR_is_100mHz_2mV.t,
    asymssol_i_1S_SR_is_100mHz_2mV.Jn, @(coeff, t)
    coeff(1) + coeff(2) * sin(coeff(3) + 2 * pi *
    200 * t))
```

**ISwave\_single\_analysis** – Calculate impedance and phase from impedance spectroscopy data. The imaginary and real components of complex impedance (respectively reactance and resistance) are extracted using either ISwave\_EA\_single\_demodulation or ISwave\_EA\_single\_fit.

*Inputs:* 1) a structure with a solution being perturbed by an oscillating voltage, as generated from ISwave\_EA\_single\_exec; 2) logical, when true graphics does not get created and ISwave\_subtracting\_analysis does

not get launched, useful when launched under parallelization; 3) logical, get phase via demodulation instead of using a fitting.

*Outputs:* 1) array of background current, half peak to peak amplitude of oscillation and phase of total electronic current; 2) array of background current, half peak to peak amplitude of oscillation and phase of ionic displacement current; 3) array of background current, half peak to peak amplitude of oscillation and phase of recombining charge per unit time; 4) array of background current, half peak to peak amplitude of oscillation and phase of accumulating current, this is the real capacitive current, obtained comparing the free charges profiles at different times; 5) array of background current, half peak to peak amplitude of oscillation and phase of non ionic current as obtained via subtraction of ionic current from total electronic current.

*Requires:* ISwave\_subtracting\_analysis, ISwave\_EA\_single\_fit, ISwave\_EA\_single\_demodulation, pinana.

*Required by:* fromISwaveEAStructToTxt, ISwave\_full\_exec, ISwave\_full\_exec\_nonparallel.

*Example:* plot current profile, reference profiles and calculate the phase using demodulation approach.

```
>> ISwave_single_analysis(
    asymssol_i_1S_SR_is_100mHz_2mV, false, true)
```

**ISwave\_subtracting\_analysis – Calculates the time derivative of the total charge in the device.** The charge excess in a device compared with the previous time point gets expressed as a current. This is used as a reference for impedance spectroscopy and for separating the ionic contribution.

*Inputs:* a structure with a solution being perturbed by an oscillating voltage, as generated from ISwave\_EA\_single\_exec.

*Outputs:* 1) charge variation over time in the whole device; 2) charge variation over time in the perovskite layer.

*Required by:* fromISwaveEAStructToTxt, ISwave\_single\_analysis.

*Example:* extract reference values.

```
>> [subtracting_n_t, subtracting_n_intr_t] =
    ISwave_subtracting_analysis(
        asymssol_i_1S_SR_is_100mHz_2mV)
```

**ISwave\_full\_exec** – **Simulates impedance spectroscopy at various frequencies on many provided solutions.** A single structure can be provided as steady state solution to start from for simulating impedance spectroscopy. Alternatively, a cell containing various structures can be provided. For example, if a cell generated using `genIntStructs` (see page 184) is provided, the impedance at various light intensities can be compared. Or, if the provided cell has been generated using `genVappStructs` (see page 184), solutions with different background voltage bias can be compared. If Matlab’s Parallel Computing Toolbox is available, this script runs in parallel on all the available physical CPU cores, otherwise it just runs on one core.

*Inputs:* 1) can be a cell structure containing either symmetrical or asymmetrical structures. Various background light intensities can be provided using `genIntStructs` and various applied voltages using `genVappStructs`. Otherwise it can be a single structure as created by `pindrift`; 2) highest frequency limit; 3) lowest frequency limit; 4) number of points to simulate between the lowest and the highest frequency; 5) voltage oscillation amplitude in volts, 1 mV should be enough but larger values can be employed for reducing the noise or having a large perturbation simulation; 6) logical, after stabilisation sets the mobility of ionic defects to zero to simulate the impedance with effectively frozen ions; 7) logical, determines which method to use for extracting phase and amplitude of the current. If false, always uses fitting via `ISwave_EA_single_fit`, if true uses demodulation via `ISwave_EA_single_demodulation`. Anyway if the obtained phase is weird, fit will be used automatically for confirming the result; 8) logical, whether to graph the individual solutions and the overall graphics.

6

*Outputs:* a structure containing the most important results of the simulation.

*Requires:* `asymmetricize`, `ISwave_EA_single_exec`, `ISwave_single_analysis`, `ISwave_full_analysis_nyquist`, `IS_full_analysis_impedance`, `ISwave_full_analysis_phase`, `pinana`, `stabilize`.

*Required by:* `examples_unit_test`.

*Example:* This is the most typical of the performed simulations: calculate on 8 different illumination intensities including dark, do not freeze ions, use a half peak to peak voltage oscillation amplitude of 2 mV, on 23 points from frequencies of 1 GHz to 0.01 Hz and plot all graphics, including the ones for each solution.

```
>> ISwave_oc = ISwave_full_exec(genIntStructs(
    ssol_i_eq_SR, 1, 1e-3, 7, true), 1e9, 1e-2, 56,
    2e-3, false, true, true)
```

**ISwave\_full\_exec\_nonparallel – Non parallelized version of ISwave\_full\_exec.** The fundamental difference from `ISwave_full_exec` is the lack of `parfor` for parallel computation. This allows more flexibility at the cost of a more time demanding simulation.

*Inputs:* 1-5) identical to `ISwave_full_exec` 1-5 ones; 6) logical, if true do not check that the oscillating solution reached a (oscillating) stabilisation, instead take always the first solution and use its final time point as the starting point of the next frequency simulation. This can be useful when it is known that the starting solution is not stabilised and a realistic simulation of the solution evolving during the measurement is wanted. 7-9) identical to `ISwave_full_exec` 6-8 ones; 10) logic, defines whether to save in volatile base workspace each of the calculated solutions.

*Outputs:* a structure containing the most important results of the simulation.

*Requires:* `asymmetricize`, `ISwave_EA_single_exec`, `ISwave_single_analysis`, `ISwave_full_analysis_nyquist`, `IS_full_analysis_impedance`, `ISwave_full_analysis_phase`, `pinana`, `stabilize`.

*Required by:* `examples_unit_test`.

*Example:* Identical to the example shown for `ISwave_full_exec` but this also saves to base workspace the single oscillating solutions and starts each simulation from the last time point of the previous, strictly sequentially without reaching stabilisation.

```
>> ISwave_oc_sequential =
    ISwave_full_exec_nonparallel(genIntStructs(
        ssol_i_eq_SR, 1, 1e-3, 7, true), 1e9, 1e-2, 56,
        2e-3, true, false, true, true)
```

**ISwave\_full\_analysis\_phase – Represents Bode plots of phase from impedance spectroscopy.** The phase of the current oscillation with regards to the applied voltage is plotted as obtained from simulations made with `ISwave_full_exec` or `ISwave_full_exec_nonparallel`.

*Inputs:* a structure containing the most important results of the simulation.

*Required by:* `ISwave_full_exec`, `ISwave_full_exec_nonparallel`.

*Example:* do phase Bode plots.

```
>> ISwave_full_analysis_phase(ISwave_oc)
```

**IS\_full\_analysis\_impedance** – Represents Bode plots of impedance and apparent capacitance from impedance spectroscopy. Plot the value of absolute impedance magnitude  $|Z|$ , resistance  $Z'$  (real component), reactance  $Z''$  (imaginary component), and apparent capacitance defined as  $\omega^{-1} \operatorname{Im}(Z^{-1})$  at various frequencies and various illumination or background voltage bias conditions. As a reference, the following currents are also used for plotting the mentioned quantities: ionic displacement current, recombination current, and total charge time derivative as obtained from `ISwave_subtracting_analysis`.

*Inputs:* a structure containing the most important results of the simulation.

*Required by:* `ISwave_full_exec`, `ISwave_full_exec_nonparallel`.

*Example:* do impedance and apparent capacitance Bode plots.

```
>> IS_full_analysis_impedance(ISwave_oc)
```

**ISwave\_full\_analysis\_nyquist** – Plots Nyquist graph for impedance spectroscopy. Nyquist plot refers the imaginary component of the impedance to its real component. A normalized spectra is also plotted and the rescaling factors are indicated in the legend.

*Inputs:* a structure containing the most important results of the simulation.

*Required by:* `ISwave_full_exec`, `ISwave_full_exec_nonparallel`.

*Example:* do Nyquist plot.

```
>> ISwave_full_analysis_nyquist(ISwave_oc)
```

**fromISwaveEAstructToTxt** – Exports single impedance simulation data to text files. This helper saves the main data from a oscillating solution created by `ISwave_EA_single_exec` to text files, for easing the import with Origin (from OriginLab).

*Inputs:* 1) a structure with a solution being perturbed by an oscillating voltage, as generated from `ISwave_EA_single_exec`; 2) char array, prefix to be used for the text files names.

*Example:* save single simulation data to text files.

```
>> fromISwaveEAstructToTxt(
    asymssol_i_1S_SR_is_100mHz_2mV, '
    asymssol_i_1S_SR_is_100mHz_2mV')
```

**fromISwaveResultsToTxt – Exports data of a set of impedance simulations to text files.** This helper saves the main data from a complete impedance spectroscopy simulation including various solutions created by `ISwave_full_exec` to text files, for easing the import with Origin (from OriginLab).

*Inputs:* 1) a structure containing the most important results of the simulation; 2) char array, prefix to be used for the text files names.

*Example:* save data from a set of simulations to text files.

```
>> fromISwaveResultsToTxt(ISwave_oc, 'ISwave_oc')
```

**examples\_unit\_test – Runs unit testing on all the implemented experiments.** Runs various simulations in order to test the functioning of pindrift and many other implemented functions. Additionally it verifies that the results satisfies some basic checks. For profiling the time spent running each function run `profile` on before running the tests and `profile viewer` after. Using Matlab's Coverage Reports, the unused code can be easily spotted.

*Requires:* `ideality_from_dark_jVpoints`, `ideality_from_Voc`, `ISwave_full_exec`, `ISwave_full_exec_nonparallel`, `equilibrate_minimal`, `genIntStructs`, `genVappStructs`.

## 6.8 Conclusions

We simulated the output of impedance spectroscopy on illuminated and biassed perovskite solar cells in frequency-domain via drift-diffusion modelling. The code has been released as open source and has been designed to ease the simulation of other frequency-domain characterisation techniques for electronic devices composed of stacked semiconductors with the possibility to consider the presence of mobile ionic species. From the outcome of this model we serendipitously found the likely origin of giant and negative capacitance in perovskite solar cells. These phenomena are explained in detail considering the influence of ionic migration on the recombination and injection current.



# Chapter 7

## Software Development for Drift-Diffusion Modelling, Data Acquisition, and Data Analysis

*“GIGO: Garbage In, Garbage Out”*

**Publication.** The source code of software included in this chapter has been released and can be accessed online. The drift-diffusion Matlab routines have been published on the 2018-EIS branch of the Driftfusion repository, directly accessible from <https://github.com/barnesgroupICL/Driftfusion/tree/2018-EIS>. The current-voltage sweep acquisition Python software can be downloaded from <https://github.com/ilario/PyPV>. The data processing R routines can be examined at <https://github.com/ilario/photophysics-data-processing-R>.

**Abstract.** During my PhD thesis I wrote code mainly for three projects: physical modelling of perovskite solar cells, current-voltage sweep data acquisition, processing and analysis routines for various kinds of characterisation data. All of this work is intended to be re-used by others, so this chapter will detail how to use it and describe the design choices.

---

## Table of Contents

---

**Contributions to Driftfusion**

## INTRODUCTION

## ADDITIONS TO THE DRIFTFUSION CORE

**equilibrate\_minimal** – Generate a reduced set of solutions at standard conditions, 181 • **verifyStabilization** – Verifies if the provided solution has evolved until its steady state, 182 • **stabilize** – Evolves a solution until its steady state, 183 • **asymmetricize** – Break a symmetrical solution, 183 • **changeLight** – Change the illumination intensity of a solution, 183 • **genIntStructs** – Generates a list of solutions at various light intensities, 184 • **genVappStructs** – Generates a list of solutions at various applied voltages, 184 • **findOptimVoc** – Find the exact  $V_{OC}$  minimizing the current output, 184 • **genIntStructsRealVoc** – Generates a list of solutions at various light intensities ensuring open circuit, 185 • **fromSteadyStateStructToTxt** – Exports stabilised solutions data to text for plotting externally, 185 • **plot\_charges\_single** – Plots various density and energy profiles over time, 186 • **ideality\_from\_Voc** – Obtains ideality factor from voltage versus illumination intensity relation, 186 • **ideality\_from\_dark\_jVpoints** – Obtains voltage dependent ideality factor from the stabilised current at different voltages, 186

## CHARGE EXTRACTION

**CE\_full\_exec** – Do Charge Extraction in a range of background light intensities, 187 • **CE\_single\_exec** – Do a single Charge Extraction experiment, 187 • **CE\_full\_analysis** – Plot Charge Extraction in a range of background light intensity *versus* open circuit voltage, 187 • **CE\_full\_fit** – Calculate geometric and chemical capacitance from CE data, 187 • **CE\_ISstep\_single\_analysis** – Calculate charge extracted by Charge Extraction integrating the current, 188 • **CE\_ISstep\_subtracting\_analysis** – Calculate the charge excess in device under illumination, 188

## TRANSIENT PHOTOVOLTAGE

**TPVconst\_full\_exec** – Simulate Transient PhotoVoltage in a range of background light intensities without varying the pulse intensity, 188 • **TPVvariab\_full\_exec** – Simulate Transient PhotoVoltage in a range of background light intensities adapting the pulse intensity for each simulation, 189 • **TPV\_single\_exec** – Perform a single TPV simulation, 189 • **TPV\_full\_analysis** – Plot TPV, 189 • **TPV\_single\_analysis** – Fit voltage decays from single TPV solutions using MultiStart and do graphics, 189 • **TPV\_single\_analysis\_noMultiStart** – Fit voltage decays from single TPV solutions and do graphics, 190

## ELECTROABSORPTION

**EA\_full\_exec** – Perform ElectroAbsorption simulation on all the provided solutions, 191 • **EA\_single\_analysis** – Calculate ElectroAbsorbance and phase, 192 • **EA\_full\_analysis\_Efield** – Plot electric field amplitude from ElectroAbsorption in a range of background light intensities or applied DC voltages, 192 • **EA\_full\_analysis\_phase** –

Plot phase Bode plots from EA in a range of background light intensities or applied DC voltages, 193

## **PyPV: An easy Current-Voltage curves acquisition interface**

### INTRODUCTION

History of the project, 194 • User's requests, 195

### IMPLEMENTATION

Coding language, 195 • Files structure, 195 •  $V_{OC}$  and  $J_{SC}$  estimation, 196 • PCE estimation, 196 • Series and shunt resistances, 196

### USER INTERFACE

Organisation of the main user interface, 196 • User and experiment identification data, 198 • Voltage range and step, 198 • Compliance, 198 • Scale and “Auto Scale”, 198 • Integration time, delay time, and scan speed calculation, 198 • Shutter control, 199 • Quick screening buttons, 199 • Irradiance, device and diode identification, scan direction, 199 • Latest measured parameters output, 199 • Unsaved results indicator, 199 • “Run IV” button, 200 • “Save As...” button, 200 • “AutoSave” button, 200 • “Run a List...” button, 200 • “AutoMeasure” button, 201 • Saved measurements table, 201 • Warnings and pop-up dialogs, 201 • Additional output, 202

### OUTPUT FILES

Directories naming, 203 • Files naming, 203 • Files content, 203 • Configuration saving, 204 • Logging and recovery files, 204

### LIMITATIONS

## **Robust and quick data analysis via R scripts**

### INTRODUCTION

### HELPERS

`limits_for_graphics.R` – Set graphical parameters, 205 • `devices--identification.R` – Define grouping of devices, 205 • `run-all-photophysics.R` – Runs routine data analysis on one device's data, 206 • `run-all-photophysics-comparisons.R` – Plots comparisons between devices, 206

### CHARGE EXTRACTION (CE)

`from_ce_to_table.R` – Converts CE output, 206 • `ce.R` – Integrates CE transients directly, 206 • `ce-subtractDark.R` – Integrates CE transients after subtracting a transformed noise profile, 206 • `ce-integrateExp.R` – Integrates a fit to CE transients, 207 • `ce-from_output_to_graph.R` – Plots the extracted charge versus light bias, 207 • `ce-from_many_output_to_graph.R` – Compares between CE of various devices, 207

### TRANSIENT PHOTOVOLTAGE (TPV)

`from_tpv_tpc_to_table.R` – Converts CE output, 207 • `tpv.R` – Fits TPV decays, 207 • `tpv-from_output_to_graph.R` – Plots TPV lifetimes versus light bias, 208 • `tpv-from_many_output_to_graph.R` – Compares between TPV of various devices, 208

### TRANSIENT PHOTOCURRENT (TPC)

`tpc.R` – Integrates TPC transients, 208

### DIFFERENTIAL CAPACITANCE (DC)

`dc-from_output_to_graph.R` – Calculates and plots capacitance and charge from DC, 208 • `dc-from_many_output_to_graph_capacitance.R`

and `dc-from_many_output_to_graph_charge.R` – Compares between DC of various devices, 209

TRANSIENT PHOTOVOLTAGE REFERRED TO CHARGE FROM CE OR DC (TPV-CE AND TPV-DC)

`tpvce-from_many_output_to_graph.R` and `tpvdc-from_many_output_to_graph.R` – Compare TPV lifetimes related to either CE or DC charge of various devices, 209

#### Contributions to mppTracker

---

## 7.1 Contributions to Driftfusion

*“Wow, this is a gold mine!”*

### 7.1.1 Introduction

During my 3-month stay in Dr. Piers R. F. Barnes and Prof. Jenny Nelson groups in Imperial College London, I utilized and expanded a modelling software developed by Dr. Phil Calado, Dr. Mohammed Azzouzi, Benjamin Hilton, and Piers R. F. Barnes. As the modelling software had already demonstrated a great descriptive power [28, 98, 210], I implemented a few more characterisation techniques with the objective of reproducing and understanding real-world data. The impedance spectroscopy simulation is not included here as it has been treated in chapter 6. Driftfusion [98, 265] is a time resolved, one dimensional, drift-diffusion modelling platform. It takes advantage of Matlab `pdepe` solver for partial differential equations with boundary conditions in time and one spatial dimension. Currently, it can simulate the electrostatic potential, and the density of electrons, holes and one ionic species at specified depths in a multi-layered electronic device and at specified time points. Even if an heterojunction version of the code is available, I implemented functions for the homojunction (every material has the same bandgap) release, which is much more stable and tested. All the described scripts can be obtained from <https://github.com/barnesgroupICL/Driftfusion/tree/2018-EIS>.

### 7.1.2 Additions to the Driftfusion Core

```
>> 0.1 + 0.2 == 0.3
ans =
logical
0
```

MATLAB

7

`equilibrate_minimal` – **Generate a reduced set of solutions at standard conditions.** It is a reduced version of `equilibrate`. Uses analytical initial conditions and runs to equilibrium and steady state, obtaining

just the most important solutions Takes the parameters from `pinParams.m` file and tries to obtain a steady state solution (as if the device has been left for a long period of time). This solution can then be used as accurate initial conditions for other simulations, e.g. a JV scan. Note that the stabilisation time is consistently adjusted to appropriate values for to ensure there are numerous mesh points where large gradients in the time dimension are present.

*Inputs:* optional, struct containing the needed parameters as obtained from `pinParams.m`.

*Outputs:* `sol_eq` - short circuit, dark, no mobile ionic defects, no SRH; `sol_i_eq` - short circuit, dark, mobile ionic defects, no SRH; `sol_i_eq_SR` - short circuit, dark, mobile ionic defects, with SRH; `ssol_i_eq_SR` - open circuit, dark, mobile ionic defects, no SRH; `ssol_i_eq_SR` - open circuit, dark, mobile ionic defects, with SRH; `sol_i_1S_SR` - short circuit, 1 sun, mobile ionic defects, with SRH; `ssol_i_1S_SR` - open circuit, 1 sun, mobile ionic defects, with SRH.

*Requires:* `pindrift`, `pinParams`, `stabilize`.

*Required by:* `examples_unit_test`.

**verifyStabilization – Verifies if the provided solution has evolved until its steady state.** Checks if the solution reached a stabilised (i.e. steady state) status comparing the final time point with a manually specified time point. Beware that this can have false positives when the analysed solution had been run over a time which is so small that the ionic movement did not even start. For each variable under study, the comparison integrates over the solution thickness the absolute value of the difference in the profile of this variable at two different times in the solution. If this integrated difference is larger than  $1 \times 10^{-4}$  times the integrated profile of the same variable at the final time point at which its spatial average value has been subtracted, the solution is considered as not stabilised yet. The definition of this last threshold, will cause completely flat profiles to be unsuitable for this check. The variables which are employed are: ionic density, electrostatic potential, decimal logarithm of electrons density and decimal logarithm of holes density.

*Inputs:* 1) a solution matrix, not the full structure, as contained in structures created by `pindrift`; 2) the time mesh array, as generated by `meshgen_t` and included in structures created by `pindrift`; 3) the fraction of final time that can be used as a reference. In case of a stabilisation, the smaller the stricter the check, for example if a solution has been run over 10 s, and the provided fraction is  $1 \times 10^{-5}$ , the script will compare the

solution at  $0.1\text{ }\mu\text{s}$  with the final one at  $10\text{ s}$ . In case of a periodic time evolution, a specific value corresponding to the previous-to last cycle have to be used. The value needs to be strictly between 0 and 1.

*Outputs:* a logic (true/false) asserting if the solution in input reached its stability.

*Required by:* `CE_full_exec`, `CE_single_exec`, `findOptimVoc`, `ISwave_EA_single_exec`, `stabilize`, `TPVconst_full_exec`, `TPV_single_exec`.

**stabilize – Evolves a solution until its steady state.** Simulates the solution increasing the maximum time until when steady state is reached. `verifyStabilization` is used for checking the reaching of the steady state. For all the simulations including transients, the stabilisation of the starting solution is of utmost importance.

*Inputs:* 1) a solution structure as created by `pindrift`; 2) optional boolean, true by default, if true forces the simulation to run at least once, if false the stabilisation is run just when needed.

*Outputs:* a solution structure that reached its steady state.

*Requires:* `pindrift`, `verifyStabilization`.

*Required by:* `CE_full_exec`, `changeLight`, `equilibrate`, `equilibrate_minimal`, `findOptimVoc`, `genIntStructsRealVoc`, `genVappStructs`, `ideality_from_dark_jVpoints`, `ISwave_EA_single_exec`, `ISwave_full_exec`, `ISwave_full_exec_nonparallel`, `TPV_single_exec`.

**asymmetrize – Break a symmetrical solution.** Break a symmetrical solution (a symmetrical solution it is a repeated  $p-i-n-n-i-p$  stack, mainly used for simulating open circuit conditions, so that no boundary condition has to be set for the cathode) in two halves. Has the opposite use of the `symmetricize` function. Please note that further stabilisation could be required.

*Inputs:* a symmetric structure as created by `pindrift` using the OC parameter set to 1.

*Outputs:* an asymmetric structure as created by `pindrift` using the OC parameter set to 0 and applied voltage identical to the open circuit voltage taken from the input symmetric structure.

*Requires:* `pindrift`

*Required by:* `CE_full_exec`, `genIntStructsRealVoc`, `ISwave_full_exec`, `ISwave_full_exec_nonparallel`, `EA_full_exec`.

**changeLight – Change the illumination intensity of a solution.** Generate solutions at a new light intensity.

*Inputs:* 1) a solution structure as created by `pindrift`; 2) the requested light intensity, zero is not supported as it is much more robust to obtain a dark solution directly from `equilibrate`; 3) the initial stabilisation time, can be zero for an automatic guess.

*Outputs:* a solution structure at the new light intensity.

*Requires:* `pindrift`, `stabilize`.

*Required by:* `equilibrate_minimal`, `genIntStructs`.

**genIntStructs – Generates a list of solutions at various light intensities.** Generates a cell containing structures of solutions at logarithmically spaced light intensities, starting from the one at lower light illumination. Can be used for both symmetrical (for obtaining open circuit solutions) or asymmetrical solutions.

*Inputs:* 1) a solution structure as created by `pindrift` in dark conditions; 2) highest requested illumination; 3) lowest requested illumination; 4) number of illumination requested between the lowest and the highest illumination points, including extrema, except dark; 5) logical, whether to include the dark solution in the output structure

*Outputs:* 1) a cell containing structures of solutions at various light intensities; 2) an array with the voltages present in the solution, which is an approximation of the  $V_{OC}$ , getting populated just if the input structures were at open circuit; 3) an array with the currents present in the solutions.

*Requires:* `changeLight`, `pindrift`, `pinana`.

*Required by:* `examples_unit_test`, `genIntStructsRealVoc`.

**genVappStructs – Generates a list of solutions at various applied voltages.** Generates a cell containing asymmetric structures of solutions at various applied voltages. Differently from `genIntStructs` case, here the voltage array has to be specified.

*Inputs:* 1) a solution asymmetric struct as created by `pindrift`; 2) an array containing the requested applied voltages list.

*Outputs:* a cell containing structures of solutions at various applied voltages, ordered with ascending voltages.

*Requires:* `pindrift`, `pinana`, `stabilize`.

*Required by:* `examples_unit_test`.

**findOptimVoc – Find the exact  $V_{OC}$  minimizing the current output.**

Stabilize an asymmetric solution to the real open circuit voltage which is the applied voltage where the current is minimized, starting from the voltage present in the given solution. The suggested workflow is to

stabilise a symmetric solution (so that the charges profile are close to OC conditions) and break in a half with `asymmetricize`. Differently from `findVoc`, this version requires MATLAB's Optimization Toolbox. While the  $V_{OC}$  can be conveniently obtained from the symmetrical solution, in some cases the zero current condition is not matched. For this reason, the search for an applied voltage that minimizes the residual current can be needed.

*Inputs:* an asymmetric structure as created by `pindrift`, ideally breaking a symmetric solution using `asymmetricize` function so that the starting applied voltage is already close to the real  $V_{OC}$ .

*Outputs:* 1) an asymmetric structure as created by `pindrift` using the OC parameter set to 0 and applied voltage identical to the real open circuit voltage; 2) the value of the obtained open circuit voltage.

*Requires:* `pindrift`, `pinana`, `stabilize`.

*Required by:* `genIntStructsRealVoc`.

**genIntStructsRealVoc – Generates a list of solutions at various light intensities ensuring open circuit.** Generates a cell containing structures of asymmetric solutions at various light intensities at an accurate  $V_{OC}$ . This script just uses other three scripts: `genIntStructs`, `findOptimVoc` and `asymmetricize`. Both symmetric and asymmetric solutions are supported in input, but the usage of symmetric solutions is strongly encouraged as the `findOptimVoc` will start from a condition closer to the  $V_{OC}$ .

*Inputs:* 1) a solution structure as created by `pindrift` in dark conditions, preferably a symmetric (open circuit) solution; 2) higher requested illumination; 3) lower requested illumination; 4) number of requested illumination points between the lowest and the highest illuminations, including extrema, except dark; 5) logical, whether to include the dark solution in the output structure.

*Outputs:* 1) cell containing structures of asymmetric solutions at various light intensities with an applied voltage equal to the  $V_{OC}$ ; 2) an array with the  $V_{OC}$  values.

*Requires:* `changeLight`, `pindrift`, `genIntStructs`, `asymmetricize`, `findOptimVoc`, `stabilize`.

**fromSteadyStateStructToTxt – Exports stabilised solutions data to text for plotting externally.** Save the main data from a stabilised solution created by `pindrift` to text files, using a format easy to import

with Origin (from OriginLab). *Inputs:* 1) a structure as created by `pindrift`; 2) a char array to be used as prefix for the saved files names.

**`plot_charges_single` – Plots various density and energy profiles over time.** Plot free charges and ions densities, and energy levels over device thickness and over time. This is inspired by Dr. Phil Calado's `pinExtract2.m` but rewritten. The created graphics include: profiles of net charge density and comparison with the final profile; conduction and valence bands and quasi-Fermi levels profiles; profiles of total concentration of particles densities and comparison with the final profile, divided per particle type; time evolution of voltage, current and specific particles types in specific positions.

*Inputs:* 1) a symmetric or asymmetric structure of a solution evolving over time; 2) optional char array, if provided saves the images in the current directory with the name starting with it.

**`ideality_from_Voc` – Obtains ideality factor from voltage versus illumination intensity relation.** As explained in page 63, the ideality factor can be obtained relating  $V_{OC}$  to the light intensity.

*Inputs:* a cell containing structures at open circuit and various light intensities. The open circuit can be either obtained from symmetric solutions (from `genIntStructs`) or from asymmetric solutions with applied voltage (from `genIntStructsRealVoc`).

*Outputs:* the numeric ideality factor.

*Requires:* `pinana`.

*Required by:* `examples_unit_test`.

**`ideality_from_dark_jVpoints` – Obtains voltage dependent ideality factor from the stabilised current at different voltages.** A voltage dependent ideality factor can be obtained from a dark current-voltage sweep (or stabilised points in the case of hysteretic devices) [266].

*Inputs:* 1) an asymmetric solution structure as created by `pindrift` in dark conditions; 2) the maximum voltage point; 3) the distance between voltage points.

*Outputs:* an array of ideality factor at different applied voltages.

*Requires:* `pindrift`, `pinana`, `stabilize`.

*Required by:* `examples_unit_test`.

### 7.1.3 Charge Extraction

Careful stabilisation of illuminated solutions is crucial, especially for avoiding glitches appearing at high light illumination (minority charges accumulation at the edges of the symmetric solution).

**CE\_full\_exec – Do Charge Extraction in a range of background light intensities.** *Inputs:* 1) can be a cell structure containing structures at various background light intensities. This can be generated using `genIntStructs`. Otherwise it can be a single structure as created by `pindrift`; 2) logical, whether to graph the individual solutions and the overall graphics; 3) logical, whether to assign in volatile base workspace the calculated solutions of single CE decays.

*Outputs:* a structure containing the most important results of the simulation.

*Requires:* `CE_single_exec`, `CE_ISstep_single_analysis`, `CE_ISstep_subtracting_analysis`, `CE_full_fit`, `CE_full_analysis`, `asymmetricize`, `pinana`.

**CE\_single\_exec – Do a single Charge Extraction experiment.** *Inputs:* 1) a single asymmetric structure as created by `pindrift`; 2) a first guess for maximum time which should be enough for registering the full extraction.

*Outputs:* a structure with a solution evolving after the start of the CE experiment.

*Requires:* `pindrift`, `verifyStabilization`.

*Required by:* `CE_full_exec`.

**CE\_full\_analysis – Plot Charge Extraction in a range of background light intensity versus open circuit voltage.** *Inputs:* a structure containing the most important results of the CE simulation.

*Required by:* `CE_full_exec`.

**CE\_full\_fit – Calculate geometric and chemical capacitance from CE data.** *Inputs:* 1) an array containing the voltage drops which were imposed in the CE experiments. As usually the CE experiments goes from open circuit to short circuit, the voltage drop is equal to the  $V_{OC}$ ; 2) an array with the extracted charges from CE at various light intensities.

*Outputs:* an array with the values from the linear + exponential fit: linear gradient, exponential function linear factor, exponent.

*Required by:* CE\_full\_exec.

**CE\_ISstep\_single\_analysis – Calculate charge extracted by Charge Extraction integrating the current.** *Inputs:* 1) a structure with a solution being perturbed by CE; 2) original light intensity is needed in input as the solution provided in input for CE is in dark; 3) logical, whether the residual current should be subtracted, usually false for CE; 4) logical, whether to calculate the ionic contribution and graph the solution.

*Outputs:* 1) array of cumulative charge extracted at each time point; 2) index of the previous array indicating the end of the early extraction, time at which the electronic charge have been extracted but the ionic defects did not move yet.

*Required by:* CE\_full\_exec.

**CE\_ISstep\_subtracting\_analysis – Calculate the charge excess in device under illumination.** The carriers density profile in the illuminated steady state solution is subtracted from the profiles at all time points of the solution evolving during the charge extraction experiment. These profiles are integrated over the device thickness, obtaining a time resolved excess charge amount. This is used as a reference for Charge Extraction.

*Inputs:* 1) structure of the stable solution before the CE experiment, to be used as a reference; 2) structure of the solution perturbed by CE.

*Outputs:* 1) array of excess charges in the whole device versus time; 2) array of excess charges in the intrinsic layer versus time.

*Required by:* CE\_full\_exec.

#### 7.1.4 Transient PhotoVoltage

7

**TPVconst\_full\_exec – Simulate Transient PhotoVoltage in a range of background light intensities without varying the pulse intensity.** The pulse intensity is tuned to be a small perturbation compared to the 1 sun background illumination, then the TPV is simulated for all the provided solutions without changing the chosen pulse intensity.

*Inputs:* 1) can be a cell structure containing structures at various background light intensities. This can be generated using genIntStructs. Otherwise it can be a single structure as created by pindrift; 2) logical, whether to assign in volatile base workspace the calculated solutions of single TPV decays.

*Outputs:* a structure containing the most important results of the simulation.

*Requires:* TPV\_single\_exec, TPV\_single\_analysis.

**TPVvariab\_full\_exec – Simulate Transient PhotoVoltage in a range of background light intensities adapting the pulse intensity for each simulation.** For each of the provided solutions, the pulse intensity is tuned to be a small perturbation compared to the background illumination intensity, then the TPV is simulated.

*Inputs:* 1) can be a cell structure containing structures at various background light intensities. This can be generated using genIntStructs. Otherwise it can be a single struct as created by pindrift; 2) logical, whether to assign in volatile base workspace the calculated solutions of single TPV decays.

*Outputs:* a structure containing the most important results of the simulation.

*Requires:* TPV\_single\_exec, TPV\_single\_analysis.

**TPV\_single\_exec – Perform a single TPV simulation.** *Inputs:* 1) a single symmetric (i.e. open circuit) structure as created by pindrift; 2) a first guess for maximum time which should be enough for simulating the full decay, if zero is provided a value of  $1 \times 10^{-5}$  s is used and no further exploration of the simulation time is performed (this is useful when we are just interested in the amount of voltage variation, rather than in the full decay); 3) intensity of the perturbing light pulse.

*Outputs:* a structure with a solution being perturbed by a light pulse.

*Requires:* pindrift, verifyStabilization.

*Required by:* TPVconst\_full\_exec, TPVvariab\_full\_exec.

**TPV\_full\_analysis – Plot TPV.** Both mono and bi exponential fitting results are plotted *versus* light-bias.

*Inputs:* a structure containing the most important results of the TPV simulation.

*Required by:* TPVconst\_full\_exec, TPVvariab\_full\_exec.

**TPV\_single\_analysis – Fit voltage decays from single TPV solutions using MultiStart and do graphics.** Fit the voltage *versus* time profile of the provided perturbed solution with a mono-exponential and a bi-exponential formula. Use Matlab's MultiStart from Global

Optimization Toolbox in order to find the best bi-exponential fitting avoiding local minima. An initial guess from a previous fitting can be provided in input.

*Inputs:* 1) a structure with a solution being perturbed by a light pulse; 2) optional, initial guess for linear factor of fast decay of bi-exponential fit; 3) optional, initial guess for lifetime of fast decay of bi-exponential fit; 4) optional, initial guess for linear factor of slow decay of bi-exponential fit; 5) optional, initial guess for lifetime of slow decay of bi-exponential fit.

*Outputs:* 1) steady state voltage being present before the pulse; 2) maximum voltage variation due to the pulse; 3) linear factor of mono-exponential fit; 4) lifetime of mono-exponential fit; 5) linear factor of fast decay of bi-exponential fit; 6) lifetime of fast decay of bi-exponential fit; 7) linear factor of slow decay of bi-exponential fit; 8) lifetime of slow decay of bi-exponential fit.

*Required by:* TPVconst\_full\_exec, TPVvariab\_full\_exec.

#### TPV\_single\_analysis\_noMultiStart – Fit voltage decays from single

**TPV solutions and do graphics.** Fit the voltage versus time profile of the provided perturbed solution with a mono-exponential and a bi-exponential formula. Try various starting point for helping the convergence of bi-exponential fitting. An initial guess from a previous fitting can be provided in input.

*Inputs:* 1) a structure with a solution being perturbed by a light pulse; 2) optional, initial guess for linear factor of fast decay of bi-exponential fit; 3) optional, initial guess for lifetime of fast decay of bi-exponential fit; 4) optional, initial guess for linear factor of slow decay of bi-exponential fit; 5) optional, initial guess for lifetime of slow decay of bi-exponential fit.

*Outputs:* 1) steady state voltage being present before the pulse; 2) maximum voltage variation due to the pulse; 3) linear factor of mono-exponential fit; 4) lifetime of mono-exponential fit; 5) linear factor of fast decay of bi-exponential fit; 6) lifetime of fast decay of bi-exponential fit; 7) linear factor of slow decay of bi-exponential fit; 8) lifetime of slow decay of bi-exponential fit.

### 7.1.5 ElectroAbsorption

First Law of Software Quality:  
 errors = more code<sup>2</sup>  
 $e = mc^2$

The public release of these routines is waiting for the publication of the related work. We refer to ElectroAbsorption or Stark spectroscopy as the study of the dependency of the absorbance on the oscillating voltage applied on a complete device with semi-transparent electrodes, caused by Franz-Keldysh effect. We simulate the whole *p-i-n* stack but consider the absorption just in the intrinsic layer. Clearly, the Stark effect has to be evaluated locally at any position through the perovskite layer. The attention has been focussed on the first and the second harmonic effects, respectively with the same and the double frequency as the applied voltage. The first harmonic component is driven by the product of the steady state electric field  $E_{DC}(x)$  and the amplitude of the first harmonic of the oscillating electric field  $|E_{AC}|$  at each spatial point. The second harmonic component is related to the square of the oscillating electric field amplitude  $|E_{AC}^2|$  at each spatial point. Thanks to the modularity of the developed routines, some of the functions coded for the impedance spectroscopy modelling are called by ElectroAbsorption routines, specifically: `ISwave_EA_single_fit`, `ISwave_EA_single_demodulation`, and `ISwave_EA_single_exec`.

**EA\_full\_exec – Perform ElectroAbsorption simulation on all the provided solutions.** Similarly to the impedance simulation performed with `ISwave_full_exec`, this routine applies an oscillating voltage on all the provided solutions. One relevant difference is the fact that the current calculation is disabled, making the analysis faster. If Matlab’s Parallel Computing Toolbox is available, this script runs in parallel on all the available physical CPU cores, otherwise it just runs on one core.

*Inputs:* 1) can be a cell structure containing structures at various background light intensities. This can be generated using `genIntStructs`. Otherwise it can be a single structure as created by `pindrift`; 2) higher frequency limit; 3) lower frequency limit; 4) number of frequency points to simulate; 5) voltage oscillation amplitude in volts, one mV should be enough; 6) logical, after stabilisation sets the mobility of ionic defects to zero; 7) logical, whether to graph the individual solutions and the overall graphics.

*Outputs:* a structure containing the most important results of the simulation.

*Requires:* `asymmetricize`, `ISwave_EA_single_exec`, `EA_single_analysis`, `EA_full_analysis_phase`, `pinana`, `EA_full_analysis_Efield`.

**EA\_single\_analysis – Calculate ElectroAbsorbance and phase.** The first and second harmonics are locally calculated and averaged over the device thickness.

*Inputs:* 1) a structure where a solution has been perturbed by an oscillating voltage, as generated from `ISwave_EA_single_exec`; 2) logical, when true graphics does not get created, useful when launched under parallelization (where graphics does not work anyway); 3) logical, whether to fit the position resolved data; 4) logical, get phase via demodulation instead of using a fitting; 5) string, set the directory where to save `.fig` and `.png` image files for second harmonic versus position. To save in the current directory set the dot directory `\.`. To disable saving set `\missing`" value.

*Outputs:* 1) an array of bias, amplitude and phase of the first harmonic; 2) a matrix of bias, amplitude and phase of the first harmonic, each column is a space point; 3) an array of bias, amplitude and phase of the first harmonic for ionic profile; 4) a matrix of bias, amplitude and phase of the first harmonic for ionic profile, each column is a space point; 5) an array of bias, amplitude and phase of the second harmonic; 6) a matrix of bias, amplitude and phase of the second harmonic, each column is a space point; 7) an array of bias, amplitude and phase of the second harmonic for ionic profile; 8) a matrix of bias, amplitude and phase of the second harmonic for ionic profile, each column is a space point; 9) the value of the average squared amplitude of the AC electric field. It would be identical to the amplitude of the second harmonic if the contributions from each spatial point was in phase; 10) a matrix of bias, amplitude and phase of the AC electric field, each column is a space point.

*Requires:* `ISwave_EA_single_fit`, `ISwave_EA_single_demodulation`.

*Required by:* `EA_full_exec`.

**EA\_full\_analysis\_Efield – Plot electric field amplitude from ElectroAbsorption in a range of background light intensities or applied DC voltages.** The amplitude of the spatially averaged electric field first harmonic  $(x_2 - x_1)^{-1} \int_{x_1}^{x_2} x_2 E_{DC}(x) \cdot E_{AC}(x) dx$  and second harmonic  $(x_2 - x_1)^{-1} \int_{x_1}^{x_2} x_2 E_{AC}^2(x) dx$  are plotted versus the applied voltage frequency.

*Inputs:* a structure containing the most important results of the EA simulation.

*Required by:* EA\_full\_exec.

**EA\_full\_analysis\_phase** – Plot phase Bode plots from EA in a range of background light intensities or applied DC voltages. Plots the first and second harmonic phase shift with regards to the applied voltage.

*Inputs:* a structure containing the most important results of the EA simulation.

*Required by:* EA\_full\_exec.

## 7.2 PyPV: An easy Current-Voltage curves acquisition interface

*“So this bug is 7 years old,  
right? Why nobody tried to fix  
it?”*

### 7.2.1 Introduction

The route to a reliable and efficient device is inevitably a long iterative process. In each optimization step a device is fabricated, measured, and the design modified for the next step. Part of the evaluation is just a repetitive process which can be automatized without any loss. Current-voltage sweeps is the most frequently employed characterisation technique for solar cells, for this reason a fast and easy data acquisition software has been developed. The complete software can be downloaded from <https://github.com/ilario/PyPV>.

**History of the project.** As a proof of concept, Dr. Daniel Fernandez Pinto developed in 2015 a Python library and a small graphical user interface (GUI) for communicating with Tektronix Keithley 2400 equipment

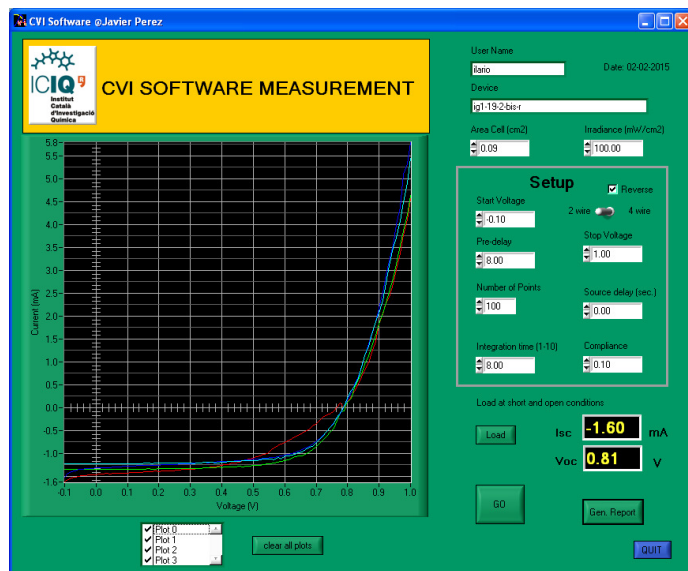


**Figure 7.1:** Legacy software for current-voltage sweep measurement.

via NI-VISA [267] and running basic operations like current-voltage sweeps. I went on adding functions and expanding the GUI until obtaining a fully functional alternative to the legacy LabView software shown in fig. 7.1. In comparison to the mentioned legacy software, PyPV has the advantage of not needing any commercial license which allowed us to use it on various computers. Additionally some of the features which will be described below were just missing in the previous software. As far as I know, PyPV is currently used in the following research institutions: ICIQ (Institut Català d'Investigació Química), URV (Universitat Rovira i Virgili), İzmir Katip Çelebi Üniversitesi, and Karamanoglu Mehmetbey University.

**User's requests.** The feedback from the new users of the software helped me improving PyPV with the following features: solar simulator shutter control, more robust connection to the GPIB-USB-HS adapter, better installation instructions.

### 7.2.2 Implementation

*“Ok, I finally completed it, by the way, why did you start developing this?”*

*“Well, it was just a proof of concept, but it’s nice you worked on it”*

**Coding language.** Python 2, rather than the most recent Python 3, has been chosen for the software development. This apparently stupid choice was motivated by the requirement of running the software on the obsolete Windows XP machines still used for the data acquisition. Anyway, the usage of Python has two paramount advantages: it can be used without the need of commercial licenses (which was not the case for the previous software relying on LabView) and it is one of the most popular and easy to read coding languages, which will help the future development by other researchers. In order to further ease the future development, PEP8 coding style guide was respected [268].

**Files structure.** The software is distributed with the following files:

- `PyPV.py` – launcher;

- `mainwindow.py` – main file where quite everything happens;
- `Keithley2400.py` – library for communicating with the hardware;
- `VICurves.py` – where the parameters are extracted from the raw data;
- `mainwindow.ui` – Qt4 graphical interface.

**$V_{OC}$  and  $J_{SC}$  estimation.** The data point respectively closer to zero current or to zero voltage is taken as a first rough approximation. Then, the preceding and following 3 data points are selected, if available. The set of 7 data points is fitted with a parabolic curve and the final  $V_{OC}$  and  $J_{SC}$  values are obtained from the result of the fit.

**PCE estimation.** Instead, for obtaining the maximum power point no fitting is performed and the data point having the maximum  $J \cdot V$  value is returned. From this point and the aforementioned  $V_{OC}$  and  $J_{SC}$  points, the fill factor is calculated (see page 56).

**Series and shunt resistances.** The resistances estimation from current-voltage sweeps have been implemented but should not be considered for measurements on hysteretic devices, as explained in page 61. Series resistance is obtained from a linear fit of 6 current points at the highest applied voltage and should be taken in consideration just for measurements in dark [164]. In order to avoid including points affected by the compliance limit, a check of strict monotonicity for the considered current points is included. Shunt resistance is obtained from the linear fit of 12 current points close to zero applied voltage, if available.

## 7

### 7.2.3 User interface

**Organisation of the main user interface.** The components of the graphical user interface are organised with the following order (from top left to bottom right):

- user and experiment identification;
- experiment setup;
- quick screening buttons;

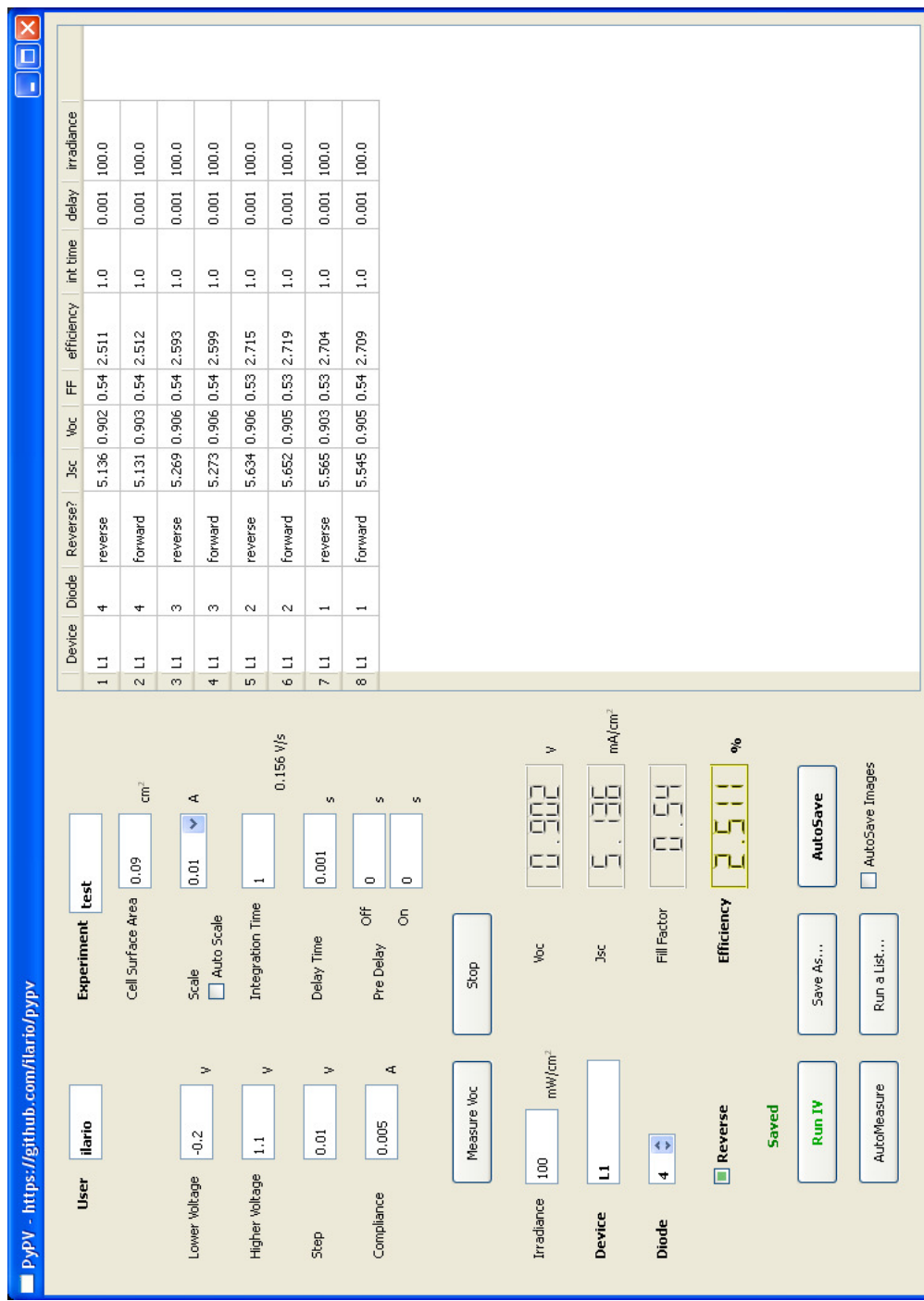


Figure 7.2: PyPV graphical user interface.

- sample identification and single measurement setup;
- single measurement output;
- measurement buttons;
- saved measurements log, from newest to oldest.

**User and experiment identification data.** The user name is prompted, this will be stored in the savings header and, if the “AutoSave” or “AutoMeasure” function is used, a directory named after the user name will be created. The experiment codename is prompted for being prepended in the savings suggested and automatic filenames. The active area is also prompted at this point.

**Voltage range and step.** Then, the lowest and highest voltage limits (i.e. :SOURce:VOLTage:STARt or :SOURce:VOLTage:STOP) are prompted, together with the voltage step (i.e. :SOURce:VOLTage:STEP). The number of measured points (used for the buffer size in :TRACe:POINTs and for the trigger count in :TRIGger:COUNt) can be calculated dividing the voltage range by the voltage step.

**Compliance.** This introduces a maximum limit to the current that can flow in the connected device, in order to avoid overheating and related damages to the solar cell. In order to respect this limit, Keithley equipment reduces the applied voltage (this does not get reflected in the saved output, where the capped regions appears simply as a plateau). The compliance value (i.e. :SENSe:CURRent:PROTection) has to be smaller than the chosen scale.

**Scale and “Auto Scale”.** As it was explained in page 60, the “automatic scale” feature of the Keithley is detrimental for perovskite solar cells dynamic (like a current-voltage sweep) measurements. For this reason a check and a combo box have been added for enabling/disabling automatic scale and setting the manual scale (i.e. :SOURce:CURRent:RANGe).

**Integration time, delay time, and scan speed calculation.** Integration time (i.e. :SENSe:VOLTage:NPLCycles) is the number of power line cycles during which each current point is measured [269]. For example, on a 50 Hz electrical network, an integration time of 1 means that the

current is measured during 20 ms for each voltage point. Delay time (i.e. :SOURce:DELy) is the time waited for the current stabilisation after the voltage step. The scan speed  $s[V/s]$  is obtained from the voltage step :SENSe:VOLTage:STEP  $V_{\text{step}}[V]$ , integration time  $i$  and the delay time :SOURce:DELy  $t_{\text{delay}}[s]$  Keithley's parameters with the following *empirical* expression estimated by Werther Cambarau:

$$s = \frac{V_{\text{step}}}{0.003 + t_{\text{delay}} + 0.06 \cdot i} \quad (7.1)$$

where  $t_{\text{delay}}$  is 1 ms for our measurement conditions.

**Shutter control.** If the employed solar simulator has a remotely controlled shutter, this should be possible to connect to the RS-232 serial port on Keithley. Two parameters control the opening and closing of the illumination shutter: “pre-delay off” and “pre-delay on”. The former indicates how long the illumination should be off, after this, the shutter gets opened and the latter time is waited before running the sweep. The off time is mainly useful when using the “AutoMeasure” feature, which will be mentioned further in the text. During all these steps, the device is kept at open circuit. If the parameters are set to zero, the shutter control is disabled.

**Quick screening buttons.** Open circuit voltage real time measurement is available. This helps the user to have a quick idea of which diodes are worth measuring.

**Irradiance, device and diode identification, scan direction.** Here the user can find the parameters which most likely will vary within an experiment: the illumination intensity, the device identification string (substrate codename), the identification number of the diode in the substrate (with a numeric up-down, in case there are more than one, see fig. 2.1), and the sweep scan direction (with a check box, see page 56).

**Latest measured parameters output.** At the end of each measurement, the calculated performance parameters are printed in four large boxes.

**Unsaved results indicator.** Just after each measurement, a red “Not saved” text remembers to the user that the data needs to be saved, or it will be lost when the next measurement is performed. A green “Saved” text confirms to the user that the latest measurement has been saved.

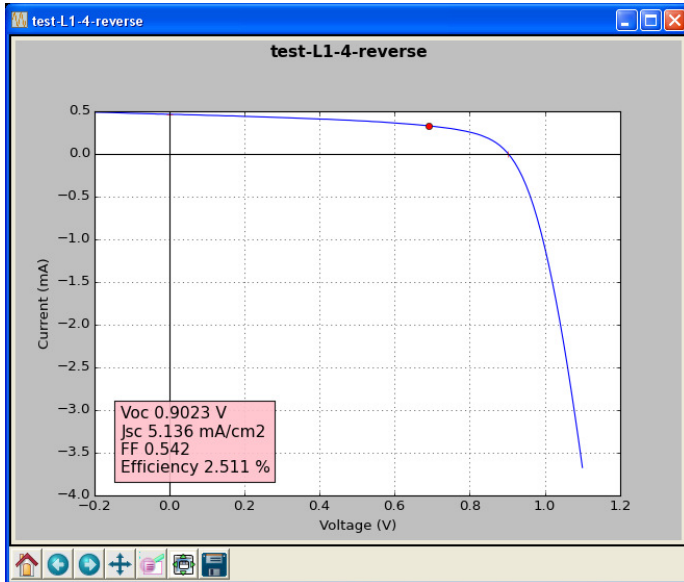


**Figure 7.3:** Current-voltage plot window of PyPV. The plot window includes the main performance data and can be manually resized, zoomed, and saved as an image.

**“Run IV” button.** After closing and opening the illumination shutter, it starts a single current-voltage scan, then updates the parameters shown in the large boxes and spawns a plot window like the one in fig. 7.3.

**“Save As...” button.** Opens a prompt for choosing the saving directory and file name. A suggested file name is provided, as described in page 203, but can be changed. This also adds a line in the saved measurements table on the right side of GUI.

**“AutoSave” button.** Alike the “Save As...” button but it directly employs the directory and the file name obtained from the user name, date, experiment codename, device codename, diode number, illumination intensity, and scan direction as described in page 203. Then adds an entry in the saved measurements table. If the “AutoSave Images” check is active, this also saves a PNG image of the plot in the same directory and with the same base name as the text file but with extension .png.

**“Run a List...” button.** This function allows the user to select a CSV file in which a series of measurements is specified and runs all of these required sweeps. This can be used for saving time in setting up every day the same set of measurements.

**“AutoMeasure” button.** This runs a pre-defined list of sweeps, like the “Run a List...” functions but without asking for an input file. Currently, the measurement steps for AutoMeasure is hard-coded in `mainwindow.py` file. Hopefully I will change this feature to relay on an external file, like for the aforementioned “Run a List...” button. In the current configuration, the measurement procedure is:

1. tells the user (using Keithley’s display and buzzer) to select the diode number 1 in the device under measurement;
2. after waiting for the shutter delays, the illumination shutter is opened;
3. the steady state  $V_{OC}$  is measured;
4. a reverse sweep is measured from  $V_{OC} + 0.2\text{ V}$  to the lowest voltage set in the GUI (the highest voltage setting is ignored);
5. a plot window is spawned and the AutoSave function is called;
6. a forward sweep is measured from the lowest voltage to  $V_{OC} + 0.2\text{ V}$ ;
7. a plot window is spawned and the AutoSave function is called;
8. tells the user to select the next diode and repeats the steps from step #2 on.

**Saved measurements table.** In this table on the right side of the software (see fig. 7.2), the saved measurement identification and parameters are displayed.

**Warnings and pop-up dialogs.** In a few cases, a small window appears warning the user of some problem or asking confirmations:

- no data to save, if the “Save as...” or the “AutoSave” buttons are pressed before any measurement was performed;
- data already saved, when the same measurement is getting saved twice, usually means that one of the two files needs to be deleted, warn the user;
- overwrite, when using “AutoSave”, if a file with the same name is already present ask confirmation for overwriting;



**Figure 7.4: Additional output of PyPV.** In (a) the textual output from console is shown. The printed information is usually not important for normal software usage but can help for debugging. In (b) instructions to the user are delivered via Keithley's display and buzzer.

- saving problem, if the file cannot be saved, for example due to invalid characters in the file name, warn the user;
- unsaved data, whether to run another measurement without saving previous measurement data;
- invalid user, experiment, device, diode, active area, or irradiance, warn the user if these fields cannot be read;
- zero voltage point not crossed, if the requested lowest and highest voltages does not include the zero voltage point, the  $J_{SC}$  will not be measured, a question asks confirmation to the user;
- zero current point not crossed, usually the user is interested to have information also about the  $V_{OC}$ , for this reason a warning is summoned when the sweep did not measure both negative and positive currents;
- when using “Run a List...” button, user handled checkpoints can be introduced and this spawns a question of whether to continue with the measurement;
- when using the “AutoMeasure” button, a warning tells the user that the measured steady state  $V_{OC}$  is out of the requested range.

**Additional output.** Python console in fig. 7.4a is used mainly for reporting additional data e.g. where the files got saved or each of the measured steady state  $V_{OC}$  points. Keithley's display in fig. 7.4b is used for communicating to the user which diode has to be measured during the

“AutoMeasure”. Moreover, the same information is also outputted using Keithley’s buzzer as a number of beeps.

### 7.2.4 Output files

**Directories naming.** When using the “AutoSave” of the “AutoMeasure” functions, the following directory structure is created, if not already existing: `user name/YYYY-MM-DD` where the subdirectory is the measurement date in little endian format.

**Files naming.** When using the “AutoSave” of the “AutoMeasure” functions, inside the aforementioned directory the measurements are named with the following schema: `experiment name-device name-<diode>-<direction>.txt` where `<diode>` is the identification number of the specific diode under measurement, in case there is more than one per substrate (e.g. in our case, each device has four independent diodes, as can be seen in fig. 2.1) and `<direction>` can be either `forward` or `reverse`, as explained in page 56 for the sweep scan direction. In case an illumination different from  $100 \text{ mW cm}^{-2}$  was used, a field is added specifying it in the file name. For example, a typical path and file name could be: `ilario/2019-06-18/ig79-c26-2-0.25sun-reverse.txt`. In order to improve the compatibility with different file systems, the accents in the user name, experiment name, and device name fields are removed using `unicodedata.normalize` function.

**Files content.** In the txt files, the first 22 lines include some information about: user, date and time, experiment name, device name, diode number, scan direction, lowest and highest sweep voltage, voltage step size, compliance (maximum current), scale, calculated voltage and current density of maximum power point, integration time and the related scan speed, delay time for each measured point, pre-delays for closed and opened illumination shutter, calculated series resistance (from the high voltage points) and shunt resistance (from close-to-zero voltage points), active area, irradiance (illumination intensity in  $\text{mW cm}^{-2}$ ), calculated  $J_{SC}$ ,  $V_{oc}$ , fill factor, and PCE. The 23<sup>rd</sup> row include the header for the data. From the 24<sup>th</sup> row on, two columns with applied voltage and measured current follow, separated by a tabulation. The rows are terminated by a `\n` newline, following the Unix standard.

**Configuration saving.** Usually, the setup does not change between experiment and experiment. To reduce the risk of setting wrongly some parameters, some of them are saved in the `last_configuration.lnk` file at the program's closing and restored at its opening. The parameters which get saved are: user name, experiment name, lower and higher voltages, voltage step size, compliance value, scale, integration time, and cell area.

**Logging and recovery files.** The software execution dates and the main parameters of all the performed measurements are stored in a log file: `measurements_log.txt`. In case the user closes the software forgetting to save the last measurement, the data is also saved in two temporary files: `last_measurement_raw.txt` and `last_measurement.txt` containing respectively the latest raw and processed measurement output.

### 7.2.5 Limitations

The interface development has been started with the “Monkey Studio” software, which development has ceased even before the start of PyPV. This demonstrated to be a failure in long term development planning.

## 7.3 Robust and quick data analysis via R scripts

*“Is there an Origin version for Linux?”  
“No”*

### 7.3.1 Introduction

To process the large amount of data which can be obtained using multiple techniques during the characterisation of solar cells can be a very tedious and repetitive work. We developed routines for data processing and representation, like fittings, integrations and plots. I am describing the routines here in order to allow others to use and modify them. The described routines have been tested to work on Linux and Windows systems. All of the described functions can be downloaded from <https://github.com/ilario/photophysics-data-processing-R>. Just the scripts which are relevant for the data published in this thesis will be reported, while many others (e.g. parameter extraction from current-voltage sweeps, statistics on the performance parameters, Tauc plot fitting, logarithmic smoothing of transient absorption spectroscopy data...) can be found online.

### 7.3.2 Helpers

`limits_for_graphics.R` – **Set graphical parameters.** In this file I tried to centralize the parameters which should be edited by the user and will be used by the scripts. This is for avoiding the need to edit “hardcoded” values in the middle of complex scripts. The parameters which can be customized here are: device active area, limits for the axes, string to prepend to the file names, switch between raster or vector image output, resolution of raster images output, size of vector image output.

`devices-identification.R` – **Define grouping of devices.** The devices are labelled with an alphanumeric codename, which is not insightful at the time of categorizing them for a statistical analysis. In this file the samples codes are grouped depending on one or two characteristics. Up to now, this system is just employed by `iv-generate_mydata_with_comments.R` for adding supplementary information to the extracted parameters and

by `iv-generate_statistics.R` for plotting the boxplots separating the samples by kind.

**run-all-photophysics.R – Runs routine data analysis on one device’s data.** An extremely basic but multiplatform GUI has been implemented. Running it, the data folder gets prompted. By default, all the data analysis routinely performed in Palomares group is run. It can be edited to unselect the non-needed data analysis routines.

**run-all-photophysics-comparisons.R – Plots comparisons between devices.** This basic GUI prompts the user for the directories containing the data of each of the devices to be compared. Then it plots the characterisation data of all the selected devices in single plots, in order to help the visual comparison of the results.

### 7.3.3 Charge Extraction (CE)

For details on CE technique, see page 66.

**from\_ce\_to\_table.R – Converts CE output.** The output from CE measurement software is rather minimal, as it lacks the time column. This script generates a two column file output which is more convenient for plotting with other commonly employed software. It works both for the TPV and for the TPC outputs.

**ce.R – Integrates CE transients directly.** Subtracts a base line from the voltage profile (a line joining the first voltage points to the last ones, so it could result in a slightly tilted base line) and divides it by the known instrumental resistance of  $50\Omega$  in order to obtain the current. Then it integrates the current profile over time starting from time zero, which is the moment when circuit gets closed but due to some delay induced by the transistors the current flows just a few tenths of microsecond after, as shown in fig. 3.7a.

**ce-subtractDark.R – Integrates CE transients after subtracting a transformed noise profile.** Uses a pure noise signal obtained for each sample from a measurement in dark (no extracted charge, just instrumental noise due to transistors closing/opening) for fitting the noise profile in the illuminated solutions. Then subtracts the transformed noise profile

and integrates the result over time. See page 69 and fig. 3.7b for a more complete description.

**ce-integrateExp.R – Integrates a fit to CE transients.** Determines the start of the CE decay from the last zero before the voltage maximum, then fits the decay with an exponential function. The fit is performed using a robust fitting routine (as implemented in `robustbase` [177]) in order to avoid the influence from the voltage rise points. The integral function of the fitted exponential function is plotted and its value at infinite time is taken for the extracted charge. See page 69 and fig. 3.7c for a more complete description.

**ce-from\_output\_to\_graph.R – Plots the extracted charge versus light bias.** Plots the output of a series of extracted charges versus light bias voltages. Then it fits the trend using eq. (3.13).

**ce-from\_many\_output\_to\_graph.R – Compares between CE of various devices.** Plots the charge versus light bias trends of all the devices' data in the current directory, like in fig. 4.6a. This is used for comparisons like the one in the right column of fig. 3.7.

### 7.3.4 Transient PhotoVoltage (TPV)

For details on TPV technique, see page 78.

**from\_tpv\_tpc\_to\_table.R – Converts CE output.** Similarly to `from_ce_to_table.R`, this converts the one column raw file to a two columns text file.

**tpv.R – Fits TPV decays.** This rather large routine fits the single TPV decays. The following features can be activated or deactivated editing the script header: bi-exponential fitting, robust fitting [177], save the plots to PNG or PDF files, plot all the data points or use a 2D histogram for reducing the overplotting problem (see fig. 3.16), additionally plot with abscissa and/or ordinate axis in logarithmic scale, plot residuals, allow the fitting to match negative peaks. In order to successfully perform the bi-exponential fits using eq. (3.18), a good initial guess is provided at first and then, if convergence is not obtained, random initial guesses. If cases where this is not enough, some data points from the beginning of the

decay (the most noisy part of the decay) are removed until when the fit converges. Additionally, the voltage increase value  $\Delta V$  is also calculated here and will be used by DC scripts, as explained in page 98.

#### **tpv-from\_output\_to\_graph.R – Plots TPV lifetimes versus light bias.**

This script plots the lifetimes obtained from mono or bi exponential fits in **tpv.R** versus light bias voltage, like in fig. 3.17. Additionally, it fits the high voltage points using eq. (3.20).

#### **tpv-from\_many\_output\_to\_graph.R – Compares between TPV of various devices.**

Similarly to the aforementioned **tpv-from\_output\_to\_graph.R** script, this plots the mono-exponential lifetime versus light bias data for various devices in the same plot, allowing the user to make a graphical comparison.

### 7.3.5 Transient PhotoCurrent (TPC)

For details on TPC technique, see page 95.

#### **tpc.R – Integrates TPC transients.**

Similarly to what **ce.R** does for integrating the CE voltage transient, also this script directly integrates the voltage transients versus time after subtracting a baseline, like in fig. 3.23.

### 7.3.6 Differential Capacitance (DC)

For details on DC technique, see page 98.

#### **dc-from\_output\_to\_graph.R – Calculates and plots capacitance and charge from DC.**

This script takes the photogenerated charge  $\Delta n$  output from **tpc.R** and the voltage increase  $\Delta V$  output from **tpv.R** and obtains the voltage dependent capacitance using eq. (3.23). In case the values from different TPC measures differs, for example due to the presence of background illumination, the first quartile of all the measured  $\Delta n$  is used. The value of the geometric capacitance is obtained fitting the capacitance using eq. (3.25) and then taking the  $C_g$  parameter value. The chemical capacitance profile is obtained subtracting  $C_g$  to the calculated capacitance profile. The obtained capacitance versus light bias discrete profiles are converted to a continuous profile using R's **Vectorize** function and integrated over voltage (see eq. (3.24)) for obtaining the excess charge versus light bias trends with or without geometric capacitance.

`dc-from_many_output_to_graph_capacitance.R` and `dc-from_many_output_to_graph_charge.R` – **Compares between DC of various devices.** The comparison of capacitance and charge from DC is plotted for various devices and fitted using eq. (3.25), like in fig. 3.25. The data to be plotted is taken from the output of `dc-from_output_to_graph.R` script.

### 7.3.7 Transient PhotoVoltage referred to charge from CE or DC (TPV-CE and TPV-DC)

For details on TPV-CE and TPV-DC techniques, see page 92.

`tpvce-from_many_output_to_graph.R` and `tpvdc-from_many_output_to_graph.R` – **Compare TPV lifetimes related to either CE or DC charge of various devices.** The mono-exponential lifetimes from `tpv.R` are plotted versus various charge profiles obtained from CE or DC. In order to squash the light bias axes from the different techniques, the CE or DC charge versus voltage profiles are fitted and the employed charge value at the TPV light biases is obtained from the fit. The charge profiles employed are: complete charge including geometric capacitance, chemical charge subtracting  $C_g$  obtained either with eq. (3.13) for CE or with eq. (3.25) for DC. Fitting the small perturbation lifetimes versus chemical charge using eq. (3.21), the recombination order  $\Phi$  is obtained. This  $\Phi$  is used for correcting the small perturbation lifetimes to total carrier lifetimes (pseudo first order lifetimes) using eq. (3.21) and is plotted again versus chemical charge. An example of all the mentioned plots can be observed in figs. 3.21 and 4.7.

## 7.4 Contributions to mppTracker

*“A student of mine sells a complete system for that, just go and buy it”*

As seen in page 62, a MPPT system ensures to obtain a PCE value closer to the real world working conditions [163]. The hysteretic phenomena in perovskite solar cells requires new procedures for MPPT [270–272] and a few commercial systems are already available for that [273, 274]. An interesting project for having robust MPPT measurable with Tektronix Keithley 2400 is mppTracker [275]. I made a few contributions which are accessible on <https://github.com/AFMD/mppTracker/pulls?q=is%3Apr>. As the effort in this project were very limited on my side, I will not further describe that but an example of the output is reported in fig. 7.5. If confirmed, recent reports on “bistable short circuit current” in perovskite solar cells by Calado [4] would further complicate the implementation of a MPPT.

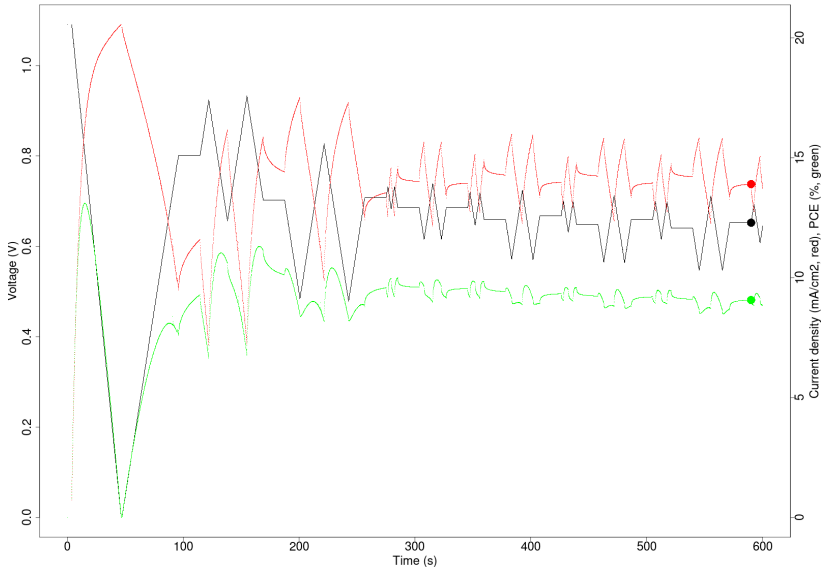


**Figure 7.5: Example of maximum power tracking measurement.** A perovskite solar cell has been measured with an improved version of mppTracker. The black line is the applied voltage and refers to the left axis. The red line is the measured current and refers to the right axis. Te resulting PCE is the green line and is also on the right axis.

# Overall Conclusions

In this thesis, perovskite solar cells have been fabricated and characterised by means of advanced techniques. These techniques have been critically analysed taking advantage of drift-diffusion modelling. The provided contributions have widened the understanding of perovskite solar cells characterisation output, allowing the scientific community to get more information from the already available techniques. This knowledge will help in the identification of performance bottlenecks of photovoltaic devices, easing the solar cells optimization.

The main findings can be summarised as follows:

1. The advanced characterisation output has to be interpreted with great care and the theoretical framework from previous type of photovoltaic devices is no longer enough for perovskite solar cells. In chapter 3 I described and critically analysed the employed characterisation techniques. For each, the strategy for noise reduction is explained and compared with the tested alternatives. Taking advantage of the insight obtained from drift-diffusion modelling the following hypotheses are thrown: time resolved photoluminescence will also evolve with time due to slow ionic profile adaptation to the new illumination conditions; charge extraction experiments should show a long lasting ionic displacement current giving information about ionic capacitance rather than geometric capacitance; I confirm that the exponential trend in charge extraction can be explained with the chemical capacitance and should start at light biases close to the built-in voltage; the fast component of bi-exponential decays in transient photovoltage observed at low background light intensity could be due to ionic profile update before the generated charge recombines.
2. The difference between the contacts' energy levels provides an unreliable estimation of the built-in voltage of perovskite solar cells. In chapter 4 and in [3] we have fabricated bottom cathode devices

with four different HTM ensuring to fulfil the conditions for having a fair comparison. Comparing the built-in voltage of the different solar cells using CE and DC techniques we realised that the involved energy levels are rather different than the values expected from cyclic voltammetry measurements. After excluding major differences in the carriers lifetimes in the four devices, we have measured the *in situ* work function of the HTM. We have observed significant deviations from the substrate value just for some of the HTM and used this result for explained the measured  $V_{OC}$  and built-in voltage.

3. In top cathode ITO/PEDOT:PSS/MAPbI<sub>3</sub>/PC<sub>70</sub>BM/Ag perovskite solar cells, the photogenerated charge at low light intensity and at open circuit conditions is storage location has been observed. In chapter 5 and in [1] we have shown that the holes are accumulated where expected, which is in a depletion layer in the PEDOT:PSS at the interface with the perovskite layer. Regarding the electrons, we have demonstrated that the storage location is not at the PC<sub>70</sub>BM interface with the perovskite, rather it can be close to the metallic electrode/selective contact interface or through the whole ETM layer.
4. Giant and negative capacitance observed in perovskite solar cells via impedance spectroscopy do not involve a giant charge accumulation. In chapter 6 and in [2] we showed that they rather stem from the influence of the ionic movement respectively on the recombination and on the injection barriers. Additionally, the whole apparent capacitance spectra is explained taking advantage of the drift-diffusion results. The simulation method and modular structure is explained in detail.

# Index

## C

charge extraction, 38, 39, 67–77, 80, 85, 92, 93, 98–101, 104, 118–121, 123, 125, 132–136, 138, 206–209

chemical capacitance, 72, 73, 90, 92–94, 104, 118, 119, 187, 208

## D

differential capacitance, 72, 81, 82, 89, 90, 98, 100–102, 104, 118–121, 123, 125, 132–136, 138, 208, 209

displacement current, 13, 14, 69, 77, 78, 118, 148, 150, 155, 156, 171, 174

## E

electron transporting material, 21, 23, 24, 43, 75, 87, 109, 112, 132, 134–136, 138, 151, 158

## G

geometric capacitance, 72, 74, 76, 77, 90, 91, 119, 121, 132–138, 151, 153–155, 157, 158, 208, 209

giant capacitance, 142, 143, 155, 157, 161, 164

## H

highest-energy occupied molecular orbital, 5, 6, 19, 109, 111–113, 118, 123

hole transporting material, 17, 21–24, 35, 41, 43, 45, 47, 48, 109, 110,

112–118, 121–123, 129, 137, 151, 154, 158

hysteresis, 26, 27, 58–62, 64, 117, 130, 143, 186, 196, 210

## L

lowest-energy unoccupied molecular orbital, 6, 17, 19, 20, 113

## M

maximum power point tracking, 61, 62, 210

## N

negative capacitance, 58, 142, 143, 164–166

## S

space charge layer, 8, 10–12, 15, 25, 64, 72, 74–76, 91, 122, 132, 135, 138, 149, 151–153, 157

## T

TAE-1, 33, 47, 109, 111, 112, 118, 122  
TAE-3, 33, 47, 111–113, 117, 118, 122, 123

TAE-4, 33, 41, 47, 111–113, 117, 118, 120, 122, 123

transient photocurrent, 38, 57, 96–99, 101, 166, 208

transient photovoltage, 38, 58, 72, 73, 79–82, 85, 87–90, 92, 93, 96, 98–101, 104, 119–121, 123, 166, 188, 189, 207, 209



# Bibliography

- [1] I. Gelmetti, L. Cabau, N. F. Montcada, and E. Palomares. “Selective Organic Contacts for Methyl Ammonium Lead Iodide (MAPI) Perovskite Solar Cells: Influence of Layer Thickness on Carriers Extraction and Carriers Lifetime”. In: *ACS Applied Materials & Interfaces* 9.26 (July 2017), pp. 21599–21605. DOI: [10.1021/acsmami.7b06638](https://doi.org/10.1021/acsmami.7b06638) (cit. on pp. xxii, 74, 125, 129, 212).
- [2] D. Moia, I. Gelmetti, P. Calado, W. Fisher, M. Stringer, O. Game, Y. Hu, P. Docampo, D. Lidzey, E. Palomares, J. Nelson, and P. R. F. Barnes. “Ionic-to-electronic current amplification in hybrid perovskite solar cells: ionically gated transistor-interface circuit model explains hysteresis and impedance of mixed conducting devices”. In: *Energy & Environmental Science* 12.4 (May 2019), pp. 1296–1308. DOI: [10.1039/C8EE02362J](https://doi.org/10.1039/C8EE02362J). arXiv: [1805.06446](https://arxiv.org/abs/1805.06446) (cit. on pp. xxii, 15, 27, 58, 61, 76, 106, 139, 142, 143, 148, 161, 163, 164, 216, 212).
- [3] I. Gelmetti, N. F. Montcada, A. Pérez-Rodríguez, E. Barrena, C. Ocal, I. García-Benito, A. Molina-Ontoria, N. Martín, A. Vidal-Ferran, and E. Palomares. “Energy alignment and recombination in perovskite solar cells: weighted influence on the open circuit voltage”. In: *Energy & Environmental Science* 12.4 (2019), pp. 1309–1316. DOI: [10.1039/C9EE00528E](https://doi.org/10.1039/C9EE00528E) (cit. on pp. xxii, 24, 25, 27, 33, 43, 68, 81, 84, 92, 93, 96, 100, 101, 107, 111, 113–115, 117, 211).
- [4] P. Calado. “Transient optoelectronic characterisation and simulation of perovskite solar cells”. PhD thesis. Imperial College London, 2018. URL: <https://spiral.imperial.ac.uk/handle/10044/1/66894> (cit. on pp. ii, 83, 85, 91, 144, 210).
- [5] G. Kopp and J. L. Lean. “A new, lower value of total solar irradiance: Evidence and climate significance”. In: *Geophysical Research Letters* 38.1 (Jan. 2011), pp. 1–7. DOI: [10.1029/2010GL045777](https://doi.org/10.1029/2010GL045777) (cit. on p. 3).
- [6] Solargis. *Solar resource maps of World*. 2018. URL: <https://solargis.com/maps-and-gis-data/download/world> (cit. on p. 4).

- [7] UNDP. *Human Development Index*. 2018. URL: <http://hdr.undp.org/en/content/human-development-index-hdi> (cit. on p. 4).
- [8] CIA. *CIA Factbook - Electricity consumption*. URL: <https://www.cia.gov/library/publications/the-world-factbook/rankorder/2233rank.html> (cit. on p. 4).
- [9] CIA. *CIA Factbook - Country land area*. URL: <https://www.cia.gov/library/publications/the-world-factbook/fields/2147.html> (cit. on p. 4).
- [10] R. Margolis, C. Phillips, R. Elmore, P. Gagnon, and J. Melius. “Rooftop Solar Photovoltaic Technical Potential in the United States: A Detailed Assessment”. In: *National Renewable Energy Laboratory* January (2016) (cit. on p. 3).
- [11] IEA. *World Bank with IEA Statistics data*. URL: <https://data.worldbank.org/indicator/EG.USE.PCAP.KG.OE> (cit. on p. 3).
- [12] Wikipedia. *Particle in a one-dimensional lattice*. 2019. URL: [https://en.wikipedia.org/wiki/Particle%7B%5C\\_%7Din%7B%5C\\_%7Da%7B%5C\\_%7Done-dimensional%7B%5C\\_%7Dlattice](https://en.wikipedia.org/wiki/Particle%7B%5C_%7Din%7B%5C_%7Da%7B%5C_%7Done-dimensional%7B%5C_%7Dlattice) (cit. on p. 6).
- [13] C. Kittel. *Introduction To Solid State Physics*. Ed. by S. Johnson. 8th Editio. Wiley, 2004, p. 704 (cit. on p. 6).
- [14] O. Stenzel. *The physics of thin film optical spectra: an introduction*. New York : Springer, 2005, p. 275 (cit. on pp. 6, 112).
- [15] Wikipedia. *Debye length*. 2019. URL: [https://en.wikipedia.org/wiki/Debye%7B%5C\\_%7Dlength](https://en.wikipedia.org/wiki/Debye%7B%5C_%7Dlength) (cit. on p. 12).
- [16] L. M. Herz. “Charge-Carrier Mobilities in Metal Halide Perovskites: Fundamental Mechanisms and Limits”. In: *ACS Energy Letters* 2.7 (July 2017), pp. 1539–1548. DOI: [10.1021/acsenergylett.7b00276](https://doi.org/10.1021/acsenergylett.7b00276) (cit. on pp. 15, 27).
- [17] T. Leijtens, S. D. Stranks, G. E. Eperon, R. Lindblad, E. M. J. Johansson, I. J. McPherson, H. Rensmo, J. M. Ball, M. M. Lee, and H. J. Snaith. “Electronic Properties of Meso-Superstructured and Planar Organometal Halide Perovskite Films: Charge Trapping, Photodoping, and Carrier Mobility”. In: *ACS Nano* 8.7 (July 2014), pp. 7147–7155. DOI: [10.1021/nn502115k](https://doi.org/10.1021/nn502115k) (cit. on pp. 15, 27, 85).
- [18] A. Miyata, A. Mitioglu, P. Plochocka, O. Portugall, J. T.-W. Wang, S. D. Stranks, H. J. Snaith, and R. J. Nicholas. “Direct measurement of the exciton binding energy and effective masses for charge carriers in organic-inorganic tri-halide perovskites”. In: *Nature Physics* 11.7 (July 2015), pp. 582–587. DOI: [10.1038/nphys3357](https://doi.org/10.1038/nphys3357) (cit. on p. 15).

- [19] K. Galkowski, A. Mitioglu, A. Miyata, P. Plochocka, O. Portugall, G. E. Eperon, J. T.-W. Wang, T. Stergiopoulos, S. D. Stranks, H. J. Snaith, and R. J. Nicholas. “Determination of the exciton binding energy and effective masses for methylammonium and formamidinium lead tri-halide perovskite semiconductors”. In: *Energy & Environmental Science* 9.3 (2016), pp. 962–970. DOI: 10.1039/C5EE03435C (cit. on p. 15).
- [20] K. Tvingstedt, O. Malinkiewicz, A. Baumann, C. Deibel, H. J. Snaith, V. Dyakonov, and H. J. Bolink. “Radiative efficiency of lead iodide based perovskite solar cells”. In: *Scientific Reports* 4.1 (May 2015), p. 6071. DOI: 10.1038/srep06071 (cit. on pp. 15, 25).
- [21] C. Wehrenfennig, G. E. Eperon, M. B. Johnston, H. J. Snaith, and L. M. Herz. “High Charge Carrier Mobilities and Lifetimes in Organolead Trihalide Perovskites”. In: *Advanced Materials* 26.10 (Mar. 2014), pp. 1584–1589. DOI: 10.1002/adma.201305172 (cit. on pp. 15, 24, 27).
- [22] J. Nelson. *The Physics of Solar Cells*. Imperial College Press, May 2003. DOI: 10.1142/p276. URL: <https://www.worldscientific.com/worldscibooks/10.1142/p276> (cit. on pp. 15–18, 24, 57, 64, 144).
- [23] M. Stolterfoht, P. Caprioglio, C. M. Wolff, J. A. Márquez, J. Nordmann, S. Zhang, D. Rothhardt, U. Hörmann, A. Redinger, L. Kegelmann, S. Albrecht, T. Kirchartz, M. Saliba, T. Unold, and D. Neher. “The perovskite/transport layer interfaces dominate non-radiative recombination in efficient perovskite solar cells”. In: (Oct. 2018). arXiv: 1810.01333 (cit. on pp. 16, 17, 24, 72, 113).
- [24] D. Bi, W. Tress, M. I. Dar, P. Gao, J. Luo, C. Renevier, K. Schenk, A. Abate, F. Giordano, J.-P. Correa Baena, J.-D. Decoppet, S. M. Zakeeruddin, M. K. Nazeeruddin, M. Grätzel, and A. Hagfeldt. “Efficient luminescent solar cells based on tailored mixed-cation perovskites”. In: *Science Advances* 2.1 (Jan. 2016), e1501170. DOI: 10.1126/sciadv.1501170 (cit. on pp. 16, 25, 79).
- [25] W. Shockley and W. T. Read. “Statistics of the Recombinations of Holes and Electrons”. In: *Physical Review* 87.5 (Sept. 1952), pp. 835–842. DOI: 10.1103/PhysRev.87.835 (cit. on p. 16).
- [26] T. Kirchartz, T. Markwart, U. Rau, and D. A. Egger. “Impact of Small Phonon Energies on the Charge-Carrier Lifetimes in Metal-Halide Perovskites”. In: *The Journal of Physical Chemistry Letters* 9.5 (Mar. 2018), pp. 939–946. DOI: 10.1021/acs.jpclett.7b03414 (cit. on p. 16).

- [27] T. Kirchartz. “High Open-Circuit Voltages in Lead-Halide Perovskite Solar Cells - Experiment, Theory and Open Questions”. In: (Mar. 2019). arXiv: 1904.08752 (cit. on pp. 16, 24, 25).
- [28] P. Calado, D. Burkitt, J. Yao, J. Troughton, T. M. Watson, M. J. Carnie, A. M. Telford, B. C. O'Regan, J. Nelson, and P. R. Barnes. “Identifying Dominant Recombination Mechanisms in Perovskite Solar Cells by Measuring the Transient Ideality Factor”. In: *Physical Review Applied* 11.4 (Apr. 2019), p. 044005. DOI: 10.1103/PhysRevApplied.11.044005. arXiv: 1804.09049 (cit. on pp. 16, 17, 24, 56, 62, 64, 65, 118, 181).
- [29] J. Jiménez-López, B. M. D. Puscher, W. Cambarau, R. H. Fink, E. Palomares, and D. M. Guldi. “Hot Electron Injection into Semiconducting Polymers in Polymer Based-Perovskite Solar Cells and Their Fate”. In: *SSRN Electronic Journal* (2018). DOI: 10.2139/ssrn.3305584 (cit. on pp. 17, 113).
- [30] N. Droseros, B. Dänekamp, D. Tsokkou, P. P. Boix, and N. Banerji. “Charge injection and trapping at perovskite interfaces with organic hole transporting materials of different ionization energies”. In: *APL Materials* 7.4 (Apr. 2019), p. 041115. DOI: 10.1063/1.5086692 (cit. on pp. 17, 113).
- [31] M. J. Carnie, J. Troughton, B. O. Regan, P. Barnes, D. Bryant, T. Watson, and D. Worsley. “Identifying recombination mechanisms through materials development in perovskite solar cells”. In: *2015 IEEE 42nd Photovoltaic Specialist Conference (PVSC)*. IEEE, June 2015, pp. 1–3. DOI: 10.1109/PVSC.2015.7355675. URL: <http://ieeexplorer.ieee.org/document/7355675/> (cit. on pp. 17, 27, 83).
- [32] W. Tress, M. Yavari, K. Domanski, P. Yadav, B. Niesen, J. P. Correa Baena, A. Hagfeldt, and M. Graetzel. “Interpretation and evolution of open-circuit voltage, recombination, ideality factor and subgap defect states during reversible light-soaking and irreversible degradation of perovskite solar cells”. In: *Energy & Environmental Science* 11.1 (2018), pp. 151–165. DOI: 10.1039/C7EE02415K (cit. on pp. 17, 24).
- [33] J.-P. Correa-Baena, S.-H. Turren-Cruz, W. Tress, A. Hagfeldt, C. Aranda, L. Shooshtari, J. Bisquert, and A. Guerrero. “Changes from Bulk to Surface Recombination Mechanisms between Pristine and Cycled Perovskite Solar Cells”. In: *ACS Energy Letters* 2.3 (Mar. 2017), pp. 681–688. DOI: 10.1021/acsenergylett.7b00059 (cit. on p. 17).
- [34] C. K. Møller. “Crystal Structure and Photoconductivity of Cæsium Plumbohalides”. In: *Nature* 182.4647 (Nov. 1958), pp. 1436–1436. DOI: 10.1038/1821436a0 (cit. on p. 23).

- [35] D. Weber. “CH<sub>3</sub>NH<sub>3</sub>PbX<sub>3</sub>, ein Pb(II)-System mit kubischer Perowskitstruktur / CH<sub>3</sub>NH<sub>3</sub>PbX<sub>3</sub>, a Pb(II)-System with Cubic Perovskite Structure”. In: *Zeitschrift für Naturforschung B* 33.12 (Dec. 1978), pp. 1443–1445. DOI: 10.1515/znb-1978-1214 (cit. on p. 23).
- [36] A. Kojima, K. Teshima, Y. Shirai, and T. Miyasaka. “Organometal halide perovskites as visible-light sensitizers for photovoltaic cells.” In: *Journal of the American Chemical Society* 131.17 (May 2009), pp. 6050–6051. DOI: 10.1021/ja809598r (cit. on p. 23).
- [37] J.-H. Im, C.-R. Lee, J.-W. Lee, S.-W. Park, and N.-G. Park. “6.5% efficient perovskite quantum-dot-sensitized solar cell”. In: *Nanoscale* 3.10 (Oct. 2011), p. 4088. DOI: 10.1039/c1nr10867k (cit. on pp. 23, 39).
- [38] H.-S. Kim, C.-R. Lee, J.-H. Im, K.-B. Lee, T. Moehl, A. Marchioro, S.-J. Moon, R. Humphry-Baker, J.-H. Yum, J. E. Moser, M. Grätzel, and N.-G. Park. “Lead Iodide Perovskite Sensitized All-Solid-State Submicron Thin Film Mesoscopic Solar Cell with Efficiency Exceeding 9%”. In: *Scientific Reports* 2.1 (Dec. 2012), p. 591. DOI: 10.1038/srep00591 (cit. on p. 23).
- [39] M. M. Lee, J. Teuscher, T. Miyasaka, T. N. Murakami, and H. J. Snaith. “Efficient hybrid solar cells based on meso-superstructured organometal halide perovskites.” In: *Science* 338.6107 (Nov. 2012), pp. 643–7. DOI: 10.1126/science.1228604 (cit. on p. 23).
- [40] M. A. Green, Y. Hishikawa, E. D. Dunlop, D. H. Levi, J. Hohl-Ebinger, M. Yoshita, and A. W. Ho-Baillie. “Solar cell efficiency tables (Version 53)”. In: *Progress in Photovoltaics: Research and Applications* 27.1 (Jan. 2019), pp. 3–12. DOI: 10.1002/pip.3102 (cit. on p. 23).
- [41] Q. Jiang, Z. Chu, P. Wang, X. Yang, H. Liu, Y. Wang, Z. Yin, J. Wu, X. Zhang, and J. You. “Planar-Structure Perovskite Solar Cells with Efficiency beyond 21%”. In: *Advanced Materials* 29.46 (Dec. 2017), p. 1703852. DOI: 10.1002/adma.201703852 (cit. on p. 23).
- [42] A. Pockett, G. E. Eperon, T. Peltola, H. J. Snaith, A. Walker, L. M. Peter, and P. J. Cameron. “Characterization of Planar Lead Halide Perovskite Solar Cells by Impedance Spectroscopy, Open-Circuit Photovoltage Decay, and Intensity-Modulated Photovoltage/Photocurrent Spectroscopy”. In: *The Journal of Physical Chemistry C* 119.7 (Feb. 2015), pp. 3456–3465. DOI: 10.1021/jp510837q. arXiv: 1011.1669 (cit. on pp. 24, 65, 76, 91, 155, 166).

- [43] R. Gottesman, E. Haltzi, L. Gouda, S. Tirosh, Y. Bouhadana, A. Zaban, E. Mosconi, and F. De Angelis. “Extremely Slow Photoconductivity Response of CH<sub>3</sub>NH<sub>3</sub>PbI<sub>3</sub> Perovskites Suggesting Structural Changes under Working Conditions”. In: *The Journal of Physical Chemistry Letters* 5.15 (Aug. 2014), pp. 2662–2669. DOI: 10.1021/jz501373f. arXiv: 1011.1669 (cit. on p. 24).
- [44] M. Saliba, J.-P. Correa-Baena, C. M. Wolff, M. Stolterfoht, N. Phung, S. Albrecht, D. Neher, and A. Abate. “How to Make over 20% Efficient Perovskite Solar Cells in Regular (n-i-p) and Inverted (p-i-n) Architectures”. In: *Chemistry of Materials* 30.13 (July 2018), pp. 4193–4201. DOI: 10.1021/acs.chemmater.8b00136 (cit. on pp. 24, 109).
- [45] C. Wehrenfennig, M. Liu, H. J. Snaith, M. B. Johnston, and L. M. Herz. “Charge-carrier dynamics in vapour-deposited films of the organolead halide perovskite CH<sub>3</sub>NH<sub>3</sub>PbI<sub>3-x</sub>Cl<sub>x</sub>”. In: *Energy Environ. Sci.* 7.7 (2014), pp. 2269–2275. DOI: 10.1039/C4EE01358A (cit. on pp. 24, 27).
- [46] S. D. Stranks, G. E. Eperon, G. Grancini, C. Menelaou, M. J. P. Alcocer, T. Leijtens, L. M. Herz, A. Petrozza, and H. J. Snaith. “Electron-Hole Diffusion Lengths Exceeding 1 Micrometer in an Organometal Trihalide Perovskite Absorber”. In: *Science* 342.6156 (Oct. 2013), pp. 341–344. DOI: 10.1126/science.1243982 (cit. on pp. 24, 27).
- [47] G. Xing, N. Mathews, S. Sun, S. S. Lim, Y. M. Lam, M. Gratzel, S. Mhaisalkar, and T. C. Sum. “Long-Range Balanced Electron- and Hole-Transport Lengths in Organic-Inorganic CH<sub>3</sub>NH<sub>3</sub>PbI<sub>3</sub>”. In: *Science* 342.6156 (Oct. 2013), pp. 344–347. DOI: 10.1126/science.1243167 (cit. on pp. 24, 27).
- [48] D. Shi, V. Adinolfi, R. Comin, M. Yuan, E. Alarousu, A. Buin, Y. Chen, S. Hoogland, A. Rothenberger, K. Katsiev, Y. Losovyj, X. Zhang, P. A. Dowben, O. F. Mohammed, E. H. Sargent, and O. M. Bakr. “Low trap-state density and long carrier diffusion in organolead trihalide perovskite single crystals”. In: *Science* 347.6221 (Jan. 2015), pp. 519–522. DOI: 10.1126/science.aaa2725 (cit. on pp. 24, 27).
- [49] G. E. Eperon, S. D. Stranks, C. Menelaou, M. B. Johnston, L. M. Herz, and H. J. Snaith. “Formamidinium lead trihalide: a broadly tunable perovskite for efficient planar heterojunction solar cells”. In: *Energy & Environmental Science* 7.3 (2014), p. 982. DOI: 10.1039/c3ee43822h (cit. on pp. 24, 25, 27).
- [50] S. Liu, W. Huang, P. Liao, N. Pootrakulchote, H. Li, J. Lu, J. Li, F. Huang, X. Shai, X. Zhao, Y. Shen, Y.-B. Cheng, and M. Wang. “17% efficient printable mesoscopic PIN metal oxide framework perovskite solar cells using cesium-containing triple cation perovskite”. In: *Journal*

- of Materials Chemistry A* 5.44 (2017), pp. 22952–22958. DOI: 10.1039/C7TA07660F (cit. on pp. 24, 27).
- [51] J. Jiménez-López, W. Cambarau, L. Cabau, and E. Palomares. “Charge Injection, Carriers Recombination and HOMO Energy Level Relationship in Perovskite Solar Cells”. In: *Scientific Reports* 7.1 (Dec. 2017), p. 6101. DOI: 10.1038/s41598-017-06245-5 (cit. on pp. 24, 109).
- [52] K. Valadez-Villalobos, J. Idígoras, L. P. Delgado, D. Meneses-Rodríguez, J. A. Anta, and G. Oskam. “Correlation between the Effectiveness of the Electron-Selective Contact and Photovoltaic Performance of Perovskite Solar Cells”. In: *The Journal of Physical Chemistry Letters* 10.4 (Feb. 2019), pp. 877–882. DOI: 10.1021/acs.jpclett.8b03834 (cit. on p. 24).
- [53] W. Peng, B. Anand, L. Liu, S. Sampat, B. E. Bearden, A. V. Malko, and Y. J. Chabal. “Influence of growth temperature on bulk and surface defects in hybrid lead halide perovskite films”. In: *Nanoscale* 8.3 (2016), pp. 1627–1634. DOI: 10.1039/C5NR06222E (cit. on p. 24).
- [54] M. Stolterfoht, C. M. Wolff, J. A. Márquez, S. Zhang, C. J. Hages, D. Rothhardt, S. Albrecht, P. L. Burn, P. Meredith, T. Unold, and D. Neher. “Visualization and suppression of interfacial recombination for high-efficiency large-area pin perovskite solar cells”. In: *Nature Energy* 3.10 (Oct. 2018), pp. 847–854. DOI: 10.1038/s41560-018-0219-8 (cit. on pp. 24, 72).
- [55] Y. Shao, Y. Yuan, and J. Huang. “Correlation of energy disorder and open-circuit voltage in hybrid perovskite solar cells”. In: *Nature Energy* 1.1 (Jan. 2016), p. 15001. DOI: 10.1038/nenergy.2015.1 (cit. on pp. 24, 25, 27, 112, 135).
- [56] J.-P. Correa-Baena, W. Tress, K. Domanski, E. H. Anaraki, S.-H. Turren-Cruz, B. Roose, P. P. Boix, M. Grätzel, M. Saliba, A. Abate, and A. Hagfeldt. “Identifying and suppressing interfacial recombination to achieve high open-circuit voltage in perovskite solar cells”. In: *Energy & Environmental Science* 10.5 (2017), pp. 1207–1212. DOI: 10.1039/C7EE00421D (cit. on pp. 24, 109).
- [57] Y. Hou, W. Chen, D. Baran, T. Stubhan, N. A. Luechinger, B. Hartmeier, M. Richter, J. Min, S. Chen, C. O. R. Quiroz, N. Li, H. Zhang, T. Heumueller, G. J. Matt, A. Osvet, K. Forberich, Z.-G. Zhang, Y. Li, B. Winter, P. Schweizer, E. Spiecker, and C. J. Brabec. “Overcoming the Interface Losses in Planar Heterojunction Perovskite-Based Solar Cells”. In: *Advanced Materials* 28.25 (July 2016), pp. 5112–5120. DOI: 10.1002/adma.201504168 (cit. on p. 24).

- [58] W. Tress. "Perovskite Solar Cells on the Way to Their Radiative Efficiency Limit - Insights Into a Success Story of High Open-Circuit Voltage and Low Recombination". In: *Advanced Energy Materials* 7.14 (July 2017), p. 1602358. doi: 10.1002/aenm.201602358 (cit. on pp. 24, 25, 109).
- [59] W. Tress, N. Marinova, O. Inganäs, M. K. Nazeeruddin, S. M. Zakeeruddin, and M. Graetzel. "Predicting the Open-Circuit Voltage of CH<sub>3</sub>NH<sub>3</sub>PbI<sub>3</sub> Perovskite Solar Cells Using Electroluminescence and Photovoltaic Quantum Efficiency Spectra: the Role of Radiative and Non-Radiative Recombination". In: *Advanced Energy Materials* 5.3 (Feb. 2015), p. 1400812. doi: 10.1002/aenm.201400812 (cit. on p. 24).
- [60] C.-G. Wu, C.-H. Chiang, and S. H. Chang. "A perovskite cell with a record-high-V<sub>oc</sub> of 1.61 V based on solvent annealed CH<sub>3</sub>NH<sub>3</sub>PbBr<sub>3</sub>/ICBA active layer". In: *Nanoscale* 8.7 (2016), pp. 4077–4085. doi: 10.1039/C5NR07739G (cit. on p. 24).
- [61] R. A. Belisle, P. Jain, R. Prasanna, T. Leijtens, and M. D. McGehee. "Minimal Effect of the Hole-Transport Material Ionization Potential on the Open-Circuit Voltage of Perovskite Solar Cells". In: *ACS Energy Letters* 1.3 (Sept. 2016), pp. 556–560. doi: 10.1021/acsenergylett.6b00270 (cit. on pp. 25, 109).
- [62] D. P. McMeekin, G. Sadoughi, W. Rehman, G. E. Eperon, M. Saliba, M. T. Horantner, A. Haghhighirad, N. Sakai, L. Korte, B. Rech, M. B. Johnston, L. M. Herz, and H. J. Snaith. "A mixed-cation lead mixed-halide perovskite absorber for tandem solar cells". In: *Science* 351.6269 (Jan. 2016), pp. 151–155. doi: 10.1126/science.aad5845 (cit. on p. 25).
- [63] J. H. Noh, S. H. Im, J. H. Heo, T. N. Mandal, and S. I. Seok. "Chemical management for colorful, efficient, and stable inorganic-organic hybrid nanostructured solar cells." In: *Nano letters* 13.4 (Apr. 2013), pp. 1764–9. doi: 10.1021/nl400349b (cit. on p. 25).
- [64] S. Wheeler, D. Bryant, J. Troughton, T. Kirchartz, T. Watson, J. Nelson, and J. R. Durrant. "Transient Optoelectronic Analysis of the Impact of Material Energetics and Recombination Kinetics on the Open-Circuit Voltage of Hybrid Perovskite Solar Cells". In: *The Journal of Physical Chemistry C* 121.25 (June 2017), pp. 13496–13506. doi: 10.1021/acs.jpcc.7b02411 (cit. on pp. 25, 74, 92, 94, 96, 98, 101, 104, 135).

- [65] X. Zheng, B. Chen, J. Dai, Y. Fang, Y. Bai, Y. Lin, H. Wei, X. C. Zeng, and J. Huang. “Defect passivation in hybrid perovskite solar cells using quaternary ammonium halide anions and cations”. In: *Nature Energy* 2.7 (July 2017), p. 17102. DOI: 10.1038/nenergy.2017.102 (cit. on p. 25).
- [66] X. Wu, M. T. Trinh, D. Niesner, H. Zhu, Z. Norman, J. S. Owen, O. Yaffe, B. J. Kudisch, and X.-Y. Zhu. “Trap States in Lead Iodide Perovskites”. In: *Journal of the American Chemical Society* 137.5 (Feb. 2015), pp. 2089–2096. DOI: 10.1021/ja512833n (cit. on p. 25).
- [67] Y. H. Lee, J. Luo, R. Humphry-Baker, P. Gao, M. Grätzel, and M. K. Nazeeruddin. “Unraveling the Reasons for Efficiency Loss in Perovskite Solar Cells”. In: *Advanced Functional Materials* 25.25 (July 2015), pp. 3925–3933. DOI: 10.1002/adfm.201501024 (cit. on p. 25).
- [68] N. F. Montcada, J. M. Marín-Beloqui, W. Cambarau, J. Jiménez-López, L. Cabau, K. T. Cho, M. K. Nazeeruddin, and E. Palomares. “Analysis of Photoinduced Carrier Recombination Kinetics in Flat and Mesoporous Lead Perovskite Solar Cells”. In: *ACS Energy Letters* 2.1 (Jan. 2017), pp. 182–187. DOI: 10.1021/acsenergylett.6b00600 (cit. on pp. 25, 85).
- [69] W. Qiu, T. Merckx, M. Jaysankar, C. Masse de la Huerta, L. Rakocevic, W. Zhang, U. W. Paetzold, R. Gehlhaar, L. Froyen, J. Poortmans, D. Cheyns, H. J. Snaith, and P. Heremans. “Pinhole-free perovskite films for efficient solar modules”. In: *Energy & Environmental Science* 9.2 (2016), pp. 484–489. DOI: 10.1039/C5EE03703D (cit. on p. 25).
- [70] A. Marchioro, J. Teuscher, D. Friedrich, M. Kunst, R. van de Krol, T. Moehl, M. Grätzel, and J.-E. Moser. “Unravelling the mechanism of photoinduced charge transfer processes in lead iodide perovskite solar cells”. In: *Nature Photonics* 8.3 (Jan. 2014), pp. 250–255. DOI: 10.1038/nphoton.2013.374 (cit. on p. 25).
- [71] S. Shao, M. Abdu-Aguye, T. S. Sherkar, H.-H. Fang, S. Adjokatse, G. ten Brink, B. J. Kooi, L. J. A. Koster, and M. A. Loi. “The Effect of the Microstructure on Trap-Assisted Recombination and Light Soaking Phenomenon in Hybrid Perovskite Solar Cells”. In: *Advanced Functional Materials* 26.44 (Nov. 2016), pp. 8094–8102. DOI: 10.1002/adfm.201602519 (cit. on p. 25).
- [72] Wikipedia. *Shockley-Queisser limit*. 2019. URL: [https://en.wikipedia.org/wiki/Shockley%20%93Queisser%7B%5C\\_%7Dlimit](https://en.wikipedia.org/wiki/Shockley%20%93Queisser%7B%5C_%7Dlimit) (cit. on p. 25).

- [73] A. Walsh, D. O. Scanlon, S. Chen, X. G. Gong, and S.-H. Wei. “Self-Regulation Mechanism for Charged Point Defects in Hybrid Halide Perovskites”. In: *Angewandte Chemie International Edition* 54.6 (Feb. 2015), pp. 1791–1794. DOI: [10.1002/anie.201409740](https://doi.org/10.1002/anie.201409740) (cit. on pp. 26, 28, 144).
- [74] W.-J. Yin, T. Shi, and Y. Yan. “Unusual defect physics in CH<sub>3</sub>NH<sub>3</sub>PbI<sub>3</sub> perovskite solar cell absorber”. In: *Applied Physics Letters* 104.6 (Feb. 2014), p. 063903. DOI: [10.1063/1.4864778](https://doi.org/10.1063/1.4864778) (cit. on p. 26).
- [75] S. T. Birkhold, J. T. Precht, R. Giridharagopal, G. E. Eperon, L. Schmidt-Mende, and D. S. Ginger. “Direct Observation and Quantitative Analysis of Mobile Frenkel Defects in Metal Halide Perovskites Using Scanning Kelvin Probe Microscopy”. In: *The Journal of Physical Chemistry C* 122.24 (June 2018), pp. 12633–12639. DOI: [10.1021/acs.jpcc.8b03255](https://doi.org/10.1021/acs.jpcc.8b03255) (cit. on p. 26).
- [76] S. T. Birkhold, J. T. Precht, H. Liu, R. Giridharagopal, G. E. Eperon, L. Schmidt-Mende, X. Li, and D. S. Ginger. “Interplay of Mobile Ions and Injected Carriers Creates Recombination Centers in Metal Halide Perovskites under Bias”. In: *ACS Energy Letters* 3.6 (June 2018), pp. 1279–1286. DOI: [10.1021/acsenergylett.8b00505](https://doi.org/10.1021/acsenergylett.8b00505) (cit. on pp. 26, 28).
- [77] J. L. Minns, P. Zajdel, D. Chernyshov, W. van Beek, and M. A. Green. “Structure and interstitial iodide migration in hybrid perovskite methylammonium lead iodide”. In: *Nature Communications* 8.1 (Aug. 2017), p. 15152. DOI: [10.1038/ncomms15152](https://doi.org/10.1038/ncomms15152) (cit. on pp. 26, 28).
- [78] E. Mosconi, D. Meggiolaro, H. J. Snaith, S. D. Stranks, and F. De Angelis. “Light-induced annihilation of Frenkel defects in organo-lead halide perovskites”. In: *Energy & Environmental Science* 9.10 (2016), pp. 3180–3187. DOI: [10.1039/C6EE01504B](https://doi.org/10.1039/C6EE01504B) (cit. on p. 26).
- [79] H. Uratani and K. Yamashita. “Charge Carrier Trapping at Surface Defects of Perovskite Solar Cell Absorbers: A First-Principles Study”. In: *The Journal of Physical Chemistry Letters* 8.4 (Feb. 2017), pp. 742–746. DOI: [10.1021/acs.jpclett.7b00055](https://doi.org/10.1021/acs.jpclett.7b00055) (cit. on p. 26).
- [80] J. Kim, S.-H. Lee, J. H. Lee, and K.-H. Hong. “The Role of Intrinsic Defects in Methylammonium Lead Iodide Perovskite”. In: *The Journal of Physical Chemistry Letters* 5.8 (Apr. 2014), pp. 1312–1317. DOI: [10.1021/jz500370k](https://doi.org/10.1021/jz500370k) (cit. on p. 26).
- [81] A. Buin, P. Pietsch, J. Xu, O. Voznyy, A. H. Ip, R. Comin, and E. H. Sargent. “Materials Processing Routes to Trap-Free Halide Perovskites”. In: *Nano Letters* 14.11 (Nov. 2014), pp. 6281–6286. DOI: [10.1021/nl502612m](https://doi.org/10.1021/nl502612m) (cit. on p. 26).

- [82] M.-H. Du. “Density Functional Calculations of Native Defects in CH<sub>3</sub>NH<sub>3</sub>PbI<sub>3</sub>: Effects of Spin–Orbit Coupling and Self-Interaction Error”. In: *The Journal of Physical Chemistry Letters* 6.8 (Apr. 2015), pp. 1461–1466. DOI: 10.1021/acs.jpclett.5b00199 (cit. on p. 26).
- [83] J. Mizusaki, K. Arai, and K. Fueki. “Ionic conduction of the perovskite-type halides”. In: *Solid State Ionics* 11.3 (Nov. 1983), pp. 203–211. DOI: 10.1016/0167-2738(83)90025-5 (cit. on p. 26).
- [84] K. Yamada. “Chloride ion conductor CH<sub>3</sub>NH<sub>3</sub>GeCl<sub>3</sub> studied by Rietveld analysis of X-ray diffraction and <sup>35</sup>Cl NMR”. In: *Solid State Ionics* 79 (July 1995), pp. 152–157. DOI: 10.1016/0167-2738(95)00055-B (cit. on p. 26).
- [85] K. Yamada, Y. Kuranaga, K. Ueda, S. Goto, T. Okuda, and Y. Furukawa. “Phase Transition and Electric Conductivity of ASnCl<sub>3</sub> (A = Cs and CH<sub>3</sub>NH<sub>3</sub>)”. In: *Bulletin of the Chemical Society of Japan* 71.1 (Jan. 1998), pp. 127–134. DOI: 10.1246/bcsj.71.127 (cit. on p. 26).
- [86] M. S. Islam. “Ionic transport in ABO<sub>3</sub> perovskite oxides: a computer modelling tour”. In: *Journal of Materials Chemistry* 10.4 (2000), pp. 1027–1038. DOI: 10.1039/a908425h (cit. on p. 26).
- [87] T.-Y. Yang, G. Gregori, N. Pellet, M. Grätzel, and J. Maier. “The Significance of Ion Conduction in a Hybrid Organic-Inorganic Lead-Iodide-Based Perovskite Photosensitizer”. In: *Angewandte Chemie International Edition* 54.27 (June 2015), pp. 7905–7910. DOI: 10.1002/anie.201500014 (cit. on pp. 26, 155).
- [88] A. Senocrate, I. Moudrakovski, G. Y. Kim, T.-Y. Yang, G. Gregori, M. Grätzel, and J. Maier. “The Nature of Ion Conduction in Methylammonium Lead Iodide: A Multimethod Approach”. In: *Angewandte Chemie International Edition* 56.27 (June 2017), pp. 7755–7759. DOI: 10.1002/anie.201701724 (cit. on p. 26).
- [89] C. Eames, J. M. Frost, P. R. F. Barnes, B. C. O'Regan, A. Walsh, and M. S. Islam. “Ionic transport in hybrid lead iodide perovskite solar cells”. In: *Nature Communications* 6.1 (Dec. 2015), p. 7497. DOI: 10.1038/ncomms8497 (cit. on p. 26).
- [90] S. Meloni, T. Moehl, W. Tress, M. Franckevičius, M. Saliba, Y. H. Lee, P. Gao, M. K. Nazeeruddin, S. M. Zakeeruddin, U. Rothlisberger, and M. Graetzel. “Ionic polarization-induced current–voltage hysteresis in CH<sub>3</sub>NH<sub>3</sub>PbX<sub>3</sub> perovskite solar cells”. In: *Nature Communications* 7.1 (Apr. 2016), p. 10334. DOI: 10.1038/ncomms10334 (cit. on p. 26).

- [91] J. Haruyama, K. Sodeyama, L. Han, and Y. Tateyama. “First-Principles Study of Ion Diffusion in Perovskite Solar Cell Sensitizers”. In: *Journal of the American Chemical Society* 137.32 (Aug. 2015), pp. 10048–10051. DOI: 10.1021/jacs.5b03615 (cit. on p. 26).
- [92] J. M. Azpiroz, E. Mosconi, J. Bisquert, and F. De Angelis. “Defect migration in methylammonium lead iodide and its role in perovskite solar cell operation”. In: *Energy & Environmental Science* 8.7 (2015), pp. 2118–2127. DOI: 10.1039/C5EE01265A (cit. on p. 26).
- [93] E. Mosconi and F. De Angelis. “Mobile Ions in Organohalide Perovskites: Interplay of Electronic Structure and Dynamics”. In: *ACS Energy Letters* 1.1 (July 2016), pp. 182–188. DOI: 10.1021/acsenergylett.6b00108 (cit. on p. 26).
- [94] A. Senocrate, I. Moudrakovski, T. Acartürk, R. Merkle, G. Y. Kim, U. Starke, M. Grätzel, and J. Maier. “Slow CH<sub>3</sub>NH<sub>3</sub><sup>+</sup> Diffusion in CH<sub>3</sub>NH<sub>3</sub>PbI<sub>3</sub> under Light Measured by Solid-State NMR and Tracer Diffusion”. In: *The Journal of Physical Chemistry C* 122.38 (Sept. 2018), pp. 21803–21806. DOI: 10.1021/acs.jpcc.8b06814 (cit. on p. 26).
- [95] E. L. Unger, E. T. Hoke, C. D. Bailie, W. H. Nguyen, A. R. Bowring, T. Heumüller, M. G. Christoforo, and M. D. McGehee. “Hysteresis and transient behavior in current–voltage measurements of hybrid-perovskite absorber solar cells”. In: *Energy Environ. Sci.* 7.11 (Aug. 2014), pp. 3690–3698. DOI: 10.1039/C4EE02465F (cit. on pp. 26, 27, 60, 62).
- [96] Z. Xiao, Y. Yuan, Y. Shao, Q. Wang, Q. Dong, C. Bi, P. Sharma, A. Gruverman, and J. Huang. “Giant switchable photovoltaic effect in organometal trihalide perovskite devices”. In: *Nature Materials* 14.2 (Feb. 2015), pp. 193–198. DOI: 10.1038/nmat4150 (cit. on pp. 26, 27).
- [97] W. Tress, N. Marinova, T. Moehl, S. M. Zakeeruddin, M. K. Nazeeruddin, and M. Grätzel. “Understanding the rate-dependent J–V hysteresis, slow time component, and aging in CH<sub>3</sub>NH<sub>3</sub>PbI<sub>3</sub> perovskite solar cells: the role of a compensated electric field”. In: *Energy & Environmental Science* 8.3 (2015), pp. 995–1004. DOI: 10.1039/C4EE03664F (cit. on pp. 26, 27, 60, 150).
- [98] P. Calado, A. M. Telford, D. Bryant, X. Li, J. Nelson, B. C. O'Regan, and P. R. Barnes. “Evidence for ion migration in hybrid perovskite solar cells with minimal hysteresis”. In: *Nature Communications* 7 (Dec. 2016), p. 13831. DOI: 10.1038/ncomms13831. arXiv: 1606.00818 (cit. on pp. 26, 27, 58, 79, 80, 144, 146, 181).

- [99] D. A. Jacobs, H. Shen, F. Pfeffer, J. Peng, T. P. White, F. J. Beck, R. Kylie, D. A. Jacobs, H. Shen, F. Pfeffer, J. Peng, T. P. White, F. J. Beck, and K. R. Catchpole. “The two faces of capacitance: New interpretations for electrical impedance measurements of perovskite solar cells and their relation to hysteresis”. In: *Journal of Applied Physics* 225702.124 (2018). DOI: 10.1063/1.5063259 (cit. on pp. 26, 58, 59, 61, 106, 143, 163, 166).
- [100] D. Bryant, S. Wheeler, B. C. O’Regan, T. Watson, P. R. F. Barnes, D. Worsley, and J. Durrant. “Observable Hysteresis at Low Temperature in “Hysteresis Free” Organic–Inorganic Lead Halide Perovskite Solar Cells”. In: *The Journal of Physical Chemistry Letters* 6.16 (2015), pp. 3190–3194. DOI: 10.1021/acs.jpclett.5b01381 (cit. on pp. 26, 61).
- [101] G. Richardson, S. E. J. O’Kane, R. G. Niemann, T. A. Peltola, J. M. Foster, P. J. Cameron, and A. B. Walker. “Can slow-moving ions explain hysteresis in the current–voltage curves of perovskite solar cells?” In: *Energy & Environmental Science* 9.4 (2016), pp. 1476–1485. DOI: 10.1039/C5EE02740C (cit. on pp. 26, 60).
- [102] A. Pockett, G. E. Eperon, N. Sakai, H. J. Snaith, L. M. Peter, and P. J. Cameron. “Microseconds, milliseconds and seconds: deconvoluting the dynamic behaviour of planar perovskite solar cells”. In: *Physical Chemistry Chemical Physics* 19.8 (2017), pp. 5959–5970. DOI: 10.1039/C6CP08424A (cit. on pp. 27, 61, 91, 142).
- [103] H. Yu, H. Lu, F. Xie, S. Zhou, and N. Zhao. “Native Defect-Induced Hysteresis Behavior in Organolead Iodide Perovskite Solar Cells”. In: *Advanced Functional Materials* 26.9 (Mar. 2016), pp. 1411–1419. DOI: 10.1002/adfm.201504997 (cit. on p. 27).
- [104] J. Beilsten-Edmands, G. E. Eperon, R. D. Johnson, H. J. Snaith, and P. G. Radaelli. “Non-ferroelectric nature of the conductance hysteresis in CH<sub>3</sub>NH<sub>3</sub>PbI<sub>3</sub> perovskite-based photovoltaic devices”. In: *Applied Physics Letters* 106.17 (Apr. 2015), p. 173502. DOI: 10.1063/1.4919109 (cit. on p. 27).
- [105] J. Carrillo, A. Guerrero, S. Rahimnejad, O. Almora, I. Zarazua, E. Mas-Marza, J. Bisquert, and G. Garcia-Belmonte. “Ionic Reactivity at Contacts and Aging of Methylammonium Lead Triiodide Perovskite Solar Cells”. In: *Advanced Energy Materials* 6.9 (May 2016), p. 1502246. DOI: 10.1002/aenm.201502246 (cit. on pp. 27, 28, 112).

- [106] P. R. F. Barnes, K. Miettunen, X. Li, A. Y. Anderson, T. Bessho, M. Grätzel, and B. C. O'Regan. "Interpretation of Optoelectronic Transient and Charge Extraction Measurements in Dye-Sensitized Solar Cells". In: *Advanced Materials* 25.13 (Apr. 2013), pp. 1881–1922. DOI: [10.1002/adma.201201372](https://doi.org/10.1002/adma.201201372) (cit. on pp. 27, 59, 101).
- [107] B. C. O'Regan, P. R. F. Barnes, X. Li, C. Law, E. Palomares, and J. M. Marin-Beloqui. "Optoelectronic Studies of Methylammonium Lead Iodide Perovskite Solar Cells with Mesoporous TiO<sub>2</sub>: Separation of Electronic and Chemical Charge Storage, Understanding Two Recombination Lifetimes, and the Evolution of Band Offsets during J – V Hysteresis". In: *Journal of the American Chemical Society* 137.15 (Apr. 2015), pp. 5087–5099. DOI: [10.1021/jacs.5b00761](https://doi.org/10.1021/jacs.5b00761) (cit. on pp. 27, 69, 79, 80, 83, 101, 104).
- [108] D. Kiermasch, A. Baumann, M. Fischer, V. Dyakonov, and K. Tvingstedt. "Revisiting lifetimes from transient electrical characterization of thin film solar cells; a capacitive concern evaluated for silicon, organic and perovskite devices". In: *Energy & Environmental Science* 11.3 (2018), pp. 629–640. DOI: [10.1039/C7EE03155F](https://doi.org/10.1039/C7EE03155F) (cit. on pp. 27, 76, 83, 89, 91, 94).
- [109] T. M. Clarke, C. Lungenschmied, J. Peet, N. Drolet, and A. J. Mozer. "A Comparison of Five Experimental Techniques to Measure Charge Carrier Lifetime in Polymer/Fullerene Solar Cells". In: *Advanced Energy Materials* 5.4 (Feb. 2015), p. 1401345. DOI: [10.1002/aenm.201401345](https://doi.org/10.1002/aenm.201401345) (cit. on p. 27).
- [110] A. Maurano, C. G. Shuttle, R. Hamilton, A. M. Ballantyne, J. Nelson, W. Zhang, M. Heeney, and J. R. Durrant. "Transient Optoelectronic Analysis of Charge Carrier Losses in a Selenophene/Fullerene Blend Solar Cell". In: *The Journal of Physical Chemistry C* 115.13 (Apr. 2011), pp. 5947–5957. DOI: [10.1021/jp109697w](https://doi.org/10.1021/jp109697w) (cit. on pp. 27, 98, 104).
- [111] A. Foertig, J. Rauh, V. Dyakonov, and C. Deibel. "Shockley equation parameters of P3HT:PCBM solar cells determined by transient techniques". In: *Physical Review B* 86.11 (Sept. 2012), p. 115302. DOI: [10.1103/PhysRevB.86.115302](https://doi.org/10.1103/PhysRevB.86.115302) (cit. on p. 27).
- [112] Y. Reyna, A. Pérez-Tomás, A. Mingorance, and M. Lira-Cantú. "Stability of Molecular Devices: Halide Perovskite Solar Cells". In: *Molecular Devices for Solar Energy Conversion and Storage*. Ed. by H. Tian, G. Boschloo, and A. Hagfeldt. Singapore: Springer, 2018, pp. 477–531. DOI: [10.1007/978-981-10-5924-7\\_13](https://doi.org/10.1007/978-981-10-5924-7_13) (cit. on pp. 27, 28).

- [113] M. Lira-Cantú. “Perovskite solar cells: Stability lies at interfaces”. In: *Nature Energy* 2.7 (July 2017), p. 17115. DOI: [10.1038/nenergy.2017.115](https://doi.org/10.1038/nenergy.2017.115) (cit. on p. 27).
- [114] A. Mingorance, H. Xie, H. Kim, Z. Wang, M. Balsells, A. Morales-Melgares, N. Domingo, N. Kazuteru, W. Tress, J. Fraxedas, N. Vlachopoulos, A. Hagfeldt, and M. Lira-Cantu. “Interfacial Engineering of Metal Oxides for Highly Stable Halide Perovskite Solar Cells”. In: *Advanced Materials Interfaces* 5.22 (Nov. 2018), p. 1800367. DOI: [10.1002/admi.201800367](https://doi.org/10.1002/admi.201800367) (cit. on pp. 27, 28).
- [115] T. Malinauskas, D. Tomkute-Luksiene, R. Sens, M. Daskeviciene, R. Send, H. Wonneberger, V. Jankauskas, I. Bruder, and V. Getautis. “Enhancing Thermal Stability and Lifetime of Solid-State Dye-Sensitized Solar Cells via Molecular Engineering of the Hole-Transporting Material Spiro-OMeTAD”. In: *ACS Applied Materials & Interfaces* 7.21 (June 2015), pp. 11107–11116. DOI: [10.1021/am5090385](https://doi.org/10.1021/am5090385) (cit. on p. 28).
- [116] T. Malinauskas, M. Saliba, T. Matsui, M. Daskeviciene, S. Urnikaite, P. Gratia, R. Send, H. Wonneberger, I. Bruder, M. Graetzel, V. Getautis, and M. K. Nazeeruddin. “Branched methoxydiphenylamine-substituted fluorene derivatives as hole transporting materials for high-performance perovskite solar cells”. In: *Energy & Environmental Science* 9.5 (2016), pp. 1681–1686. DOI: [10.1039/C5EE03911H](https://doi.org/10.1039/C5EE03911H) (cit. on p. 28).
- [117] N. K. Noel, M. Congiu, A. J. Ramadan, S. Fearn, D. P. McMeekin, J. B. Patel, M. B. Johnston, B. Wenger, and H. J. Snaith. “Unveiling the Influence of pH on the Crystallization of Hybrid Perovskites, Delivering Low Voltage Loss Photovoltaics”. In: *Joule* 1.2 (Oct. 2017), pp. 328–343. DOI: [10.1016/j.joule.2017.09.009](https://doi.org/10.1016/j.joule.2017.09.009) (cit. on p. 28).
- [118] W. Zhang, S. Pathak, N. Sakai, T. Stergiopoulos, P. K. Nayak, N. K. Noel, A. A. Haghighirad, V. M. Burlakov, D. W. DeQuilettes, A. Sadhanala, W. Li, L. Wang, D. S. Ginger, R. H. Friend, and H. J. Snaith. “Enhanced optoelectronic quality of perovskite thin films with hypophosphorous acid for planar heterojunction solar cells”. In: *Nature Communications* 6.1 (Dec. 2015), p. 10030. DOI: [10.1038/ncomms10030](https://doi.org/10.1038/ncomms10030) (cit. on p. 28).
- [119] P. K. Nayak, D. T. Moore, B. Wenger, S. Nayak, A. A. Haghighirad, A. Fineberg, N. K. Noel, O. G. Reid, G. Rumbles, P. Kukura, K. A. Vincent, and H. J. Snaith. “Mechanism for rapid growth of organic–inorganic halide perovskite crystals”. In: *Nature Communications* 7.1 (Dec. 2016), p. 13303. DOI: [10.1038/ncomms13303](https://doi.org/10.1038/ncomms13303) (cit. on p. 28).

- [120] G. Sadoughi, D. E. Starr, E. Handick, S. D. Stranks, M. Gorgoi, R. G. Wilks, M. Bär, and H. J. Snaith. “Observation and Mediation of the Presence of Metallic Lead in Organic–Inorganic Perovskite Films”. In: *ACS Applied Materials & Interfaces* 7.24 (June 2015), pp. 13440–13444. DOI: [10.1021/acsami.5b02237](https://doi.org/10.1021/acsami.5b02237) (cit. on p. 28).
- [121] A. Buin, R. Comin, J. Xu, A. H. Ip, and E. H. Sargent. “Halide-Dependent Electronic Structure of Organolead Perovskite Materials”. In: *Chemistry of Materials* 27.12 (June 2015), pp. 4405–4412. DOI: [10.1021/acs.chemmater.5b01909](https://doi.org/10.1021/acs.chemmater.5b01909) (cit. on p. 28).
- [122] U.-G. Jong, C.-J. Yu, G.-C. Ri, A. P. McMahon, N. M. Harrison, P. R. F. Barnes, and A. Walsh. “Influence of water intercalation and hydration on chemical decomposition and ion transport in methylammonium lead halide perovskites”. In: *Journal of Materials Chemistry A* 6.3 (2018), pp. 1067–1074. DOI: [10.1039/C7TA09112E](https://doi.org/10.1039/C7TA09112E) (cit. on p. 28).
- [123] J. Schlipf, Y. Hu, S. Pratap, L. Bießmann, N. Hohn, L. Porcar, T. Bein, P. Docampo, and P. Müller-Buschbaum. “Shedding Light on the Moisture Stability of 3D/2D Hybrid Perovskite Heterojunction Thin Films”. In: *ACS Applied Energy Materials* 2.2 (Feb. 2019), pp. 1011–1018. DOI: [10.1021/acsaem.9b00005](https://doi.org/10.1021/acsaem.9b00005) (cit. on p. 28).
- [124] Y. Hu, M. F. Aygüler, M. L. Petrus, T. Bein, and P. Docampo. “Impact of Rubidium and Cesium Cations on the Moisture Stability of Multiple-Cation Mixed-Halide Perovskites”. In: *ACS Energy Letters* 2.10 (Oct. 2017), pp. 2212–2218. DOI: [10.1021/acsenergylett.7b00731](https://doi.org/10.1021/acsenergylett.7b00731) (cit. on p. 28).
- [125] Y. Han, S. Meyer, Y. Dkhissi, K. Weber, J. M. Pringle, U. Bach, L. Spiccia, and Y.-B. Cheng. “Degradation observations of encapsulated planar CH<sub>3</sub>NH<sub>3</sub>PbI<sub>3</sub> perovskite solar cells at high temperatures and humidity”. In: *Journal of Materials Chemistry A* 3.15 (2015), pp. 8139–8147. DOI: [10.1039/C5TA00358J](https://doi.org/10.1039/C5TA00358J) (cit. on p. 28).
- [126] A. M. A. Leguy, Y. Hu, M. Campoy-Quiles, M. I. Alonso, O. J. Weber, P. Azarhoosh, M. van Schilfgaarde, M. T. Weller, T. Bein, J. Nelson, P. Docampo, and P. R. F. Barnes. “Reversible Hydration of CH<sub>3</sub>NH<sub>3</sub>PbI<sub>3</sub> in Films, Single Crystals, and Solar Cells”. In: *Chemistry of Materials* 27.9 (May 2015), pp. 3397–3407. DOI: [10.1021/acs.chemmater.5b00660](https://doi.org/10.1021/acs.chemmater.5b00660) (cit. on p. 28).
- [127] A. Senocrate, T. Acartürk, G. Y. Kim, R. Merkle, U. Starke, M. Grätzel, and J. Maier. “Interaction of oxygen with halide perovskites”. In: *Journal of Materials Chemistry A* 6.23 (2018), pp. 10847–10855. DOI: [10.1039/C8TA04537B](https://doi.org/10.1039/C8TA04537B) (cit. on pp. 28, 48).

- [128] N. Aristidou, C. Eames, I. Sanchez-Molina, X. Bu, J. Kosco, M. S. Islam, and S. A. Haque. “Fast oxygen diffusion and iodide defects mediate oxygen-induced degradation of perovskite solar cells”. In: *Nature Communications* 8.1 (Aug. 2017), p. 15218. DOI: 10.1038/ncomms15218 (cit. on pp. 28, 48).
- [129] S.-W. Lee, S. Kim, S. Bae, K. Cho, T. Chung, L. E. Mundt, S. Lee, S. Park, H. Park, M. C. Schubert, S. W. Glunz, Y. Ko, Y. Jun, Y. Kang, H.-S. Lee, and D. Kim. “UV Degradation and Recovery of Perovskite Solar Cells”. In: *Scientific Reports* 6.1 (Dec. 2016), p. 38150. DOI: 10.1038/srep38150 (cit. on p. 28).
- [130] B. Philippe, B.-W. Park, R. Lindblad, J. Oscarsson, S. Ahmadi, E. M. J. Johansson, and H. Rensmo. “Chemical and Electronic Structure Characterization of Lead Halide Perovskites and Stability Behavior under Different Exposures—A Photoelectron Spectroscopy Investigation”. In: *Chemistry of Materials* 27.5 (Mar. 2015), pp. 1720–1731. DOI: 10.1021/acs.chemmater.5b00348 (cit. on p. 28).
- [131] B. Conings, J. Drijkoningen, N. Gauquelin, A. Babayigit, J. D’Haen, L. D’Olieslaeger, A. Ethirajan, J. Verbeeck, J. Manca, E. Mosconi, F. D. Angelis, and H.-G. Boyen. “Intrinsic Thermal Instability of Methylammonium Lead Trihalide Perovskite”. In: *Advanced Energy Materials* 5.15 (Aug. 2015), p. 1500477. DOI: 10.1002/aenm.201500477 (cit. on p. 28).
- [132] S. Kim, S. Bae, S.-W. Lee, K. Cho, K. D. Lee, H. Kim, S. Park, G. Kwon, S.-W. Ahn, H.-M. H.-S. Lee, Y. Kang, H.-M. H.-S. Lee, and D. Kim. “Relationship between ion migration and interfacial degradation of CH<sub>3</sub>NH<sub>3</sub>PbI<sub>3</sub> perovskite solar cells under thermal conditions”. In: *Scientific Reports* 7.1 (Dec. 2017), p. 1200. DOI: 10.1038/s41598-017-00866-6 (cit. on pp. 28, 112).
- [133] H.-S. Kim, J.-Y. Seo, and N.-G. Park. “Impact of Selective Contacts on Long-Term Stability of CH<sub>3</sub>NH<sub>3</sub>PbI<sub>3</sub> Perovskite Solar Cells”. In: *The Journal of Physical Chemistry C* 120.49 (Dec. 2016), pp. 27840–27848. DOI: 10.1021/acs.jpcc.6b09412 (cit. on pp. 28, 112).
- [134] M. De Bastiani, G. Dell’Erba, M. Gandini, V. D’Innocenzo, S. Neutzner, A. R. S. Kandada, G. Grancini, M. Binda, M. Prato, J. M. Ball, M. Caironi, and A. Petrozza. “Ion Migration and the Role of Preconditioning Cycles in the Stabilization of the J - V Characteristics of Inverted Hybrid Perovskite Solar Cells”. In: *Advanced Energy Materials* 6.2 (Jan. 2016), p. 1501453. DOI: 10.1002/aenm.201501453 (cit. on p. 28).

- [135] Y. Kato, L. K. Ono, M. V. Lee, S. Wang, S. R. Raga, and Y. Qi. “Silver Iodide Formation in Methyl Ammonium Lead Iodide Perovskite Solar Cells with Silver Top Electrodes”. In: *Advanced Materials Interfaces* 2.13 (Sept. 2015), p. 1500195. DOI: 10.1002/admi.201500195 (cit. on p. 28).
- [136] A. Guerrero, J. You, C. Aranda, Y. S. Kang, G. Garcia-Belmonte, H. Zhou, J. Bisquert, and Y. Yang. “Interfacial Degradation of Planar Lead Halide Perovskite Solar Cells”. In: *ACS Nano* 10.1 (Jan. 2016), pp. 218–224. DOI: 10.1021/acsnano.5b03687 (cit. on p. 28).
- [137] H. Back, G. Kim, J. Kim, J. Kong, T. K. Kim, H. Kang, H. Kim, J. Lee, S. Lee, and K. Lee. “Achieving long-term stable perovskite solar cells via ion neutralization”. In: *Energy & Environmental Science* 9.4 (2016), pp. 1258–1263. DOI: 10.1039/C6EE00612D (cit. on p. 28).
- [138] L. Zhao, R. A. Kerner, Z. Xiao, Y. L. Lin, K. M. Lee, J. Schwartz, and B. P. Rand. “Redox Chemistry Dominates the Degradation and Decomposition of Metal Halide Perovskite Optoelectronic Devices”. In: *ACS Energy Letters* 1.3 (Sept. 2016), pp. 595–602. DOI: 10.1021/acsenergylett.6b00320 (cit. on p. 28).
- [139] K. Domanski, J.-P. Correa-Baena, N. Mine, M. K. Nazeeruddin, A. Abate, M. Saliba, W. Tress, A. Hagfeldt, and M. Grätzel. “Not All That Glitters Is Gold: Metal-Migration-Induced Degradation in Perovskite Solar Cells”. In: *ACS Nano* 10.6 (June 2016), pp. 6306–6314. DOI: 10.1021/acsnano.6b02613 (cit. on pp. 28, 112).
- [140] L. Cabau, I. Garcia-Benito, A. Molina-Ontoria, N. F. Montcada, N. Martin, A. Vidal-Ferran, and E. Palomares. “Diarylamino-substituted tetraarylethene (TAE) as an efficient and robust hole transport material for 11% methyl ammonium lead iodide perovskite solar cells”. In: *Chemical Communications* 51.73 (2015), pp. 13980–13982. DOI: 10.1039/C5CC05236J (cit. on pp. 33, 109, 111).
- [141] H. Choi, K. Do, S. Park, J.-S. Yu, and J. Ko. “Efficient Hole Transporting Materials with Two or Four N,N-Di(4-methoxyphenyl)aminophenyl Arms on an Ethene Unit for Perovskite Solar Cells”. In: *Chemistry - A European Journal* 21.45 (Nov. 2015), pp. 15919–15923. DOI: 10.1002/chem.201502741 (cit. on pp. 33, 109).
- [142] I. Horcas, R. Fernández, J. M. Gómez-Rodríguez, J. Colchero, J. Gómez-Herrero, and A. M. Baro. “WSXM : A software for scanning probe microscopy and a tool for nanotechnology”. In: *Review of Scientific Instruments* 78.1 (Jan. 2007), p. 013705. DOI: 10.1063/1.2432410 (cit. on p. 37).

- [143] D. Prochowicz, P. Yadav, M. Saliba, D. J. Kubicki, M. M. Tavakoli, S. M. Zakeeruddin, J. Lewiński, L. Emsley, and M. Grätzel. “One-step mechanochemical incorporation of an insoluble cesium additive for high performance planar heterojunction solar cells”. In: *Nano Energy* 49 (July 2018), pp. 523–528. DOI: 10.1016/j.nanoen.2018.05.010 (cit. on p. 40).
- [144] J. Burschka, F. Kessler, M. K. Nazeeruddin, and M. Grätzel. “Co(III) Complexes as p-Dopants in Solid-State Dye-Sensitized Solar Cells”. In: *Chemistry of Materials* 25.15 (Aug. 2013), pp. 2986–2990. DOI: 10.1021/cm400796u (cit. on p. 48).
- [145] Fluxim. *Paios 4, Flexible Contacting*. URL: <https://www.fluxim.com/paios%7B%5C%7Dflexible-device-contacting> (cit. on p. 57).
- [146] R. Brinser. *PDF 2.0 release: should we bid farewell to XFA forms?* 2017. URL: <http://blog.pdfshareforms.com/pdf-2-0-release-bid-farewell-xfa-forms/> (cit. on p. 58).
- [147] Nature Research. *Solar Cells Reporting Summary*. 2017. URL: <https://www.nature.com/nmat/for-authors/preparing-your-submission> (cit. on p. 58).
- [148] J. A. Christians, J. S. Manser, and P. V. Kamat. “Best Practices in Perovskite Solar Cell Efficiency Measurements. Avoiding the Error of Making Bad Cells Look Good”. In: *The Journal of Physical Chemistry Letters* 6.5 (Mar. 2015), pp. 852–857. DOI: 10.1021/acs.jpclett.5b00289 (cit. on pp. 58, 62).
- [149] M. O’Kane. *Perovskite Solar Cells: Causes of Degradation*. 2019. URL: <https://www.ossila.com/pages/perovskite-solar-cell-degradation-causes> (cit. on p. 58).
- [150] D. R. Ceratti, Y. Rakita, L. Cremonesi, R. Tenne, V. Kalchenko, M. Elbaum, D. Oron, M. A. C. Potenza, G. Hodes, and D. Cahen. “Self-Healing Inside APbBr<sub>3</sub> Halide Perovskite Crystals”. In: *Advanced Materials* 30.10 (Mar. 2018), p. 1706273. DOI: 10.1002/adma.201706273 (cit. on p. 58).
- [151] E. Knapp and B. Ruhstaller. “Analysis of negative capacitance and self-heating in organic semiconductor devices”. In: *Journal of Applied Physics* 117.13 (Apr. 2015), p. 135501. DOI: 10.1063/1.4916981 (cit. on pp. 58, 142).

- [152] I. Levine, S. Gupta, A. Bera, D. Ceratti, G. Hodes, D. Cahen, D. Guo, T. J. Savenije, J. Ávila, H. J. Bolink, O. Millo, D. Azulay, and I. Balberg. “Can we use time-resolved measurements to get steady-state transport data for halide perovskites?” In: *Journal of Applied Physics* 124.10 (Sept. 2018), p. 103103. DOI: 10.1063/1.5037637. arXiv: 1805.00263 (cit. on p. 59).
- [153] Edinburgh Instruments. *Pulsed LEDs - UV/VIS*. 2019. URL: <https://www.edinst.com/products/picosecond-pulsed-led/> (cit. on p. 59).
- [154] S. G. Motti, M. Gandini, A. J. Barker, J. M. Ball, A. R. Srimath Kandada, and A. Petrozza. “Photoinduced Emissive Trap States in Lead Halide Perovskite Semiconductors”. In: *ACS Energy Letters* 1.4 (Oct. 2016), pp. 726–730. DOI: 10.1021/acsenergylett.6b00355 (cit. on p. 59).
- [155] S. Chen, X. Wen, S. Huang, R. Sheng, M. A. Green, and A. Ho-Baillie. “Illumination dependent carrier dynamics of CH<sub>3</sub>NH<sub>3</sub>PbBr<sub>3</sub> perovskite”. In: *SPIE Micro+Nano Materials, Devices, and Applications*. Ed. by B. J. Eggleton and S. Palomba. Dec. 2015, 96681R. DOI: 10.1117/12.202176 (cit. on p. 59).
- [156] S. Chen, X. Wen, S. Huang, F. Huang, Y.-B. Cheng, M. Green, and A. Ho-Baillie. “Light Illumination Induced Photoluminescence Enhancement and Quenching in Lead Halide Perovskite”. In: *Solar RRL* 1.1 (Jan. 2017), p. 1600001. DOI: 10.1002/solr.201600001 (cit. on p. 59).
- [157] C. Li, S. Tscheuschner, F. Paulus, P. E. Hopkinson, J. Kießling, A. Köhler, Y. Vaynzof, and S. Huettner. “Iodine Migration and its Effect on Hysteresis in Perovskite Solar Cells”. In: *Advanced Materials* 28.12 (Mar. 2016), pp. 2446–2454. DOI: 10.1002/adma.201503832 (cit. on p. 60).
- [158] H. J. Snaith, A. Abate, J. M. Ball, G. E. Eperon, T. Leijtens, N. K. Noel, S. D. Stranks, J. T.-W. Wang, K. Wojciechowski, and W. Zhang. “Anomalous Hysteresis in Perovskite Solar Cells”. In: *The Journal of Physical Chemistry Letters* 5.9 (May 2014), pp. 1511–1515. DOI: 10.1021/jz500113x (cit. on p. 60).
- [159] Y. Zhang, M. Liu, G. E. Eperon, T. C. Leijtens, D. McMeekin, M. Saliba, W. Zhang, M. de Bastiani, A. Petrozza, L. M. Herz, M. B. Johnston, H. Lin, and H. J. Snaith. “Charge selective contacts, mobile ions and anomalous hysteresis in organic–inorganic perovskite solar cells”. In: *Materials Horizons* 2.3 (2015), pp. 315–322. DOI: 10.1039/C4MH00238E (cit. on p. 60).

- [160] T. Du, J. Kim, J. Ngiam, S. Xu, P. R. F. Barnes, J. R. Durrant, and M. A. McLachlan. "Elucidating the Origins of Subgap Tail States and Open-Circuit Voltage in Methylammonium Lead Triiodide Perovskite Solar Cells". In: *Advanced Functional Materials* 28.32 (Aug. 2018), p. 1801808. DOI: [10.1002/adfm.201801808](https://doi.org/10.1002/adfm.201801808) (cit. on pp. 60, 61, 70, 74, 85, 92, 94, 96, 104).
- [161] J. P. Correa Baena, L. Steier, W. Tress, M. Saliba, S. Neutzner, T. Matsui, F. Giordano, T. J. Jacobsson, A. R. Srimath Kandada, S. M. Zakeeruddin, A. Petrozza, A. Abate, M. K. Nazeeruddin, M. Grätzel, and A. Hagfeldt. "Highly efficient planar perovskite solar cells through band alignment engineering". In: *Energy & Environmental Science* 8.10 (2015), pp. 2928–2934. DOI: [10.1039/C5EE02608C](https://doi.org/10.1039/C5EE02608C) (cit. on p. 60).
- [162] D. Walter, A. Fell, Y. Wu, T. Duong, C. Barugkin, N. Wu, T. White, and K. Weber. "Transient Photovoltage in Perovskite Solar Cells: Interaction of Trap-Mediated Recombination and Migration of Multiple Ionic Species". In: *The Journal of Physical Chemistry C* 122.21 (May 2018), pp. 11270–11281. DOI: [10.1021/acs.jpcc.8b02529](https://doi.org/10.1021/acs.jpcc.8b02529) (cit. on p. 60).
- [163] E. Zimmermann, K. K. Wong, M. Müller, H. Hu, P. Ehrenreich, M. Kohlstädt, U. Würfel, S. Mastrianni, G. Mathiazhagan, A. Hinsch, T. P. Gujar, M. Thelakkat, T. Pfadler, and L. Schmidt-Mende. "Characterization of perovskite solar cells: Towards a reliable measurement protocol". In: *APL Materials* 4.9 (Sept. 2016), p. 091901. DOI: [10.1063/1.4960759](https://doi.org/10.1063/1.4960759) (cit. on pp. 61, 62, 210).
- [164] D. Pysch, A. Mette, and S. Glunz. "A review and comparison of different methods to determine the series resistance of solar cells". In: *Solar Energy Materials and Solar Cells* 91.18 (Nov. 2007), pp. 1698–1706. DOI: [10.1016/j.solmat.2007.05.026](https://doi.org/10.1016/j.solmat.2007.05.026) (cit. on pp. 61, 196).
- [165] M. Christoforo, E. Hoke, M. McGehee, and E. Unger. "Transient Response of Organo-Metal-Halide Solar Cells Analyzed by Time-Resolved Current-Voltage Measurements". In: *Photonics* 2.4 (Nov. 2015), pp. 1101–1115. DOI: [10.3390/photonics2041101](https://doi.org/10.3390/photonics2041101) (cit. on p. 62).
- [166] R. B. Dunbar, B. C. Duck, T. Moriarty, K. F. Anderson, N. W. Duffy, C. J. Fell, J. Kim, A. Ho-Baillie, D. Vak, T. Duong, Y. Wu, K. Weber, A. Pascoe, Y.-B. Cheng, Q. Lin, P. L. Burn, R. Bhattacharjee, H. Wang, and G. J. Wilson. "How reliable are efficiency measurements of perovskite solar cells? The first inter-comparison, between two accredited and eight non-accredited laboratories". In: *Journal of Materials Chemistry A* 5.43 (2017), pp. 22542–22558. DOI: [10.1039/C7TA05609E](https://doi.org/10.1039/C7TA05609E) (cit. on p. 62).

- [167] R. B. Dunbar, W. Moustafa, A. R. Pascoe, T. W. Jones, K. F. Anderson, Y.-B. Cheng, C. J. Fell, and G. J. Wilson. “Device pre-conditioning and steady-state temperature dependence of CH<sub>3</sub>NH<sub>3</sub>PbI<sub>3</sub> perovskite solar cells”. In: *Progress in Photovoltaics: Research and Applications* 25.7 (July 2017), pp. 533–544. DOI: [10.1002/pip.2839](https://doi.org/10.1002/pip.2839) (cit. on p. 62).
- [168] D. Credginton, R. Hamilton, P. Atienzar, J. Nelson, and J. R. Durrant. “Non-Geminate Recombination as the Primary Determinant of Open-Circuit Voltage in Polythiophene:Fullerene Blend Solar Cells: an Analysis of the Influence of Device Processing Conditions”. In: *Advanced Functional Materials* 21.14 (July 2011), pp. 2744–2753. DOI: [10.1002/adfm.201100225](https://doi.org/10.1002/adfm.201100225) (cit. on pp. 63, 72, 91).
- [169] K. Tvingstedt and C. Deibel. “Temperature Dependence of Ideality Factors in Organic Solar Cells and the Relation to Radiative Efficiency”. In: *Advanced Energy Materials* 6.9 (May 2016), p. 1502230. DOI: [10.1002/aenm.201502230](https://doi.org/10.1002/aenm.201502230) (cit. on p. 63).
- [170] T. Kirchartz and J. Nelson. “Meaning of reaction orders in polymer:fullerene solar cells”. In: *Physical Review B* 86.16 (Oct. 2012), p. 165201. DOI: [10.1103/PhysRevB.86.165201](https://doi.org/10.1103/PhysRevB.86.165201) (cit. on pp. 64, 65, 70, 74, 85, 94).
- [171] K. Tvingstedt, L. Gil-Escríg, C. Momblona, P. Rieder, D. Kiermasch, M. Sessolo, A. Baumann, H. J. Bolink, and V. Dyakonov. “Removing Leakage and Surface Recombination in Planar Perovskite Solar Cells”. In: *ACS Energy Letters* 2.2 (Feb. 2017), pp. 424–430. DOI: [10.1021/acsenergylett.6b00719](https://doi.org/10.1021/acsenergylett.6b00719) (cit. on pp. 64, 89, 91, 112).
- [172] T. Kirchartz, B. E. Pieters, J. Kirkpatrick, U. Rau, and J. Nelson. “Recombination via tail states in polythiophene:fullerene solar cells”. In: *Physical Review B* 83.11 (Mar. 2011), p. 115209. DOI: [10.1103/PhysRevB.83.115209](https://doi.org/10.1103/PhysRevB.83.115209) (cit. on p. 65).
- [173] O. Breitenstein, P. Altermatt, K. Ramspeck, and A. Schenk. “The Origin of Ideality factors  $n > 2$  of Shunts and Surfaces in the Dark I-V Curves of Si Solar Cells”. In: *Proceedings of the 21st European photovoltaic solar energy conference* (2006), pp. 625–628 (cit. on p. 65).
- [174] N. W. Duffy, L. M. Peter, R. M. G. Rajapakse, and K. G. U. Wijayantha. “Investigation of the Kinetics of the Back Reaction of Electrons with Tri-Iodide in Dye-Sensitized Nanocrystalline Photovoltaic Cells”. In: *The Journal of Physical Chemistry B* 104.38 (Sept. 2000), pp. 8916–8919. DOI: [10.1021/jp001185z](https://doi.org/10.1021/jp001185z) (cit. on p. 66).

- [175] P. R. F. Barnes, A. Y. Anderson, M. Juozapavicius, L. Liu, X. Li, E. Palomares, A. Forneli, and B. C. O'Regan. "Factors controlling charge recombination under dark and light conditions in dye sensitised solar cells". In: *Phys. Chem. Chem. Phys.* 13.8 (2011), pp. 3547–3558. DOI: 10.1039/C0CP01855D (cit. on pp. 66, 94).
- [176] B. C. O'Regan, S. Scully, A. C. Mayer, E. Palomares, and J. Durrant. "The effect of Al<sub>2</sub>O<sub>3</sub> barrier layers in TiO<sub>2</sub>/dye/CuSCN photovoltaic cells explored by recombination and DOS characterization using transient photovoltage measurements." In: *The Journal of Physical Chemistry B* 109.10 (Mar. 2005), pp. 4616–4623. DOI: 10.1021/jp0468049 (cit. on pp. 66, 79, 98, 101).
- [177] M. Maechler, P. Rousseeuw, C. Croux, V. Todorov, A. Ruckstuhl, M. Salibian-Barrera, T. Verbeke, M. Koller, E. Concicão, and M. Anna di Palma. *robustbase: Basic robust statistics R package version 0.93-5*. 2019. URL: <http://robustbase.r-forge.r-project.org/> (cit. on pp. 69, 207).
- [178] B. E. Pieters, H. Stiebig, M. Zeman, and R. A. C. M. M. van Swaaij. "Determination of the mobility gap of intrinsic  $\mu$ c-Si:H in p-i-n solar cells". In: *Journal of Applied Physics* 105.4 (Feb. 2009), p. 044502. DOI: 10.1063/1.3078044 (cit. on p. 70).
- [179] N. F. Montcada, M. Méndez, K. T. Cho, M. K. Nazeeruddin, and E. Palomares. "Photo-induced dynamic processes in perovskite solar cells: the influence of perovskite composition in the charge extraction and the carrier recombination". In: *Nanoscale* 10.13 (2018), pp. 6155–6158. DOI: 10.1039/C8NR00180D (cit. on p. 72).
- [180] J. W. Ryan and E. Palomares. "Photo-Induced Charge Carrier Recombination Kinetics in Small Molecule Organic Solar Cells and the Influence of Film Nanomorphology". In: *Advanced Energy Materials* 7.10 (May 2017), p. 1601509. DOI: 10.1002/aenm.201601509 (cit. on pp. 72, 74).
- [181] D. Credgington, S.-W. Liu, J. Nelson, and J. R. Durrant. "In Situ Measurement of Energy Level Shifts and Recombination Rates in Subphthalocyanine/C<sub>60</sub> Bilayer Solar Cells". In: *The Journal of Physical Chemistry C* 118.40 (Oct. 2014), pp. 22858–22864. DOI: 10.1021/jp50297u (cit. on pp. 72, 74, 89, 98, 99).
- [182] L. Barnea-Nehoshtan, S. Kirmayer, E. Edri, G. Hodes, and D. Cahen. "Surface Photovoltage Spectroscopy Study of Organo-Lead Perovskite Solar Cells". In: *The Journal of Physical Chemistry Letters* 5.14 (July 2014), pp. 2408–2413. DOI: 10.1021/jz501163r (cit. on p. 72).

- [183] C. G. Shuttle, A. Maurano, R. Hamilton, B. O'Regan, J. C. de Mello, and J. R. Durrant. "Charge extraction analysis of charge carrier densities in a polythiophene/fullerene solar cell: Analysis of the origin of the device dark current". In: *Applied Physics Letters* 93.18 (Nov. 2008), p. 183501. DOI: 10.1063/1.3006316 (cit. on pp. 73, 101).
- [184] C. G. Shuttle, A. Maurano, R. Hamilton, B. O'Regan, J. C. de Mello, and J. R. Durrant. *EPAPS Document No. E-APPLAB-93-043843*. 2008. URL: [http://ftp.aip.org/epaps/app1%7B%5C\\_%7Dphys%7B%5C\\_%7Dlett/E-APPLAB-93-043843/Supporting%20information043843APL.pdf](http://ftp.aip.org/epaps/app1%7B%5C_%7Dphys%7B%5C_%7Dlett/E-APPLAB-93-043843/Supporting%20information043843APL.pdf) (cit. on p. 73).
- [185] J. Ajuria, I. Etxebarria, E. Azaceta, R. Tena-Zaera, N. Fernández-Montcada, E. Palomares, and R. Pacios. "Novel ZnO nanostructured electrodes for higher power conversion efficiencies in polymeric solar cells". In: *Physical Chemistry Chemical Physics* 13.46 (2011), p. 20871. DOI: 10.1039/c1cp22830g (cit. on p. 73).
- [186] F. Deledalle, T. Kirchartz, M. S. Vezie, M. Campoy-Quiles, P. Shakya Tuladhar, J. Nelson, and J. R. Durrant. "Understanding the Effect of Unintentional Doping on Transport Optimization and Analysis in Efficient Organic Bulk-Heterojunction Solar Cells". In: *Physical Review X* 5.1 (Mar. 2015), p. 011032. DOI: 10.1103/PhysRevX.5.011032 (cit. on pp. 74, 85).
- [187] F. Deledalle, P. Shakya Tuladhar, J. Nelson, J. R. Durrant, and T. Kirchartz. "Understanding the Apparent Charge Density Dependence of Mobility and Lifetime in Organic Bulk Heterojunction Solar Cells". In: *The Journal of Physical Chemistry C* 118.17 (May 2014), pp. 8837–8842. DOI: 10.1021/jp502948y (cit. on pp. 74, 85).
- [188] D. Credgington, F. C. Jamieson, B. Walker, T.-Q. Nguyen, and J. R. Durrant. "Quantification of Geminate and Non-Geminate Recombination Losses within a Solution-Processed Small-Molecule Bulk Heterojunction Solar Cell". In: *Advanced Materials* 24.16 (Apr. 2012), pp. 2135–2141. DOI: 10.1002/adma.201104738 (cit. on p. 74).
- [189] V. V. Brus, C. M. Proctor, N. A. Ran, and T.-Q. Nguyen. "Capacitance Spectroscopy for Quantifying Recombination Losses in Nonfullerene Small-Molecule Bulk Heterojunction Solar Cells". In: *Advanced Energy Materials* 6.11 (June 2016), p. 1502250. DOI: 10.1002/aenm.201502250 (cit. on pp. 76, 142).
- [190] C. G. Shuttle, B. O'Regan, A. M. Ballantyne, J. Nelson, D. D. C. Bradley, J. de Mello, and J. R. Durrant. "Experimental determination of the rate law for charge carrier decay in a polythiophene: Fullerene

- solar cell". In: *Applied Physics Letters* 92.9 (Mar. 2008), p. 093311. DOI: 10.1063/1.2891871 (cit. on pp. 79, 83, 91, 94, 98).
- [191] B. C. O'Regan and F. Lenzmann. "Charge Transport and Recombination in a Nanoscale Interpenetrating Network of n-Type and p-Type Semiconductors: Transient Photocurrent and Photovoltage Studies of TiO<sub>2</sub>/Dye/CuSCN Photovoltaic Cells". In: *The Journal of Physical Chemistry B* 108.14 (Apr. 2004), pp. 4342–4350. DOI: 10.1021/jp035613n (cit. on pp. 79, 95).
- [192] B. C. O'Regan, K. Bakker, J. Kroeze, H. Smit, P. Sommeling, and J. R. Durrant. "Measuring Charge Transport from Transient Photovoltage Rise Times. A New Tool To Investigate Electron Transport in Nanoparticle Films". In: *The Journal of Physical Chemistry B* 110.34 (Aug. 2006), pp. 17155–17160. DOI: 10.1021/jp062761f (cit. on pp. 79, 98, 101).
- [193] V. Roiati, S. Colella, G. Lerario, L. De Marco, A. Rizzo, A. Listorti, and G. Gigli. "Investigating charge dynamics in halide perovskite-sensitized mesostructured solar cells". In: *Energy Environ. Sci.* 7.6 (2014), pp. 1889–1894. DOI: 10.1039/C3EE43991G (cit. on p. 79).
- [194] J. M. Marin-Beloqui, J. P. Hernández, and E. Palomares. "Photo-induced charge recombination kinetics in MAPbI<sub>3</sub>-xCl<sub>x</sub> perovskite-like solar cells using low band-gap polymers as hole conductors". In: *Chem. Commun.* 50.93 (Oct. 2014), pp. 14566–14569. DOI: 10.1039/C4CC06338D (cit. on p. 79).
- [195] Radiant Dyes Laser. *List of Laser Dyes*. URL: <https://www.radiant-dyes.com/index.php/products/laser-dyes/list-of-laser-dyes> (cit. on p. 79).
- [196] W. Tress, J. P. Correa Baena, M. Saliba, A. Abate, and M. Graetzel. "Inverted Current-Voltage Hysteresis in Mixed Perovskite Solar Cells: Polarization, Energy Barriers, and Defect Recombination". In: *Advanced Energy Materials* 6.19 (Oct. 2016), p. 1600396. DOI: 10.1002/aenm.201600396 (cit. on pp. 79, 142).
- [197] L. Bertoluzzi, R. S. Sanchez, L. Liu, J.-W. Lee, E. Mas-Marza, H. Han, N.-G. Park, I. Mora-Sero, and J. Bisquert. "Cooperative kinetics of depolarization in CH<sub>3</sub>NH<sub>3</sub>PbI<sub>3</sub> perovskite solar cells". In: *Energy & Environmental Science* 8.3 (2015), pp. 910–915. DOI: 10.1039/C4EE03171G (cit. on p. 83).
- [198] M. P. Eng, P. R. F. Barnes, and J. R. Durrant. "Concentration-Dependent Hole Mobility and Recombination Coefficient in Bulk Heterojunctions Determined from Transient Absorption Spectroscopy". In: *The Journal of Physical Chemistry Letters* 1.20 (Oct. 2010), pp. 3096–3100. DOI: 10.1021/jz1011803 (cit. on p. 85).

- [199] C. G. Shuttle, R. Hamilton, J. Nelson, B. C. O'Regan, and J. R. Durrant. "Measurement of Charge-Density Dependence of Carrier Mobility in an Organic Semiconductor Blend". In: *Advanced Functional Materials* 20.5 (Mar. 2010), pp. 698–702. DOI: [10.1002/adfm.200901734](https://doi.org/10.1002/adfm.200901734) (cit. on p. 85).
- [200] C. Deibel, A. Wagenpfahl, and V. Dyakonov. "Origin of reduced polaron recombination in organic semiconductor devices". In: *Physical Review B* 80.7 (Aug. 2009), p. 075203. DOI: [10.1103/PhysRevB.80.075203](https://doi.org/10.1103/PhysRevB.80.075203) (cit. on p. 85).
- [201] G. Y. Kim, A. Senocrate, T.-Y. Yang, G. Gregori, M. Grätzel, and J. Maier. "Large tunable photoeffect on ion conduction in halide perovskites and implications for photodecomposition". In: *Nature Materials* 17.5 (May 2018), pp. 445–449. DOI: [10.1038/s41563-018-0038-0](https://doi.org/10.1038/s41563-018-0038-0) (cit. on p. 88).
- [202] C. G. Shuttle, B. O'Regan, A. M. Ballantyne, J. Nelson, D. D. C. Bradley, and J. R. Durrant. "Bimolecular recombination losses in polythiophene: Fullerene solar cells". In: *Physical Review B* 78.11 (Sept. 2008), p. 113201. DOI: [10.1103/PhysRevB.78.113201](https://doi.org/10.1103/PhysRevB.78.113201) (cit. on p. 91).
- [203] E. H. Hellen. "Verifying the diode-capacitor circuit voltage decay". In: *American Journal of Physics* 71.8 (Aug. 2003), pp. 797–800. DOI: [10.1119/1.1578070](https://doi.org/10.1119/1.1578070) (cit. on p. 91).
- [204] L. Castaner, E. Vilamajo, J. Llaberia, and J. Garrido. "Investigations of the OCVD transients in solar cells". In: *Journal of Physics D: Applied Physics* 14.10 (Oct. 1981), pp. 1867–1876. DOI: [10.1088/0022-3727/14/10/019](https://doi.org/10.1088/0022-3727/14/10/019) (cit. on p. 91).
- [205] S. Lederhandler and L. Giacoletto. "Measurement of Minority Carrier Lifetime and Surface Effects in Junction Devices". In: *Proceedings of the IRE* 43.4 (1955), pp. 477–483. DOI: [10.1109/JRPROC.1955.277857](https://doi.org/10.1109/JRPROC.1955.277857) (cit. on p. 91).
- [206] J. Mahan and D. Barnes. "Depletion layer effects in the open-circuit-voltage-decay lifetime measurement". In: *Solid-State Electronics* 24.10 (Oct. 1981), pp. 989–994. DOI: [10.1016/0038-1101\(81\)90124-6](https://doi.org/10.1016/0038-1101(81)90124-6) (cit. on p. 91).
- [207] B. C. O'Regan, J. R. Durrant, P. M. Sommeling, and N. J. Bakker. "Influence of the TiCl<sub>4</sub> Treatment on Nanocrystalline TiO<sub>2</sub> Films in Dye-Sensitized Solar Cells. 2. Charge Density, Band Edge Shifts, and Quantification of Recombination Losses at Short Circuit". In: *The Journal of Physical Chemistry C* 111.37 (Sept. 2007), pp. 14001–14010. DOI: [10.1021/jp073056p](https://doi.org/10.1021/jp073056p) (cit. on p. 94).

- [208] P. R. F. Barnes, A. Y. Anderson, J. R. Durrant, and B. C. O'Regan. "Simulation and measurement of complete dye sensitised solar cells: including the influence of trapping, electrolyte, oxidised dyes and light intensity on steady state and transient device behaviour". In: *Physical Chemistry Chemical Physics* 13.13 (2011), p. 5798. DOI: 10.1039/c0cp01554g (cit. on pp. 94, 104).
- [209] D. Kiermasch, L. Gil-Escriv, A. Baumann, H. J. Bolink, V. Dyakonov, and K. Tvingstedt. "Unravelling steady-state bulk recombination dynamics in thick efficient vacuum-deposited perovskite solar cells by transient methods". In: *Journal of Materials Chemistry A* 7.24 (2019), pp. 14712–14722. DOI: 10.1039/C9TA04367E (cit. on p. 94).
- [210] R. A. Belisle, W. H. Nguyen, A. R. Bowring, P. Calado, X. Li, S. J. C. Irvine, M. D. McGehee, P. R. F. Barnes, and B. C. O'Regan. "Interpretation of inverted photocurrent transients in organic lead halide perovskite solar cells: proof of the field screening by mobile ions and determination of the space charge layer widths". In: *Energy Environ. Sci.* 13.1 (2017), p. 6050. DOI: 10.1039/C6EE02914K (cit. on pp. 95, 181).
- [211] Wikipedia. *Capacitance*. 2019. URL: <https://en.wikipedia.org/wiki/Capacitance> (cit. on p. 98).
- [212] S. Wheeler, F. Deledalle, N. Tokmoldin, T. Kirchartz, J. Nelson, and J. R. Durrant. "Influence of Surface Recombination on Charge-Carrier Kinetics in Organic Bulk Heterojunction Solar Cells with Nickel Oxide Interlayers". In: *Physical Review Applied* 4.2 (2015), p. 024020. DOI: 10.1103/PhysRevApplied.4.024020 (cit. on pp. 104, 134).
- [213] Q. Jiang, X. Zhang, and J. You. "SnO<sub>2</sub>: A Wonderful Electron Transport Layer for Perovskite Solar Cells". In: *Small* 14.31 (Aug. 2018), p. 1801154. DOI: 10.1002/smll.201801154 (cit. on p. 109).
- [214] M. Saliba, T. Matsui, J.-Y. Seo, K. Domanski, J.-P. Correa-Baena, M. K. Nazeeruddin, S. M. Zakeeruddin, W. Tress, A. Abate, A. Hagfeldt, and M. Grätzel. "Cesium-containing triple cation perovskite solar cells: improved stability, reproducibility and high efficiency". In: *Energy Environ. Sci.* 9.6 (Aug. 2016), pp. 1989–1997. DOI: 10.1039/C5EE03874J. arXiv: 1408.1149 (cit. on pp. 109, 114, 116).
- [215] C. Rodríguez-Seco, L. Cabau, A. Vidal-Ferran, and E. Palomares. "Advances in the Synthesis of Small Molecules as Hole Transport Materials for Lead Halide Perovskite Solar Cells". In: *Accounts of Chemical Research* 51.4 (Apr. 2018), pp. 869–880. DOI: 10.1021/acs.accounts.7b00597 (cit. on p. 109).

- [216] F. B. Kooistra, J. Knol, F. Kastenberg, L. M. Popescu, W. J. H. Verhees, J. M. Kroon, and J. C. Hummelen. “Increasing the Open Circuit Voltage of Bulk-Heterojunction Solar Cells by Raising the LUMO Level of the Acceptor”. In: *Organic Letters* 9.4 (Feb. 2007), pp. 551–554. DOI: [10.1021/o1062666p](https://doi.org/10.1021/o1062666p) (cit. on p. 109).
- [217] A. Gadisa, M. Svensson, M. R. Andersson, and O. Inganäs. “Correlation between oxidation potential and open-circuit voltage of composite solar cells based on blends of polythiophenes/fullerene derivative”. In: *Applied Physics Letters* 84.9 (Mar. 2004), pp. 1609–1611. DOI: [10.1063/1.1650878](https://doi.org/10.1063/1.1650878) (cit. on p. 109).
- [218] C. J. Brabec, A. Cravino, D. Meissner, N. S. Sariciftci, T. Fromherz, M. T. Rispens, L. Sanchez, and J. C. Hummelen. “Origin of the Open Circuit Voltage of Plastic Solar Cells”. In: *Advanced Functional Materials* 11.5 (Oct. 2001), pp. 374–380. DOI: [10.1002/1616-3028\(200110\)11:5<374::AID-ADFM374>3.0.CO;2-W](https://doi.org/10.1002/1616-3028(200110)11:5<374::AID-ADFM374>3.0.CO;2-W) (cit. on p. 109).
- [219] A. Wilke, J. Endres, U. Hörmann, J. Niederhausen, R. Schlesinger, J. Frisch, P. Amsalem, J. Wagner, M. Gruber, A. Opitz, A. Vollmer, W. Brütting, A. Kahn, and N. Koch. “Correlation between interface energetics and open circuit voltage in organic photovoltaic cells”. In: *Applied Physics Letters* 101.23 (Dec. 2012), p. 233301. DOI: [10.1063/1.4769360](https://doi.org/10.1063/1.4769360) (cit. on p. 109).
- [220] H.-Y. Chen, J. Hou, S. Zhang, Y. Liang, G. Yang, Y. Yang, L. Yu, Y. Wu, and G. Li. “Polymer solar cells with enhanced open-circuit voltage and efficiency”. In: *Nature Photonics* 3.11 (Nov. 2009), pp. 649–653. DOI: [10.1038/nphoton.2009.192](https://doi.org/10.1038/nphoton.2009.192) (cit. on p. 109).
- [221] W. Tress, K. Leo, and M. Riede. “Influence of Hole-Transport Layers and Donor Materials on Open-Circuit Voltage and Shape of I-V Curves of Organic Solar Cells”. In: *Advanced Functional Materials* 21.11 (June 2011), pp. 2140–2149. DOI: [10.1002/adfm.201002669](https://doi.org/10.1002/adfm.201002669) (cit. on p. 109).
- [222] A. Sánchez-Díaz, M. Izquierdo, S. Filippone, N. Martin, and E. Palomares. “The Origin of the High Voltage in DPM12/P3HT Organic Solar Cells.” In: *Advanced Functional Materials* 20.16 (Aug. 2010), pp. 2695–2700. DOI: [10.1002/adfm.201000549](https://doi.org/10.1002/adfm.201000549) (cit. on p. 109).
- [223] L. E. Polander, P. Pahner, M. Schwarze, M. Saalfrank, C. Koerner, and K. Leo. “Hole-transport material variation in fully vacuum deposited perovskite solar cells”. In: *APL Materials* 2.8 (Aug. 2014), p. 081503. DOI: [10.1063/1.4889843](https://doi.org/10.1063/1.4889843) (cit. on p. 109).

- [224] A. Abate, M. Planells, D. J. Hollman, V. Barthi, S. Chand, H. J. Snaith, and N. Robertson. “Hole-transport materials with greatly-differing redox potentials give efficient TiO<sub>2</sub>-[CH<sub>3</sub>NH<sub>3</sub>][PbX<sub>3</sub>] perovskite solar cells”. In: *Physical Chemistry Chemical Physics* 17.4 (2015), pp. 2335–2338. DOI: [10.1039/C4CP04685D](https://doi.org/10.1039/C4CP04685D) (cit. on p. 109).
- [225] Y. S. Kwon, J. Lim, H.-J. Yun, Y.-H. Kim, and T. Park. “Diketopyrrolopyrrole-containing hole transporting conjugated polymer for use in efficient stable organic-inorganic hybrid solar cells based on a perovskite”. In: *Energy & Environmental Science* 7.4 (2014), p. 1454. DOI: [10.1039/c3ee44174a](https://doi.org/10.1039/c3ee44174a) (cit. on p. 109).
- [226] K. Rakstys, A. Abate, M. I. Dar, P. Gao, V. Jankauskas, G. Jacopin, E. Kamarauskas, S. Kazim, S. Ahmad, M. Grätzel, and M. K. Nazeeruddin. “Triazatruxene-Based Hole Transporting Materials for Highly Efficient Perovskite Solar Cells”. In: *Journal of the American Chemical Society* 137.51 (Dec. 2015), pp. 16172–16178. DOI: [10.1021/jacs.5b11076](https://doi.org/10.1021/jacs.5b11076) (cit. on p. 109).
- [227] F. Wu, J. Liu, G. Wang, Q. Song, and L. Zhu. “m -Methoxy Substituents in a Tetraphenylethylene-Based Hole-Transport Material for Efficient Perovskite Solar Cells”. In: *Chemistry - A European Journal* 22.46 (Nov. 2016), pp. 16636–16641. DOI: [10.1002/chem.201603672](https://doi.org/10.1002/chem.201603672) (cit. on p. 109).
- [228] N. Ishida, A. Wakamiya, and A. Saeki. “Quantifying Hole Transfer Yield from Perovskite to Polymer Layer: Statistical Correlation of Solar Cell Outputs with Kinetic and Energetic Properties”. In: *ACS Photonics* 3.9 (Sept. 2016), pp. 1678–1688. DOI: [10.1021/acspophotonics.6b00331](https://doi.org/10.1021/acspophotonics.6b00331) (cit. on p. 109).
- [229] S. M. Park, S. M. Mazza, Z. Liang, A. Abtahi, A. M. Boehm, S. R. Parkin, J. E. Anthony, and K. R. Graham. “Processing Dependent Influence of the Hole Transport Layer Ionization Energy on Methylammonium Lead Iodide Perovskite Photovoltaics”. In: *ACS Applied Materials & Interfaces* 10.18 (May 2018), pp. 15548–15557. DOI: [10.1021/acsami.7b16894](https://doi.org/10.1021/acsami.7b16894) (cit. on p. 109).
- [230] A. E. Labban, H. Chen, M. Kirkus, J. Barbe, S. Del Gobbo, M. Neophytou, I. McCulloch, and J. Eid. “Improved Efficiency in Inverted Perovskite Solar Cells Employing a Novel Diarylamino-Substituted Molecule as PEDOT:PSS Replacement”. In: *Advanced Energy Materials* 6.11 (June 2016), p. 1502101. DOI: [10.1002/aenm.201502101](https://doi.org/10.1002/aenm.201502101) (cit. on p. 109).

- [231] F. Wu, B. Wang, R. Wang, Y. Shan, D. Liu, K. Y. Wong, T. Chen, and L. Zhu. “Investigation on a dopant-free hole transport material for perovskite solar cells”. In: *RSC Advances* 6.73 (2016), pp. 69365–69369. DOI: 10.1039/C6RA07603C (cit. on p. 109).
- [232] C. Tao, J. Van Der Velden, L. Cabau, N. F. Montcada, S. Neutzner, A. R. Srimath Kandada, S. Marras, L. Brambilla, M. Tommasini, W. Xu, R. Sorrentino, A. Perinot, M. Cairoli, C. Bertarelli, E. Palomares, and A. Petrozza. “Fully Solution-Processed n-i-p-Like Perovskite Solar Cells with Planar Junction: How the Charge Extracting Layer Determines the Open-Circuit Voltage”. In: *Advanced Materials* 29.15 (Apr. 2017), p. 1604493. DOI: 10.1002/adma.201604493 (cit. on p. 109).
- [233] C. Bi, Q. Wang, Y. Shao, Y. Yuan, Z. Xiao, and J. Huang. “Non-wetting surface-driven high-aspect-ratio crystalline grain growth for efficient hybrid perovskite solar cells”. In: *Nature Communications* 6.1 (Dec. 2015), p. 7747. DOI: 10.1038/ncomms8747 (cit. on p. 109).
- [234] I. García-Benito. “Molecular engineering of hole and electron transporting materials for perovskite solar cells”. PhD thesis. Universidad Complutense de Madrid, 2017. URL: <https://eprints.ucm.es/45603/> (cit. on p. 111).
- [235] B. W. D’Andrade, S. Datta, S. R. Forrest, P. Djurovich, E. Polikarpov, and M. E. Thompson. “Relationship between the ionization and oxidation potentials of molecular organic semiconductors”. In: *Organic Electronics* 6.1 (Feb. 2005), pp. 11–20. DOI: 10.1016/j.orgel.2005.01.002 (cit. on p. 112).
- [236] B. Wei, K. Zheng, Y. Ji, Y. Zhang, Z. Zhang, and X. Han. “Size-Dependent Bandgap Modulation of ZnO Nanowires by Tensile Strain”. In: *Nano Letters* 12.9 (Sept. 2012), pp. 4595–4599. DOI: 10.1021/nl301897q (cit. on p. 112).
- [237] Y. Kashimoto, K. Yonezawa, M. Meissner, M. Gruenewald, T. Ueba, S. Kera, R. Forker, T. Fritz, and H. Yoshida. “The Evolution of Intermolecular Energy Bands of Occupied and Unoccupied Molecular States in Organic Thin Films”. In: *The Journal of Physical Chemistry C* 122.22 (June 2018), pp. 12090–12097. DOI: 10.1021/acs.jpcc.8b02581 (cit. on p. 112).
- [238] Wikipedia. *Tauc plot*. 2019. URL: [https://en.wikipedia.org/wiki/Tauc%7B%5C\\_%7Dplot](https://en.wikipedia.org/wiki/Tauc%7B%5C_%7Dplot) (cit. on p. 112).

- [239] E. M. Miller, Y. Zhao, C. C. Mercado, S. K. Saha, J. M. Luther, K. Zhu, V. Stevanović, C. L. Perkins, and J. van de Lagemaat. “Substrate-controlled band positions in CH<sub>3</sub>NH<sub>3</sub>PbI<sub>3</sub> perovskite films”. In: *Phys. Chem. Chem. Phys.* 16.40 (Sept. 2014), pp. 22122–22130. DOI: 10.1039/C4CP03533J (cit. on p. 122).
- [240] S. Olthof and K. Meerholz. “Substrate-dependent electronic structure and film formation of MAPbI<sub>3</sub> perovskites”. In: *Scientific Reports* 7.1 (Dec. 2017), p. 40267. DOI: 10.1038/srep40267 (cit. on p. 122).
- [241] A. Pérez-Rodríguez. “Nanoscale interpretation of performances in organic solar cells and field effect transistors”. PhD thesis. Universitat Autònoma de Barcelona, 2018. URL: <https://www.tesisenred.net/handle/10803/565824%20https://ddd.uab.cat/record/195368> (cit. on p. 122).
- [242] J. Schindelin, I. Arganda-Carreras, E. Frise, V. Kaynig, M. Longair, T. Pietzsch, S. Preibisch, C. Rueden, S. Saalfeld, B. Schmid, J.-Y. Tinevez, D. J. White, V. Hartenstein, K. Eliceiri, P. Tomancak, and A. Cardona. “Fiji: an open-source platform for biological-image analysis”. In: *Nature Methods* 9.7 (July 2012), pp. 676–682. DOI: 10.1038/nmeth.2019 (cit. on p. 131).
- [243] E. von Hauff, V. Dyakonov, and J. Parisi. “Study of field effect mobility in PCBM films and P3HT:PCBM blends”. In: *Solar Energy Materials and Solar Cells* 87.1-4 (May 2005), pp. 149–156. DOI: 10.1016/j.solmat.2004.06.014 (cit. on p. 134).
- [244] J. Seo, S. Park, Y. Chan Kim, N. J. Jeon, J. H. Noh, S. C. Yoon, and S. I. Seok. “Benefits of very thin PCBM and LiF layers for solution-processed p-i-n perovskite solar cells”. en. In: *Energy & Environmental Science* 7.8 (July 2014), p. 2642. DOI: 10.1039/C4EE01216J (cit. on p. 135).
- [245] S. A. Rutledge and A. S. Helmy. “Carrier mobility enhancement in poly(3,4-ethylenedioxythiophene)-poly(styrenesulfonate) having undergone rapid thermal annealing”. In: *Journal of Applied Physics* 114.13 (Oct. 2013), p. 133708. DOI: 10.1063/1.4824104 (cit. on p. 137).
- [246] O. Almora, K. T. Cho, S. Aghazada, I. Zimmermann, G. J. Matt, C. J. Brabec, M. K. Nazeeruddin, and G. Garcia-Belmonte. “Discerning recombination mechanisms and ideality factors through impedance analysis of high-efficiency perovskite solar cells”. In: *Nano Energy* 48.February (June 2018), pp. 63–72. DOI: 10.1016/j.nanoen.2018.03.042 (cit. on pp. 142, 155).

- [247] E. Guillén, F. J. Ramos, J. A. Anta, and S. Ahmad. “Elucidating Transport-Recombination Mechanisms in Perovskite Solar Cells by Small-Perturbation Techniques”. In: *The Journal of Physical Chemistry C* 118.40 (Oct. 2014), pp. 22913–22922. DOI: 10.1021/jp5069076 (cit. on pp. 142, 166).
- [248] E. J. Juarez-Perez, R. S. Sanchez, L. Badia, G. Garcia-Belmonte, Y. S. Kang, I. Mora-Sero, and J. Bisquert. “Photoinduced Giant Dielectric Constant in Lead Halide Perovskite Solar Cells”. In: *The Journal of Physical Chemistry Letters* 5.13 (July 2014), pp. 2390–2394. DOI: 10.1021/jz5011169. arXiv: arXiv:1011.1669v3 (cit. on pp. 142, 155, 162).
- [249] H.-S. Kim, I.-H. Jang, N. Ahn, M. Choi, A. Guerrero, J. Bisquert, and N.-G. Park. “Control of I-V Hysteresis in CH<sub>3</sub>NH<sub>3</sub>PbI<sub>3</sub> Perovskite Solar Cell”. In: *The Journal of Physical Chemistry Letters* 6.22 (Nov. 2015), pp. 4633–4639. DOI: 10.1021/acs.jpclett.5b02273 (cit. on pp. 142, 155).
- [250] E. Ghahremanirad, A. Bou, S. Olyaei, and J. Bisquert. “Inductive Loop in the Impedance Response of Perovskite Solar Cells Explained by Surface Polarization Model”. In: *The Journal of Physical Chemistry Letters* 8.7 (Apr. 2017), pp. 1402–1406. DOI: 10.1021/acs.jpclett.7b00415 (cit. on pp. 142, 164).
- [251] A. Guerrero, G. Garcia-Belmonte, I. Mora-Sero, J. Bisquert, Y. S. Kang, T. J. Jacobsson, J.-P. Correa-Baena, and A. Hagfeldt. “Properties of Contact and Bulk Impedances in Hybrid Lead Halide Perovskite Solar Cells Including Inductive Loop Elements”. In: *The Journal of Physical Chemistry C* 120.15 (Apr. 2016), pp. 8023–8032. DOI: 10.1021/acs.jpcc.6b01728 (cit. on pp. 142, 148, 155, 164).
- [252] R. S. Sanchez, V. Gonzalez-Pedro, J.-W. Lee, N.-G. Park, Y. S. Kang, I. Mora-Sero, and J. Bisquert. “Slow Dynamic Processes in Lead Halide Perovskite Solar Cells. Characteristic Times and Hysteresis”. In: *The Journal of Physical Chemistry Letters* 5.13 (July 2014), pp. 2357–2363. DOI: 10.1021/jz5011187 (cit. on pp. 142, 164).
- [253] I. Mora-Seró, J. Bisquert, F. Fabregat-Santiago, G. Garcia-Belmonte, G. Zoppi, K. Durose, Y. Proskuryakov, I. Oja, A. Belaidi, T. Dittrich, R. Tena-Zaera, A. Katty, C. Lévy-Clément, V. Barrio, and S. J. C. Irvine. “Implications of the Negative Capacitance Observed at Forward Bias in Nanocomposite and Polycrystalline Solar Cells”. In: *Nano Letters* 6.4 (Apr. 2006), pp. 640–650. DOI: 10.1021/nl052295q (cit. on p. 142).

- [254] J. Jamnik and J. Maier. “Generalised equivalent circuits for mass and charge transport: chemical capacitance and its implications”. In: *Physical Chemistry Chemical Physics* 3.9 (2001), pp. 1668–1678. DOI: 10.1039/b100180i (cit. on p. 142).
- [255] I. Zarazua, G. Han, P. P. Boix, S. Mhaisalkar, F. Fabregat-Santiago, I. Mora-Seró, J. Bisquert, and G. Garcia-Belmonte. “Surface Recombination and Collection Efficiency in Perovskite Solar Cells from Impedance Analysis”. In: *The Journal of Physical Chemistry Letters* 7.24 (Dec. 2016), pp. 5105–5113. DOI: 10.1021/acs.jpclett.6b02193 (cit. on pp. 142, 155).
- [256] M. García-Rosell, A. Bou, J. A. Jiménez-Tejada, J. Bisquert, and P. Lopez-Varo. “Analysis of the Influence of Selective Contact Heterojunctions on the Performance of Perovskite Solar Cells”. In: *The Journal of Physical Chemistry C* 122.25 (June 2018), pp. 13920–13925. DOI: 10.1021/acs.jpcc.8b01070 (cit. on p. 142).
- [257] P. Lopez-Varo, J. A. Jiménez-Tejada, M. García-Rosell, S. Ravishankar, G. Garcia-Belmonte, J. Bisquert, and O. Almora. “Device Physics of Hybrid Perovskite Solar cells: Theory and Experiment”. In: *Advanced Energy Materials* 8.14 (May 2018), p. 1702772. DOI: 10.1002/aenm.201702772 (cit. on p. 142).
- [258] K. Shimizu, Y. Tanaka, Y. Noguchi, and H. Ishii. “Negative capacitance in an organic solar cell observed by displacement current measurement”. In: *Journal of Physics: Conference Series* 924 (Nov. 2017), p. 012012. DOI: 10.1088/1742-6596/924/1/012012 (cit. on p. 142).
- [259] F. Ebadi, N. Taghavinia, R. Mohammadpour, A. Hagfeldt, and W. Tress. “Origin of apparent light-enhanced and negative capacitance in perovskite solar cells”. In: *Nature Communications* 10.1 (Dec. 2019), p. 1574. DOI: 10.1038/s41467-019-109079-z (cit. on pp. 143, 150, 163, 166).
- [260] K. S. Cole. “Electro-Ionics of Nerve Action”. In: *IRE Transactions on Medical Electronics* PGME-6 (Oct. 1956), pp. 28–48. DOI: 10.1109/IRET-ME.1956.5008582 (cit. on p. 143).
- [261] Wikipedia. *Lock-in amplifier*. 2019. URL: [https://en.wikipedia.org/wiki/Lock-in\\_amplifier](https://en.wikipedia.org/wiki/Lock-in_amplifier) (cit. on p. 147).
- [262] I. Zarazua, J. Bisquert, and G. Garcia-Belmonte. “Light-Induced Space-Charge Accumulation Zone as Photovoltaic Mechanism in Perovskite Solar Cells”. In: *The Journal of Physical Chemistry Letters* 7.3 (Feb. 2016), pp. 525–528. DOI: 10.1021/acs.jpclett.5b02810 (cit. on p. 155).

- [263] R. Schwarz. “Dispersive transport in disordered semiconductors”. In: *Journal of Non-Crystalline Solids* 227-230 (May 1998), pp. 148–152. DOI: 10.1016/S0022-3093(98)00029-5 (cit. on p. 163).
- [264] O. Almora, C. Aranda, E. Mas-Marzá, and G. Garcia-Belmonte. “On Mott-Schottky analysis interpretation of capacitance measurements in organometal perovskite solar cells”. In: *Applied Physics Letters* 109.17 (Oct. 2016), p. 173903. DOI: 10.1063/1.4966127 (cit. on p. 166).
- [265] P. Calado, I. Gelmetti, M. Azzouzi, B. Hilton, and P. R. F. Barnes. *Driftfusion*. 2019. URL: <https://github.com/barnesgroupICL/Drift-fusion> (cit. on p. 181).
- [266] C. Honsberg and S. Bowden. *Measuring Ideality Factor*. 2019. URL: <https://www.pveducation.org/pvcdrom/characterisation/measuring-ideality-factor> (cit. on p. 186).
- [267] National Instruments. *National Instruments VISA*. 2019. URL: <http://www.ni.com/visa/> (cit. on p. 195).
- [268] G. van Rossum, B. Warsaw, and N. Coghlan. *PEP 8 - Style Guide for Python Code*. 2017. URL: <https://www.python.org/dev/peps/pep-008/> (cit. on p. 195).
- [269] Keithley Instruments. *Series 2400 SourceMeter User’s Manual Manual*. 2011. URL: <https://www.tek.com/keithley-source-measure-units/keithley-smu-2400-series-sourcemeter-manual/series-2400-sourcemeter> (cit. on p. 198).
- [270] A. J. Cimaroli, Y. Yu, C. Wang, W. Liao, L. Guan, C. R. Grice, D. Zhao, and Y. Yan. “Tracking the maximum power point of hysteretic perovskite solar cells using a predictive algorithm”. In: *J. Mater. Chem. C* 5.39 (2017), pp. 10152–10157. DOI: 10.1039/C7TC03482B (cit. on p. 210).
- [271] N. Pellet, F. Giordano, M. Ibrahim Dar, G. Gregori, S. M. Zakeeruddin, J. Maier, and M. Grätzel. “Hill climbing hysteresis of perovskite-based solar cells: a maximum power point tracking investigation”. In: *Progress in Photovoltaics: Research and Applications* 25.11 (Nov. 2017), pp. 942–950. DOI: 10.1002/pip.2894. arXiv: 1303.4604 (cit. on p. 210).
- [272] L. Rakocevic, F. Ernst, N. T. Yimga, S. Vashishtha, T. Aernouts, T. Heumueller, C. J. Brabec, R. Gehlhaar, and J. Poortmans. “Reliable Performance Comparison of Perovskite Solar Cells Using Optimized Maximum Power Point Tracking”. In: *Solar RRL* 3.2 (Feb. 2019), p. 1800287. DOI: 10.1002/solr.201800287 (cit. on p. 210).
- [273] CicciResearch srl. 2019. URL: <http://www.cicciresearch.it/> (cit. on p. 210).

- [274] Candlelight Systems. *Stability testing equipment*. URL: <http://candlelight-systems.com/> (cit. on p. 210).
- [275] AFMD. *mppTracker*. 2017. URL: <https://github.com/AFMD/mppTracker> (cit. on p. 210).





